A complete simulation of neutron scattering experiments: From model systems to liquid germanium

Virginie Hugouvieux

ACADEMIE DE MONTPELLIER

Université Montpellier II

– SCIENCES ET TECHNIQUES DU LANGUEDOC –

THESE

présentée à l'Université de Montpellier II Sciences et Techniques du Languedoc
pour obtenir le diplôme de DOCTORAT

Spécialité :	Milieux Denses et Matériaux
Formation Doctorale :	Physique de la Matière Condensée
Ecole Doctorale :	Sciences Chimiques et Physiques

Simulation complète d'une expérience de diffusion de neutrons : des systèmes modèles au germanium liquide.

A complete simulation of neutron scattering experiments: From model systems to liquid germanium.

par

Virginie HUGOUVIEUX

soutenue le 26 novembre 2004 devant le Jury composé de :

Jean-Louis SAUVAJOL	Université Montpellier 2	Président
Robert BELLISSENT	CEA-Grenoble	Rapporteur
Robert L. MCGREEVY	Rutherford Appleton Laboratory	Rapporteur
Andreas MEYER	Technische Universität München	Examinateur
Walter KOB	Université Montpellier II	Directeur de thèse
Mark R. JOHNSON	Institut Laue-Langevin, Grenoble	Directeur de thèse
Emmanuel FARHI	Institut Laue-Langevin, Grenoble	Membre invité

Remerciements

Voilà une aventure de trois ans qui s'achève. Vous êtes nombreux à avoir contribué, de près ou de loin, à ce travail.

Je tiens tout d'abord à remercier chaleureusement mon trio d'encadrants Emmanuel Farhi, Mark Johnson et Walter Kob qui m'ont guidée dans ce sujet qui mettait en jeu chacune de leurs expertises respectives. Tous les trois, vous avez toujours su m'aiguiller dans mon travail et me faire partager vos connaissances tout en me laissant la marge de manoeuvre qui me permettait de progresser à ma façon, en satisfaisant les choix de chacun d'entre vous.

Mes remerciements vont aussi à Messieurs Jean-Louis Sauvajol, Robert Bellissent, Robert McGreevy et Andreas Meyer qui ont accepté de porter un regard critique sur mon travail et de prendre part à mon jury de soutenance.

Je remercie aussi les thésards, techniciens, ingénieurs et chercheurs de l'ILL et du LDV pour leur collaboration et les conversations (scientifiques ou non) que j'ai pu avoir avec eux. Je remercie plus particulièrement Patrick Ganster, Miguel Gonzalez et Magali Benoit pour ce qui concerne les simulations, Paul Martin et Robert Bellissent pour les aspects expérimentaux, et Emanuela Del Gado, Marie Plazanet et Jacques Ollivier. Pour les expériences de diffusion de neutrons, j'ai été aidée par Fanni Juranyi du Paul Scherrer Institute, et par Philippe Bourges et Philippe Boutrouille du Laboratoire Léon Brillouin ; je les remercie vivement pour leur collaboration.

Mes remerciements vont aussi aux membres du groupe CS à l'ILL, Fabien, Julian, Marie-Rose, Alain, Didier, Ron et Christian avec qui j'ai partagé ces trois années. Je remercie aussi Michel Ferrand et Serge Crouzy, qui m'ont fait connaître et apprécier le monde de la recherche.

Je remercie aussi mes amis : les "anciens", Anne (mangue ou passion ?), Laurent, Claire, Lucie, Nicolas et les "nouveaux" Katy, Hala, Antoine, Bruno, Alejandro, Ioana, Clara et Lola. Quel "melting pot" ! Ces trois (six) dernières années à Grenoble auraient été moins amusantes et épanouissantes sans vous tous !
Je remercie aussi Sébastien : à traverser la même "épreuve" en même temps, on se comprend mieux ! Merci pour ton soutien.
Enfin, je n'oublie pas mes parents et Marilen qui m'ont toujours encouragée et laissée libre de choisir ma voie.

Table of contents

Introduction (en français)

Dans la vie de tous les jours, la notion de liquide est familière car elle fait référence à l'un des trois états communs de la matière, avec les états gazeux et solide. Certaines caractéristiques de l'état liquide sont proches de celles de l'état solide, d'autres de l'état gazeux. Comme les solides, les liquides sont très peu compressibles et on associe aux particules d'un liquide une faible énergie cinétique. De façon comparable aux gaz, les liquides ont tendance à couler sous l'effet d'une pression de cisaillement même faible et à prendre la forme du récipent qui les contient. Les liquides sont présents dans une gamme de températures et de pressions relativement réduites, en comparaison des solides et des gaz.
A l'échelle atomique, la phase liquide est compacte et partiellement désordonnée. Pour des atomes approximativement sphériques, comme c'est effectivement le cas pour les gaz rares, seul le désordre de type translationnel est possible. Pour les molécules, qui sont loin d'être sphériques, on peut aussi noter la présence d'un désordre rotationnel.

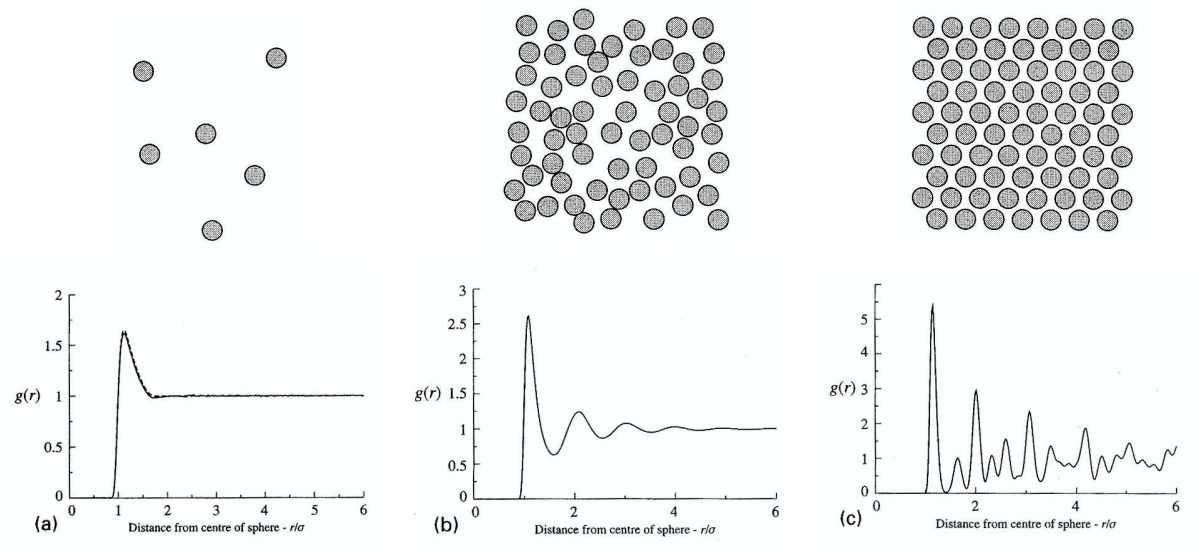

Figure 1: Structure typique d'un gaz (à gauche), d'un liquide (au milieu) et d'un solide (à droite). En haut : configurations atomiques typiques des trois phases. En bas : formes typiques des fonctions de corrélation de paires pour un gas (à gauche), un liquide (au milieu) et un solide (à droite) (extrait de [1]).

Il existe de nombreuses techniques, soit expérimentales, soit théoriques, pour l'investigation

des propriétés structurales et dynamiques des liquides. Sur le plan expérimental, la diffusion de la lumière est une des méthodes les plus accessibles : cette méthode donne des informations sur la structure et la dynamique du matériau car elle sonde à la fois les évolutions spatiales et temporelles. Elle donne accès aux grandes échelles en espace (typiquement de 1 μm à 1 cm) et aux hautes fréquences (de 10^7 à 10^{14} Hz).
Par ailleurs, les grands instruments donnent accès à la diffusion de neutrons et de rayons X. Grâce à ces méthodes, les expérimentateurs peuvent améliorer leur compréhension de l'arrangement structural des atomes ou molécules dans l'échantillon. La figure 1 montre la fonction de corrélation de paires, aussi notée $g(r)$: pour une distance interatomique donnée r, cette fonction donne une mesure de la probabilité de trouver deux atomes à une distance r l'un de l'autre. $g(r)$ donne des informations concernant les corrélations spatiales entre atomes. La fonction $g(r)$ peut être déterminée à partir des données obtenues lors d'expériences de diffraction de neutrons ou de rayons X. Pour un cristal, $g(r)$ a plusieurs pics fins et intenses. Ces pics proviennent des distances interatomiques bien définies qui existent dans un matériau ordonné. Au contraire, pour les gaz la fonction de corrélation de paires ne présente pas de propriétés structurales marquées étant donné qu'il s'agit de systèmes très dilués, sans distance de corrélation bien définie mise à part la condition de non recouvrement des atomes à faibles distances. Dans le cas des liquides, on remarque un premier maximum bien défini et plusieurs oscillations à des distances interatomiques plus élevées. Même si ces caractéristiques sont bien plus larges et moins marquées que dans la phase cristalline, elles démontrent l'existence de distances interatomiques privilégiées dans le liquide. L'élargissement des pics associés aux distances interatomiques prépondérantes dans le liquide (par comparaison au cristal) est la marque d'un système désordonné : les distances interatomiques ne sont pas définies de façon précises comme c'est le cas dans la phase cristalline.

La structure des liquides mais aussi les aspects d'évolution dans le temps, ou aspects dynamiques, peuvent être déterminés par diffusion de neutrons ou de rayons X. Ces techniques donnent accès aux caractéristiques des mouvements des atomes qui donnent lieu à l'évolution du liquide au cours du temps. Tout comme dans le cas de la structure, ce type d'expériences, appelées diffusion inélastique, peut aussi être utilisé avec des cristaux. Dans ces derniers, certaines des vibrations mesurées, appelées phonons, sont liées à la conductivité thermique du matériau. Ces vibrations ne donnent pas lieu à un déplacement global des atomes dans le cristal mais plutôt à des vibrations corrélées des atomes autour de leur position d'équilibre. Dans les liquides, les propriétés dynamiques mesurées sont associées soit à la conductivité thermique soit à la relaxation de certaines fluctuations de densité et au déplacement global des atomes dans le fluide. Par exemple, le comportement diffusif gouverné par la loi de Fick est observable dans les spectres mesurés par diffusion de neutrons ou de rayons X. Ces propriétés dynamiques sont détectées grâce à l'échange d'énergie entre les neutrons (ou rayons X) et l'échantillon. Ces transferts d'énergie sont observés dans les spectres mesurés, ils contribuent à l'intensité détectée hors de la ligne élastique, cette dernière correspondant aux caractéristiques de la structure.
Par conséquent, les expériences de diffusion de neutrons et de rayons X permettent de sonder non seulement la structure mais aussi la dynamique des matériaux. Dans le cas de la diffusion de neutrons, on peut accéder à des distances comprises entre 0.1 Å et 10 μm et à des temps allant de 1 fs à 10 μs comme cela est représenté dans la figure 2. Ces échelles d'espace et de temps sont caractéristiques de celles observées dans la matière condensée. La diffusion de neutrons est donc bien adaptée pour déterminer la structure et la dynamique des liquides.
Toutefois, dans une expérience de diffusion de neutrons, le signal mesuré contient différentes contributions, dont un bon nombre ne sont pas intéressantes pour le physicien. Le signal expérimental est en effet la convolution de la fonction de résolution de l'instrument avec la fonction

de diffusion de l'échantillon. Le signal provient aussi du porte-échantillon et de l'environnement échantillon (four, cryostat par exemple) ainsi que du bruit de fond présent lors de la mesure. De plus, l'interaction entre les neutrons et l'échantillon est complexe et inclut des effets tels que la diffusion multiple et l'absorption. Par conséquent, avant de pouvoir extraire des informations sur la structure et la dynamique de l'échantillon, les données expérimentales doivent être soigneusement corrigées pour prendre en compte les différentes contributions mentionnées plus haut.

Du point de vue théorique, il existe deux grandes classes de méthodes pour l'investigation des propriétés des matériaux. Ces techniques consistent à disposer dans une "boite" de simulation un ensemble d'atomes et de molécules décrits par leurs positions et vitesses. Dans les simulations par méthode de Monte Carlo [2], de nombreuses configurations d'un même système sont générées en déplaçant de façon aléatoire un atome d'une configuration précédente du système. Si la différence d'énergie entre le nouveau système et le précédent est favorable au nouveau système, la nouvelle configuration est acceptée. Au contraire, si la nouvelle configuration est énergétiquement moins favorable que la précédente, la décision de garder cette nouvelle configuration est prise aléatoirement en utilisant un critère faisant intervenir la différence d'énergie entre les deux configurations. Ce type d'algorithme explore l'espace des phases du système. Toutefois, si cette méthode de simulation donne des informations sur la structure du système, les propriétés dynamiques peuvent seulement être obtenues de façon indirecte (voire pas du tout).
L'autre méthode théorique permettant l'investigation de la structure et la dynamique des matériaux est la simulation par dynamique moléculaire. Cette méthode consiste à résoudre les équations du mouvement pour chaque atome du système : l'énergie potentielle du système permet de déterminer les forces s'exerçant sur chaque atome et, par conséquent, leur position et leur vitesse. Cette méthode donne donc accès non seulement à la structure mais aussi à la dynamique du système étudié. L'évolution du système en fonction du temps n'est pas aléatoire comme dans la méthode de Monte Carlo, elle suit une loi physique. Parmi les simulations par dynamique moléculaire, on doit distinguer les méthodes empiriques des méthodes *ab initio*. Empirique signifie ici que les atomes évoluent dans un potentiel choisi afin de représenter correctement certaines propriétés (distances interatomiques, angles de liaison par exemple) ou certaines phases du système (phases amorphe et cristalline par exemple). L'expression analytique de tels potentiels est déterminée de telle sorte que les propriétés calculées à partir de ce potentiel soient en accord avec les valeurs mesurées de ces propriétés. Des interactions à deux et trois corps peuvent être incluses dans ces potentiels, faisant intervenir les contributions des paires et triplets d'atomes. A partir de ces potentiels, les forces exercées par et agissant sur chaque atome sont calculées, elles sont à l'origine de l'évolution des positions et des vitesses des atomes du sytème. D'autre part, les simulations par dynamique moléculaire *ab initio* ne reposent pas sur la définition de potentiels empiriques. Ces simulations sont basées sur le calcul de l'état électronique fondamental du système et la détermination des forces, dues à l'interaction des nuages électroniques, agissant sur les noyaux. La théorie de la fonctionnelle de la densité (DFT), dans laquelle les fonctions d'onde électroniques sont remplacées par la densité électronique, est l'une des théories les plus puissantes utilisées dans les simulations *ab initio*. Dans la dynamique moléculaire *ab initio*, l'état électronique fondamental est déterminé dans le cadre de la DFT à chaque pas de temps. Ensuite, les forces agissant sur chaque atome sont déterminées à partir de la nouvelle densité électronique et chaque atome est déplacé, ainsi que ses électrons. L'étape suivante consiste à déterminer le nouvel état électronique fondamental, et ainsi de suite.
Les deux méthodes de dynamique moléculaire permettent de calculer les propriétés microscopiques des systèmes physiques, tant du point de vue de la structure que de la dynamique.

Elles donnent accès à des quantités non mesurables mais ont toutefois un certain nombre de limitations. Les systèmes simulés sont extrêmement petits par rapport à la taille des systèmes réels. Actuellement, les temps accessibles dans les simulations sont de l'ordre de la nanoseconde voire de la microseconde, dans le cas où on utilise des potentiels empiriques pour lesquels les forces sont relativement faciles et rapides à calculer. Les restrictions en taille et en temps sont beaucoup plus importantes dans le cas des simulations *ab initio* qui nécessitent des calculs très coûteux en temps. Ces limitations en temps et en espace peuvent conduire à des problèmes de corrélations artificielles dans le système en raison de sa taille finie.

En comparant les échelles de temps et de longueur accessibles grâce à la diffusion de neutrons et aux simulations de dynamique moléculaire, on remarque que ces deux méthodes donnent accès à des propriétés structurales et dynamiques similaires. La comparaison entre expérience et simulation est par conséquent directe et peut donner des informations détaillées et microscopiques. L'une des études pionnières en matière de comparaison des données expérimentales de diffusion de neutrons et des simulations de dynamique moléculaire concernait l'argon liquide : cette étude théorique a été conduite par Rahman [3], qui a calculé la constante de diffusion et les fonctions de corrélation ("self" et distincte) de van Hove. Quelques années plus tard, Sköld et ses collaborateurs ont déterminé, par diffusion inélastique de neutrons, le spectre en fréquence de l'argon liquide [4] et l'ont comparé avec les calculs de Rahman. En 1974, une étude couplée du rubidium liquide utilisant la diffusion de neutrons et la dynamique moléculaire a été entreprise par Copley (expérience, [5, 6]) et Rahman (simulation, [7, 8]). Le facteur de structure dynamique cohérent a été déterminé et les résultats théoriques et expérimentaux ont montré un bon accord. Notons toutefois que ce type d'études couplées n'est pas réservé aux liquides. En 2003, l'équipe de Arbe [9] a montré le changement de comportement de la chaîne pirncipale d'un polymère lors de la relaxation α ; ce résultat a été obtenu expérimentalement sur un spectromètre à écho de spin et a été confirmé par les simulations de dynamique moléculaire, qui permettent d'interpréter le changement de comportement dynamique de l'échantillon. Par ailleurs, l'interaction entre propriétés structurales et dynamiques de certains systèmes peut être investiguée par diffusion de neutrons et simulation de dynamique moléculaire, comme l'ont montré Meyer et ses collaborateurs [10] dans le cas des liquides et des verres de silicate de sodium. Ce type d'approche expérimentale et théorique peut aussi être appliqué au cas des macromolécules : par exemple, la dynamique des molécules d'eau dans les nanotubes de carbone [11] et la caractérisation des molécules d'eau en surface des protéines [12] peuvent être déduites d'expériences de diffusion de neutrons et de simulations de dynamique moléculaire. Une tendance récente dans ce type d'études couplées est l'utilisation de méthodes de simulation *ab initio* à la place des méthodes classiques utilisant un potentiel empirique. C'est par exemple le cas pour l'étude de la structure de Sn [13].
Un autre type d'approche est la modélisation par "reverse Monte Carlo" (RMC) [14]. Cette méthode tire parti des échelles comparables accessibles par méthode de Monte Carlo et en diffusion de neutrons par exemple. RMC est une méthode générale de modélisation de la structure à partir des données expérimentales. Au départ destinée à l'étude de la structure des matériaux non cristallins (liquides, verres, polymères), elle a été étendue au cas des structures cristallines et magnétiques. Cette méthode a pour but de fournir un ensemble de modèles structuraux en accord avec les données expérimentales relatives à la structure.

Pendant la dernière décennie, les méthodes Monte Carlo de tracé de rayons ont été développées pour reproduire la propagation des neutrons dans les instruments de diffusion de neutrons. En couplant les simulations d'instrument et d'échantillon (simulations globales), le signal mesuré

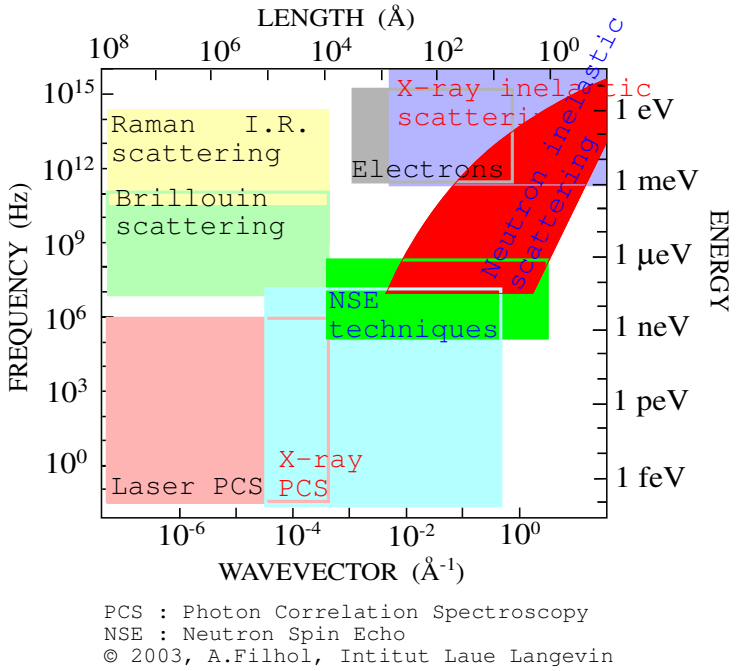

Figure 2: Données collectées par A. Filhol. Ref.: Raman/Brillouin : C. Ecolivet, Univ. Rennes. X-ray PCS : G. Grübel, ESRF, Grenoble. Neutrons : R. Currat, ILL, Grenoble.

peut être calculé et les contributions de l'intrument et de l'échantillon ainsi que leur couplage dans le signal réel peuvent être mieux comprises.
Pour effectuer ces simulations d'expériences, nous avons fait des simulations d'instrument avec un code Monte Carlo de tracé de rayons dans lequel l'instrument est décrit comme une succession de composants tels que les guides, les monochromateurs, les choppers ou les détecteurs. Les neutrons se propagent de composant en composant en suivant les règles de sélection relatives à chaque composant (par exemple diffraction pour un monochromateur, réflection pour un guide). Ce type de simulation a souvent été utilisé depuis la fin des années quatre-vingt dix et ce pour plusieurs raisons. Tout d'abord, l'utilisation de simulations d'instrument permet de mieux connaître les caractéristiques du faisceau de neutrons lorsqu'il parvient à l'échantillon. Ces simulations peuvent aussi être utilisées pour concevoir de nouveaux instruments et améliorer ceux qui existent. Par ailleurs, la configuration expérimentale et donc le temps de faisceau utilisé pour une expérience peuvent être optimisés grâce à ces simulations. Par conséquent, les simulations d'instrument sont intéressantes pour mieux connaître les caractéristiques du faisceau et pour améliorer l'utilisation des instruments et du temps de faisceau.
Quant à l'échantillon, il est décrit par ses propriétés structurales et dynamiques determinées par simulation de dynamique moléculaire. La structure et la dynamique constituent une bonne représentation de l'échantillon étant donné que la diffusion de neutrons sonde ces propriétés par l'intermédiaire des transferts d'énergie et de moment qui ont lieu lors de l'interaction entre les neutrons et l'échantillon.
Dans cette thèse, les simulations globales d'expériences de diffusion de neutrons sont développées dans différentes perspectives. Ces simulations permettront de mieux comprendre l'impact des différentes contributions sur les données brutes. Nous espérons en effet avoir des informations

sur les tendances observées dans le signal mesuré. Alors les données collectées sur un même échantillon mais sur des instruments différents devraient être plus facilement comparables. Une fois la fonction de diffusion théorique calculée, la simulation complète permettra d'évaluer la faisabilité sur différents instruments des expériences proposées. Enfin, la simulation d'expérience telle qu'introduite ici, mais aussi incluant le contrôle d'instrument, pemettra aux nouveaux utilisateurs de se familiariser avec ce type d'expériences et d'élaborer des stratégies de mesures. L'importance de ces enjeux est démontrée par le fait que les procédures de traitement de données pour les nouvelles sources de neutrons, telles que SNS (Spallation Neutron Source, US), incluent la notion d'expériences virtuelles.
Dans l'optique de développer et tester cette approche, nous avons étudié des échantillons diffusant de façon isotrope qui sont plus faciles à inclure dans le module de simulation d'échantillon de l'instrument virtuel. Par ailleurs, pour les sytèmes désordonnés tels que les liquides, le signal expérimental relatif à la structure et à la dynamique présente des caractéristiques peu prononcées, il est donc grandement influencé par les contributions parasites. Dans de tels cas, les simulations théoriques doivent reproduire les moindres détails des données, ce qui signifie que les nombreuses contributions relatives à l'échantillon et à l'instrument doivent être bien comprises. Dans ce contexte, nous avons développé des simulations globales dans le cas de l'hélium liquide et du rubidium liquide et nous avons effectué de nouvelles mesures sur le germanium liquide ainsi que les simulations globales correspondantes.

Les sujets présentés plus haut sont décrits de façon plus détaillée dans cette thèse. Le premier chapitre donne les principales quantités nécessaires à la description de la structure et de la dynamique des liquides. De ces quantités, on peut extraire des informations sur les corrélations spatiales et temporelles entre atomes, qui peuvent faire référence soit à des propriétés collectives soit à des propriétés des particules isolées du liquide, et peuvent être extraites d'expériences de diffusion de neutrons et de simulations de dynamique moléculaire.
Dans le deuxième chapitre, les méthodes de diffusion de neutrons et de simulation de dynamique moléculaire sont présentées. Ce sont les méthodes utilisées dans ce travail pour investiguer les propriétés présentées dans le premier chapitre. La technique de diffusion de neutrons est présentée en lien avec les quantitiés structurales et dynamiques d'intérêt. Ensuite, les simulations de dynamique moléculaire, classiques d'une part et *ab initio* d'autre part, sont présentées.
Dans le troisième chapitre, les détails de l'algorithme développé pour la simulation des expériences de diffusion de neutrons sont expliqués, ainsi que les différents effets liés à l'interaction entre neutrons et échantillon, tels que l'absorption ou la diffusion multiple. Deux exemples sont ensuite présentés pour montrer les possibilités offertes par ces simulations dans le cas des liquides. Le premier exemple consiste à utiliser un échantillon test avec une courbe de dispersion bien définie comme celle de l'hélium superfluide. Le deuxième cas est celui du rubidium liquide pour lequel des expériences de diffusion inélastique des neutrons ont été faites [5, 6]. Dans cet exemple, l'échantillon a été simulé par dynamique moléculaire classique en utisant un code "fait maison". A partir de cette simulation, les propriétés structurales et dynamiques utiles pour le couplage avec une simulation d'instrument sont extraites.
Le dernier chapitre est consacré à l'étude du germanium liquide. Nous nous sommes particulièrement focalisés sur les propriétés structurales inhabituelles de ce liquide ainsi que sur ses propriétés dynamiques. Nous avons fait deux types d'expériences de diffusion de neutrons sur cet échantillon, afin de déterminer ses propriétés dynamiques. D'autre part, nous avons fait des simulations de dynamique moléculaire sur le germanium liquide en utilisant d'une part un potentiel empirique, et d'autre part une méthode *ab initio*. La simulation de dynamique moléculaire classique a été faite avec un code "fait maison" qui permet la prise en compte du potentiel

à deux et trois corps, de tels potentiels étant autrement difficiles à inclure dans des codes de dynamique moléculaire standards. Enfin, des simulations complètes d'expériences de diffusion de neutrons sont présentées, elles concernent l'étude du germanium liquide sur un spectromètre à temps de vol.
Dans la conclusion finale, les perspectives associées à ce projet sont discutées.

Introduction

In daily life, the notion of liquid is quite familiar since it is one of the three common states of matter, with the solid and gaseous states. The liquid state has some of the characteristics of the solid state and some of the gaseous state. Like the solid state, the liquid state tends to have very little ability to be compressed and it is associated with somewhat low kinetic energy of the particles. It can be compared to the gaseous state in that the liquid state tends to flow under a shear stress however small, or it tends to have fluidity and to take on the shape of the container that it is in. Liquids exist in a relatively small part of the range of temperatures and pressures compared to solids and gases.
On the atomic scale, a liquid is a compact and partially disordered phase. For roughly spherical molecules, and in particular for the actually spherical rare gases, only one kind of disorder is possible, namely disorder of translational motion. For molecules which are far from spherical, there is also the possibility of rotational disorder.

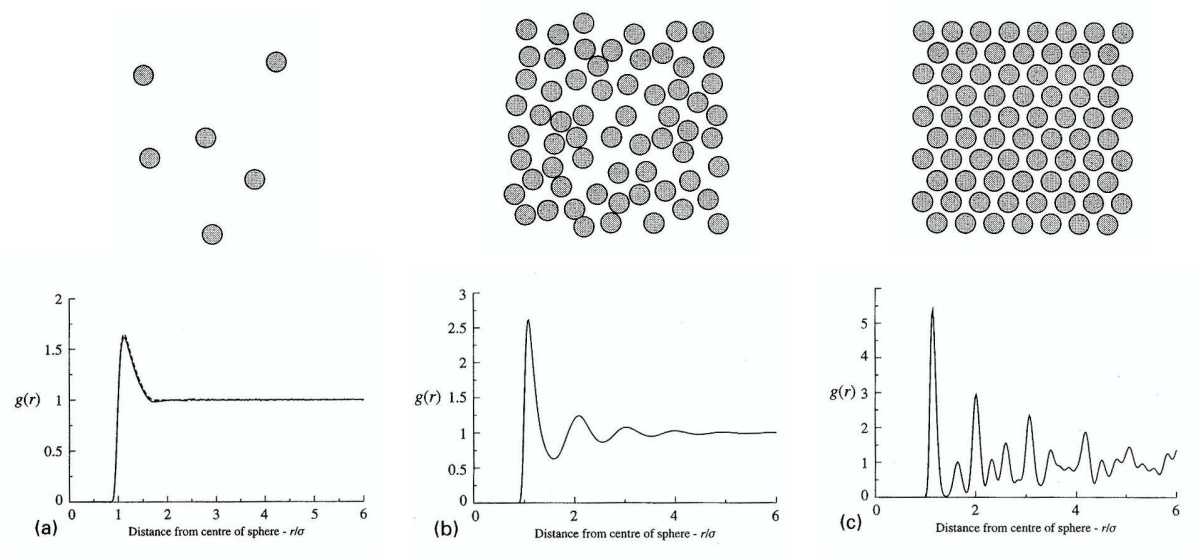

Figure 1: Typical structure of a gas (left), a liquid (middle) and a solid (right). Top: typical atomic configurations in the three phases. Bottom: typical pair correlation functions for a gas (left), a liquid (middle) and a solid (right) (from [1]).

Many techniques exist for investigating the structural and dynamical properties of liquids. These may be either experimental or theoretical methods. From the experimental point of view,

light scattering is one of the most accessible techniques: it gives insight into the structural and dynamical features of the material. It probes both spatial arrangements and time evolution of the materials. It can give access to long length scales (typically from 1 μm up to 1 cm) and high frequencies (from 10^7 to 10^{14} Hz).
On the other hand both neutron scattering and X-ray scattering techniques are available at large facilities. With both of these methods, experimentalists can gain insight into the structure of their sample and get a better understanding of the spatial arrangement of the atoms or molecules. Figure 1 depicts $g(r)$, the pair correlation function: for a given distance r, it gives a measure of the probability of finding two atoms separated by the specified distance r. $g(r)$ gives information about the spatial correlations between the atoms. The function $g(r)$ can be extracted from the measurements performed either with neutron or X-ray diffraction. For a crystal, $g(r)$ shows several sharp and intense peaks. These are associated with the well-defined interatomic distances existing in an ordered material. In contrast with crystals, gases would not show any pronounced structural features since they are very dilute systems, without well-defined correlation distances, apart from the so-called "correlation hole" at small distances. In the case of liquids, we notice a first well-defined maximum and then several oscillations at higher interatomic distances. Although these features are much broader and weaker than for the crystalline phase, they show the existence of privileged interatomic distances in the liquid. Nevertheless the broadening of the features by comparison with the crystal is a sign of a disordered system: the interatomic distances are not sharply defined as in crystals.

Not only the structure but also the time behaviour of liquids can be determined from neutron or X-ray scattering experiments. These techniques give insight into the features of the motions that are responsible for the time evolution of the liquid. Of course as for the structural features, this kind of experiment, called inelastic scattering, can also be performed for crystals. In the latter, some of the measured vibrations called phonons are related to the thermal conductivity of the material. They do not lead to a global motion of the atoms in the crystal but to correlated vibrations of the atoms around a mean equilibrium position. In liquids, the measured time evolutions are associated either with thermal conductivity or with relaxation of the density fluctuations and global displacement of the fluid. For example, the diffusion behaviour governed by Fick's law can be observed in the spectra measured by scattering of neutrons or X-rays. Such dynamical features can be detected thanks to the exchange of energy occurring when neutrons or X-rays interact with the sample. Such energy transfers are observed in the measured spectra: they contribute to the intensity detected outside the elastic line, the latter corresponding to the structural features.
Consequently both information about the spatial and temporal features of liquids can be determined from neutron or X-ray scattering experiments. In the case of neutron scattering, the accessible spatial range is of the order of 0.1 Å to 10 μm while the available time scales range from to 1 fs to 10 μs as shown in Figure 2. These time and space scales are typical of condensed matter and thus neutron scattering is well suited for determining the structure and dynamics of liquids.
However when performing a neutron scattering experiment, the measured signal accounts for different contributions, many of which are not interesting for the physicist. The experimental signal is actually the convolution of the resolution of the instrument with the scattering function of the sample. The signal also accounts for the sample holder and sample environment and for the background noise during the measurement. Furthermore, the interaction between neutrons and sample is complex and includes effects such as multiple scattering and absorption. Consequently, the experimental data have to be carefully corrected for these contributions before

getting information about the structure and dynamics of the sample.

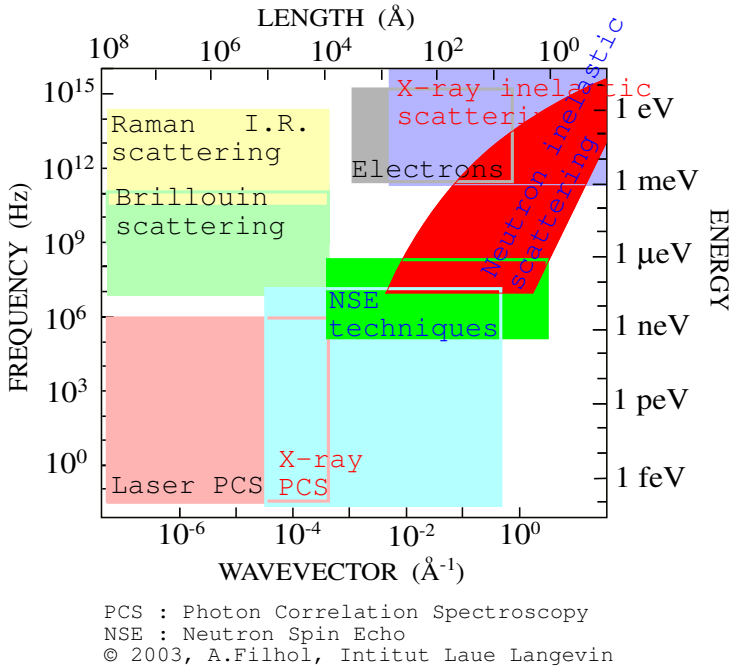

Figure 2: Data collected by A. Filhol. Ref.: Raman/Brillouin : C. Ecolivet, Univ. Rennes. X-ray PCS : G. Grübel, ESRF, Grenoble. Neutrons : R. Currat, ILL, Grenoble.

From the theoretical point of view, two main kinds of methods exist for the investigation of the properties of materials. These techniques consist of placing a set of atoms or molecules described by their positions in a simulation box. The first one is Monte Carlo simulations [2]. In this method, many configurations of the same system are generated by randomly displacing one atom from a previous configuration. If the change in the potential energy of the system favours the new configuration, the scheme consists of keeping the newly generated configuration of the system. On the contrary, if the new configuration is energetically less favourable than the former one, the decision to keep it or not is randomly chosen as a function of the difference in energy between the two configurations. This kind of algorithm leads to the exploration of the phase space of the system. However, if it is likely to give insight into the structural features of the system, dynamical properties can only be obtained indirectly, if at all.
The other main theoretical method for the investigation of the properties of materials is called molecular dynamics (MD) simulations. This method consists of solving Newton's equation of motion for each atom in the simulation box: the forces acting on each atom, and thus their respective positions and velocities, are determined from the potential energy of the system. Thus this type of simulation gives access not only to the structure of the system but also to its dynamics. The time evolution of the system is not random as in Monte Carlo simulations, it obeys a physical law of motion. In MD simulations, we may distinguish empirical simulations from *ab initio* methods. Empirical means here that the potential in which the atoms evolve is designed in order to be suitable for the representation of some properties (interatomic distances or bond angles for instance) or some phase of the system (amorphous and crystalline for example). The

analytical expression of such potentials is determined so that the properties obtained from this potential match some experimentally determined properties; they may involve two- and three-body contributions from the pairs and triplets of atoms respectively. From these potentials, the forces exerted by and acting on each atom of the system can be calculated, leading to the evolution of the positions and velocities of the system. On the other hand, *ab initio* MD simulations do not rely on such empirical potentials. They are based on the calculation of the ground state of the electrons together with the determination of the forces acting on the nuclei and due to the interactions between their electron clouds. One of the most powerful theories associated with this method is the density functional theory (DFT), where the electronic wavefunctions are replaced by the electronic density. In *ab initio* MD, at each time step, the electronic ground state is determined in the framework of DFT. Then from the newly determined electronic density, the forces acting on each atom are determined and the atoms are moved together with the electrons. The next step starts with the calculation of the electronic ground state and so on.
Both MD simulation methods allow the microscopic features of physical systems, both structure and dynamics, to be calculated. They give access to quantities that cannot be measured. However they also have some limitations. The simulated systems are extremely small compared to the size of real systems. The simulation times nowadays reaches some nanoseconds or even microseconds in the case of empirical MD simulations, where the forces are relatively easy and quick to compute. The restrictions in the size of the system and the simulation length are more drastic in the case of *ab initio* MD simulations which involve very time-consuming calculations. The limitations in time and space may yield some problems of artificial correlations in the system due to its finite size.

Considering the time and space scales probed respectively by neutron scattering and molecular dynamics simulations, we realize that the two techniques give access to similar structural and dynamical properties. The confrontation between experiment and simulation is therefore direct and can yield detailed, microscopic information.
One of the pioneering studies involving a comparison between neutron scattering experiments and molecular dynamics simulations dealt with liquid argon: the theoretical calculations were performed by Rahman [3], who computed the self-diffusion constant and the distinct and self Van Hove correlation functions. Some years later, Sköld and collaborators determined the frequency spectrum of l-Ar from inelastic neutron scattering experiments [4] and compared it with the theoretical results from Rahman. In 1974, another coupled study using neutron scattering and molecular dynamics simulation was performed by Copley (experiment,[5, 6]) and Rahman (simulation, [7, 8]) and concerns liquid rubidium. The coherent dynamic structure factor of l-Rb was determined and the experimental and theoretical results were found to be in good agreement. However this kind of coupled experimental and theoretical studies is not devoted only to liquids. In 2003, Arbe and collaborators [9] showed the change in the behaviour of the main chain protons in a polymer in the α-relaxation regime; this result was obtained from a neutron spin-echo experiment and corroborated by molecular dynamics simulations. The latter enable an interpretation of the change in the dynamic behaviour of the sample. Also the interplay between structural and dynamical aspects of some systems can be investigated by neutron scattering and molecular dynamics simulations, as shown by Meyer and coworkers for the case of sodium silicate melts and glasses [10]. Also macromolecules can be studied in this way: for instance the dynamics of water molecules in carbon nanotubes [11] and the characterization of the protein surface hydration water [12] can be inferred from neutron scattering experiments and molecular dynamics simulations. A recent trend in this kind of coupled studies is the use of first-principle molecular dynamics simulations instead of classical ones, as for the study of the

structure of liquid Sn [13].
Another kind of approach is called reverse Monte Carlo modelling (RMC) [14]. It takes advantage of the similar spatial scales accessible in Monte Carlo simulations and neutron scattering experiments for instance. RMC is a general method of structural modelling based on experimental data. It was originally devised for studying the structure of non-crystalline materials (liquids, glasses, polymers) but has been extended to the cases of crystalline and magnetic structures. The aim of this method is to produce a set of structural models consistent with experimental data dealing with structural properties.

Over the last decade Monte Carlo ray-tracing methods have been developed for handling the propagation of neutrons in the instrument. By coupling instrument and sample simulations (global simulations), the measured signal can be calculated and insight gained into contributions of instrument and sample and their coupling in the real signal.
With a view to this complete simulation of experiments, we performed instrument simulations using a Monte Carlo ray-tracing code: the instrument is described as a succession of components such as guides, monochromators, choppers or detectors. The neutrons propagate from component to component according to the rules of selection relevant for each of them (e.g. diffraction in the monochromator or reflection on the guide). This kind of simulation has been extensively used since the end of the nineties and has been promoted for several reasons. First, the use of instrument simulations is useful for getting a deeper insight into the features of the beam incident onto the sample. Such simulations may also be used for designing new instruments or tuning existing ones. They also enable the experimental configuration and thus the time dedicated to each experiment to be optimized. Consequently such instrument simulations are of interest for getting a better insight into the experimental data and for improving the experimental setup and use of beamtime.
Concerning the sample, it is described through its structural and dynamical features determined from the molecular dynamics simulation. The structure and dynamics are the quantities relevant to neutron scattering since the interaction between neutrons and nuclei leads to changes in the energy and direction of the scattered neutrons and the latter are related to the structural and dynamical features of the sample.
Global simulations of neutron scattering experiments are developed in this thesis with a number of future goals in mind. The global simulation will allow more insight to be gained into the many factors influencing the raw data. We actually expect global simulation to give information about the trends observed in the measured signal. Data collected on the same sample but different instruments should become more readily comparable. Once the theoretical scattering function has been determined, the complete simulation will allow proposed experiments to be evaluated concerning their feasibility on different instruments. Finally the global simulation as introduced here, but also including instrument control software, will allow new users of neutron facilities to familiarize themselves with neutron scattering experiments and even develop measurement strategies. The importance of these issues is reflected in the fact that data analysis schemes for new sources, such as SNS (Spallation Neutron Source, US), include virtual experiments.
For the purpose of developing and testing this approach, we have pursued isotropic scatterers which are simplest to include in the scattering module of the instrument simulation. Furthermore, disordered systems like liquids have smoothly varying experimental signal of structure and dynamics which are strongly influenced by parasitic contributions to the signal. In these cases , theoretical simulations must reproduce the fine detail of the data, which means that the many sample and instrument related contributions to the measured signal must be well-understood. In this context, we have developed global simulations for liquid helium and liquid rubidium and

have performed new measurements and simulations (sample and instrument) on liquid germanium.

The topics presented above are described in more details in this thesis. In the first chapter, the main quantities relevant for the description of the structure and dynamics of liquids are given. They give insight into the space and time correlations between the atoms. These correlations may be linked either to collective or single-particle features of the liquid and can be extracted from both neutron scattering experiments and molecular dynamics simulations.
The second chapter deals with the two methods, experimental for neutron scattering and theoretical for molecular dynamics simulations, used in this work for the investigation of the properties introduced in the previous chapter. The theory of neutron scattering is presented and the relation with the structural and dynamical quantities of interest is given. The last part of this chapter is dedicated to the molecular dynamics simulation, either using empirical interatomic potentials or *ab initio* methods.
In the third chapter, the details of the algorithm devised for the simulation of total neutron scattering experiments is explained, together with the different effects arising from the interaction between neutrons and sample, such as absorption or multiple scattering. Two examples of what can be inferred from these simulations in the case of liquids are shown: the first one deals with the simulation of a test sample with a well defined dispersion curve such as that of superfluid helium. The second one is about liquid rubidium for which inelastic neutron scattering experiments were performed [5, 6]. For this second test, we performed a classical molecular dynamics simulation with a "home made" code from which we extracted the structural and dynamical properties relevant for the coupling with an instrument simulation. With these two examples, the abilities of the simulation scheme are shown.
The last chapter is dedicated to the study of liquid germanium. Our interest is mainly focused on the unusual structural properties of this liquid together with its dynamical properties. We performed two kinds of neutron scattering experiments on this sample, in order to determine its dynamical properties. On the other hand, molecular dynamics simulations have been carried out in both the empirical potential and *ab initio* frameworks. For the classical MD simulation, we used a "home made" code with three-body potentials, which are otherwise difficult to include in standard MD codes. In the end, we present complete simulations of the neutron scattering experiment dealing with liquid germanium on a time-of-flight spectrometer.
In the final conclusion, perspectives for the future of this project are discussed.

1

Structure and dynamics of liquids

Contents

In this chapter, we focus only on monatomic systems in the liquid state. This topic was extensively described in textbooks by Egelstaff [15] who gives an introduction to the liquid state, by Hansen and McDonald [16] who derived the theoretical formulas dealing with liquids and by Balucani and Zoppi [17] who explain the connections between what happens in a liquid and what can be measured by spectroscopic methods. More recently, Damay [18] published an introduction to the topological aspects of disorder in liquids, while Barrat and Hansen [1] have given an overview of the fundamental concepts related to simple and complex fluids.

From the macroscopic point of view, the equilibrium state of a liquid can be described by its volume V, its temperature T and its pressure P. The influence of these thermodynamic variables on the transitions encountered by the liquid are usually represented in a phase diagram. The latter shows that at low pressures, only solid and vapour phases may exist. Apart from the glass state, these two states can be described by ideal models: the solid state is explained by the structural model of the ideal crystal lattice coupled with thermal vibrations of the atoms, while the behaviour of the gas is represented by random motions constrained by the condition of non-overlap of the atoms. At higher pressures, a third state is present, which is the liquid state. It exists in a temperature range which separates the solid phase from the vapour one. Unlike both gas and solid, no reliable microscopic model exists which could describe both structural and dynamic/thermal features of liquids. The structure itself is a much more complex

problem than for a crystal or a gas, since a liquid consists of a disordered system of N particles in interaction. In a crystal, the arrangement of atoms is periodic which enables the use of few parameters for characterizing its structure. In a gas, there are no interactions between atoms, except the non-overlap condition, hence a statistical description can be used. A general feature of the structure of liquids is the existence of a short-range order due to the interactions between atoms (the positions of atoms are not random like in gases) and the lack of long-range order (unlike in crystals). However, the density of liquids and solids are usually close for neighbouring pressures and temperatures, and the binding properties of liquids may be close to those of solids since the latent heat is lower for fusion than for vaporization.

From a microscopic point of view, different techniques, such as neutron, X-ray or light scattering, but also simulations, can give much information about the structural and dynamical (either individual or collective) properties of a liquid, over a large range of space and time correlations. In this microscopic description, we have to account for the individual contributions of each constituent of the liquid. Since the thermodynamic variables are not relevant any more in the microscopic description, the liquid will be described by the positions of its N particles $\mathbf{r}_i(t), i = 1 \cdots N$ and their respective momenta $\mathbf{p}_i(t), i = 1 \cdots N$. The Hamiltonian $\mathcal{H}$ of the system is then given by:

$$\mathcal{H} = \sum_{i=1}^{N} \frac{p_i^2}{2m} + V_N(\mathbf{r}_1, \mathbf{r}_2, \mathbf{r}_3, \cdots, \mathbf{r}_N)$$

where m is the mass of each particle and $V_N(\mathbf{r}_1, \mathbf{r}_2, \mathbf{r}_3, \cdots, \mathbf{r}_N)$ is the potential energy of the system, which depends on the many-body interactions:

$$V_N(\mathbf{r}_1, \mathbf{r}_2, \mathbf{r}_3, \cdots, \mathbf{r}_N) = \sum_{i=1}^{N} v_1(i) + \sum_{i,j;i<j}^{N} v_2(i,j) + \sum_{i,j,k;i<j<k}^{N} v_3(i,j,k) + \cdots + v_N(1,2,\cdots,N).$$

The one-body v_1 contribution terms describe the external forces to which the system is subject; in the case studied by us, there are no external constraints. For usual modelling, the functions v_n converge quickly to zero with increasing n and lead to reduced expressions consisting only of two and three-body interactions. The two-body interaction term is usually written as:

$$\sum_{i,j;i<j}^{N} v_2(i,j) = \frac{1}{2} \sum_{i \neq j} \varphi(r_{ij})$$

where the pair potential φ depends on the interatomic distance r_{ij}. This potential $\varphi(r)$ consists of both attractive ($\varphi'(r) < 0$) and repulsive parts ($\varphi(r)' > 0$), the latter being the most important at short interatomic distances.

One of the most well-known empirical, interatomic pair potentials is the Lennard-Jones potential depicted in figure 1.1, which is given by the equation (see [15] for instance):

$$\varphi(r) = 4\varepsilon \left[\left(\frac{\sigma}{r}\right)^{12} - \left(\frac{\sigma}{r}\right)^{6} \right] \tag{1.1}$$

where ε is the depth of the attractive well and σ is the point at which $\varphi(r) = 0$.

For three-body interaction terms, the angle between each triplet of neighbours intervenes and favours specific angular arrangements.

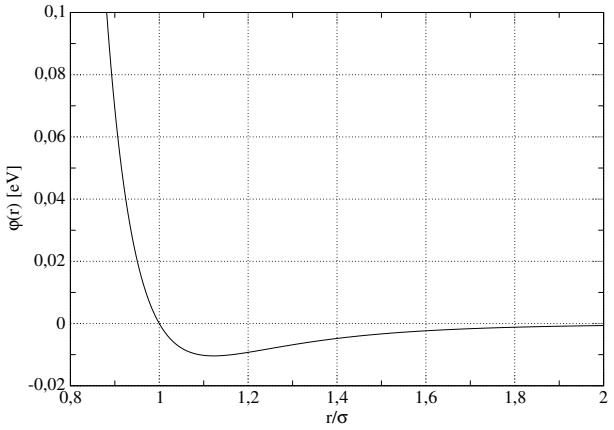

Figure 1.1: Lennard-Jones potential with $\sigma = 3.4$ Å and $\varepsilon = 0.0104$ eV.

Let us now move on to the description of the structure and dynamics of liquids in terms of distribution and correlation functions.

1.1 The structure of liquids

The atoms of a liquid, like those of a solid (and unlike those of a gas), are quite close together. While molecules in a solid are held in fixed positions by intermolecular forces, molecules in a liquid have too much thermal energy to be bound by these forces and move about freely within the liquid, although they cannot escape the liquid easily. Such features give an idea of the complexity of the structure of liquids.

In this section, we introduce distribution functions useful for dealing with the structural features of liquids in both real and reciprocal spaces.

1.1.1 The pair distribution function

The structure of simple monatomic fluids is characterized by a set of distribution functions of the atomic positions. The most common of them is the pair distribution function $g(r)$ introduced below. Let us now consider a monatomic liquid consisting of N atoms occupying a volume V. The mean number density of the system is given by:

$$\rho = \frac{N}{V}.$$

The microscopic density (or density of particles at a position $\boldsymbol{r}$) can be defined as

$$\hat{\rho}(\boldsymbol{r}) = \sum_{i=1}^{N} \delta(\boldsymbol{r} - \boldsymbol{r}_i), \tag{1.2}$$

where $\boldsymbol{r}_i$ is the position of the center of mass of each atom. We notice that $\int_V \hat{\rho}(\boldsymbol{r}) d\boldsymbol{r} = N$. The statistical average of $\hat{\rho}(\boldsymbol{r})$ is the local density of the liquid

$$\rho(\boldsymbol{r}) = \langle \hat{\rho}(\boldsymbol{r}) \rangle \tag{1.3}$$

which corresponds to the average number of atoms which will be found around any position $\boldsymbol{r}$ per unit volume. If the liquid is homogeneous, $\rho(\boldsymbol{r})$ reduces to the macroscopic density ρ.
In a liquid, the probabilities of finding atoms within neighbouring volume elements are highly correlated due to packing and non-overlap considerations. Consequently the correlation between fluctuations of the microscopic density is the quantity of interest: let us consider two different points $\boldsymbol{r}$ and $\boldsymbol{r}'$. We are interested in the fluctuations around the mean number density ρ. For a homogeneous liquid at equilibrium, we define the density-density correlation function $H(\boldsymbol{r}, \boldsymbol{r}')$ as:

$$H(\boldsymbol{r}, \boldsymbol{r}') = \frac{1}{N}\langle[\hat{\rho}(\boldsymbol{r}') - \rho][\hat{\rho}(\boldsymbol{r} + \boldsymbol{r}') - \rho]\rangle = \frac{1}{N}\left[\langle\hat{\rho}(\boldsymbol{r}')\hat{\rho}(\boldsymbol{r} + \boldsymbol{r}')\rangle - \rho^2\right]. \tag{1.4}$$

Thanks to homogeneity, this correlation function only depends on the separation vector $\boldsymbol{r}$. (1.4) can be integrated over $\boldsymbol{r}'$ to account for translational invariance and $\hat{\rho}(\boldsymbol{r})$ may be given by (1.2):

$$\begin{aligned} H(\boldsymbol{r}) &= \frac{1}{N}\int_V \langle\hat{\rho}(\boldsymbol{r}')\hat{\rho}(\boldsymbol{r} + \boldsymbol{r}')\rangle d\boldsymbol{r}' - \rho \\ &= \frac{1}{N}\sum_{i=1}^{N}\int_V \langle\delta(\boldsymbol{r}' - \boldsymbol{r}_i)\delta(\boldsymbol{r}' + \boldsymbol{r} - \boldsymbol{r}_i)\rangle d\boldsymbol{r}' - \rho + \frac{1}{N}\sum_{i=1}^{N}\sum_{j\neq i}\int_V \langle\delta(\boldsymbol{r}' - \boldsymbol{r}_i)\delta(\boldsymbol{r}' + \boldsymbol{r} - \boldsymbol{r}_j)\rangle d\boldsymbol{r}' \\ &= \frac{1}{N}\sum_{i=1}^{N}\sum_{j\neq i}\langle\delta(\boldsymbol{r} + \boldsymbol{r}_i - \boldsymbol{r}_j)\rangle + \delta(\boldsymbol{r}) - \rho \end{aligned} \tag{1.5}$$

and we define the *pair correlation function* $g(\boldsymbol{r})$:

$$\rho g(\boldsymbol{r}) = \frac{1}{N}\sum_{i=1}^{N}\sum_{j\neq i}\langle\delta(\boldsymbol{r} + \boldsymbol{r}_i - \boldsymbol{r}_j)\rangle \tag{1.6}$$

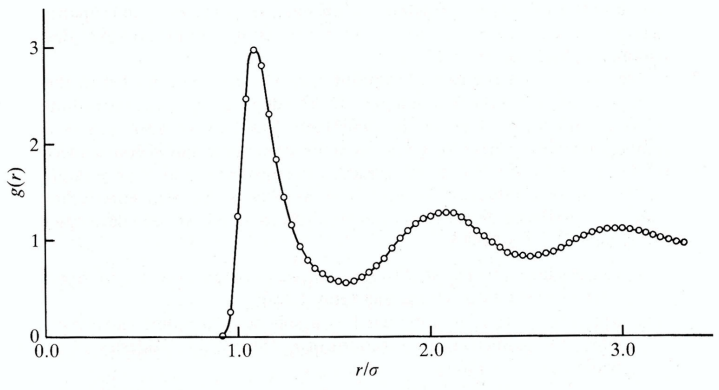

Figure 1.2: Pair distribution function $g(r)$ for a Lennard-Jones fluid close to the triple point [27].

Figure 1.2 shows a typical pair distribution function for a monatomic liquid. (Note that $g(r)$ and $g(\boldsymbol{r})$ are different: the former has a factor $1/(4\pi r^2)$). At low values of r, $g(r)$ is almost zero since at small distances the interaction forces which avoid overlapping of the atoms are strong, it reflects the so-called *excluded volume condition*. At a distance of the order of the

atomic diameter, there is a pronounced peak which denotes the first coordination sphere. At small pressures, the value of r for the maximum of the first sharp peak is close to the principal minimum in the interaction potential. As r increases, the oscillations in $g(r)$ are less and less defined.
The first peak, which corresponds to the first neighbours, is intense and sharp, which shows that the distribution of the distances is narrow around the most probable value of r. The following oscillations, which are damped and larger, correspond to more distant neighbours. At large distances, the correlation disappears and $g(r)$ approaches the unit mean density of the system. In molten salts, around ten correlation spheres can be observed while in van der Waals fluids, only 3 or 4 of them are defined.

We can also define the radial distribution function as:

$$RDF(r) = 4\pi\rho r^2 g(r) \tag{1.7}$$

which enables the calculation of the number of nearest neighbours through the integral:

$$n_{coor} = \int_0^{r_m} RDF(r)dr \tag{1.8}$$

where r_m refers to the first minimum in $g(r)$. $G(r)$ shows the deviation from total disorder, it is defined as:

$$G(r) = 4\pi\rho r[g(r) - 1]. \tag{1.9}$$

Also more complicated quantities can be evaluated, which involve the consideration of n-particle distribution functions describing the probability of occurrence of clusters of n particles with specific inter-cluster distances. Besides $g(r)$, the triplet distribution function is often evaluated:

$$\rho^2 g^{(3)}(\boldsymbol{r}, \boldsymbol{r}') = \frac{1}{N}\sum_{i=1}^{N}\sum_{j\neq i}\sum_{l\neq i}\langle\delta(\boldsymbol{r} - \boldsymbol{r}_{ij})\delta(\boldsymbol{r}' - \boldsymbol{r}_{il})\rangle \tag{1.10}$$

which gives information about the local orientational order.

1.1.2 The static structure factor

Equation (1.6) is the basis for the definition of the static structure factor $S(q)$:

$$S(\boldsymbol{q}) = 1 + \rho\int_V [g(\boldsymbol{r}) - 1]e^{i\boldsymbol{q}.\boldsymbol{r}}d\boldsymbol{r} \tag{1.11}$$

where $\boldsymbol{q}$ is the wave vector, also denoted by $\boldsymbol{k}$ or $\boldsymbol{Q}$. Note that for isotropic liquids, both $g(\boldsymbol{r})$ and $S(\boldsymbol{q})$ are only dependent on r and q respectively. (1.11) then reduces for an homogeneous and isotropic system to:

$$S(q) = 1 + \rho\int_0^{\infty} [g(r) - 1]\frac{\sin(qr)}{qr}4\pi r^2 dr. \tag{1.12}$$

$S(\boldsymbol{q})$ is the measured quantity in a neutron diffraction experiment (see Section 2.1.4). It gives information on the structure of the liquid in the reciprocal space.

However $S(\boldsymbol{q})$ can be defined differently. Let us define the Fourier transform of the density of particles at point $\boldsymbol{r}$:

$$\begin{aligned}\rho_{\boldsymbol{q}} &= \int e^{-i\boldsymbol{q}.\boldsymbol{r}}\hat{\rho}(\boldsymbol{r})d\boldsymbol{r} \\ &= \sum_{i=1}^{N} e^{-i\boldsymbol{q}.\boldsymbol{r}_i}\end{aligned} \tag{1.13}$$

with: $\hat{\rho}(\boldsymbol{r}) = \sum_{i=1}^{N}\delta(\boldsymbol{r}-\boldsymbol{r}_i)$. $S(\boldsymbol{q})$ may be defined as the autocorrelation of the Fourier components of the particle density:

$$S(\boldsymbol{q}) = \frac{1}{N}\langle\rho_{\boldsymbol{q}}\rho_{-\boldsymbol{q}}\rangle = \frac{1}{N}\sum_{j}^{N}\sum_{l}^{N}\langle e^{i\boldsymbol{q}\cdot(\boldsymbol{r}_j-\boldsymbol{r}_l)}\rangle \tag{1.14}$$

The right-hand side term of the last equation can be written as:

$$\begin{aligned}\frac{1}{N}\sum_{j}^{N}\sum_{l}^{N}\langle e^{i\boldsymbol{q}\cdot(\boldsymbol{r}_j-\boldsymbol{r}_l)}\rangle &= 1 + \frac{1}{N}\sum_{j=1}^{N}\sum_{l\neq j}\left\langle\int\int e^{i\boldsymbol{q}\cdot(\boldsymbol{r}-\boldsymbol{r}')}\delta(\boldsymbol{r}-\boldsymbol{r}_i)\delta(\boldsymbol{r}'-\boldsymbol{r}_j)d\boldsymbol{r}d\boldsymbol{r}'\right\rangle \\ &= 1 + \rho\int e^{i\boldsymbol{q}\cdot\boldsymbol{r}}g(\boldsymbol{r})d\boldsymbol{r} \\ &= 1 + (2\pi^3)\rho\delta(\boldsymbol{q}) + \rho\int e^{i\boldsymbol{q}\cdot\boldsymbol{r}}[g(\boldsymbol{r})-1]d\boldsymbol{r}.\end{aligned} \tag{1.15}$$

From the last expression, one usually subtracts the δ term and we are left with the expression of $S(\boldsymbol{q})$ given in (1.11).

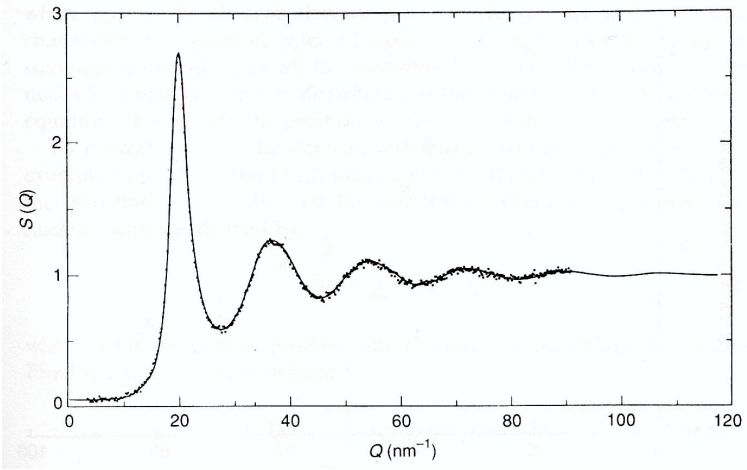

Figure 1.3: Static structure factor for liquid argon close to the triple point (from Yarnell *et al.* 1973)

Figure 1.3 shows the typical shape of a static structure factor, which, roughly speaking, is rather similar to the pair distribution function $g(r)$. The first sharp peak in $S(q)$ is due to a nearly regular arrangement of the particles in real space. If this peak is observed at $q = q_0$, the corresponding typical nearest neighbour distance is $2\pi/q_0$, close to the value of the atomic diameter.

1.2 Dynamics of the liquid state

The motion of atoms is certainly easier to understand in gases or crystals than in liquids or amorphous materials. In gases, the trajectories of atoms are linear apart from collisions and their velocities are governed by the Maxwell-Boltzmann distribution. The mean free path is $l = \langle v \rangle \tau$ where $\langle v \rangle$ is the mean velocity and τ is the mean time between two collisions. In crystals, the motions of atoms are expected to be localized around a mean equilibrium position. However these oscillations may be collective and for small $\boldsymbol{q}$ give rise to phonon propagation, with frequency ω and wave vector $\boldsymbol{q}$. The dependence of ω and $\boldsymbol{q}$ is given by the dispersion curve $\omega(\boldsymbol{q})$. Since the system is periodic, determining the dispersion curves for the acoustic and optic phonons in the Brillouin zone is enough for characterizing all the collective excitations.

In disordered systems, dynamics are rather complex: the vibrations of molecules are due to individual atomic motions while their rotations are often correlated. Moreover, atoms and molecules will diffuse and there also exist collective motions of long wavelength; the latter are acoustic waves, whose velocities depend on the density and the compressibility of the system.

The presentation of the dynamics of liquids is here divided in two main parts: the first one deals with the representation of the correlation functions in time and space while the following part focuses on the description in reciprocal space and frequency. Both sections deal with single-particle properties on the one hand and collective properties on the other hand, which are directly connected to the quantities measured in a neutron scattering experiment.

1.2.1 Correlations in space and time

1.2.1.1 The Van Hove correlation function

In Section (1.1) several quantities describing the structure of a liquid were defined. However, even if there exist structural features in a liquid, the atoms or molecules of the latter are perpetually moving: the structure of a liquid can only be defined as the time average of its configurations. Let us define the *van Hove correlation function*, which describes the time and space correlations in the liquid:

$$G(\boldsymbol{r}, \tau) = \frac{1}{N} \sum_{i=1}^{N} \sum_{j=1}^{N} \int_V \langle \delta[\boldsymbol{r}_i(0) - \boldsymbol{r}' + \boldsymbol{r}] \delta[\boldsymbol{r}_j(\tau) - \boldsymbol{r}'] d\boldsymbol{r}' \rangle \tag{1.16}$$

In the case of a homogeneous and classical liquid, the latter equation becomes:

$$G(\boldsymbol{r}, \tau) = \frac{1}{N} \sum_{i=1}^{N} \sum_{j=1}^{N} \langle \delta[\boldsymbol{r} - (\boldsymbol{r}_j(\tau) - \boldsymbol{r}_i(0))] \rangle \tag{1.17}$$

This expression can be obtained by considering density correlations.
Let us define the time-dependent density of particles at point $\boldsymbol{r}$:

$$\hat{\rho}(\boldsymbol{r}, t) = \sum_{i=1}^{N} \delta[\boldsymbol{r} - \boldsymbol{r}_i(t)]. \tag{1.18}$$

The density-density time correlation function is given by:

$$G(\boldsymbol{r},\boldsymbol{r}',\tau) = \frac{1}{N}\langle\hat{\rho}(\boldsymbol{r}+\boldsymbol{r}',\tau)\hat{\rho}(\boldsymbol{r}',0)\rangle$$
$$= \frac{1}{N}\sum_{i=1}^{N}\sum_{j=1}^{N}\langle\delta[\boldsymbol{r}'+\boldsymbol{r}-\boldsymbol{r}_i(\tau)]\delta[\boldsymbol{r}_i(0)-\boldsymbol{r}']\rangle \tag{1.19}$$

which after integration over $d\boldsymbol{r}'$ gives again (1.17).

In (1.17), one can distinguish between the *self part* of the van Hove distribution function for which $i = j$ and the *distinct part* for which $i \neq j$. The self part describes the position of an atom as a function of time while the distinct one characterizes the correlated motions of atoms:

$$G(\boldsymbol{r},\tau) = G_s(\boldsymbol{r},\tau) + G_d(\boldsymbol{r},\tau) \tag{1.20}$$

where:

$$G_s(\boldsymbol{r},\tau) = \frac{1}{N}\langle\sum_{i=1}^{N}\delta[\boldsymbol{r}-(\boldsymbol{r}_i(\tau)-\boldsymbol{r}_i(0))]\rangle \tag{1.21}$$

$$G_d(\boldsymbol{r},\tau) = \frac{1}{N}\langle\sum_{i=1}^{N}\sum_{j\neq i}\delta[\boldsymbol{r}-(\boldsymbol{r}_j(\tau)-\boldsymbol{r}_i(0))]\rangle \tag{1.22}$$

Consequently: $G_s(\boldsymbol{r},0) = \delta(\boldsymbol{r})$ and $G_d(\boldsymbol{r},0) = \rho g(\boldsymbol{r})$.
$G(\boldsymbol{r},\tau)d\boldsymbol{r}$ is proportional to the probability of finding a particle i in a volume $d\boldsymbol{r}$ around $\boldsymbol{r}$ at time τ given that there was a particle j at the origin at time $\tau = 0$. The distinction between self and distinct part corresponds to the fact that i and j may be the same particles or not. In other words, the van Hove correlation function is a description of the influence of the presence or absence of a particle on the behaviour of other particles as a function of space and time.

As for $g(\boldsymbol{r})$, for isotropic liquids, $G(\boldsymbol{r},\tau)$ only depends on r.

1.2.1.2 Mean squared displacement and velocity autocorrelation function

Let us now introduce the *mean squared displacement* of a particle:

$$\delta r^2(t) = \langle[\boldsymbol{r}_i(t)-\boldsymbol{r}_i(0)]^2\rangle \tag{1.23}$$

and the velocity of particle i at time t $\boldsymbol{v}_i(t)$. The relation between the velocity autocorrelation function $\langle\boldsymbol{v}_i(0)\cdot\boldsymbol{v}_i(\tau)\rangle$ and the mean squared displacement comes from: $\boldsymbol{r}_i(t)-\boldsymbol{r}_i(0) = \int_0^t \boldsymbol{v}_i(t_1)dt_1$.
Therefore:

$$\delta r^2(t) = \langle\int_0^t \boldsymbol{v}_i(t_1)dt_1\cdot\int_0^t \boldsymbol{v}_i(t_2)dt_2\rangle = 2\int_0^t d\tau(t-\tau)\langle\boldsymbol{v}_i(0)\cdot\boldsymbol{v}_i(\tau)\rangle. \tag{1.24}$$

In a liquid, at short times, the tagged particle experiences the local disorder due to the liquid state. At longer times, the dynamic rearrangement of the initial neighbours of the particle leads to a dislocation of the initial shell of atoms: the particle escapes from the cage of its initial neighbours. The short time behaviour of the tagged particle may be compared to the oscillatory

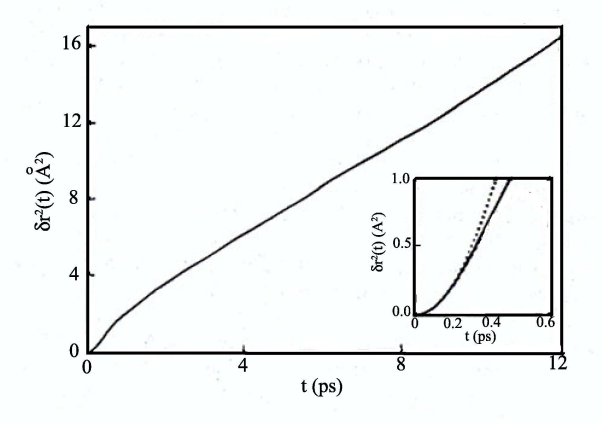

Figure 1.4: Typical time dependence of the mean squared displacement of a particle in a monatomic fluid near melting. Result of a simulation of liquid Cs. Insert: short-time portion and behaviour expected for free particles (dotted line) (from [17]).

motions of a crystal lattice while at long times, it propagates without any correlation to its short-time features through diffusive motion.
At times t so long that $\boldsymbol{v}_i(t)$ and $\boldsymbol{v}_i(0)$ are not correlated any more, (1.24) becomes:

$$\delta r^2(t) = 2\int_0^t t\langle \boldsymbol{v}_i(0).\boldsymbol{v}_i(\tau)d\tau\rangle \tag{1.25}$$

At very long times, the velocity autocorrelation function is negligibly small and the integration can be extended to $t \to \infty$. The latter equation may thus be written as:

$$\delta r^2(t) = 6Dt \qquad (t \to \infty) \tag{1.26}$$

where D is the diffusion coefficient:

$$D = \frac{1}{3}\int_0^\infty \langle \boldsymbol{v}_i(0).\boldsymbol{v}_i(\tau)\rangle d\tau \tag{1.27}$$

From Fig. 1.4, it is apparent that the parabolic increase of the mean squared displacement corresponding to free-particle behaviour is only valid for very short times. This quadratic behaviour comes from the Taylor expansion of the trajectory at short times. At longer times, the result is consistent with the linear time dependence typical of the diffusive regime from (1.26).

From Fig. 1.5, we may notice the negative correlation region in the velocity autocorrelation function. This is usually interpreted as being due to the particle bouncing against the cage formed by its nearest neighbours. This picture of the liquid dynamics is a solid-like one, and indeed, this feature only appears in dense fluids and at low temperatures. Also for dense fluids, a few secondary oscillations are observed at longer times. However, this solid-like behaviour is only valid at rather short times, and the diffusive regime then prevails as shown by the mean squared displacement.

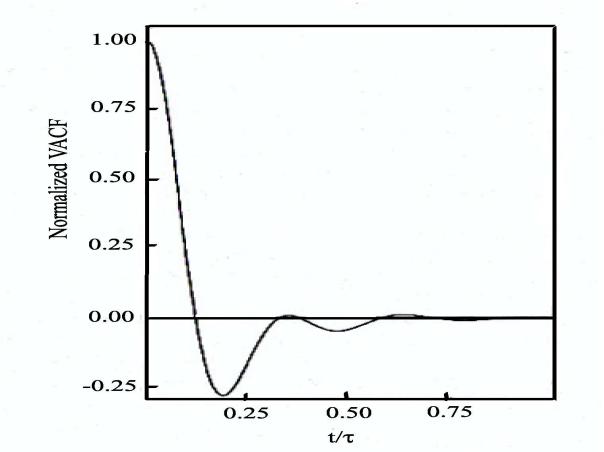

Figure 1.5: Normalized velocity autocorrelation function for liquid Na (with $n\sigma^3 = 0.895$; $T = 308$ K ; $\varepsilon/k_B =$ 386 K ; $\sigma = 4.761$ Å) (from [17]).

1.2.2 Correlations in reciprocal space

1.2.2.1 Single-particle properties

Let us consider the probability that after a time t a given particle has moved a specified distance from its initial position. The single-particle density of atom i at point $\boldsymbol{r}$ and time t is the following dynamical variable:

$$n_{s,i}(\boldsymbol{r}, t) = \delta(\boldsymbol{r} - \boldsymbol{r}_i(t)). \tag{1.28}$$

The interpretation as a density is given by the normalization condition:

$$\int_V n_{s,i}(\boldsymbol{r}, t) d\boldsymbol{r} = 1 \tag{1.29}$$

which means that at any time t the i^{th} particle is somewhere in the volume. If we consider the space Fourier transform of this quantity, we obtain:

$$n_{s,i}(\boldsymbol{q}, t) = \int_V n_{s,i}(\boldsymbol{r}, t) e^{i\boldsymbol{q}.\boldsymbol{r}} d\boldsymbol{r} = e^{i\boldsymbol{q}.\boldsymbol{r}_i(t)}. \tag{1.30}$$

The time correlation associated with $n_{s,i}(\boldsymbol{q}, t)$ is known as the *self-intermediate scattering function*:

$$F_s(\boldsymbol{q}, t) = \langle n^*_{s,i}(\boldsymbol{q}, 0) n_{s,i}(\boldsymbol{q}, t) \rangle = \langle e^{i\boldsymbol{q}.(\boldsymbol{r}_i(t) - \boldsymbol{r}_i(0))} \rangle. \tag{1.31}$$

The inverse Fourier transform of $F_s(\boldsymbol{q}, t)$ goes back to the real space and gives a relation with the self correlation function (or self part of the van Hove distribution function, Eq. (1.20)):

$$\begin{aligned} \frac{1}{(2\pi)^3} \int F_s(\boldsymbol{q}, t) e^{-i\boldsymbol{q}.\boldsymbol{r}} d\boldsymbol{q} &= \langle \delta(\boldsymbol{r} - (\boldsymbol{r}_i(t) - \boldsymbol{r}_i(0))) \rangle \\ &= G_s(\boldsymbol{r}, t) \end{aligned} \tag{1.32}$$

Now if we perform the time Fourier transform of $F_s(\boldsymbol{q}, t)$, we obtain its frequency spectrum:

$$S_s(\boldsymbol{q}, \omega) = \frac{1}{2\pi} \int_{-\infty}^{\infty} F_s(\boldsymbol{q}, t) e^{-i\omega t} dt \tag{1.33}$$

which is directly connected to the incoherent part of the inelastic neutron scattering cross-section (see Section 2.1.4).
Accounting for some general properties of time autocorrelation functions [17], we may establish that $F_s(\boldsymbol{q},t)$ is real and even in both the time and space variables, that is: $F_s(\boldsymbol{q},t) = F_s(-\boldsymbol{q},t)$ and $F_s(\boldsymbol{q},t) = F_s(\boldsymbol{q},-t)$. These considerations lead to the *short-time expansion* of the self-intermediate scattering function:

$$\begin{aligned} F_s(\boldsymbol{q},t) &= F_s(\boldsymbol{q},0)[1 - \langle\omega_q^2\rangle_s \frac{t^2}{2} + \langle\omega_q^4\rangle_s \frac{t^4}{4!} + \cdots] \\ &= 1 - \langle\omega_q^2\rangle_s \frac{t^2}{2} + \langle\omega_q^4\rangle_s \frac{t^4}{4!} + \cdots \end{aligned} \tag{1.34}$$

since $F_s(\boldsymbol{q},0) = 1$.
The quantities $\langle\omega_q^n\rangle_s$ are related to the time derivatives of $F_s(\boldsymbol{q},t)$ at $t = 0$.
The second frequency moment $\langle\omega_q^2\rangle_s$ may be evaluated as [17]:

$$\langle\omega_q^2\rangle_s = -\langle n_{s,i}^*(\boldsymbol{q},0)\ddot{n}_{s,i}(\boldsymbol{q},0)\rangle. \tag{1.35}$$

The use of properties of the time derivatives of correlation functions and of the Maxwellian velocity distribution yields the following expression of the second frequency moment:

$$\langle\omega_q^2\rangle_s = \frac{k_B T}{m} q^2 \tag{1.36}$$

which is valid for any classical system. Thus the short-time decay of $F_s(\boldsymbol{q},t)$ is governed by the second frequency moment which does not depend on the interaction among the particles.
The fourth frequency moment shows the dependence on the interatomic potential $\varphi(r)$:

$$\langle\omega_q^4\rangle_s = \frac{k_B T}{m} q^2 \left[\left(\frac{3k_B T}{m}\right) q^2 + \Omega_0^2\right] \tag{1.37}$$

where Ω_0 is the so-called *Einstein frequency* defined by $\Omega_0^2 = (n/3m)\int d\boldsymbol{r}\nabla^2\varphi(\boldsymbol{r})g(\boldsymbol{r})$. However for sufficiently large q vectors (that is $q \gg \Omega_0(3k_BT/m)^{-1/2}$), the fourth moment (1.37) reduces to the free-particle term: the limiting case of free particles is reached and $F_s(\boldsymbol{q},t)$ essentially probes noninteracting particles.

In the diffusive regime, that is in the range of low wave vectors and long times, the intermediate scattering function is described by the equation [16]:

$$F_s(q,t) = e^{(-Dq^2|t|)} \tag{1.38}$$

which violates the exact short-time behaviour as given by equation (1.34). However, this is not really surprising since these two equations do not deal with the same time-scales. (1.34) deals only with short-time behaviour, it is microscopic and can be accounted for by simple averages. On the other hand, (1.38) probes dynamic processes which comprise a large number of microscopic events and does not account for each of them.
The Fourier transform of (1.38) yields the spectral signal associated with the usual Fick's law diffusion equation:

$$S_s(q,\omega) = \frac{1}{\pi}\frac{Dq^2}{\omega^2 + (Dq^2)^2} \tag{1.39}$$

which is a Lorentzian spectrum with a half width at half maximum $\Gamma_s(q) = Dq^2$. Consequently, the spectra, which exhibit a monotonous decay with frequency at all wave vectors, are expected to become broader with increasing wave vector values, in the limit of small wave vectors.

1.2.2.2 Collective properties

In analogy with the self-particle density introduced for the single-particle properties, let us now use the time-dependent number density of particles at point $\boldsymbol{r}$ of (1.18) for the collective properties. $\hat{\rho}(\boldsymbol{r},t)$ is here the dynamical variable of interest for the calculation of autocorrelation functions.
The space Fourier transform of this quantity is given by:

$$\hat{\rho}(\boldsymbol{q},t) = \sum_{j=1}^{N} e^{i\boldsymbol{q}.\boldsymbol{r}_j(t)} \tag{1.40}$$

Then the time correlation function is defined by:

$$\begin{aligned} F(\boldsymbol{q},t) &= \frac{1}{N}\langle\hat{\rho}^*(\boldsymbol{q},0)\hat{\rho}(\boldsymbol{q},t)\rangle \\ &= \frac{1}{N}\sum_{i=1}^{N}\sum_{j=1}^{N}\langle e^{i\boldsymbol{q}.(\boldsymbol{r}_j(t)-\boldsymbol{r}_i(0))}\rangle \end{aligned} \tag{1.41}$$

This function, also called *intermediate scattering function*, is useful for investigating the collective dynamics of the particles in liquids. Note that at time $t = 0$, $F(q,0)$ is the static structure factor $S(q)$.
As in (1.33) for the incoherent features of the dynamics, the collective properties of the system may be determined in the frequency domain, via the *dynamic structure factor* $S(\boldsymbol{q},\omega)$, which is the time Fourier transform of $F(\boldsymbol{q},t)$:

$$\begin{aligned} S(\boldsymbol{q},\omega) &= \frac{1}{2\pi}\int_{-\infty}^{\infty} F(\boldsymbol{q},t)e^{-i\omega t}dt \\ &= \frac{1}{2\pi N}\int_{-\infty}^{\infty}\langle\hat{\rho}^*(\boldsymbol{q},0)\hat{\rho}(\boldsymbol{q},t)\rangle e^{-i\omega t}dt. \end{aligned} \tag{1.42}$$

In other words, $S(q,\omega)$ is the double Fourier-transform is space and time of the van Hove correlation function $G(r,t)$ defined in (1.16). Both $F(q,t)$ and $S(q,\omega)$ probe the motions on the spatial range of $\frac{2\pi}{q}$ and they only depend on the norm of $\boldsymbol{q}$, due to the isotropy of the fluid. These quantities probe density fluctuations in the liquid. Note that $S(q,\omega)$ is directly linked to the coherent part of the inelastic neutron scattering cross-section (see Section 2.1.4).

In Fig. 1.6, the typical shape of the dynamic structure factor at small wave vectors and low frequencies is shown. The two side-peaks at frequency $\pm ck$ correspond to damped propagative modes with width Γk^2, while the peak centered around $\omega = 0$ is due to a diffusive mode. The latter corresponds to heat diffusion and the side peaks to the propagation of longitudinal sound waves. The damping coefficients Γ and Δ are related to the volume and shear viscosity of the fluid and to its thermal conductivity.

The short-time properties of $F(q,t)$ follow from the expansion:

$$\begin{aligned} F(q,t) &= F(q,0) + \ddot{F}(q,0)\frac{t^2}{2} + F^{(4)}(q,0)\frac{t^4}{4!} + \cdots \\ &= S(q) - \overline{\omega_q^2}\frac{t^2}{2} + \overline{\omega_q^4}\frac{t^4}{4!} + \cdots \\ &= S(q)[1 - \langle\omega_q^2\rangle\frac{t^2}{2} + \langle\omega_q^4\rangle\frac{t^4}{4!} + \cdots] \end{aligned} \tag{1.43}$$

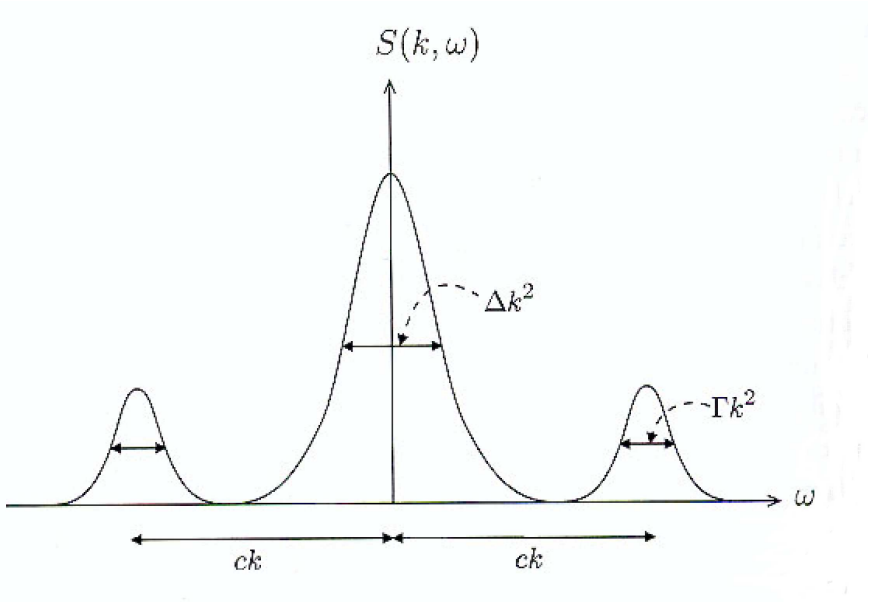

Figure 1.6: Typical dynamic structure factor of a monatomic liquid in the long-wavelength, low frequency limit (from [1]).

where:

$$\overline{\omega_q^n} = (-1)^{n/2} \left[\frac{d^n F(q,t)}{dt^n} \right]_{t=0} \tag{1.44}$$

$$\langle \omega_q^n \rangle = \overline{\omega_q^n} / S(q). \tag{1.45}$$

These equations only contain the even powers of time because $F(q,t)$ is an even function of time, due to the time reversal property of the dynamics. Equations (1.44) and (1.45) define respectively the *frequency moments* and *normalized frequency moments* of $S(q,\omega)$.
The evaluation of these frequency moments is expected to give insight into the collective dynamics probed at the different length scales.
For the second moment, the calculation gives:

$$\overline{\omega_q^2} = \frac{1}{N} \sum_i \sum_j \langle (\boldsymbol{q}.\boldsymbol{v}_i)(\boldsymbol{q}.\boldsymbol{v}_j) e^{-i\boldsymbol{q}.\boldsymbol{r}_{ij}} . \tag{1.46}$$

Since the average over the velocities vanish unless $i = j$, we obtain

$$\begin{aligned} \overline{\omega_q^2} &= \frac{1}{N} \sum_i \langle (\boldsymbol{q}.\boldsymbol{v}_i)^2 \rangle \\ &= \frac{k_B T}{m} q^2 \end{aligned} \tag{1.47}$$

The second frequency moment defined here coincides with the corresponding self-quantity $\langle \omega_q^2 \rangle_s$. However, in the collective case, the second order term of (1.43) shows that the short-time decay of $F(q,t)$ from its initial value is ruled by the normalized second frequency moment $\langle \omega_q^2 \rangle$:

$$\langle \omega_q^2 \rangle = \overline{\omega_q^2} / S(q) = \frac{k_B T}{m S(q)} q^2 \tag{1.48}$$

The qualitative features of the collective dynamics are thus affected by the presence of $S(q)$. In the region of low $\boldsymbol{q}$ vectors, the differences between $S(q,\omega)$ and $S_s(q,\omega)$ are expected to be large since $S(q) \approx S(0) \ll 1$. This region corresponds to the hydrodynamic regime where $S(q,\omega)$ is expected to show inelastic peaks associated with the propagation of sound-like excitations.
Beyond this low q range, the static structure factor $S(q)$ is still oscillatory and affects the short-time behaviour of density fluctuations. With increasing q values, the length scale becomes more and more microscopic and the liquid can not support any collective excitations: the short-time decay of $F(q,t)$ and $S(q,\omega)$ is monotonous and $\langle\omega_q^2\rangle^{1/2}$ is an approximate measure of the spectral width of $S(q,\omega)$.
For q near the position q_m of the main peak in $S(q)$, $\langle\omega_q^2\rangle$ decreases which results in the narrowing of $S(q,\omega)$ and the slowing down of $F(q,t)$. Physically the first sharp peak in $S(q)$ shows that there is a high probability of density fluctuations in the q-range around q_m ; these fluctuations cannot easily be destroyed and consequently have a long life time. This implies the slowing down of $F(q,t)$ near the value q_m. This phenomenon is the so-called *de Gennes narrowing* [19], which is characteristic of the q values of high intensity in the static structure factor. At wave vectors larger than q_m, correlation effects lose their importance and eventually, $S(q)$ reaches 1, where $F(q,t)$ and $F_s(q,t)$ are expected to have essentially the same short-time behaviour. At these high q values, $F(q,t)$ and $F_s(q,t)$ probe the limiting behaviour characteristic of free particles.

1.3 Conclusion

In this chapter, we have defined the quantities relevant for dealing with either structural or dynamic features of liquids. These distribution functions or correlation functions are closely related to quantities measured in neutron scattering experiments (see Section 2.1) and can also be computed from molecular dynamics simulations (see Section 2.2).

2

Structure and dynamics of liquids: experiment and simulation

Contents

On the experimental side, the structure and dynamics of liquids can be probed by several kinds of spectroscopic techniques such as light, X-ray and neutron scattering. Here we are focusing on the use of neutron scattering experiments. On the other hand, theoretical models can also predict the microscopic properties of materials, through atomistic simulations of the systems of interest, either by classical or *ab-initio* molecular dynamics methods.

2.1 The experimental side: neutron scattering

The neutron scattering experimental technique was extensively described in textbooks by Squires [20] and Lovesey [21]. Introductory lectures dealing with this experimental method are also periodically given by Schweizer [22] or in the course of the HERCULES school [23] where the different techniques and applications of neutron scattering are explained. The textbook by Bee [24] also gives a complete description of what can be measured with neutron quasielastic scattering in the fields of solid state chemistry, biology and materials science.
Here we introduce the basic properties of neutrons of interest for probing the features of matter and we derive the relevant quantities associated with this technique.

2.1.1 Main features of the neutron

Neutrons are neutral elementary particles which were discovered in 1932 by James Chadwick. Their neutrality is of particular interest since it enables them to probe not only the surface but also the bulk of the matter without being affected by any Coulomb interaction.
Neutrons can be considered either as particles or as waves, with wavelength related to their velocity by the relation [20]:

$$\lambda = \frac{h}{mv}$$

where h is the Planck constant, m is the mass of a neutron and v its velocity. Moreover, the energy of a neutron is the kinetic energy of the particle:

$$E = \frac{1}{2}mv^2 = \frac{\hbar^2 k^2}{2m}$$

where k is the wave number defined as: $k = \frac{2\pi}{\lambda}$.
The spin of the neutron is $s = \frac{1}{2}$: on the one hand, neutron beams can be polarized in order to perform an analysis of the beam after interaction with the sample ; on the other hand, neutrons have a magnetic moment which may interact with the electronic magnetic moments and give insight into the magnetic structures and excitations. However this feature will not be discussed further here.

If neutrons are thermalized by a moderator at 300K, their mean velocity is of the order of 2200 m/s and their average wavelength is about 1.8 Å. Such values for λ are of the same order as the interatomic distances in condensed matter, and thus thermal neutrons are well suited for

being diffracted by atomic lattices or liquids. Also their energy of the order of some meV matches the range of energy of the dynamics occurring in condensed matter. Consequently neutrons are well suited for studying both the structure and dynamics in condensed matter and especially in liquids.

2.1.2 Basic phenomena - Cross-sections

2.1.2.1 Absorption

When a neutron beam crosses matter, some neutrons may be absorbed by the nuclei of the atoms, resulting in the emission of a proton, an α-particle or a γ-photon or leading to fission of the nucleus. The ability of a given nucleus to absorb neutrons is measured by its absorption cross-section σ_a ([length^2] usually given in barns= 10^{-24} cm^2).
The intensity of the neutron beam after crossing a sample of thickness d is given by: $I = I_0 e^{(-\mu d)}$, where I_0 is the intensity of the incident beam. μ is the linear absorption coefficient given by: $\mu = N\sigma_a$ where N is the number of nuclei per unit of volume.
For most materials, μ is of the order of 0.01 to 1 cm^{-1} which shows that matter is rather transparent to neutrons (for comparison, μ is of the order of 100 to 1000 cm^{-1} for X-rays).

2.1.2.2 Refraction

In case of refraction, the incident beam changes its direction as it crosses the sample. The refractive index is usually close to 1 for neutrons and the refraction is negligible. It is used to design neutron lenses. This phenomenon also leads to total reflection when the incident angle is too small: neutrons are reflected when their angle of incidence is below the critical angle θ_c which is proportional to the wavelength λ. Refraction and total reflection are used for some optics of instruments and for guides.

2.1.2.3 Scattering

Neutron scattering experiments are based on the following principle: incident neutrons with momentum $\hbar\boldsymbol{k}_i$ and associated energy $E_i = \frac{\hbar^2 k_i^2}{2m}$ are guided towards a sample. After interaction between neutrons and sample, the scattered neutrons with desired momentum $\hbar\boldsymbol{k}_f$ and energy E_f are counted relatively far (which means the neutron may be considered as a plane wave) from the sample in a dedicated detector. The typical distance between the sample and the next optical component is of the order of 1 m.
Neutron scattering is considered to be within the limit of the linear response theory [25]. Since the intensity of the incident beam and the strength of the interaction between neutrons and sample are within the limits of this theory, the intrinsic properties of the sample are probed as if they were unperturbed by the beam. Consequently, the measured quantities yield information about the structure and dynamics of the unperturbed sample as a function of the energy transfer $\hbar\omega$ and the momentum transfer $\hbar\boldsymbol{k}$ defined by:

$$\hbar\omega = E_i - E_f \tag{2.1}$$

$$\boldsymbol{k} = \boldsymbol{k}_i - \boldsymbol{k}_f. \tag{2.2}$$

These are the conservation relations for energy and momentum between neutrons and sample. By convention, $\hbar\omega$ is positive when the neutron looses energy in the sample. The conservation equations (2.1) and (2.2) yield restrictions in the accessible dynamic range, which means that

for a given $\boldsymbol{k}$ value, only a determined range of energy transfers can be reached. Equation (2.2) leads to:

$$k^2 = k_i^2 + k_f^2 - 2k_i k_f \cos(\boldsymbol{k}_i, \boldsymbol{k}_f) = k_i^2 + k_f^2 - 2k_i k_f \cos(\theta) \tag{2.3}$$

and accounting for the relation between $\boldsymbol{k}_i$ (resp. $\boldsymbol{k}_f$) and E_i (resp. E_f):

$$\begin{aligned} \frac{\hbar^2 k^2}{2m} &= E_i + E_f - 2\sqrt{E_i E_f}\cos(\theta) \\ &= 2E_i - \hbar\omega - 2\cos(\theta)\sqrt{E_i(E_i - \hbar\omega)}. \end{aligned} \tag{2.4}$$

Figure 2.1 shows the allowed dynamic range for a neutron scattering experiment as a function of the scattering angle θ: as seen in Eq. (2.4), the energy transfer never exceeds the incident energy of neutrons and this yields a limit in the scattering spectra for positive energy transfers (the so-called 'Stokes' scattering). Moreover for a given scattering angle, only one path in the (k,ω) phase space is accessible.

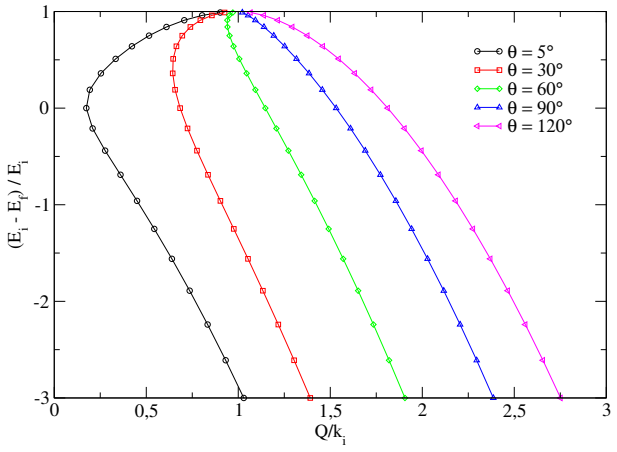

Figure 2.1: Allowed dynamic range for a neutron scattering experiment according to Eq. (2.4) (reduced units).

Let us now move on to the definition of the scattering cross-sections. In a neutron scattering experiment, the measured quantity is the fraction of the neutrons with incident energy E_i which are scattered in a solid angle $d\Omega$ with a final energy within an interval of energy dE_f around E_f. This quantity is called the *partial differential scattering cross-section* and is defined as:

$$\frac{d^2\sigma}{d\Omega dE_f} = \frac{1}{\Phi_0}\frac{\text{number of neutrons scattered per second in } d\Omega \text{ and dE}_f}{d\Omega dE_f} \tag{2.5}$$

where Φ_0 is the incident flux in [neutrons/cm^2/s]. If the energy of scattered neutrons is not analyzed and only neutrons scattered in $d\Omega$ are counted, the *differential scattering cross-section* is measured:

$$\frac{d\sigma}{d\Omega} = \frac{1}{\Phi_0}\frac{\text{number of neutrons scattered per second in } d\Omega}{d\Omega} \tag{2.6}$$

In the end, if all neutrons scattered in all directions are detected, the measured quantity is the *total scattering cross-section*:

$$\sigma_{scatt} = \frac{\text{number of neutrons scattered per second}}{\Phi_0} \tag{2.7}$$

The dimension of the partial differential cross-section is [length^2].[steradian^{-1}].[unit of energy^{-1}]. The dimensions of both differential and total scattering cross-sections can be deduced easily from their definitions.

2.1.3 Theory of thermal neutron scattering

In this paragraph, we restrict the theory to nuclear scattering and ignore the spin of the neutron. Thus the state of the neutron will be completely described by its momentum.

During the process of scattering, a neutron goes from a state described by its wavevector $\boldsymbol{k}_i$ to another state defined by $\boldsymbol{k}_f$. At the same time, the scattering system (*i.e.* the sample) goes from a state called λ to another one λ'.

2.1.3.1 Fermi's golden rule

Let us consider the differential scattering cross-section relative to all the processes for which the scattering system goes from λ to λ' and the momentum of the neutron changes from $\boldsymbol{k}_i$ to $\boldsymbol{k}_f$. The states λ and λ', the incident wavevector $\boldsymbol{k}_i$ are taken as constant and the sum runs over all the $\boldsymbol{k}_f$ in the solid angle $d\Omega$ in a given direction.
Starting from the definition of Eq. (2.6), this differential scattering cross-section can be written as:

$$\left(\frac{d\sigma}{d\Omega}\right)_{\lambda\to\lambda'} = \frac{1}{\Phi_0}\frac{1}{d\Omega}\sum_{\boldsymbol{k}_f \text{ in } d\Omega} W_{\boldsymbol{k}_i,\lambda\to\boldsymbol{k}_f,\lambda'} \tag{2.8}$$

where Φ_0 is the flux of incident neutrons and $W_{\boldsymbol{k}_i,\lambda\to\boldsymbol{k}_f,\lambda'}$ is the number of transitions per second from the state $(\boldsymbol{k}_i,\lambda)$ to the state $(\boldsymbol{k}_f,\lambda')$. The expression of the latter can be evaluated via the use of *Fermi's golden rule* of quantum mechanics [20]:

$$\sum_{\boldsymbol{k}_f \text{ in } d\Omega} W_{\boldsymbol{k}_i,\lambda\to\boldsymbol{k}_f,\lambda'} = \frac{2\pi}{\hbar}\rho_{\boldsymbol{k}_f}\left|\langle \boldsymbol{k}_f,\lambda'|V|\boldsymbol{k}_i,\lambda\rangle\right|^2 \tag{2.9}$$

where $\rho_{\boldsymbol{k}_f}$ is the density of final scattering states per unit energy range and V is the interaction potential between the neutron and the sample. This yields (for details of the calculation, see [20]) the following expression (neglecting the spin of the neutron):

$$\left(\frac{d\sigma}{d\Omega}\right)_{\lambda\to\lambda'} = \frac{k_f}{k_i}\left(\frac{m}{2\pi\hbar^2}\right)^2\left|\langle \boldsymbol{k}_f,\lambda'|V|\boldsymbol{k}_i,\lambda\rangle\right|^2. \tag{2.10}$$

Since $\boldsymbol{k}_i$, λ and λ' are fixed, the scattered neutrons all have the same energy which is determined by conservation of the energy in the system (sample+neutron):

$$E_i + E_\lambda = E_f + E_{\lambda'} \tag{2.11}$$

where E_λ and $E_{\lambda'}$ are the energies associated with the initial and final states λ and λ' of the scattering system.
The partial differential scattering cross-section includes a Dirac distribution of the energy of the scattered neutrons. From Eq. (2.10) we thus obtain:

$$\left(\frac{d^2\sigma}{d\Omega dE_f}\right)_{\lambda\to\lambda'} = \frac{k_f}{k_i}\left(\frac{m}{2\pi\hbar^2}\right)^2\left|\langle \boldsymbol{k}_f,\lambda'|V|\boldsymbol{k}_i,\lambda\rangle\right|^2\delta(E_\lambda - E_{\lambda'} + E_i - E_f) \tag{2.12}$$

This is a basic and general expression for the double differential scattering cross-section, from which more specific cases may be derived.

2.1.3.2 The Fermi pseudo-potential

Now we have to insert a specific function for the interaction potential V, which represents the interaction between the neutron and the sample. In the energy range of the neutrons used for condensed matter studies, the neutron-nucleus interaction potential is a central one, which can be described by the single parameter b_j, the coherent scattering length relative to the nucleus j. This pseudopotential was introduced by Fermi:

$$V_j(\boldsymbol{r}_j) = \frac{2\pi\hbar^2}{m} b_j \delta(\boldsymbol{r}_j) \tag{2.13}$$

where $\boldsymbol{r}_j$ is the distance between the neutron and the j^{th} nucleus. Moreover, the total potential to describe the interaction between the scattering system and the neutron is the sum of the interaction potentials for each nucleus j of the sample: $V(\boldsymbol{r}) = \sum_j V_j(\boldsymbol{r}_j)$ where $\boldsymbol{r}$ is the position of the neutron and $\boldsymbol{r}_j$ is the vector between the neutron and the j^th nucleus.
Upon insertion of the pseudo-potential defined in (2.13) into (2.12), we obtain by assuming that the neutron is a plane wave:

$$\left(\frac{d^2\sigma}{d\Omega dE_f}\right)_{\lambda\to\lambda'} = \frac{k_f}{k_i} \left| \langle\lambda'| \sum_j b_j e^{(i\boldsymbol{Q}.\boldsymbol{R}_j)} |\lambda\rangle \right|^2 \delta(E_\lambda - E_{\lambda'} + E_i - E_f) \tag{2.14}$$

where $\boldsymbol{Q} = \boldsymbol{k}_i - \boldsymbol{k}_f$ is the scattering vector.

2.1.3.3 Expression of the δ-function for energy as an integral

The Dirac-function in Eq. (2.14) can be expressed as an integral over time, with $\hbar\omega = E_i - E_f$:

$$\delta(E_\lambda - E_{\lambda'} + E_i - E_f) = \frac{1}{2\pi\hbar} \int_{-\infty}^{+\infty} e^{(i(E_\lambda - E_{\lambda'})t/\hbar)} e^{(-i\omega t)} dt. \tag{2.15}$$

Together with equation (2.14), we obtain:

$$\begin{aligned}\left(\frac{d^2\sigma}{d\Omega dE_f}\right)_{\lambda\to\lambda'} =& \frac{k_f}{k_i} \sum_{jj'} b_{j'} b_j \langle\lambda| e^{-i\boldsymbol{Q}.\boldsymbol{R}_{j'}} |\lambda'\rangle \langle\lambda'| e^{-i\boldsymbol{Q}.\boldsymbol{R}_j} |\lambda\rangle \\ & \times \frac{1}{2\pi\hbar} \int_{-\infty}^{+\infty} e^{(i(E_\lambda - E_{\lambda'})t/\hbar)} e^{(-i\omega t)} dt.\end{aligned} \tag{2.16}$$

Let H be the Hamiltonian of the scattering system. The states λ and λ' are two eigenfunctions of H with eigenvalues E_λ and $E_{\lambda'}$. Therefore:

$$H|\lambda\rangle = E_\lambda|\lambda\rangle \text{ and } e^{iHt/\hbar}|\lambda\rangle = e^{iE_\lambda t/\hbar}|\lambda\rangle. \tag{2.17}$$

2.1.3.4 Sum over the final states λ' and average over the initial states λ

What is actually measured in a neutron scattering experiment is the sum over all the possible final states λ' for the scattering system with fixed initial state λ and the average over all initial states λ.

If p_λ is the probability of the initial state λ, we obtain, with equations (2.16) and (2.17):

$$\begin{aligned}\frac{d^2\sigma}{d\Omega dE'} =& \sum_{\lambda\lambda'} p_\lambda \left(\frac{d^2\sigma}{d\Omega dE_f}\right)_{\lambda\to\lambda' \boldsymbol{k}_i\to\boldsymbol{k}_f} \\ =& \frac{k_f}{k_i}\frac{1}{2\pi\hbar}\sum_{jj'} b_{j'}b_j \int_{-\infty}^{+\infty} e^{(-i\omega t)}dt \sum_\lambda p_\lambda \times \langle\lambda|e^{-i\boldsymbol{Q}.\boldsymbol{R}_{j'}}e^{iHt/\hbar}e^{-i\boldsymbol{Q}.\boldsymbol{R}_j}e^{-iHt/\hbar}|\lambda\rangle \end{aligned} \quad (2.18)$$

With the time-dependent Heisenberg operators defined as: $\boldsymbol{R}_j(t) = e^{iHt/\hbar}\boldsymbol{R}_j e^{-iHt/\hbar}$, the equation (2.18) becomes:

$$\begin{aligned}\frac{d^2\sigma}{d\Omega dE'} = \frac{k_f}{k_i}\frac{1}{2\pi\hbar}\sum_{jj'} b_{j'}b_j \int_{-\infty}^{+\infty} &\langle e^{(-i\boldsymbol{Q}.\boldsymbol{R}_{j'}(0))}e^{(i\boldsymbol{Q}.\boldsymbol{R}_j(t))}\rangle \\ &\times e^{(-i\omega t)}dt \end{aligned} \quad (2.19)$$

where the value between brackets $\langle A\rangle$ represents the thermal average of the operator A at temperature T: $\langle A\rangle = \langle\lambda|A|\lambda\rangle$.
Here we have given the expression for partial differential scattering cross-section for nuclear scattering. In this equation, the behaviour of the scattering system is described by the eigenstates $|\lambda\rangle$ and the time-dependent Heisenberg operators which contain the Hamiltonian of the system. This expression is a function of the energy transfer $\hbar\omega$ and the scattering vector $\boldsymbol{Q}$.

2.1.3.5 Coherent and incoherent scattering

In order to deal with the double sum over all nuclei a discussion of the isotope disorder is needed. Many atomic species have several isotopes, which are usually randomly distributed over the atomic sites. As was said before, scattering averages over all possible distributions of the atomic isotopes. Therefore we must introduce the following averages:

$$\overline{b_j b_{j'}} = \begin{cases} \overline{b^2} & \text{if } j = j' \\ \bar{b}^2 & \text{if } j \neq j' \end{cases} \quad (2.20)$$

The following expressions are established in the case of a monatomic scattering system. Assuming that the values of the scattering cross-sections of two nuclei b_j and $b_{j'}$ are independent, we replace the term $b_j b_{j'}$ in equation (2.19) by $\overline{b_j b_{j'}}$ and split the double differential scattering cross-section in two contributions:

$$\frac{d^2\sigma}{d\Omega dE'} = \left(\frac{d^2\sigma}{d\Omega dE'}\right)_{coh} + \left(\frac{d^2\sigma}{d\Omega dE'}\right)_{inc} \quad (2.21)$$

where:

$$\left(\frac{d^2\sigma}{d\Omega dE'}\right)_{coh} = \frac{\sigma_{coh}}{4\pi}\frac{k_f}{k_i}\frac{1}{2\pi\hbar}\sum_{jj'}\int_{-\infty}^{+\infty}\langle e^{(-i\boldsymbol{Q}.\boldsymbol{R}_{j'}(0))}e^{(i\boldsymbol{Q}.\boldsymbol{R}_j(t))}\rangle \times e^{(-i\omega t)}dt \quad (2.22)$$

$$\left(\frac{d^2\sigma}{d\Omega dE'}\right)_{inc} = \frac{\sigma_{inc}}{4\pi}\frac{k_f}{k_i}\frac{1}{2\pi\hbar}\sum_{j}\int_{-\infty}^{+\infty}\langle e^{(-i\boldsymbol{Q}.\boldsymbol{R}_{j}(0))}e^{(i\boldsymbol{Q}.\boldsymbol{R}_j(t))}\rangle \times e^{(-i\omega t)}dt \quad (2.23)$$

with: $\sigma_{coh} = 4\pi\bar{b}^2$ and $\sigma_{inc} = 4\pi(\overline{b^2} - \bar{b}^2)$. σ_{coh} and σ_{inc} are respectively the coherent and incoherent scattering cross-sections.

The coherent part represents the interaction between pairs of atoms ($\sum_{jj'}$) and it is related to the square of the average of the scattering length $\bar{b}^2$. It depends on the correlation between the positions at different times of either the same nucleus or different nuclei, thus giving rise to interference effects. Unlike this, the incoherent contribution deals with the interaction of each atom with itself ($\sum_j$) and is related to $\overline{(b-\bar{b})^2}$. It depends on the correlation of the positions of the same nucleus at different times and does not give interference effects.
The incoherent scattering is due to the random distribution of the scattering length around the mean scattering length. If with the same system all scattering lengths were equal, we would only have the coherent scattering contribution. The incoherent scattering part is the difference between scattering in a system where all scattering lengths would be equal and in the actual system.

2.1.4 Correlation functions

The quantities defined above are closely linked to the correlation functions described in Chapter 1. The coherent and incoherent parts of the double differential scattering cross-sections are related to the dynamic structure factors by the following equations:

$$\left(\frac{d^2\sigma}{d\Omega dE'}\right)_{coh} = \frac{k_f}{k_i} N\bar{b}^2 S(\boldsymbol{Q},\omega)$$
$$\left(\frac{d^2\sigma}{d\Omega dE'}\right)_{inc} = \frac{k_f}{k_i} N(\overline{b^2}-\bar{b}^2) S_s(\boldsymbol{Q},\omega)$$

The static structure factor can also be measured by neutron scattering diffraction, that is by integrating over all final energies of scattered neutrons:

$$\begin{aligned}\frac{1}{N}\frac{d\sigma}{d\Omega} &= \frac{1}{N}\langle\sum_{i=1}^{N}\sum_{j=1}^{N} b_i b_j^* e^{i\boldsymbol{Q}.\boldsymbol{r}_{ij}}\rangle \\ &= \frac{1}{N}\left[\bar{b}^2\langle\sum_{i=1}^{N}\sum_{j\neq i} e^{i\boldsymbol{Q}.\boldsymbol{r}_{ij}}\rangle + \sum_{i=1}^{N}\overline{b^2}\right] \\ &= \bar{b}^2 S(\boldsymbol{Q}) + (\overline{b^2}-\bar{b}^2) \\ &= b_{coh}^2 S(\boldsymbol{Q}) + b_{inc}^2. \end{aligned} \tag{2.24}$$

2.1.5 Basic principles of neutron scattering instruments

Here we may distinguish two main kinds of neutron scattering instruments. The first group deals with diffraction and elastic scattering. These instruments are designed for the measurement of the static structure factor and neglect the energy dependence of the detected neutrons. Consequently, these measurements are dedicated to the determination of the structure of the sample. The second group consists of spectrometers, which are dedicated to the measurement of inelastic scattering. These instruments enable the measurement of both the incident and scattered wave vectors. They are useful for the investigation of excitations and vibrations in condensed matter.

Figure 2.2 depicts the different results of scattering at a given scattering angle φ. Elastic scattering corresponds to the case when both incident and scattered wave vectors have the same lengths, while inelastic scattering may be the result of either a loss or gain of energy of the neutron (and thus a decrease or increase of the wave vector).

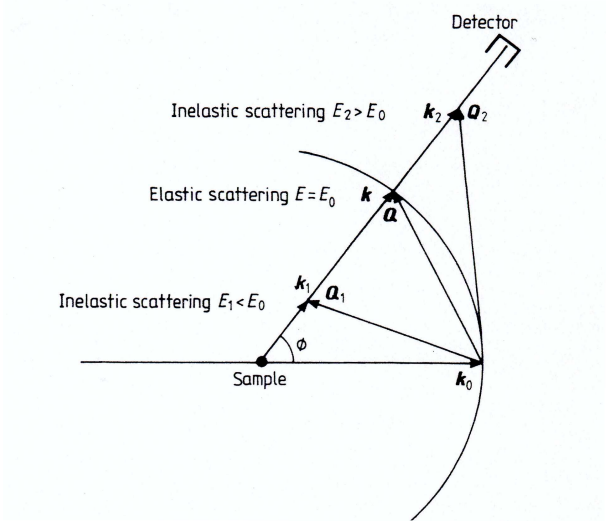

Figure 2.2: Dependence of the wavevector transfer as a function of the energy transfer for a constant scattering angle (from [24]).

2.1.6 From experimental data to physical meaning

In section 2.1.4, we presented the relation between the measured double differential scattering cross-section and the dynamic structure factor of the system, which gives insight into the density fluctuations of the system as a function of time and space. However, this corresponds to an ideal situation, which actually never happens.
In practice, the measured cross-section is affected by many factors and the experimental data have to be corrected before relating them to the dynamic structure factor $S(Q, \omega)$.
Some of these artefacts come from the instrument itself, while others are due to the sample. The instrumental effects are the finite resolution which leads to broadened or shifted features, the background noise due to the surrounding instruments. The sample environment also plays an important role. The sample cell as well as the walls of the cryostat or the furnace may also scatter neutrons. The detected signal is not only affected by the expected scattering from the sample. The beam is actually attenuated while crossing the sample and its environment, due to absorption from the sample and the sample holder; also, multiple scattering events as well as multiphonons may occur in the sample, leading to distortions of the inelastic signal.
Consequently, it is necessary to try and optimize the experimental setup, in order to avoid most of these undesired artefacts. This optimization ranges from the tuning of instrument to the choice of the size and shape of the sample cell and environment.

2.2 The theoretical side: molecular dynamics simulation

In this section, we deal with the theoretical modelling of liquid systems. This can be done either by Monte Carlo simulations [2] or by molecular dynamics (MD) simulations.
Here we focus only on the second kind of approach. It is usually considered as a theoretical tool for investigating the properties of matter, in contrast to experimental approaches. However, it can be considered as a virtual experiment, since it allows insight to be obtained into the features of the system, for instance the structure and dynamics, which can be probed by spectroscopic

means as well.
Molecular dynamics is the solution of the classical equations of motion for atoms and molecules to obtain the time evolution of the system. Such simulations can thus be applied to many-particle systems for which no analytical solution is available.
We differentiate between two kinds of MD simulations. In the first one, the potential describing the interactions is modelled or fitted according to some known properties of the system: this is called classical molecular simulation. In the second kind, *ab initio*, the interaction between nuclei is obtained from the electronic structure and total energy of all the nuclei. The main difference between classical and *ab initio* MD comes from the determination of inter-atomic interactions. In the first part, the principle of classical molecular dynamics simulations is explained while the second is dedicated to first-principle molecular dynamics.

2.2.1 Classical molecular dynamics simulation

The methods involved in classical MD simulations are extensively described in textbooks by Haile [26] or Allen and Tildesley [27] and are regularly taught, for example, during the CCP5 summer school on Molecular Simulations [28].
In the work presented in chapter 3 and 4, we used a "home made" classical MD simulation code. It allows two- and three-body potentials to be used, which are otherwise difficult to include in standard MD codes.

2.2.1.1 Basic principle

Classical molecular dynamics simulations are based on the knowledge of the interatomic potential $\varphi(\{\boldsymbol{r}_i\})$ where $\{\boldsymbol{r}_i\}$ stands for the ensemble of the positions of the atoms. The physical system is represented by a virtual box containing a set of atoms or molecules. Usually the number of atoms in the system ranges from 100 to several thousands.
The trajectories of the atoms are computed by solving the Newton's equations of motion:

$$m_j \ddot{\boldsymbol{r}}_j = -\nabla_j \varphi(\{\boldsymbol{r}_i\}) \text{ for each atom } j \text{ in the system.} \tag{2.25}$$

Usually the analytical form of φ is fitted to experimental results or *ab initio* calculations. The model potential can have many functional forms, for example, the Lennard-Jones potential.

2.2.1.2 Hamiltonian of the system

In classical molecular dynamics simulations, the Hamiltonian is expressed within the Born-Oppenheimer approximation: it only depends on the variables relative to nuclei and the rapid motion of electrons is averaged. If we assume that a classical description of the system is adequate, the Hamiltonian $\mathcal{H}$ of a system of N atoms (we may also consider molecules, however here we are only interested in atoms) may be described as the sum of potential and kinetic energies which depend respectively on the positions $\boldsymbol{r}_i$ and momenta $\boldsymbol{p}_i$ of each atom i. Thus we have:

$$\mathcal{H}(\{\boldsymbol{r}_i\}, \{\boldsymbol{p}_i\}) = \mathcal{K}(\{\boldsymbol{p}_i\}) + \mathcal{V}(\{\boldsymbol{r}_i\}). \tag{2.26}$$

(In case we consider molecules as rigid bodies, the set of positions $\{\boldsymbol{r}_i\}$ may be replaced by a description of the position of the center of mass of the molecule and angles giving the orientation

of the molecule.)
The kinetic energy $\mathcal{K}$ is of the form:

$$\mathcal{K} = \sum_{i=1}^{N} \sum_{\alpha} \frac{p_{i,\alpha}^2}{2m_i} \tag{2.27}$$

where α stands for the Cartesian components of the momentum $\boldsymbol{p}_i$. The potential energy is usually described as a sum of many-body contributions:

$$\mathcal{V} = \sum_i v_1(\boldsymbol{r}_i) + \sum_i \sum_{j>i} v_2(\boldsymbol{r}_i, \boldsymbol{r}_j) + \sum_i \sum_{j>i} \sum_{k>j>i} v_3(\boldsymbol{r}_i, \boldsymbol{r}_j, \boldsymbol{r}_k) + \cdot \tag{2.28}$$

where the first term represents the effect of an external field, the second one is the pair potential and v_3 is the three-body contribution. v_2 actually only depends on the distance between atoms i and j. It can be expected that for real systems the contributions of three-body interactions is significant at liquid densities.

2.2.1.3 Equations of motion for atomic systems

In this subsection we consider only atomic systems. In classical mechanics, the most common form for the equations of motion is the Newtonian one: it uses Newton's second law for relating the motion of an atom to the force exerted on it:

$$m_i \ddot{\boldsymbol{r}}_i = \boldsymbol{F}_i. \tag{2.29}$$

Here m_i is the mass of the atom and the acceleration is given as the second time-derivative of the position $\boldsymbol{r}_i$ of the atom. In Newtonian dynamics, if the force acting on each atom and the initial positions and velocities are known, trajectories of the atoms can be determined.

2.2.1.4 Numerical methods

Periodic boundary conditions Computer simulations are usually performed on a small number of atoms or molecules, typically of the order of some hundreds to some 10000 particles. Either the system is bound together by net attractive forces or an effective container may be represented by an external potential which confines the atoms. However a major obstacle to the simulation of such small systems is the large fraction of atoms which lie on or near the surface of any small sample. These surface atoms experience quite different forces than bulk atoms. Since we want to simulate bulk liquid, we avoid surface effects by using periodic boundary conditions, initially devised by Born and von Karman [29]. This method is applied in the simulation of most systems, but not for biopolymers or pores for instance, where either no boundary conditions or hard wall boundaries may be used. In the case that the system is confined in a cubic box, the latter is replicated to infinity in the three spatial dimensions. During the simulation, if a molecule moves in the original box, each of its periodic images in the replicated boxes moves in the same way. If an atom leaves the main box through its upper face, one of its replica enters by the bottom face of the box. There are no walls at the boundary of the main box, and consequently no surface molecules. Moreover, the number density of the main cell, and hence of its replica, is conserved.

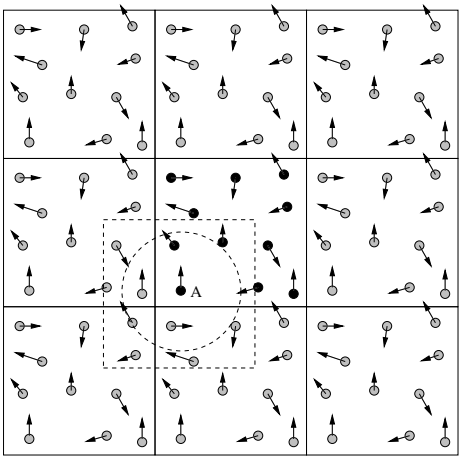

Figure 2.3: Periodic boundary conditions in two dimensions. The main cell is represented in the center with black atoms, while the images are the other eight cells with grey atoms. The dashed square shows the minimum image convention applied to atom A and the dashed circle stands for the effect of the cutoff: only the interactions between A and the atoms in the circle are accounted for when computing the forces acting on A.

This scheme is represented in Fig. 2.3 in two dimensions. The main box is shown in the center, with black atoms, while eight of the nearest images of the main box are shown with grey atoms: the latter occupy the same positions and have the same velocities and directions as the atoms of the main box, relatively to their own cell. Atoms are free to cross each of the four edges, while in three dimensions, they would be able to cross any of the six faces.
However the introduction of periodic boundary conditions may alter the behaviour of the system: the properties of a small infinitely periodic system may be quite different from those of a macroscopic system. For short-ranged forces, a sufficiently large simulation box prevents an atom from interacting with one of its images. However, with long-ranged potentials, there could be substantial forces between a given atom and its own images, thus periodicity would be imposed to a system which is disordered in reality.
Using periodic boundary conditions removes unwanted surface effects but introduces artificial periodicity in the system. This usually restricts the simulation to short-ranged phenomena in that correlations are affected by the artificial periodicity of the system for distances bigger than the half size of the simulation box. The range of spatial correlations available from the simulation consequently depends on the size of the simulated system. For equilibrium properties such as thermodynamic and structural features, earlier studies [30, 31] have shown that the effects of using periodic boundary conditions are small. However as the correlations in space beyond half cell width are artificial, the size of the box must be at least twice the cut-off distance of the potential. Concerning dynamic properties, the use of periodic boundary conditions may have important effects. The artificial spatial periodicity leads to artefacts in the time correlation function when the correlation time exceeds a certain value. The latter is determined from the time needed for a longitudinal wave to cross the simulation cell, and thus the maximum correlation time unaffected by these artefacts may be given by $\tau = L/c_s$ where c_s is the sound velocity, since the sound propagates by longitudinal waves. Periodic boundary conditions consequently prevent simulation of long-wavelength fluctuations, such as long-wavelength phonons for example. If the cubic cell is of side L, all fluctuations with wavelength larger than L are suppressed. In practice,

correlations in time beyond τ do not seem to be affected by the periodic boundary conditions.

Periodic boundary conditions are usually used together with the so-called "minimum image" convention. In fact, MD simulation programs involve the calculation of the potential energy of the system and of the forces acting on each atom. The forces acting on atom i are due to the $N-1$ other atoms in the main cell but also to the images lying in the other cells. This is an infinite number of terms and this summation is usually restricted by the following approximation for short-ranged potentials. Instead of computing the contributions of the $N-1$ atoms in the main cell on atom i, we consider that atom i rests at the center of a region of the same size as the main simulation cell. Atom i interacts with all the atoms that lie in this volume, that is with the closest periodic images of the other $N-1$ atoms: when evaluating the interaction between two atoms i and j of the main cell, the interaction which is actually computed is the one between atom i and the image of j which is closest to i. This technique was first used by Metropolis *et al.* [32].

Another approximation consists of considering that the main contributions to the forces come from the neighbours which are closest to the atom of interest. We set a spherical cutoff r_c for short-range potentials, which means that for interatomic distances larger than r_c, the pair potential is set to zero. The cutoff distance must be sufficiently large to ensure that the perturbation on the properties of the system remains small. This cutoff must also be smaller than $L/2$ for consistency with the minimum image convention.
The use of a cutoff has some consequences: there is a step in the potential at r_c since it is forced to be zero for $r > r_c$ and there is a discontinuity in the forces at r_c. Both of these artefacts are unphysical and may be fixed by using a shifted potential φ_S. The latter can be defined as :

$$\varphi_S(r) = \begin{cases} \varphi(r) - \varphi(r_c) - [r - r_c] \left(\frac{d\varphi}{dr}\right)_{r_c} & \text{if } r \leq r_c \\ 0 & \text{if } r > r_c \end{cases}$$

The constant term $\varphi(r_c)$ does not affect the forces and hence the equations of motion of the system. The last term $[r - r_c] \left(\frac{d\varphi}{dr}\right)_{r_c}$ is added in order to avoid the discontinuity of the forces at r_c. Using this shifted potential removes the energy fluctuations due to the truncation of φ. However, when using such a shifted potential for evaluating properties of the system, corrections must be included to account for the shift.

Integration algorithms For a given set of interaction potentials in a physical system, the integration algorithm used for solving Newton's equations of motion is responsible for the accuracy of the simulation results. In any finite difference algorithm, the solution is an approximation of the evolution of the system which evolves continuously in time. If the integration algorithm were exact, we would obtain the exact results for the chosen model, apart from the errors due to the small size of the simulated system.
Therefore the integrator has to be accurate, which means it must give a very good approximation of the true trajectory. It also has to be stable: it must conserve energy and small perturbations must not lead to drift in energy. The algorithm should be robust to allow large time steps and explore efficiently the phase space. Other properties of interest are the computational speed and the required memory.

The most well-known class of integration algorithms are the Verlet integrators [33]. These were derived using Taylor expansions of the positions as a function of time.

In this paragraph, the vectors $\boldsymbol{r}_i^n$ and $\boldsymbol{v}_i^n$ are respectively the position and velocity of atom i at time $n\Delta t$, while $\boldsymbol{F}_i^n$ is the force acting on atom i at time $n\Delta t$.

The Verlet algorithm gives the evolution of the position of a given atom as:

$$\boldsymbol{r}_i^{n+1} = 2\boldsymbol{r}_i^n - \boldsymbol{r}_i^{n-1} + \frac{\Delta t^2}{m_i}\boldsymbol{F}_i^n + O(\Delta t^4). \tag{2.30}$$

This is a third order estimator of the evolution of the position of atom i as a function of time since the truncation error varies as $O(\Delta t^4)$. The velocity of atom i at time t is estimated using a first-order central difference estimator:

$$\boldsymbol{v}_i^n = \frac{1}{2\Delta t}(\boldsymbol{r}_i^{n+1} - \boldsymbol{r}_i^{n-1}) + O(\Delta t^2). \tag{2.31}$$

The Verlet algorithm is a two-step method since both $\boldsymbol{r}_i^{n-1}$ and $\boldsymbol{r}_i^n$ are needed when computing $\boldsymbol{r}_i^{n+1}$. Initial positions $\boldsymbol{r}_i^0$ and velocities $\boldsymbol{v}_i^0$ are not sufficient to start a simulation.

Modifications to the Verlet algorithm have lead to the so-called *leapfrog algorithm*:

$$\boldsymbol{v}_i^{n+1/2} = \boldsymbol{v}_i^{n-1/2} + \frac{\Delta t}{m_i}\boldsymbol{F}_i^n + O(\Delta t^3) \tag{2.32}$$

$$\boldsymbol{r}_i^{n+1} = \boldsymbol{r}_i^n + \Delta t\boldsymbol{v}_i^{n+1/2} + O(\Delta t^4) \tag{2.33}$$

The so-called *velocity Verlet* algorithm was proposed more recently, which stores position, velocities and accelerations at the same time t and which minimizes rounding errors:

$$\boldsymbol{r}_i^{n+1} = \boldsymbol{r}_i^n + \Delta t\boldsymbol{v}_i^n + \frac{\Delta t^2}{2m_i}\boldsymbol{F}_i^n + O(\Delta t^4) \tag{2.34}$$

$$\boldsymbol{v}_i^{n+1} = \boldsymbol{v}_i^n + \frac{\Delta t^2}{2m_i}(\boldsymbol{F}_i^n + \boldsymbol{F}_i^{n+1}) + O(\Delta t^2) \tag{2.35}$$

After computing the position of atom i at time $n+1$ from (2.34), one can calculate the force acting on this atom at time $n+1$ $\boldsymbol{F}_i^{n+1}$. Then with (2.35) the velocity $\boldsymbol{v}_i^{n+1}$ can be computed. At this point, both kinetic and potential energies of the system are available at time $t + \Delta t$.

Other types of integration algorithms exist, for instance the more sophisticated class of predictor-corrector algorithms. Although the latter are useful for extended-system Hamiltonians such as the Nosé Hamiltonian, they are less stable than the Verlet algorithms: there are problems with energy drift with predictor-corrector algorithms which means the Hamiltonian is not accurately conserved.
The stability of the Verlet algorithms is due to its symplectic character, which means the quantity:

$$\sum_i d\boldsymbol{p}_i \wedge d\boldsymbol{q}_i \tag{2.36}$$

is conserved. In this quantity, $\boldsymbol{q}_i = \frac{d\mathcal{H}}{d\boldsymbol{p}_i}$. A symplectic discretization of the equations of motion preserves the phase-space flow characteristics of the Hamiltonian dynamics and is an exact solution of another Hamiltonian near to the original one.
The discrete dynamics generated by the Verlet algorithms satisfy properties of Hamiltonian dynamics: they preserve time-reversibility, conservation laws and phase-space flow properties. This explains why they are so efficient and stable.

Neighbour lists The most time-consuming part of a MD simulation is the calculation of the forces acting on atoms. For a system of N interacting atoms, we need to compute $\frac{1}{2}N(N-1)$ interactions uniquely associated with a distance r_{ij}. However, truncated potentials are used most of the time and thus the interaction between two atoms which are farther than the cutoff distance r_c is zero. Consequently, to save time during the computation of the distances r_{ij} larger than r_c, a bookkeeping scheme such as the one devised by Verlet [33] is used.

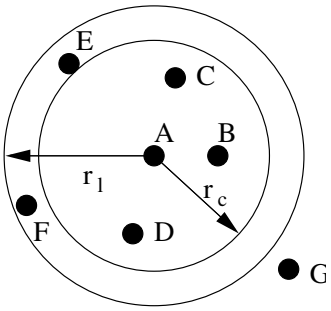

Figure 2.4: Scheme for the Verlet neighbour list: the force is computed for atom A which interacts with atoms B, C and D when the list is constructed. Atoms E and F are part of the neighbour list: they may enter the potential cutoff sphere before the next update of the list and then interact with atom A. Atom G is not part of the present neighbour list: it may enter the skin but not the smaller cutoff sphere before the next update.

In the original Verlet method, a list of neighbouring atoms which lies within a distance r_l of i is maintained for each atom in the system. The radius r_l of the sphere containing the neighbouring atoms is slightly larger than r_c and these two concentric spheres define a skin. Only atoms which are in the list (that is in the sphere of radius r_l) are taken into account when computing the forces and only the atoms which are within a distance r_c of the atom of interest actually interacts via the potential. The neighbour list is periodically updated (intervals of 10 to 20 timesteps are common); the update may be automated: when the maximum total displacement of a given atom becomes larger than $(r_l - r_c)/2$, the list has to be updated. Atoms which lie in the skin when the neighbour list of atom i is constructed may cross r_c between two reconstructions of the list and they will be properly considered for computing the forces acting on i. The algorithm is successful because the skin around the potential cutoff sphere is thick enough so that an atom which is not in the neighbour list could not penetrate into the sphere of radius r_c between two reconstructions of the list. This procedure is depicted in Fig. 2.4.

The construction of neighbour lists becomes more tricky when the potential involves three-body interaction terms as is the case for liquid Ge. For each atom i of the system, two lists are built. The first one contains all the neighbours j (in the sense defined before) arranged in the order of increasing atom number, such that $i < j$; this is called the ordered neighbour list L_i. The second one contains all the neighbours j of atom i irrespectively of atom number: this is the disordered list K_i. These lists are reconstructed when the criterion of maximum total displacement of an atom is reached.
Then the triplets of interacting atoms have to be determined: for each atom i of the system, we consider each atom j of L_i. Then for each atom k in K_j, we built the triplets according to the potential cutoff. In the next step, for each atom k in L_i, we determine the interacting triplets.

The last step consists of sorting the list of triplets and removing the repeated triplets from the list.

2.2.1.5 Overall structure of a MD simulation

For starting a series of simulation runs of a system, we need to design a starting configuration, for which both positions and velocities of the atoms are specified. For a liquid, this initial configuration may be generated by placing atoms at random at the liquid density in the simulation box. One of the main drawbacks of this scheme is the occurrence of overlaps between atoms. This may lead to large forces between atoms and cause instabilities in the solution of the differential equations of motion. This situation may be avoided by optimising the geometry of the system.
Another method consists of starting from a crystal, with a lattice that reproduces the density of the liquid. During the equilibration step of the simulation, the crystalline structure disappears and is replaced by a liquid. We may also do reverse Monte Carlo modelling [14] of $S(q)$ in order to determine the structure of the initial configuration. The last method consists of starting the new simulation from an old one.
Initial velocities may be randomly determined by drawing three random numbers ξ_α uniformly distributed in the range [-1,1] and assign the Cartesian components as $v_{i\alpha} = \frac{\xi_\alpha}{\xi}$ where ξ is the norm of the vector defined by the three random numbers. Then the velocities are scaled in order to reach the set point in energy or temperature. Another method consists of drawing the velocities from a Maxwell-Boltzmann distribution corresponding to the desired temperature.

In a molecular dynamics simulation a system will be in a state characterized by a certain density, temperature, pressure. Subsequently, we have to control some parameters of the system in order to bring it to the desired state. In a standard calculation, the density is controlled by the choice of the box volume V and the total number of atoms in the box. The temperature T is directly related to the kinetic energy by the well-known equipartition formula, assigning an average kinetic energy $k_BT/2$ per degree of freedom: $K = (3/2)Nk_BT$, where K is the kinetic energy of the system. An estimate of the temperature is therefore directly obtained from the average kinetic energy K. Temperature changes are usually achieved by rescaling periodically the velocities in order to reach the desired temperature. As a consequence of rescaling, the system no longer follows Newton's equations, and the total energy is no longer conserved. Hence statistical averages for structural and dynamical properties should not be collected in this stage of the simulation.Velocity rescaling should be used only to bring the system from one temperature to another. After velocity rescaling or after a pressure change in the system, the system has to reach equilibrium, that is the total energy should be conserved.

When equilibrium is reached and the total energy is constant, the trajectories of the atoms can be used for computing some properties of the system such as structural properties ($g(r)$, $S(q)$) or dynamical ones ($G(r,t)$, $S(q,\omega)$).

2.2.2 *Ab initio* molecular dynamics simulation

Ab initio molecular dynamics is a simulation method in which the evolution of the electrons is explicitly accounted for. This method is nowadays very important for the analysis of experimentally determined properties in a theoretical framework. In this section, we explain how *ab initio* molecular dynamics treats the calculation of the electronic structure in the framework of density

functional theory and a molecular dynamics for the nuclei as described previously in Section 2.2.1. Systems of a few hundred atoms can be treated with this approach. A serious limitation of *ab initio* MD techniques is however the limited time scale of a few tens of picoseconds.
The theory of *ab initio* MD was extensively described in several papers by Payne and coworkers [34], Pasquarello [35], Tuckerman [36], Marx and Hutter [37], Benoit [38], Pouillon[39] and Ohno *et al.* [40].

2.2.2.1 Theoretical framework

When studying matter, it is in principle possible to compute all the properties of a set of atoms from the laws of quantum mechanics. The time-dependent Schrödinger equation is:

$$\mathcal{H}\Psi(\{R_I\},\{r_i\};t) = i\hbar\frac{\partial\Psi(\{R_I\},\{r_i\};t)}{\partial t} \tag{2.37}$$

where $\{R_I\}$ describes the positions of the nuclei while $\{r_i\}$ describes the variables relative to the electrons. In this equation, the system is described by a many-body wavefunction $\Psi(\{R_I\},\{r_i\},t)$. $\mathcal{H}$ is the Hamiltonian of the system. It consists of two kinetic energy terms corresponding to the nuclei and the electrons. The term of $\mathcal{H}$ noted V_{n-e} is the potential energy operator. It describes the interactions between nuclei, between electrons and between nuclei and electrons:

$$\begin{aligned}\mathcal{H} &= -\sum_I \frac{\hbar^2}{2M_I}\nabla_I^2 - \sum_i \frac{\hbar^2}{2m_i}\nabla_i^2 + \sum_{i<j}\frac{e^2}{|\boldsymbol{r}_i-\boldsymbol{r}_j|} - \sum_{I,i}\frac{e^2 Z_I}{|\boldsymbol{R}_I-\boldsymbol{r}_i|} + \sum_{I<J}\frac{Z_I Z_J}{|\boldsymbol{R}_I-\boldsymbol{R}_J|}\\ &= -\sum_I \frac{\hbar^2}{2M_I}\nabla_I^2 - \sum_i \frac{\hbar^2}{2m_i}\nabla_i^2 + V_{n-e}(\{R_I\},\{r_i\})\\ &= -\sum_I \frac{\hbar^2}{2M_I}\nabla_I^2 + \mathcal{H}_e(\{R_I\},\{r_i\})\end{aligned} \tag{2.38}$$

The latter equations define the electronic Hamiltonian $\mathcal{H}_e$ and the interaction potential V_{n-e}. However, this description has many variables and can presently only be solved for small numbers of atoms by quantum Monte Carlo. That is why we restrict to the ground state of the system, which is described by a time-independent equation:

$$\mathcal{H}_e\Psi_0(\{R_I\},\{r_i\}) = E_0\Psi_0(\{R_I\},\{r_i\}) \tag{2.39}$$

where E_0 is the energy of the ground state described by the wavefunction Ψ_0.

Moreover, if we do not consider particular types of electronic motion independent of atomic motion (electron tunnelling, electronic transition processes with photoemission...), electrons follow very quickly the nuclear motion. This follows since the mass of the electrons is much smaller than that of nuclei. In such a case the change in electronic state is very rapid compared to the nuclear motion. Since nuclei move much slower than electrons, they may be considered as points and treated in a classical way. This is the Born-Oppenheimer adiabatic approximation. Using this approximation, the calculations of the electronic structure and the ionic motion can be performed separately at each step. The number of variables necessary to describe the wavefunction Ψ is reduced and the term related to the nuclei in $\mathcal{H}$ disappear. This approximation is the basis of the usual *ab initio* molecular dynamics method.

The Hartree-Fock approximation considers the electrons as being independent, each of them evolving in the field created by the others. The total electronic wavefunction Ψ_0 can be written as the product of orthogonal one-electron wavefunctions $\psi_i, i = 1 \cdots N_e$. From these approximations, methods were derived in order to find an exact solution of the Schrödinger equation. However this kind of calculations is restricted to very small systems [40].

These problems are avoided in the density functional theory where the electronic wavefunctions are replaced by the electronic density for solving the Schrödinger equation.

2.2.2.2 The density functional theory (DFT)

In the density functional theory, the knowledge of the electronic density $\rho(\boldsymbol{r})$ allows the properties of the fundamental state of a system consisting of N_e electrons in Coulomb interaction with N_a nuclei to be determined. This observation is of importance since it enables the quantum state to be obtained from a knowledge of the electronic density, which only depends on the position $\boldsymbol{r}$, instead of using the electronic wavefunfction Ψ_0. It is built on two basic theorems proved by Hohenberg and Kohn [41]:

1. There is a universal functional $F[\rho(\boldsymbol{r})]$ of the electron charge density distribution $\rho(\boldsymbol{r})$ that defines the total energy of the electronic system as:

$$E^{KS}[\rho(\boldsymbol{r})] = F[\rho(\boldsymbol{r})] + \int d\boldsymbol{r} v(\boldsymbol{r})\rho(\boldsymbol{r}) \tag{2.40}$$

   where $v(\boldsymbol{r})$ is a potential which is external to the electronic system. It may be created by the Coulomb interactions between the nuclei or between the nuclei and the electrons. F is unique in that it does not depend on $v(\boldsymbol{r})$ and thus the same F applies for electrons in atoms, molecules or solids.

2. For a given external potential $v(\boldsymbol{r})$ and a given number of electrons N_e, the total energy E has a minimum when the electronic density $\rho(\boldsymbol{r})$ coincides with the true charge density distribution in the ground state. The minimum total energy E_0 is obtained with respect to the density fluctuations: this is the *variational principle*:

$$E_0(\{\boldsymbol{R}_I\}) = \min_{\rho} E^{KS}[\rho(\boldsymbol{r})] = \min_{\rho} \left[F[\rho(\boldsymbol{r})] + \int d\boldsymbol{r} v(\boldsymbol{r})\rho(\boldsymbol{r}) \right] \tag{2.41}$$

The problem consists of determining the functional F.

The bases of density functional theory are completed by the contribution of Kohn and Sham [42]. They showed that a system of interacting fermions may be described as an auxiliary system of non-interacting particles.
Each electron is represented by a one-electron wavefunction ψ, such that:

$$\langle \psi_i | \psi_j \rangle = \delta_{ij} \tag{2.42}$$

The density is defined as:

$$\rho(\boldsymbol{r}) = \sum_{i}^{N_{occ}} f_i |\psi_i|^2 \text{ with } \sum_{i}^{N_{occ}} f_i = N_e \tag{2.43}$$

where the sum runs over the N_{occ} occupied states and f_i is an integer occupation number. The functional $F[\rho(\boldsymbol{r})]$ is written as:

$$F[\rho(\boldsymbol{r})] = T[\rho(\boldsymbol{r})] + \frac{e^2}{2}\int d\boldsymbol{r}d\boldsymbol{r'}\frac{\rho(\boldsymbol{r})\rho(\boldsymbol{r'})}{|\boldsymbol{r}-\boldsymbol{r'}|} + E_{xc}[\rho(\boldsymbol{r})] \tag{2.44}$$

where

$$T[\rho(\boldsymbol{r})] = \sum_i \langle\psi_i| - \frac{\hbar^2}{2m}\nabla^2|\psi_i\rangle \tag{2.45}$$

corresponds to the kinetic energy of the non-interacting electrons. The second term in (2.44) refers to the Coulomb interaction between electrons; it is the Hartree term E_H. The last term E_{xc} is the exchange-correlation energy. It represents any contribution to the energy which is not accounted for in the two other terms, such as the deviation of the kinetic energy and the corrections to the Hartree energy. These are both due to the correlations between electrons. Equation (2.44) is a formal definition of E_{xc}.

The Kohn-Sham energy of the system is given by:

$$E = E_{tot}^{KS} = \int v(\boldsymbol{r})\rho(\boldsymbol{r})d\boldsymbol{r} + T[\rho(\boldsymbol{r})] + E_H[\rho(\boldsymbol{r})] + E_{xc}[\rho(\boldsymbol{r})] \tag{2.46}$$

According to the variational principle, we take the variation of (2.46) with respect to the density $\rho(\boldsymbol{r})$ and we obtain:

$$\int \delta\rho(\boldsymbol{r})\left\{\frac{\delta T[\rho(\boldsymbol{r})]}{\delta\rho(\boldsymbol{r})} + \int\frac{\rho(\boldsymbol{r'})}{|\boldsymbol{r}-\boldsymbol{r'}|}d\boldsymbol{r'} + \frac{\delta E_{xc}[\rho(\boldsymbol{r})]}{\delta\rho(\boldsymbol{r})} + v(\boldsymbol{r})\right\}d\boldsymbol{r} = 0 \tag{2.47}$$

Accounting for the conditions: $\langle\psi_i|\psi_j\rangle = \delta_{ij}$ and $\int\rho(\boldsymbol{r})d\boldsymbol{r} = N_e$, we obtain the Kohn-Sham equation for each electron:

$$\left[-\frac{\hbar^2}{2m}\nabla^2 + e^2\int\frac{\rho(\boldsymbol{r'})}{|\boldsymbol{r}-\boldsymbol{r'}|}d\boldsymbol{r'} + \frac{\delta E_{xc}}{\delta\rho(\boldsymbol{r})} + v(\boldsymbol{r})\right]\psi_i = \epsilon_i\psi_i, i = 1\cdots N_e \tag{2.48}$$

These equations define the Kohn-Sham Hamiltonian: $\mathcal{H}_{KS}\psi_i = \epsilon_i\psi_i$. The $\{\psi_i\}$ are usually called one-electron wavefunctions or Kohn-Sham wavefunctions and the $\{\epsilon_i\}$ are the eigenvalues of the Kohn-Sham equations. The second term of these equations is usually denoted V_H while the third one is V_{xc}.
Note that the equations (2.48) must be solved self-consistently: the charge density must be related to the wavefunctions by: $\rho(\boldsymbol{r}) = \sum_i f_i|\psi_i(\boldsymbol{r})|^2$. The self-consistent solution of the system is found in the following way:

1. Perform the initial choice for the orbitals $\{\psi_i\}$ and compute: $\rho(\boldsymbol{r}) = \sum_i f_i|\psi_i|^2$;
2. Compute $V_H(\boldsymbol{r}) = \int\frac{\rho(\boldsymbol{r'})}{|\boldsymbol{r}-\boldsymbol{r'}|}d\boldsymbol{r'}$;
3. Solve the Kohn-Sham equations: $\mathcal{H}_{KS}\psi_i = \epsilon_i\psi_i$;
4. Use the eigenfunctions $\{\psi_i\}$ as new orbitals for computing the density $\rho(\boldsymbol{r})$;
5. Go back to second step until convergence is reached.

Consequently, instead of determining the ground state of a system of interacting fermions which involves a many-electron wavefunction, DFT consists of solving a system of coupled equations, each related to one particle. The main difficulty in solving the equations (2.48) lies in the exchange-correlation term which is unknown.

The exchange energy can be thought as an interaction between electrons which keeps them apart: it is related to the Pauli exclusion principle which states that two electrons cannot have the same set of quantum numbers. The correlation energy comes from the coupling of electronic motions due to their interactions.
The simplest approximation for E_{xc} is the so-called local density approximation (LDA) derived by Kohn and Sham [42]. It assumes that the exchange-correlation energy per electron at $\boldsymbol{r}$ with an electronic density $\rho(\boldsymbol{r})$ is equal to the exchange-correlation energy per electron $e_{xc}(\rho)$ in an homogeneous gas of electrons at the same density $\rho = \rho(\boldsymbol{r})$:

$$E_{xc}^{LDA}[\rho(\boldsymbol{r})] = \int d\boldsymbol{r} n(\boldsymbol{r}) e_{xc}[\rho(\boldsymbol{r})] \tag{2.49}$$

The energy per electron $e_{xc}(\rho)$ for the electron gas is computed by a Monte Carlo method [43] and has been extensively used in DFT calculations.
Nowadays the most common approximation to E_{xc} is the generalized gradient approximation (GGA), which depends not only on the local density but also on its gradient:

$$E_{xc}^{GGA}[\rho(\boldsymbol{r})] = \int d\boldsymbol{r} f_{xc}[\rho(\boldsymbol{r}), |\nabla\rho(\boldsymbol{r})|] \tag{2.50}$$

where different functions f_{xc} may be used.

2.2.2.3 Born-Oppenheimer molecular dynamics

There exist several classes of *ab initio* molecular dynamics methods. The most well-known of them is certainly Car-Parrinello molecular dynamics [44]. In 1985, Roberto Car and Michele Parrinello presented a unifying approach for electronic structure calculations, based on density functional theory, and classical molecular dynamics simulations. They implemented a computational scheme in which the electronic wavefunctions (i.e. the Kohn-Sham one-particle states) can be propagated along the motions of the atoms. This was achieved by setting the one-particle states as fictitious classical degrees of freedom that follow Newton's dynamics.
Here we use the class of *ab initio* molecular dynamics which is usually called Born-Oppenheimer molecular dynamics and consists of solving the static electronic structure problem at each molecular dynamics step for a set of fixed nuclear positions. The electronic part is reduced to solving a time-independent Schrödinger equation, while the nuclei are propagated via classical molecular dynamics. The resulting Born-Oppenheimer method is defined by:

$$M_I \ddot{\boldsymbol{R}}_I = -\nabla_I \min_{\Psi_0}\{\langle\Psi_0|\mathcal{H}|\Psi_0\rangle\} \tag{2.51}$$

$$E_0\Psi_0 = \mathcal{H}\Psi_0 \tag{2.52}$$

The time-dependence of the electronic degrees of freedom is a consequence of the nuclear motion : thanks to the Born-Oppenheimer approximation, the electrons follow the nuclei. However the electronic motion is not intrinsic. In such *ab initio* molecular dynamics (AIMD) simulations, the electronic ground state has to be reached at each MD step.

In Born-Oppenheimer MD using DFT, the Kohn-Sham equations (2.48) can be used at each MD step, for a set of fixed nuclei $\{\boldsymbol{R}_I\}$ to compute the orbitals and the ground state energy.

2.2.2.4 Representing electrons: plane-wave basis sets

In MD calculations, periodic boundary conditions are usually employed, in which the system is infinitely replicated in space. In an infinite periodic system, according to Bloch's theorem, the Kohn-Sham orbitals take the form:

$$\psi_i(\boldsymbol{r}) = e^{i\boldsymbol{k}.\boldsymbol{r}} u_i(\boldsymbol{r}) \tag{2.53}$$

where $\boldsymbol{k}$ is a vector of the first Brillouin zone, $u_i(\boldsymbol{r})$ is a cell-periodic part and the exponential is a wave-like part. A natural basis set for expanding a periodic function is the Fourier or plane-wave basis set. Consequently, u_i can be represented as a Fourier serie:

$$u_i(\boldsymbol{r}) = \sum_{\boldsymbol{G}} c_{i,\boldsymbol{G}} \exp(i\boldsymbol{G}.\boldsymbol{r}) \tag{2.54}$$

where $\boldsymbol{G}$ is a reciprocal lattice vector and $c_{i,\boldsymbol{G}}$ are complex coefficients adjusted to describe the electron density u_i (also called variational parameters). There is a function u_i for each electron. From this expression of the cell periodic part u_i, we obtain a new expression of the Kohn-Sham orbitals:

$$\psi_i(\boldsymbol{r}) = \sum_{\boldsymbol{G}} c_{i,\boldsymbol{k}+\boldsymbol{G}} \exp(i(\boldsymbol{k}+\boldsymbol{G}) \cdot \boldsymbol{r}). \tag{2.55}$$

By the use of Bloch's theorem, the problem of the infinite number of electrons has now been mapped onto the problem of expressing a finite number of wavefunctions in terms of an infinite number of reciprocal space vectors $\boldsymbol{k}$ within the first Brillouin zone of the periodic cell. This problem is dealt with by sampling the Brillouin zone at special sets of $\boldsymbol{k}$ points. This is discussed in 2.2.2.5.

The electronic wavefunctions ψ_i at each $\boldsymbol{k}$-point are now expressed in terms of a discrete plane wave basis set. In principle this Fourier series is infinite. However, the coefficients for the plane waves, $c_{i,\boldsymbol{k}+\boldsymbol{G}}$, each have a kinetic energy $\hbar^2/2m|\boldsymbol{k}+\boldsymbol{G}|^2$. The plane waves with a smaller kinetic energy typically have a more important role than those with a very high kinetic energy. The introduction of a plane wave energy cutoff reduces the basis set to a finite size. This kinetic energy cut-off will lead to an error in the total energy of the system but in principle it is possible to make this error arbitrarily small by increasing the size of the basis set by allowing a larger energy cut-off $\hbar^2/2m|\boldsymbol{k}+\boldsymbol{G}_c|^2$, where $\boldsymbol{G_c}$ stands for the largest $\boldsymbol{G}$ vector included in the expansion. This cut-off energy represents the energy of a free electron with wavevector $\boldsymbol{k}+\boldsymbol{G}_c$. With this expression of the electronic wavefunctions, the Kohn-Sham equations take a particular form [34]:

$$\sum_{\boldsymbol{G'}} \left[\frac{\hbar^2}{2m} |\boldsymbol{k}+\boldsymbol{G}|^2 \delta_{\boldsymbol{G}\boldsymbol{G'}} + v(\boldsymbol{G}-\boldsymbol{G'}) + V_H(\boldsymbol{G}-\boldsymbol{G'}) + V_{xc}(\boldsymbol{G}-\boldsymbol{G'}) \right] c_{i,\boldsymbol{k}+\boldsymbol{G'}} = \varepsilon_i c_{i,\boldsymbol{k}+\boldsymbol{G}}. \tag{2.56}$$

Hence calculations of the various terms of the Kohn-Sham equation can be performed either in real or in reciprocal space.

Equation (2.56) is solved by diagonalization of the matrix which elements are defined as [34]:

$$K_{\boldsymbol{k}+\boldsymbol{G},\boldsymbol{k}+\boldsymbol{G'}} = \frac{\hbar^2}{2m} |\boldsymbol{k}+\boldsymbol{G}|^2 \delta_{\boldsymbol{G}\boldsymbol{G'}} + v(\boldsymbol{G}-\boldsymbol{G'}) + V_H(\boldsymbol{G}-\boldsymbol{G'}) + V_{xc}(\boldsymbol{G}-\boldsymbol{G'}). \tag{2.57}$$

The size of the matrix is defined by the choice of the energy cutoff.

2.2.2.5 Sampling k-space

As stated before, Bloch's theorem changes the problem of calculating an infinite number of electronic wavefunctions to the one of calculating a finite number of electronic wavefunctions at an infinite number of $\boldsymbol{k}$-points.

At each $\boldsymbol{k}$ point, the occupied states contribute to the electronic potential: in principle, an infinite number of calculations are needed to compute this potential. To cope with this problem, we have to account for the fact that the electronic wavefunctions at $\boldsymbol{k}$ points that are close together are almost identical. Consequently, the electronic wavefunctions over a range of $\boldsymbol{k}$-space can be represented by the wavefunctions at a single $\boldsymbol{k}$ point. Hence the calculation of the electronic potential only requires the calculation of the electronic states at a finite number of $\boldsymbol{k}$ points.

Several methods have been devised for obtaining very accurate approximations to the electronic potential by calculating the electronic states at a set of $\boldsymbol{k}$ points in the Brillouin zone (see for instance, Monkhorst and Pack [45], whose scheme is used in VASP). The error induced by the $\boldsymbol{k}$-point sampling on the calculation of the total energy can be reduced by using a denser set of $\boldsymbol{k}$ points. The computed total energy will converge with increasing number of $\boldsymbol{k}$ points.

2.2.2.6 Pseudopotentials

Although the electronic wavefunctions can be expanded using plane-wave basis sets, a very large number of plane waves are necessary to describe the tightly bound core orbitals and to follow the rapid oscillations of the wavefunctions of the valence electrons in the core region. The pseudopotential approximation allows the electronic wavefunctions to be described with a much smaller set of plane waves.
This approximation is based on the knowledge that the valence electrons have a much greater influence than the core electrons on most physical properties of solids. Usually, core electrons are not important in describing, for example, the nature of the bonding between atoms in a crystal; only the valence electrons which surround the core region contribute to it. In the pseudopotential approach, the core electrons are treated with the nuclei.
Consequently, core states are eliminated and the valence electrons are described by nodeless pseudo wavefunctions, thus requiring fewer plane waves to describe them. Pseudopotentials are required to correctly represent the long-range interactions of the core and to produce pseudo-wavefunctions solutions that approach the full wavefunction outside a core radius r_c. Inside this radius, the pseudopotential and the wavefunction should be as smooth as possible in order to allow for a small plane-wave cutoff.

Figure 2.5 is an illustration of the pseudopotential approximation: the valence wavefunction Ψ_{AE} oscillates rapidly in the region occupied by the core electrons due to the strong ionic potential in this region. The pseudopotential V_{pseudo} is constructed in such a way that there are no radial nodes in the pseudo wavefunction Ψ_{pseudo} in the core region and that the pseudo wavefunctions Ψ_{pseudo} and pseudopotential V_{pseudo} are identical to the all electron wavefunction Ψ_{ae} and potential V_{ae} outside the radius cutoff r_c.

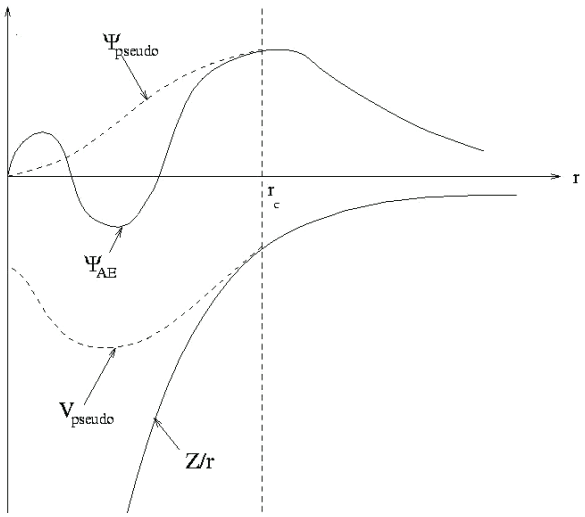

Figure 2.5: Schematic illustration of all-electron (solid lines) and pseudoelectron (dashed lines) potentials and their corresponding wavefunctions. The radius at which all-electron and pseudo-electron match is noted r_c (from [34]).

2.2.2.7 Forces

The forces acting on the ions have to be computed for each molecular dynamics step.
Classically, the force $\boldsymbol{F_i}$ acting on a particle at $\boldsymbol{R}_I$ is given by:

$$\boldsymbol{F}_I = -\nabla_I U(\{\boldsymbol{R}_I\}) \tag{2.58}$$

where $U(\{\boldsymbol{R}_I\})$ is the potential energy of the system.
The quantum mechanical equivalent is, from (2.51):

$$\boldsymbol{F}_I = -\nabla_I \langle \Psi_0 | \mathcal{H}_e | \psi_0 \rangle \tag{2.59}$$

Hence we obtain analytically:

$$\nabla_I \langle \Psi_0 | \mathcal{H}_e | \Psi_0 \rangle = \langle \Psi_0 | \nabla_I \mathcal{H}_e | \Psi_0 \rangle + \langle \nabla_I \Psi_0 | \mathcal{H}_e | \Psi_0 \rangle + \langle \Psi_0 | \mathcal{H}_e | \nabla_I \Psi_0 \rangle \tag{2.60}$$

Provided the wavefunction is an eigenfunction of the Hamiltonian $\mathcal{H}_e$, we have :

$$\langle \nabla_I \Psi_0 | \mathcal{H}_e | \Psi_0 \rangle + \langle \Psi_0 | \mathcal{H}_e | \nabla_I \Psi_0 \rangle = 0. \tag{2.61}$$

From the Hellmann-Feynman theorem [46, 47], we deduce:

$$\boldsymbol{F}_I = -\langle \Psi_0 | \nabla_I \mathcal{H}_e | \Psi_0 \rangle \tag{2.62}$$

Thus the force acting on a nucleus I can be seen as the derivative relative to $\boldsymbol{R}_I$ of the total electronic energy.

2.2.2.8 Overview of the AIMD algorithm

Figure 2.6 describes the computational procedure for *ab initio* Molecular Dynamics using the Born-Oppenheimer approximation.

The initialization consists of choosing the positions of the atoms and the random wavefunctions. From these wavefunctions the charge density $\rho(\boldsymbol{r})$ can be computed and the Kohn-Sham equations are consistently solved. Then the forces acting on the ions are computed via the Hellmann-Feynman theorem and the ions are moved. The next step of molecular dynamics starts with the determination of the new ground state of the system.

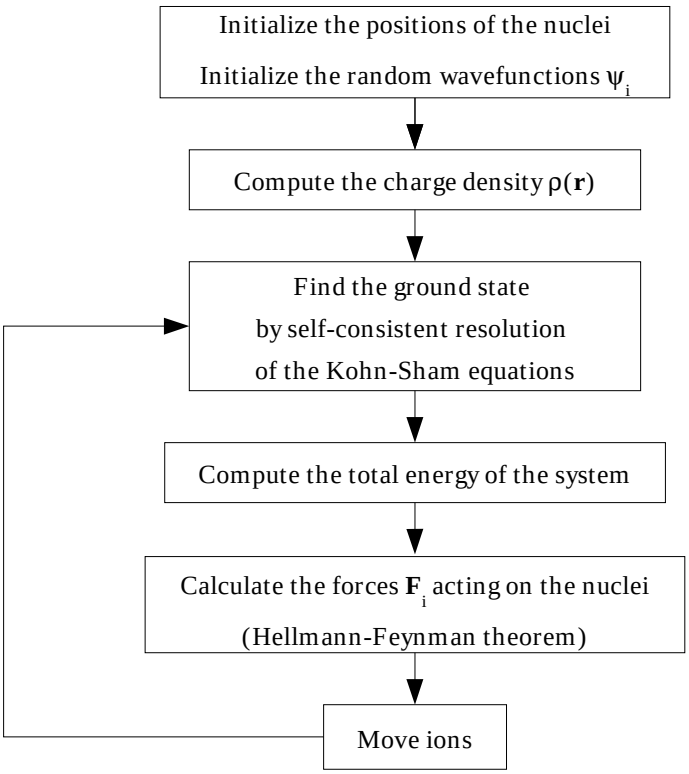

Figure 2.6: Illustration of the global algorithm used for AIMD within Born-Oppenheimer approximation.

2.3 Conclusion

In this chapter, both experimental and theoretical methods dedicated to the investigation of condensed-matter properties have been described. On the one hand, neutron scattering gives insight into the structural and dynamic properties of the system of interest. On the other hand, molecular dynamics simulations give a deeper insight into the microscopic phenomena giving rise to the experimental signal. The use of both techniques in parallel is nowadays widespread since neutron scattering experiments and molecular dynamics simulations give access to the same range of energy and momentum transfers. They are consequently well suited for comparison.

Simulations have a known, restricted set of ingredients (number of atoms, length of simulation, method of energy calculation ...) which limit the validity of this approach. Experimental results from neutron scattering are quite difficult to process: they include all effects, some of which are complicated (for example coupled instrument and sample dependent contributions to the resolution function) and difficult to treat, some of which are unknown. That is why we have developed complete neutron scattering experiments including both instrument and sample, the subject of the following chapter.

3

Simulation of neutron scattering experiments

Contents

Let us now move on to the description of the method implemented for simulating neutron scattering experiments. This relies on two kinds of calculations: the first one is related to the instrument, and is routinely used nowadays for tuning and upgrading neutron scattering instruments. Concerning the sample, molecular dynamics simulations have a real interest in the field of neutron scattering since they give access to the same range of energy and momentum transfers as the experiments.
Coupling these two kinds of simulations gives access to many quantities which may not be accessible experimentally. Some results related to two test sample simulations are discussed in the following.

3.1 Simulation of complete neutron scattering experiments

In this section, both instrument and sample simulations are presented and their coupling for simulating complete neutron scattering experiments is explained.

3.1.1 Instrument simulation

In the field of neutron scattering experiments, scientists are often concerned with the problem of finite resolution of the instruments: the resolution functions may depend on both the scattering vector and the energy transfer between the neutrons and the sample. This leads to distortions in the detected signal since the physical signal from the sample is convoluted with the instrumental resolution. This explains why analytical methods were developed in order to compute these resolution functions. The purpose of these calculations was on the one hand the improvement of the performance of the instruments and on the other hand, a better knowledge of what can be inferred from experimental results. For example, much work has been devoted to the development of the Rescal program, which is dedicated to triple-axis instrument resolution calculation and uses the original Cooper and Nathans method [48]. Although analytical methods can precisely describe complex instrument components, the integration of an increasing number of optical components in the calculation becomes time consuming and limited in accuracy.
As a consequence, since the end of the nineties, Monte-Carlo simulations of neutron scattering instruments have developed considerably: as with analytical calculations, scientists are especially interested in such simulations when they intend to build or upgrade an instrument since these simulations give insight into the influence of physical or geometrical features of the optical components on the features of the beam (intensity, energy distribution and resolution at sample position).

Several packages have been developed for this purpose, with goals being optimization of the instrument setup and assessment of the features of the neutron beam in the instrument. Among these packages are Restrax [49], which combines analytical calculations from Rescal and Monte-Carlo simulation, Vitess [50] developed for the ESS project, Nisp [51], Ideas [52] and McStas [53].
In [54], the McStas package is presented: the Monte-Carlo simulation technique is used to compute the behaviour of the neutron scattering instruments. The simulations are based on the random generation of a large number of initial neutron states (positions, velocity, direction, time of emission and spin) according to a source distribution measured at a neutron scattering facility. Then, for each neutron, a ray-tracing calculation is performed: when neutrons encounter an optical component, they may be transmitted, absorbed, scattered or reflected. They are most of the time considered as particles propagating ballistically although their wave-like character is accounted for in crystals. The parameters of interest, such as the wavelength, the Cartesian components of the wave vector or the energy of the neutrons, are computed and recorded in monitors and detectors along the path of neutrons in the instrument. This latter step gives access, at several positions in the instrument, to the intensity of the beam, the statistical errors associated with the events and the number of counts. In the present work, we use the McStas package, which consists of a library of neutron scattering components, including neutron sources, optics (such as guides, choppers or monochromators), samples and detectors.
In simulations, instruments are described as a set of components with physical (*e.g.* d-spacing for a monochromator, that is the distance between the crystallographic planes which defines the wavelength selected via Bragg's law: $\lambda = 2d\sin\theta$) and geometrical properties (*e.g.* distance

from sample to detector and their respective orientation).

The McStas package has been used for several kinds of investigations. In [55], a study of the influence of different parameters of neutron guides is reported: these simulations show that a factor of 2 to 5 may be gained, compared to present nickel coated guides, in the integrated intensity at the exit of the guide depending on the choice of the geometry, the guide coating and the source. Also the configuration of neutron scattering instruments may be optimized from such simulations as shown in [56]: the simulations were performed to determine the optimal setup of the multi-blade analyzer at the RITA-II triple-axis spectrometer at PSI. The calculations were performed with two kinds of powder samples, with either sharp or broad peaks and three different configurations of the analyzer, respectively with one, three and five blades. They showed that the signal to noise ratio may be improved by a factor 1.3 when increasing the number of blades from one to five. These simulations also prove the ability of such virtual experiments for determining the best instrument setup and optimize the use of the beam.
However, the question of the accuracy of the results obtained with these codes was still open. A recent paper [57] shows a comparative study of the packages Restrax, McStas, NISP, Vitess and Ideas [58] on the same instrument. The simulated instrument is the triple axis spectrometer which was formerly installed on beamline H8 at Brookhaven. Several monitors and detectors were placed at many positions in the simulation. The results are in good overall agreement even if some discrepancies exist which may be due to the variety of algorithms used for handling certain processes: for instance, several algorithms exist for handling the effects of misalignment (also called mosaicity) of the crystallites in the monochromators and analyzers.
Another comparison was performed, but this time between simulation and experiment. IN14, a cold, triple-axis spectrometer at ILL, was simulated with both McStas and Restrax [59]. These calculations showed a good agreement with each other and with the experimental measurements concerning the energy distribution of the incident beam.
Other developments of the McStas package deal with the improvement in the simulation of optical components. In particular, a novel Monte-Carlo algorithm was designed in order to simulate mosaïc, bent and gradient crystals [60]. In this new optical component, neutrons interact with the microscopic crystallites of the crystal, instead of obeying macroscopic laws. This provides information on the number of scattering events occurring in the crystal and on the real path length of neutrons and gives a more accurate description of the crystal.
Finally, one of the first simulations of a complete inelastic neutron scattering experiment was performed using, as sample, a high temperature superconductor [61]. The sample was described using a model of the susceptibility of the crystal which gives access to the dynamic structure factor and the simulation demonstrated the feasibility of such a virtual neutron scattering experiment. However, multiple scattering was not accounted for in this study.

Let us now give an overview of some features of the Monte-Carlo technique as used in McStas. Neutrons are described by their Cartesian coordinates, their velocities and their spins. Their past history (accounting for former events such as absorption probability for example) is accounted for through a weight which is associated with each of them and modified whenever a neutron performs a scattering or propagation event. The final weight factor p_f for the neutron after passing in the whole instrument is defined as:

$$p_f = p_i \prod_{j=1}^{n} \pi_j \tag{3.1}$$

where p_i is the initial weight factor, and π_j is the multiplication factor corresponding to the j^{th} event and n is the number of events. Simulation by weight adjustment is performed whenever possible and is explained in the following. The use of the Monte-Carlo algorithm enables more efficient computation by artificially reducing the amount of undesirable events, which, in our case, consist of neutrons lost before the detector. For example, in real neutron scattering instruments, many neutrons are lost through absorption in the primary spectrometer, before reaching the sample; in simulations, instead of being absorbed, the neutron is weighted in order to account for the probability of absorption and it goes on propagating in the instrument. This scheme increases the number of detected neutrons and enhances the statistics and efficiency of the simulation. For example, if the reflectivity of a given optical component is of the order of 10%, instead of losing 90% of the neutrons, their weight will be multiplied by a factor 0.1 and every neutron is allowed to reflect in the component.
The scheme described above in the case of absorption and reflectivity is also called *importance sampling*: it means that the simulated distribution function $f_{MC}(E, \Omega, \boldsymbol{r})$ is different from the physical one $\Pi(E, \Omega, \boldsymbol{r})$ and the weight of the neutron must be adjusted by a factor π_j. In the example of the restricted distribution of directions, if the detector area corresponds to a solid angle $d\Omega$ and scattering is isotropic, the weight has to be adjusted by a factor: $\pi_j = \frac{d\Omega}{4\pi}$.

Another advantage of simulations is the ability to compute quantities which are not accessible in real neutron scattering experiments. For example, we can directly map the (q, ω) transfers on a 4π detector and visualize the different orders of multiple scattering separately. It is also possible to restrict the computed $|q|$-range, if one wants to avoid intense elastic features which may mask weaker inelastic or quasi-elastic contributions.

Example: simulation of a triple axis spectrometer

The following results deal with the simulation of the primary spectrometer of the triple-axis spectrometer IN14 at ILL (see Fig. 4.28 for a picture of a typical TAS).

The first component of the simulated instrument is a source: neutrons are generated according to the energy distribution measured at the entrance of the guide looking at the horizontal cold neutron source at the ILL. By means of Monte-Carlo importance sampling, the neutrons coming from the source are directed to the guide entrance instead of being spread in the whole 4π solid angle. The guide is described by its geometry; further parameters determine the features of the reflectivity of the guide and the absorption properties of the material it is made of. At the exit of the guide, a monochromator is positioned to select the wavelength incident onto the sample. The monochromator is made of seven adjacent horizontal blades, which may be vertically focused to the sample; its mosaicity may be anisotropic, which means it may be different in the vertical and horizontal directions. However, as a simple approximation, the mosaicity (that is the misalignments of its crystallites) is only described from a macroscopic point of view. Finally neutrons propagate to the sample position through a collimator, which eliminates neutrons with high horizontal divergence.

In Figures 3.1, 3.2 and 3.3, the evolution of the distributions of different properties of the beam is shown between the source and the position of the sample. In each of these figures, the four plots correspond to the following positions in the primary spectrometer: on top left, the monitor is just at the guide entrance, on top right, at the exit of the guide before the monochromator; the distributions shown on the bottom left plot are taken just after the monochromator while

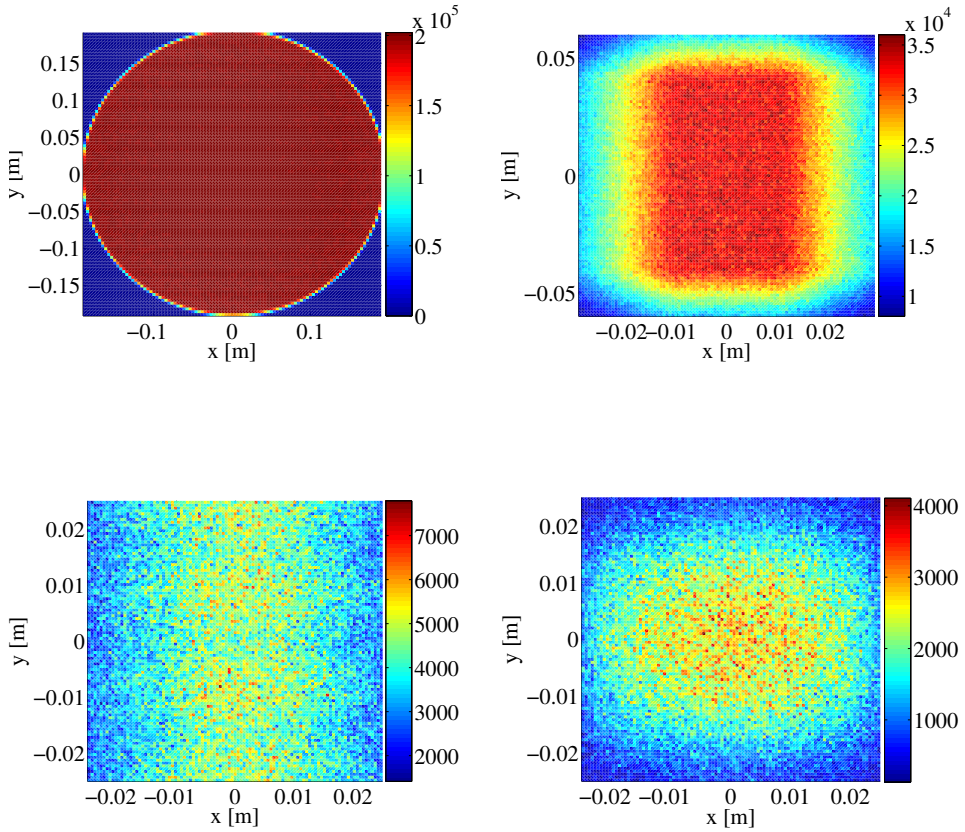

Figure 3.1: Spatial distribution of the beam from source to sample position at $k_i = 1.55$ Å^{-1} on the primary spectrometer of IN14 (top left: at the guide entrance; top right: after the guide; bottom left: after monochromator; bottom right: at sample position; intensity displayed by the color bar is in n/cm^2/s)

on the right, they describe the beam at the sample position.

Figure 3.1 shows the spatial distribution of the beam in the x-y plane, that is perpendicular to the beam (the latter is along z). Figure 3.2 is the evolution of the angular divergence of the beam and figure 3.3 shows the energy distribution. On the first two figures, the intensity represented by the colormap is in n/cm^2/s.

On the top left plots, after the source, the beam has a circular shape of radius 20 cm while its divergence is isotropic, of the order of 6 degrees. Its integrated intensity is about $1.56.10^9$ n/cm^2/s. Its energy distribution is already rather thin. The real neutron beam coming from the source comprises a wide range of energies. However in this simulation, we use the importance sampling scheme in order to generate only those neutrons with wavelength close to the range of wavelengths selected by the monochromator.
On the next plot (top right), the shape of the beam has changed since it has gone through the guide. The spatial distribution of the beam now corresponds to the shape and size of the

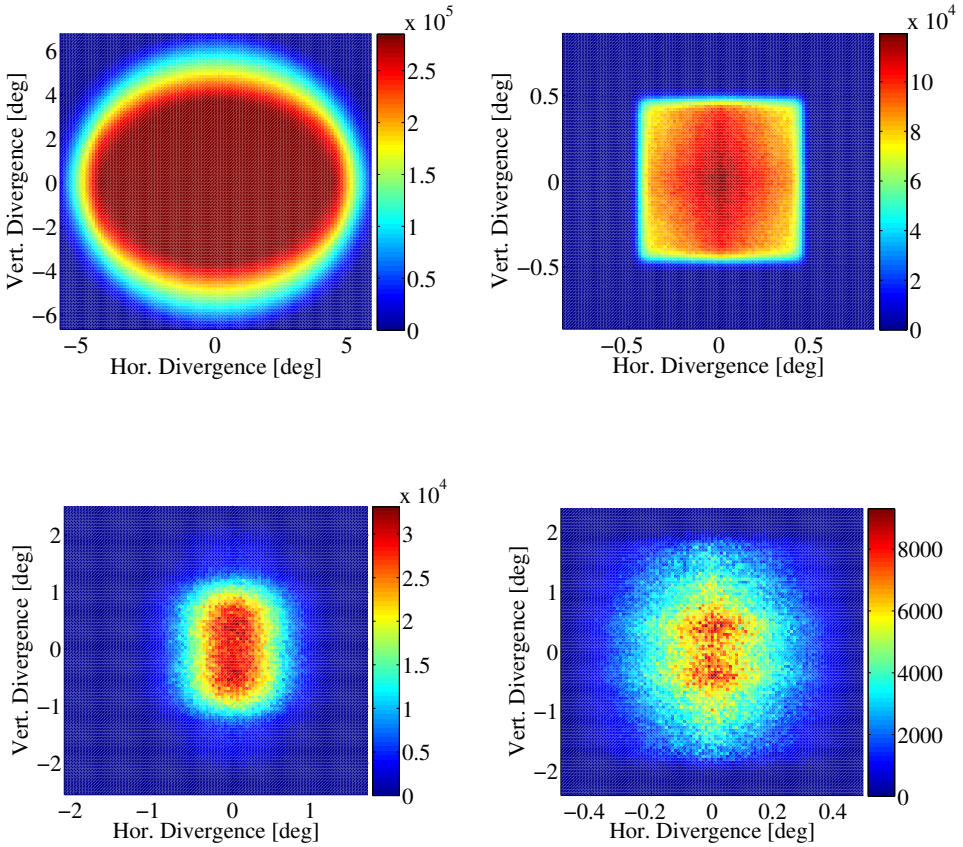

Figure 3.2: Divergence of the beam from source to sample position at $k_i = 1.55$ Å^{-1} on the primary spectrometer of IN14(top left: at the guide entrance; top right: after the guide; bottom left: after monochromator; bottom right: at sample position; intensity displayed by the color bar is in n/cm^2/s)

guide, which is 6 cm in width and 12 cm in height. The integrated intensity has decreased approximately by a factor of six: many neutrons either did not enter the guide due to their initial divergence or were absorbed by the guide due to too high incident angles on the guide walls. This explains why the divergence is also much smaller than before the guide. However, the energy distribution is the same as before except for the change in intensity.
On the bottom left plot, the monitors are now located after the monochromator. The intensity is again lower by one order of magnitude and the shape of the beam is smeared out. The divergence is higher than at the exit of the guide due to crystal mosaicity and vertical focusing and the energy distribution is now almost gaussian with a selected energy around 4.97 meV with a half width at half maximum of 80 μeV. This corresponds to a wave vector $k_i = 1.55$ Å^{-1} and a wavelength $\lambda_i = 4$ Å.
On the last plot, at the sample position, the size of the beam is about 6 cm in both height and width, which results from the vertical focusing configuration of the monochromator. The horizontal divergence is of the order of 0.4 degree, thus much lower than after the monochromator: this is the effect of the collimator placed between monochromator and sample. The energy

distribution has approximately the same shape as before the collimator. Nevertheless the peak is better defined with a smaller half width at half maximum, of the order of 50 μeV: the neutrons with trajectories horizontally divergent after the monochromator did not have the appropriate energy after Bragg scattering and these were absorbed by the collimator, leading to a sharper definition of the incident energy at sample position.
At the sample position, the detected intensity (which is the integral over the curve of energy distribution at sample position) is $1.65.10^7$ n/cm^2/s with an error of $3.35.10^4$. The corresponding measured intensity at this incident wave vector k_i is $1.6.10^7$ n/cm^2/s. These results are consequently in good agreement.

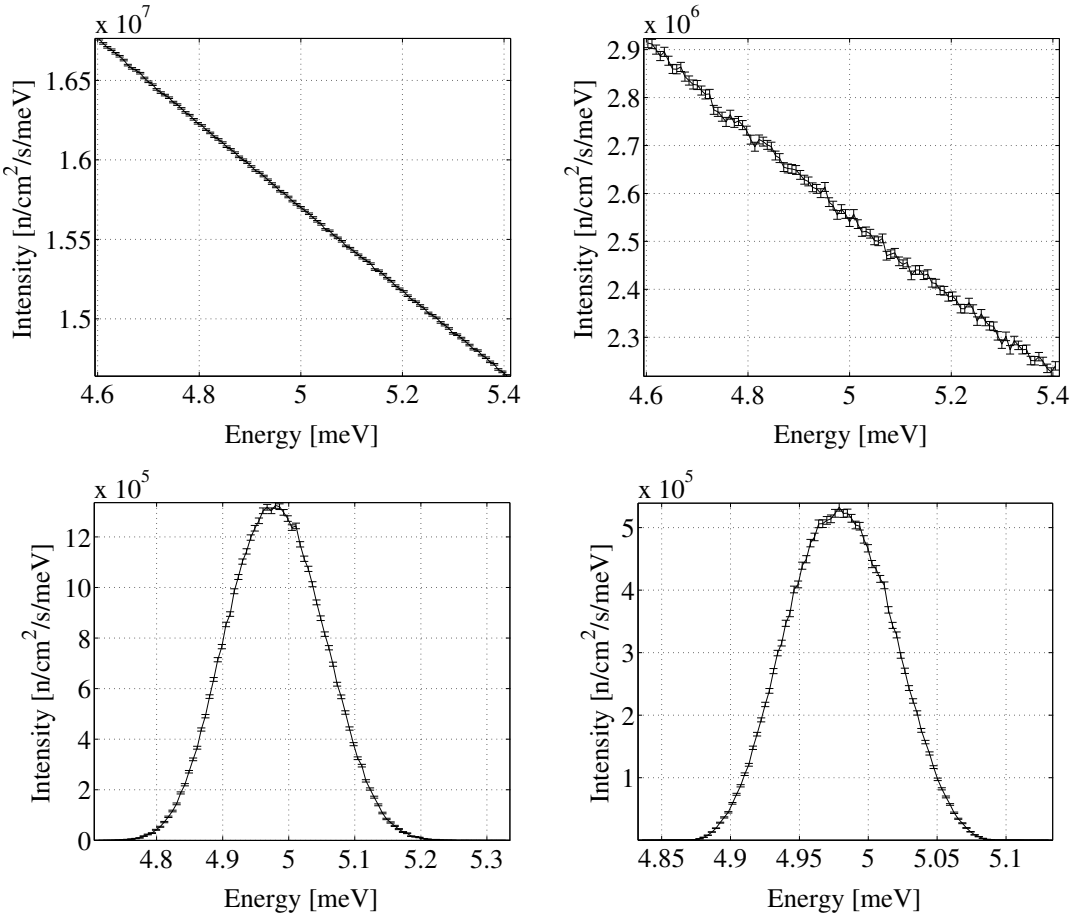

Figure 3.3: Energy distribution of the beam from source to sample position at $k_i = 1.55$ Å^{-1} on the primary spectrometer of IN14(top left: at the guide entrance; top right: after the guide; bottom left: after monochromator; bottom right: at sample position)

3.1.2 Sample simulation

In order to simulate a realistic sample, we have to account for several possible effects of the interaction between neutrons and sample. These effects range from absorption and multiple scattering to elastic, inelastic, coherent and incoherent interactions.
The sample modules presently included in McStas mainly handle elastic scattering although a

complete simulation of an inelastic neutron scattering experiment has been performed, based on a model specific to high-T_c superconductors [61].
The following paragraphs describe how a more generic and realistic sample may be simulated, including all the effects mentioned above. Several sample shapes may also be simulated, namely cylinder, hollow cylinder and box-shaped samples.

3.1.2.1 Absorption and multiple scattering

Since the beginning of neutron scattering, computing multiple scattering has been a matter of interest since any neutron scattering experiment is unavoidably contaminated by higher orders of scattering. As a matter of fact, the samples must be chosen thick enough so that the fraction of incident neutrons scattered by the sample is significant. Consequently, a non negligible fraction of the scattered neutrons may be scattered more than once, leading to artifacts in the detected signal.
In the case of crystals, multiple scattering mainly induces a smooth background, which can be easily distinguished from the discrete peaks due to single scattering from phonons for instance. However in liquids or amorphous solids, the dynamic structure factor is a smooth function of q and ω. Consequently the background due to multiple scattering is quite difficult to extract when analyzing the experimental data. Multiple scattering is expected to be particularly harmful in this case: small distortions in $S(q,\omega)$ may destroy a part of the information included in it.

One of the pioneering works dealing with multiple scattering corrections is due to Vineyard [62]: his method was based on solving a set of transport equations for neutrons. From this, the number of neutrons per unit volume at a given position $\boldsymbol{r}$ which have already scattered n times and are now proceeding in the direction of a unit vector $\boldsymbol{s}$ may be determined. This method is based on the assumption of quasi-isotropic cross-sections and neglects the effect of energy changes during scattering. It is shown that the intensity of the n^{th} order of scattering is proportional to the ratio $(\frac{\sigma_s}{\sigma_t})^n$, where σ_s is the scattering cross-section and σ_t is the total cross-section including scattering and absorption ($\sigma_t = \sigma_s + \sigma_a$). This means that a large absorption cross-section can reduce higher scattering orders compared to first order. This method is implemented in the case of a plane slab.
Twenty years later, Sears derived the effective scattering function as an expansion in terms of the orders of scattering [63]. This method may be applied to specific sample shapes. Copley developed a Monte-Carlo code, MSCAT, designed for computing multiple scattering [64]. It is based on the use of an input scattering function and is able to simulate both elastic and inelastic scattering. It may also account for scattering in the sample container. Mildner and collaborators also described an optimized Monte-Carlo technique: it was designed for the multiple scattering corrections of neutron diffraction data of isotropic systems [65]. In what concerns inelastic neutron scattering experiments, a Monte-Carlo correction procedure for multiple scattering effects was also derived [66]: it uses a combination of experimental data and the so-called "Synthetic Model", which has proved to work for liquids and polymers, for both coherent and incoherent scattering, except in the low-q limit. The corresponding code also accounts for the attenuation of the beam while crossing the sample. The method was tested for extracting the densities of vibrational states of deuterated water and ice from measured data. The effects of both elastic and inelastic multiple scattering were also computed by Wuttke [67] for three simple models describing a rigid solid, a glass and a viscous liquid . This study showed the influence of multiple scattering on the wave-number-dependent and frequency-dependent features of the dynamic structure factor. Finally, the effects of multiple scattering were studied in the case of deep in-

elastic neutron scattering by Mayers [68], who gave a very detailed explanation of the general principles of calculation of the random quantities in Monte-Carlo simulations. Finally, Seeger [69] included multiple scattering effects in the simulation of a vanadium sample and showed the correlations between effects coming from the instrument and from the sample.

In our sample module, we use the following algorithm for computing absorption and multiple scattering. It is based on the knowledge of the number density (that is the number of atoms per unit volume) and the cross-sections (σ_a for absorption and σ_s for scattering) of the material.
When entering the sample, any neutron can either interact (i.e. it can be absorbed or scattered) with the sample or be transmitted to the secondary spectrometer. The outcome of this choice is guided by the probability P_i that a neutron will interact with a sample within a distance d, as opposed to the probability of being transmitted:

$$P_i = 1 - \exp(-\mu d), \tag{3.2}$$

where μ is the attenuation factor depending on both σ_a and σ_s, and d is the distance traveled by the neutron from entry to exit of the sample. After this random choice, any neutron interacting with the sample will be weighted by the probability $P_{s/a}$ of scattering versus absorption:

$$P_{s/a} = \frac{\sigma_s}{\sigma_s + \sigma_a}. \tag{3.3}$$

This avoids losing neutrons through absorption while respecting the physical occurrence probabilities: all neutrons interacting with the sample are scattered after an appropriate weighting accounting for absorption probability.
Whenever a neutron interacts and is scattered, we have to determine where the interaction occurs. This is done by sampling a decaying exponential with parameter $\sigma_t = \sigma_a + \sigma_s$ as explained by Mayers [68]. The position x is given by:

$$x = -\frac{1}{\mu} \log[1 - \xi(1 - \exp(-\mu d))], \tag{3.4}$$

where ξ is a random number uniformly generated between 0 and 1, and d is the distance to exit of the sample and the maximum possible value of x (for a detailed explanation, see A.1).

For multiple scattering, the reasoning is similar: after changing its energy and direction of propagation (see Section 3.1.2.2), the fate of neutrons is given by the probability of interacting in the remaining part of the sample, that is in the escape distance. Note that the sample simulation enables the choice of the number of scattering events occurring in the sample: neutrons may be free to interact with the sample as many times as determined from the Monte-Carlo technique, or they may be forced to scatter a given number of times inside the sample. This gives separate access to the different orders of scattering.
Since the present sample module can handle several sample shapes (cylinder, hollow cylinder and box), the effects of sample size and shape on absorption and multiple scattering can be studied.

3.1.2.2 Using $S(q, \omega)$ for computing scattering events

We have restricted the study to the case of isotropic samples, in order to avoid the difficulties due to handling a four dimensional matrix of $S(\boldsymbol{q}, \omega)$, which would be necessary in the case of

an anisotropic sample. However, the method presented here could be generalized to anisotropic materials provided an accurate description of $S(\boldsymbol{q}, \omega)$ can be computed.
In this paragraph, $S(q, \omega)$ may designate either the coherent or the incoherent part of the signal or the contributions of both of them in case we simulate both coherent and incoherent processes. From the molecular dynamics simulations trajectories, we can calculate the dynamic structure factor $S(q, \omega)$ describing the structural and dynamical behaviour of the sample. $S(q, \omega)$ is computed with the help of either a home-made code or the nMoldyn package [70]. Both programs allow us to evaluate separately the coherent and incoherent parts of the dynamic structure factor. We can compute coherent and incoherent signals from the sample either together or separately, and we are also able to compute inelastic scattering. Consequently, the calculation of the dynamic structure factor gives insight into both structural and dynamic, coherent and incoherent properties of the sample. It is thus a relevant description of the microscopic properties of the material.
Once computed, $S(q, \omega)$ is used as a probability distribution of energy and momentum transfers, respectively, $\hbar\omega$ and q, which are the relevant parameters of any scattering event in our scheme. The principle for drawing the values of q and $\hbar\omega$ lies in the conditional probability formula:

$$P(q, \hbar\omega) = P(q \cap \hbar\omega) = P(\hbar\omega).P(q|\hbar\omega), \tag{3.5}$$

where $P(q, \hbar\omega)$ is represented by a normalized version of $S(q, \omega)$. Note that the probability of the event A is noted P(A).
Both probability distributions of energy and momentum transfers can be computed from $S(q, \omega)$, since we consider it (after relevant transformations for normalization and random choice) as a probability distribution of the scattering events (for a detailed explanation, see A.2). Subsequently the energy transfer is drawn from $S(\omega)$ which is a vibrational density of states computed by integration over all the q values available in the $S(q, \omega)$ matrix. Once $\hbar\omega$ is computed, the momentum transfer can be randomly chosen from the distribution of q given the known energy transfer (see Section 3.2 for figures of these distributions of energy and momentum transfers).
The principle of detailed balance is also accounted for. For an isotropic system, it is given by the equation:

$$S(q, -\omega) = \exp\left(\frac{-\hbar\omega}{k_B T}\right) S(q, \omega), \tag{3.6}$$

where T is the temperature of the system and k_B is the Boltzmann constant. This enables us to choose between Stokes and anti-Stokes scattering by drawing a random number which determines the sign of the energy transfer.

Once both energy and momentum transfers have been drawn, the choice of the scattered wave vector $\boldsymbol{k}_f$ has to be performed. The first step consists of determining the length of $\boldsymbol{k}_f$ accounting for the energy conservation law (2.1). This is done by solving the equation:

$$\hbar\omega = \frac{\hbar^2}{2m}(k_i^2 - k_f^2) \tag{3.7}$$

where k_f is the unknown.
Then we have to compute the direction of $\boldsymbol{k_f}$ from the momentum conservation equation (2.2). For this purpose, we use geometric considerations. Let us define $\hat{\boldsymbol{k}}_{\boldsymbol{s}}$ as the unit vector defining the direction of $\boldsymbol{k_f}$. We have: $\boldsymbol{k_f} = k_f \hat{\boldsymbol{k}}_{\boldsymbol{s}}$ and $\|\hat{\boldsymbol{k}}_{\boldsymbol{s}}\| = 1$.
After drawing the length of $\boldsymbol{q}$ from the probability distribution, we may solve: $q^2 = \|\boldsymbol{k_i^2} - \boldsymbol{k_f^2}\|$ and find the relevant $\hat{\boldsymbol{k}}_{\boldsymbol{s}}$. The set of $\hat{\boldsymbol{k}}_{\boldsymbol{s}}$ vectors satisfying the former equation is a circle (see

Appendix A.3). We thus have to draw a random angle (uniform law between 0 and 2π) for choosing a random position of $\hat{\boldsymbol{k}}_{\boldsymbol{s}}$ on the circle. Once $\hat{\boldsymbol{k}}_{\boldsymbol{s}}$ is determined, the final scattering wave vector $\boldsymbol{k}_{\boldsymbol{f}}$ is known.

3.1.3 Coupling instrument and sample simulations

3.1.3.1 General scheme

The following figure 3.4 gives an overview of the process involved in the complete simulation of a neutron scattering experiment. The instrument is simulated with the McStas package, while the sample is described by its dynamic structure factor $S(q, \omega)$. These combine in the sample module where the interaction between neutrons and sample is handled.

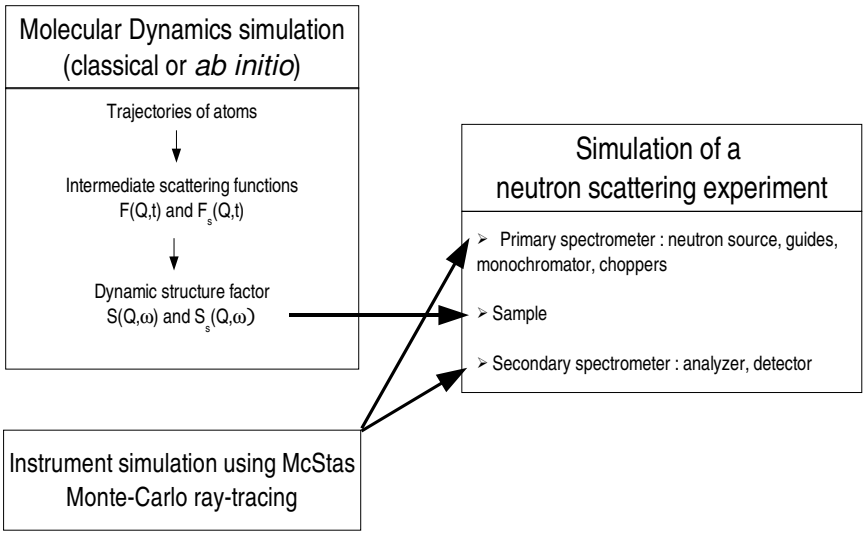

Figure 3.4: Overview of the simulation of a neutron scattering experiment

3.1.3.2 Handling the interaction between neutrons and sample

In the following algorithm, p is the statistical weight of the neutron, *mult_scatt* is a boolean (initialized to *true*) which determines if further scattering events may occur or not.

The general process involved in each scattering event needs the drawing of several random numbers: the first one determines the position where the neutron interacts with the sample, the second one guides the choice of $\hbar\omega$ in the *density of states* computed from $S(q, \omega)$ and another random number is used for accounting for the detailed balance. Once the energy transfer is known, the momentum transfer q is drawn from the conditional probability distribution of q values. The following random number determines the scattering direction $\boldsymbol{k}_f$ in agreement with both energy and momentum conservation laws. Finally the last random number determines whether the neutron scatters once again in the sample or leaves it.

How the interaction between neutrons and sample is accounted for:

Initialization

- Compute the probability distribution of the energy transfers
- For each energy transfer, compute the probability distribution of the momentum transfers

Interaction neutron/sample (assuming the trajectory of the neutron intersects the sample)

1. Compute the length of the neutron path in the sample and the absorption cross-section (depends on the velocity)
2. Compute the probabilities of interaction between neutron and sample (w_i) and of scattering vs absorption (w_s)
3. Draw a random number $alea_1$.
   If $alea_1 < w_i$ then
   $p = p * w_s$ (forcing a scattering event vs absorption); $mult\_scatt = 1$
   else
   the neutron is transmitted to the next component in the instrument and $mult\_scatt = 0$
4. While $mult\_scatt = 1$
   (a) Draw a random number $alea_1$ and compute the scattering position *dscatt* from the decaying exponential distribution
   (b) Draw a random number $alea_2$ for determining the energy transfer $\hbar\omega$
   (c) Draw a random number $alea_3$ for choosing between energy gain and loss according to the principle of detailed balance
   (d) Draw a random number $alea_4$ for determining the momentum transfer q
   (e) Compute $\|\boldsymbol{k_f}\|$ and draw $alea_5 \rightarrow$ direction of final wave vector $\boldsymbol{k_f} \rightarrow \boldsymbol{k_f}$
   (f) Compute distance to exit of sample, probabilities of interaction along this path (w_i) and of scattering vs absorption (w_s)
   (g) If $alea_6 > w_i$ then
   no further interaction; propagation to next component; $mult\_scatt = 0$
   else
   next scattering event may occur; account for absorption $p = p * w_s$

3.1.4 Contributions to experiment and theory - Restrictions

The main differences between neutron scattering experiments and simulations of such experiments arise from the description of the sample and from the quantities that are accessible. Concerning the latter, simulations give separate access to quantities which may not be measured in experiments: for example, thanks to molecular dynamics simulations, we can determine both the coherent and incoherent dynamic structure factors and simulate the experiment with either the latter or the former. Unlike this, both contributions are mixed in the detected signal of a real experiment, except with polarized neutrons or isotopic contrast methods. Moreover, in simulations, we may restrict the detection range (in q or ω for instance), thus focusing on particular features of the behaviour of the sample. We may also compute the different scattering orders as a function of energy or momentum transfers. The ability to separate the different contributions to the detected signal may also be helpful for determining the origin of correlations arising from the interactions of neutrons with either the optical components of the instrument or the sample.
Simulations can also be useful for optimizing the experiments: in fact, the former may help in determining the best size and shape of the sample in order to reach the best compromise between absorption, detected intensity and multiple scattering. This has already been shown in [56] and could be a tool for investigating the different possibilities associated with each kind of spectrometer before performing a given measurement, thus saving much beamtime.
Concerning the description of the sample, it obviously depends on the model used. In classical molecular dynamics simulation, the validity and accuracy of the simulated data depends on the quality of the empirical potential. In the case of *ab initio* MD simulation, both pseudopotential and approximation for the exchange and correlation term (LDA, GGA...) must be chosen carefully . Also the complete simulation may be a method for improving the description of the microscopic features of the sample.
The final purpose of such complete simulations of neutron scattering experiments is to look for trends in the simulated data, thus favouring a better understanding of the measurements. Another use could be training of students.

Some restrictions however must be mentioned. In the case of a dynamic structure factor computed from a classical molecular dynamics simulation, the empirical potential describing the interactions between the atoms or molecules is often well suited for a specific phase of the material or particular conditions. The parameters of these potentials often have to be tuned to describe either the solid or the liquid phase as was shown in the case of silicon and germanium by Jian *et al* [71].
In both classical and *ab initio* molecular dynamics simulations, the calculation of the dynamic structure factor is quite difficult, since the Fourier transform of the intermediate scattering function is not performed on a very long time trajectory and the signal is not periodic. This problem is more acute in first-principle simulations since the number of atoms is usually several orders of magnitude smaller than in a classical molecular dynamics simulation, which leads to poorer statistics.
Concerning the simulation of neutron scattering instruments, they also contain models of some physical features of the beam which do not exactly reflect the reality. Usually, simulations give cleaner results than experiments: for a given instrument, the simulated resolution is always better than the measured one, since, for instance, the background due to the presence of other instruments is not accounted for.

3.2 Examples

Two main test cases have been studied in order to evaluate global simulations. They were chosen either because of their well known dynamic features (this is the case of ^{4}He; see Section 3.2.1) or because their dynamic structure factor had already been measured (as for *l*-Rb; see Section 3.2.2). Both of these samples are isotropic and can be handled by the sample module described in section 3.1.2.

3.2.1 Superfluid helium

3.2.1.1 Dispersion curve and modelled dynamic structure factor

Superfluid helium was chosen as test case since it is an isotropic fluid that has a well-defined excitation. This liquid was not simulated by molecular dynamics but its dynamic structure factor was empirically modelled from the dispersion curve measured by Donnelly [72] (see Fig. 3.5): the dispersion curve was considered as a bidimensional matrix with non zero values corresponding to the $(q, \hbar\omega)$ pairs lying on the dispersion curve. This matrix was then convoluted to a square Hanning matrix. Note that this model gives a constant width to the signal along the dispersion curve and does not account for the excess of intensity at certain energy transfers nor for any quantum behaviour, except for the elementary excitation dispersion curve. Moreover the respective simulated intensities of the roton and maxon are not in agreement with the real intensities since the dynamic structure factor was modelled only for the purpose of testing the sample simulation and the contribution of processes such as multiple scattering.

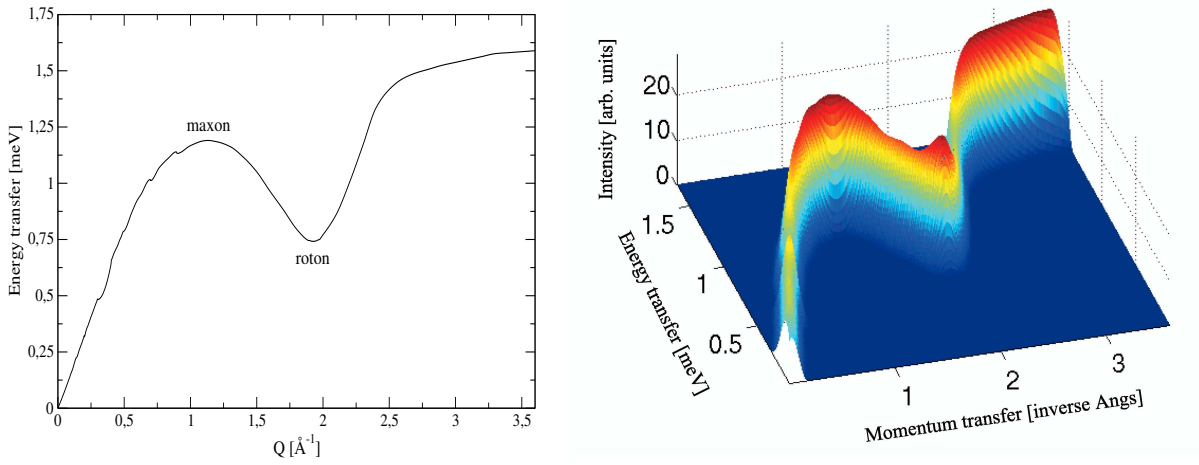

Figure 3.5: Left: dispersion curve of ^{4}He as measured by inelastic neutron scattering [72]; right: model of $S(q, \omega)$ for ^{4}He; the intensity distribution is relative to the occurrence of the (q, ω) scattering events

The modelled dynamic structure factor $S(q, \omega)$ is computed from this dispersion curve in order to obtain a bidimensional map in q and ω. Figure 3.5 gives an overview of the shape of this computed dynamic structure factor.

The values of $S(q,\omega)$, which describe the structural and dynamical behaviour of the sample, have to be processed in order to sample the Monte-Carlo events. The normalization and processing of the dynamic structure factor needed for this purpose is done during the initialization step of the sample module described in Section 3.1.3. This gives access to the repartition functions of the energy and momentum transfers as defined in A.2, from which the Monte-Carlo events can be drawn.
In figure 3.6, both energy and momentum transfers distributions are shown; these distributions also have to be processed before the Monte-Carlo scattering events are drawn. On the left, the distribution of energy transfers is shown, as computed by integrating the modelled dynamic structure factor over all the available momentum transfers. One may notice the maximum of intensity between 0.75 and 1.25 meV, corresponding to the roton and the maxon. The signal is also intense at large ω values: this reflects the weak frequency dependence of the dispersion curve in the range of high q values, where the corresponding energy transfer is approximately 1.5 meV. The figure on the right depicts the distribution of momentum transfers for a given energy transfer, which is here $\hbar\omega = 0.87$ meV. This latter corresponds to a vector of the matrix describing $S(q,\omega)$. The intense peak around $q = 0.5$ Å^{-1} corresponds to the intersection with the phonon curve at $\hbar\omega = 0.87$ meV while the two peaks around 1.75 meV are related to the roton.
The values of the energy and momentum transfers of any scattering event are drawn from these two types of distributions respectively (after normalization and construction of the corresponding repartition function, see A.2).

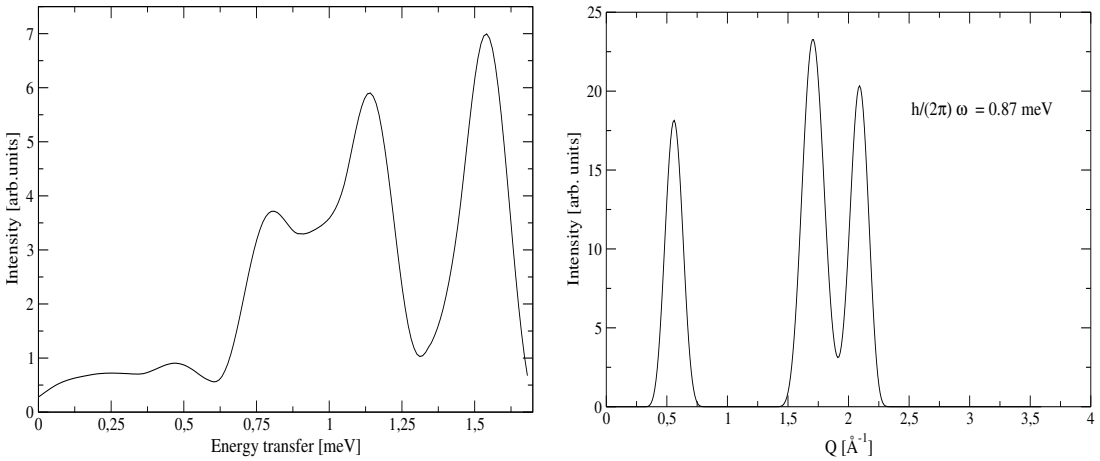

Figure 3.6: Distributions for ^{4}He; left: distribution of the energy transfers; right: distribution of the momentum transfers for a given energy transfer

3.2.1.2 Virtual experiment

In this simulation, the physics of the sample was not our main interest, but the purpose was to check the contribution of the different processes.

The relevant feature of the simulated instrument is the monochromatic beam arriving at the sample with an incident wave vector $k_i = 2.66$ Å^{-1}. The secondary spectrometer is chosen to be either the one of a triple-axis spectrometer (with analyzer and detector) or only a large detector,

as in time-of-flight spectrometers. In the latter case, a detector is sufficient since, anywhere in the simulation, we have access to the coordinates of each neutron, among which are its velocity and the time elapsed since it was emitted from the source. This means that, in simulations, unlike in experiments, we do not have to cope with the problem of determining the velocity (thus the energy) after scattering from the sample: it is directly given by the wave vector $\boldsymbol{k}_f$ at exit of the sample. Thus, for purpose of testing the sample module (that is we do not need to simulate a real kind of instrument), we do not need to chop the beam to create neutron pulses defining the time when the neutrons pass through the sample, and thus a detector is sufficient.

The features of the virtual sample were the following: it was a cylinder of radius 1 cm and height 5 cm. The values for the absorption and scattering cross-sections are those of ^{4}He.
For the first configurations of the simulated instrument, the secondary spectrometer is a large cylindrical detector at a distance 2.5 m from the sample position.

Temperature

The temperature, which influences the ratio of Stokes and anti-Stokes scattering, has an important influence on the shape of the simulated density of states. Figure 3.7 shows the evolution as a function of temperature. Note that even if these temperatures are not realistic at all for liquid helium, these may be simulated by assuming that the dynamic structure factor does not depend on temperature. We visualize here the distribution of gain and loss of energy between neutrons and sample as they interact.

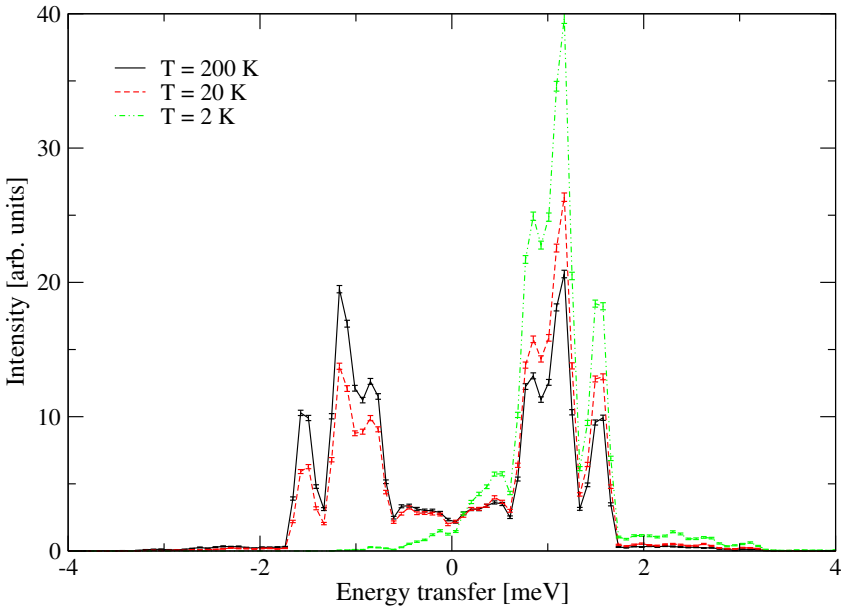

Figure 3.7: Influence of temperature on the density of states

At low temperatures, the density of states shows a strong asymmetry, with the Stokes scattering events predominant since only low level energy states are populated: the sample may not give energy to the interacting neutrons. As expected, when the temperature increases, the Stokes

and anti-Stokes events are more balanced and almost of the same amplitude at the simulated temperature of 200 K.

Multiple scattering

Tests were also performed in order to evaluate separately the contributions of the different orders of multiple scattering, as shown on the simulated density of states of Fig. 3.8. This is an important advantage of simulations on experiments since we may have access to quantities which can not actually be detected and are usually smeared out in the signal.

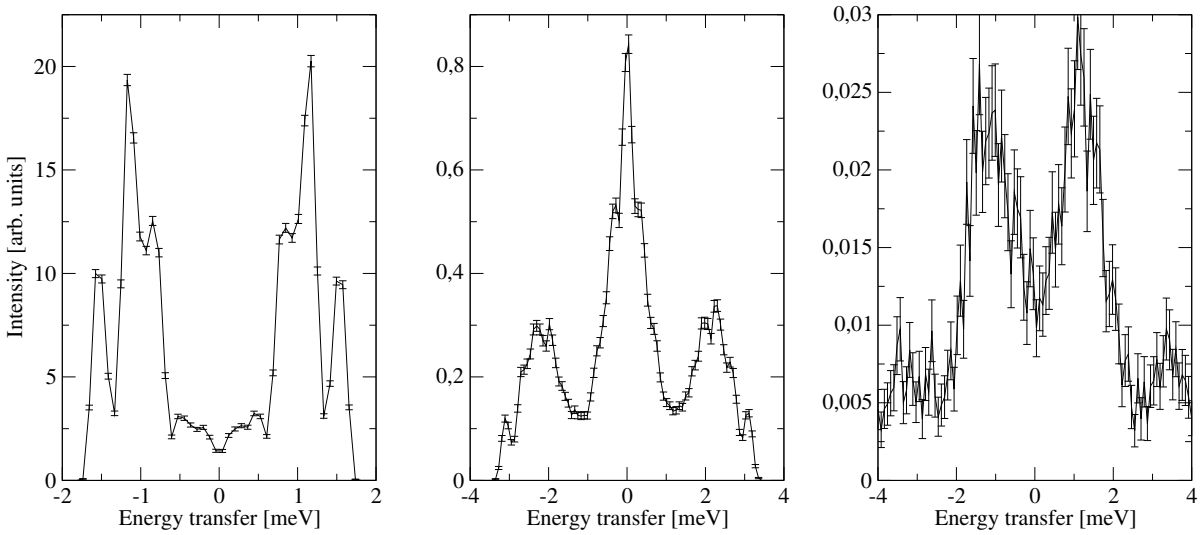

Figure 3.8: Comparison of the separate orders of multiple scattering (left: first order; middle: second order; right: third order); the arbitrary units used for the intensity are the same in the three cases.

The left graph shows the contribution of single scattering. Both Stokes and anti-Stokes scattering can be observed, with a symmetry between gain and loss events due to the rather high temperature (200 K) at which the sample is simulated. In the middle, only neutrons that have been scattered twice are detected and we observe an elastic peak: this latter is due to the presence of Stokes and anti-Stokes scattering with opposite energy transfers, which may for instance occur twice on the maxon. The peaks at ± 2 meV are due to this higher scattering order which leads to higher energy transfers: the first order peak is around 1 meV and two Stokes scattering events on this peak lead to an energy transfer of the order of 2 meV = 2*1 meV. On the right, only neutrons scattered three times are observed. We notice features similar to those of the first order at energy transfers below 2 meV, while at higher energy transfers, higher scattering order yields new peaks.
Now if we superimpose the different orders as shown on Fig. 3.9, we get insight into the ratio of multiple scattering versus single scattering for a given radius of the sample. The curves represent respectively the different orders of scattering, which means the number of scattering events for each neutron is forced to a given value in the case of scattering with a single or double events. In this simulation, with a sample of radius 1 cm, double scattering represents approximately

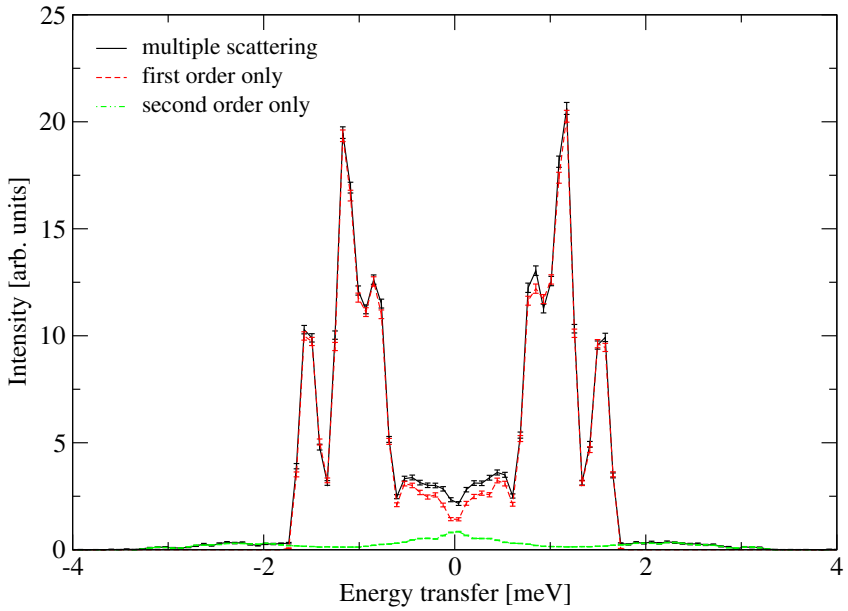

Figure 3.9: Ratio of multiple scattering (black: multiple scattering; red: single events; green: two scattering events)

6% of the total scattering and the sum of the intensities of neutrons scattered one and two times is almost equal to the total scattering, which means that higher scattering orders are almost insignificant: they actually correspond to 0.6% of the total scattered intensity in the current simulation conditions. From this observation, we may assume that, in this case, orders of multiple scattering higher than the second may be neglected compared to the influence of the second scattering order on the total signal.

Energy and momentum analysis

Now, if the secondary spectrometer is similar to the one of a triple-axis spectrometer, we may analyze the scattered neutrons in both energy and momentum transfer by performing scans as on a real triple-axis spectrometer.
The secondary spectrometer now consists of an analyzer which selects the wave vector of the neutrons scattered by the sample and of a small detector which monitors the neutrons selected by the analyzer. Between the analyzer and the detector, there may be either a slit or a collimator which helps to give a better definition of the properties of the detected signal.
By scanning the energy transfer for several given q values, the dispersion curve of the sample may be reconstructed. This simulation is performed with an incident wave vector $k_i = 1.55$ Å^{-1}. Depending on the required precision of the computed signal (from 5 to 1 %), the typical duration of a scan for twenty values of energy transfers between 0 and 2 meV at a given momentum transfer is of the order of 2 to 20 hours on a single processor.

Figure 3.10 shows how several scans in energy with constant q values enable the measured dispersion curve to be reconstructed. The colored map shows the simulated intensity for the different q values as a function of energy transfer, while the measured dispersion curve is also shown. The agreement between simulation and measurement is quite good. However we do not get from

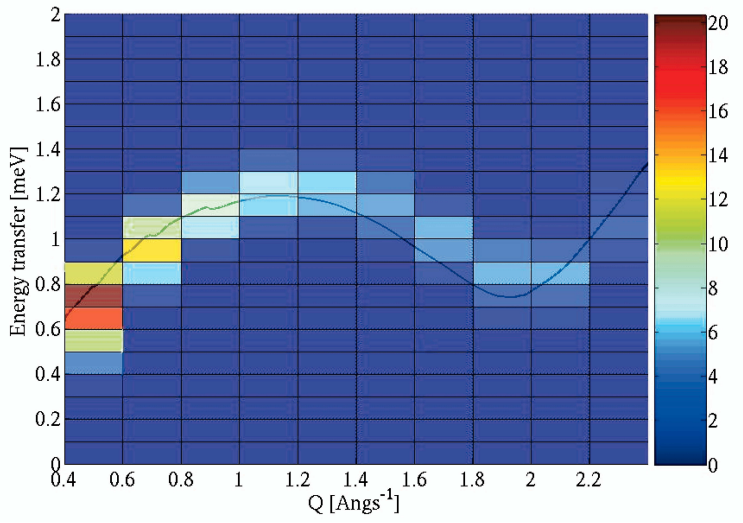

Figure 3.10: Map of the (q, ω) scattering events in ^{4}He computed from several constant q triple-axis scans (the color map shows the intensity in n/cm^2/s). The underlying line is the measured dispersion curve.

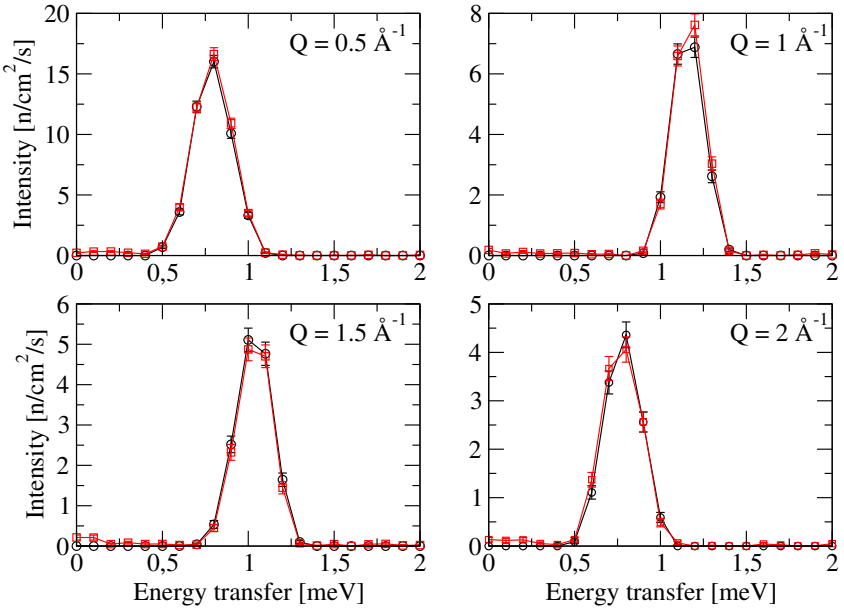

Figure 3.11: Simulation of an experiment on ^{4}He on a triple-axis spectrometer (TAS): comparison of single (black circles) and multiple (red squares) scattering for different momentum transfers.

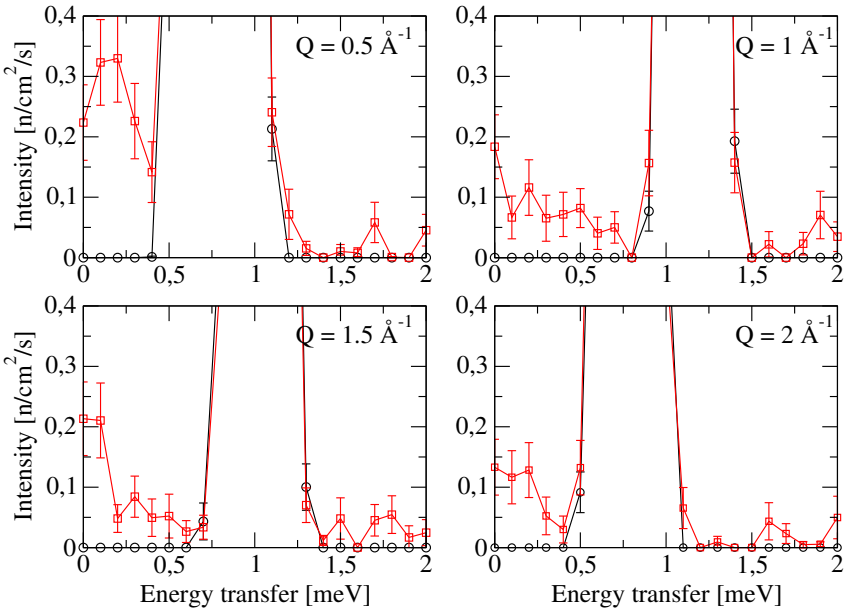

Figure 3.12: Simulation of a TAS experiment on ^{4}He: comparison of single (black circles) and multiple (red squares) scattering for different momentum transfers; contribution of multiple scattering (zoom of the low intensities region of Fig. 3.11)

the scans the dispersion curve we put in. The slight shift to higher or lower energy transfers at certain q values comes from the effect of the resolution ellipsoid: for triple-axis spectrometers, the resolution function depends on both q and ω. It is usually represented as a four-dimensional ellipsoid. Since the scans were here performed at constant k_i, the resolution ellipsoid depends on the angle of the analyzer, which is determined by k_f. This leads to the observed shifts in energy of the simulated dispersion curve.

In Fig. 3.10, the scans only included single scattering. However, the impact of multiple scattering on these inelastic scans can be determined by performing two kinds of simulation: in the first one, neutrons only scatter once in the sample, while in the second, they are free to scatter as many times as determined by the Monte-Carlo processes.
Figures 3.11 and 3.12 show a comparison of single and multiple scattering at four different q values. As expected, the main inelastic features are not modified by the presence of multiple scattering, since the modelled dynamic structure factor is rather sharp. However, as shown in Fig. 3.12, some new features appear outside the energy range associated with the main peak, although they are much less intense than the main inelastic peak. These are due, as shown in Fig. 3.8, to multiple scattering which leads to transfers at higher or lower energies associated with Stokes and anti-Stokes multiple orders of scattering. For instance, at $q = 0.5$ Å^{-1} and $q = 2$ Å^{-1}, where the main inelastic feature occurs around 0.8 meV, we see small peaks around 1.6 meV: these must come from neutrons scattering two times with the same gain in energy. Also some signal appears at energy transfers lower than the main inelastic peak: these are related to neutrons scattering with both Stokes and anti-Stokes processes.

Here we can see that multiple scattering may be of importance, depending on the size of the

sample and its scattering cross-section. In the worst cases, the signal associated with the main inelastic features may be completely washed out by parasite signals due to multiple scattering.

3.2.2 Liquid rubidium

Liquid rubidium is a fluid alkali metal which behaves differently from normal insulating fluids. Its electronic and molecular structure depend on the thermodynamic state of the liquid. For instance, the metal-non metal transition is a striking manifestation of this state dependence; it occurs when a liquid alkali metal is heated up to its liquid-vapour critical point and beyond to its supercritical state.

Several elastic and inelastic neutron scattering experiments have been performed on *l*- Rb. The first results were reported by Copley and Rowe [5, 6]. They performed inelastic neutron scattering experiments on a thermal time-of-flight spectrometer at $T = 315$ K. Since the incoherent scattering cross-section of Rb is much lower than the coherent one ($\sigma_{inc} = 0.5\ barn$ and $\sigma_{coh} = 6.32\ barns$), the measurement gives mainly access to the coherent scattering function. These experiments gave evidence of the existence of longitudinal collective excitations, which can be observed as side peaks or shoulders for q values up to 1 $\mathring{A}^{-1}$, that is far outside the hydrodynamic region. These measurements for low q values are shown in Figure 3.13. The corresponding dispersion relation resembles that of longitudinal phonons in crystalline Rb. Rahman [7, 8] performed molecular-dynamics simulations of this system using an oscillatory potential and found a good agreement with the experiments. He interpreted the presence of such modes in liquid metals and their absence in liquid argon as a consequence of the shape of the effective metallic interaction potential of *l*-Rb.

Later, Pilgrim and collaborators [73, 74, 75] concentrated on the electronic structure and both static and dynamic structure factors near the metal-non metal transition. Measurements of $S(q)$ along the liquid-vapour coexistence line were performed and showed that the main structural effect of the density decrease with increasing temperature is a reduction in the average coordination number while the mean interparticle distance remains nearly unchanged. They also performed inelastic measurements between 1073 K and 1873 K. For temperatures up to 1673 K, the acoustic excitations seem to be visible although they are highly damped.
For comparison, molecular-dynamics simulations of this system were done by Kahl and collaborators [76, 77, 78], which use a typical metallic interaction potential based on the Ashcroft empty-core pseudopotential [79] and the Ichimaru-Utsumi [80] parameterization for the local field corrections to the dielectric function of the liquid metal.
These calculations are in good agreement with experiments for temperatures up to 1673 K and densities up to $3\rho_c$, where ρ_c is the density at the liquid-vapour critical point ($\rho_c(Rb) = 0.29$ g.cm^{-3} at $T_c = 2017$ K and $P_c = 124.5$ bar). This indicates that the mean forces given by the metallic binding are still controlling the dynamics of the liquid. However at 1873 K, some discrepancies arise which may come from the metal-insulator transition which is not accounted for in the effective potential: the interatomic forces used are based on mean electronic density and they are not able to describe correctly the complex changes in the electronic structures which occur at the metal-non metal transition. In the experiment, a broad peak near 3 meV develops in $S(q, \omega)$ with intensity strongly depending on q and reaching its maximum near 1 $\mathring{A}^{-1}$. Under these experimental conditions, this feature is interpreted as the sign of the existence of pairing atoms with intramolecular dynamic effects in expanded liquid rubidium, which may characterize the onset of the metal-non metal transition near the liquid-vapour critical point. First-principle

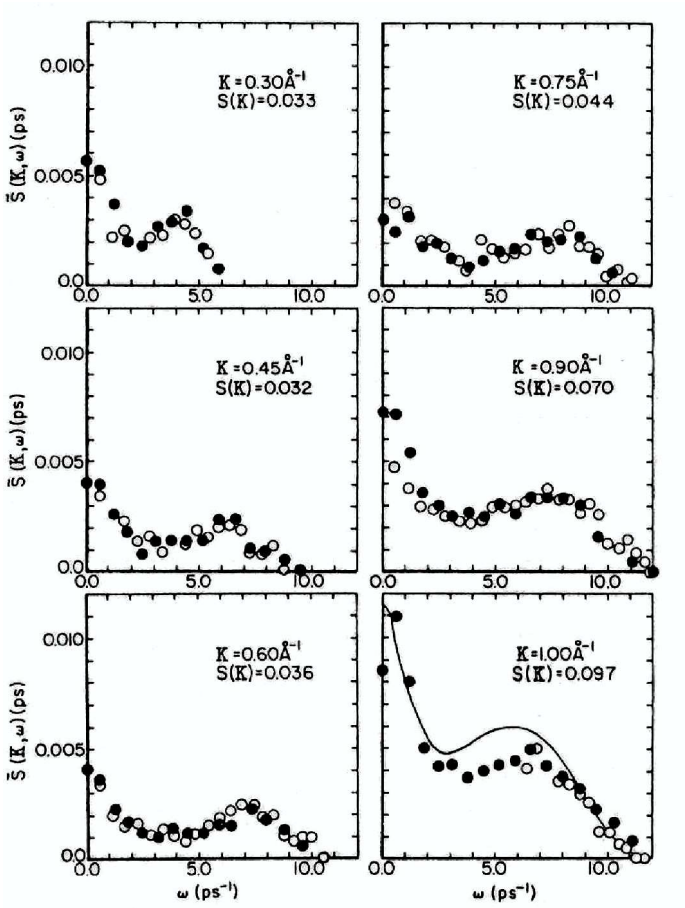

Figure 3.13: Representative results for the symmetrized $S(q, \omega)$ for l-Rb for different wave vectors K (experiment by Copley [5, 6]). Open (closed) circles represent neutron energy loss (gain).

total energy calculations [81] also predict this pairing and provide theoretical support for the appearance of molecules and the existence of a monatomic-molecular transition in expanded liquid rubidium.
Several other molecular dynamics studies were performed on this material: the dynamic structure factor was computed from simulations with different effective pair potentials [82] and showed good agreement with experimental data up to near the critical point. Other simulations were performed in order to study the temperature dependence of the velocity autocorrelation function and the diffusion coefficient D [83]. Other attempts were made to simulate the liquid state using modified pseudopotentials designed for the solid state of Rb [84, 85] and showed that some corrections to these pseudopotentials should be used for predicting the structural and thermodynamic properties with reasonable accuracy.

3.2.2.1 Molecular dynamics simulation of *l*-Rb and calculation of the dynamic structure factor

In this study, the rubidium atoms interact via an effective two-body potential $\varphi(r)$ which is based on pseudopotential theory. This potential is described by Kambayashi and Kahl in [86]. The Fourier transform of $\varphi(r)$ is given by:

$$\hat{\varphi}(q) = \frac{4\pi e^2}{q^2} + \frac{4\pi e^2}{q^2}\left(\frac{1}{\epsilon(q)} - 1\right)|\hat{v}(q)|^2, \tag{3.8}$$

where:

$$\epsilon(q) = 1 - \frac{4\pi e^2}{q^2}\chi(q)\left(1 + \frac{4\pi e^2}{q^2}G(q)\chi(q)\right). \tag{3.9}$$

In the last equation, $\chi(q)$ is the usual Lindhard susceptibility function and G(q) is the Ichimaru-Utsumi correction for the local field [80]. In (3.8), $\hat{v}(q)$ is the bare local pseudopotential represented by the Ashcroft empty-core pseudopotential [79]:

$$\hat{v}(q) = -\frac{4\pi e^2}{q^2}\cos(qr_c) \tag{3.10}$$

where r_c is the only parameter chosen to be : $r_c =$ 1.307 Å. We would like to thank Professor G. Kahl for providing us with the code for computing this potential.

As stated by Kahl [77], this potential is not able to describe liquid rubidium at temperatures ranging from the melting point $T_m = 312$ K to the critical point due to the complex changes of the electronic structure responsible of the metal-non metal transition. However, for our study, which is restricted to temperatures near the melting point, this interatomic potential has shown good agreement with the experimental data. The shape of the potential is shown in figure 3.14 on the left while the oscillatory behaviour related to Friedel oscillations is shown on the right.

Our molecular dynamics simulation of liquid rubidium was performed with a "home-made" code. The values of the potential are sampled as a function of the separation distance r; they are computed and stored in order to avoid the repeated time-consuming calculations of the potential associated with each pair of atoms in the course of the molecular dynamics simulation.
The first step consisted of equilibrating the system at the desired temperature of 350 K with a (N,V,T) equilibration. Then a production run was performed using a standard microcanonical (N,V,E) ensemble with the usual periodic boundary conditions.

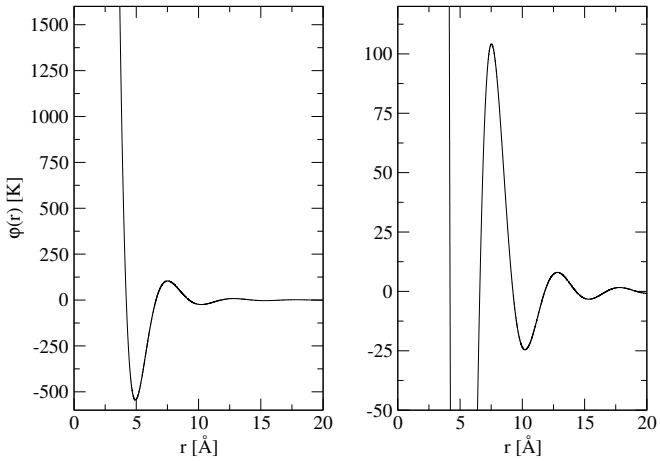

Figure 3.14: Potential used for the simulation of l- Rb: left: global shape; right: details of the Friedel oscillations

The system consisted of 520 particles with a number density of 0.010288 atoms per Å^3. The equations of motion were integrated by the velocity Verlet algorithm over 50000 time steps $\Delta t = 1$ fs. The neighbour lists were computed using the Verlet neighbour list algorithm.
The reduced units used for this simulation were the mass of the Rb atom ($m_{Rb} = 141.917 \cdot 10^{-24}$ g), the Angström and the Kelvin.

From this simulation, both the pair correlation function $g(r)$ and the static structure factor $S(q)$ were computed. These are shown in Figure 3.15. The positions of the main maxima in $g(r)$ ($r_m = 4.8$ Å) and $S(q)$ ($q_m = 1.48$ Å^{-1}) are in good agreement with the experimental values [75].

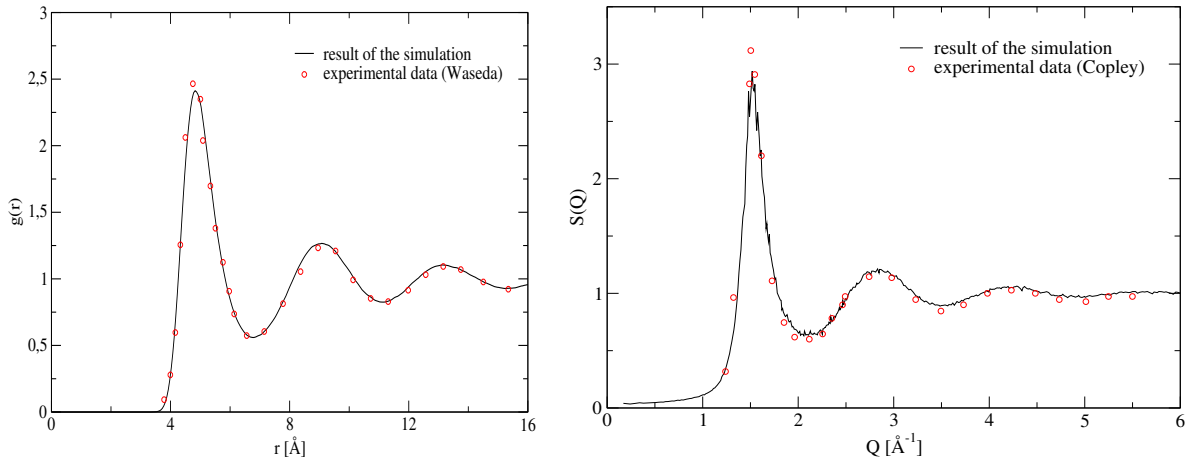

Figure 3.15: l-Rb: pair correlation function (left) and static structure factor (right): full line: computed from the MD simulation; circles: experimental data ([87] for $g(r)$ and [6] for $S(q)$).

Figures 3.16 and 3.17 show the dynamic structure factor computed from the trajectories of the molecular dynamics simulation for different q values.

Figure 3.16 shows the low q values, for which the longitudinal acoustic phonon appears. The energy transfers corresponding to this phonon for the different q values are in agreement with the data measured by Copley (see Figure 3.13), as well as the order of magnitude and the evolution of the intensity at zero energy transfer.

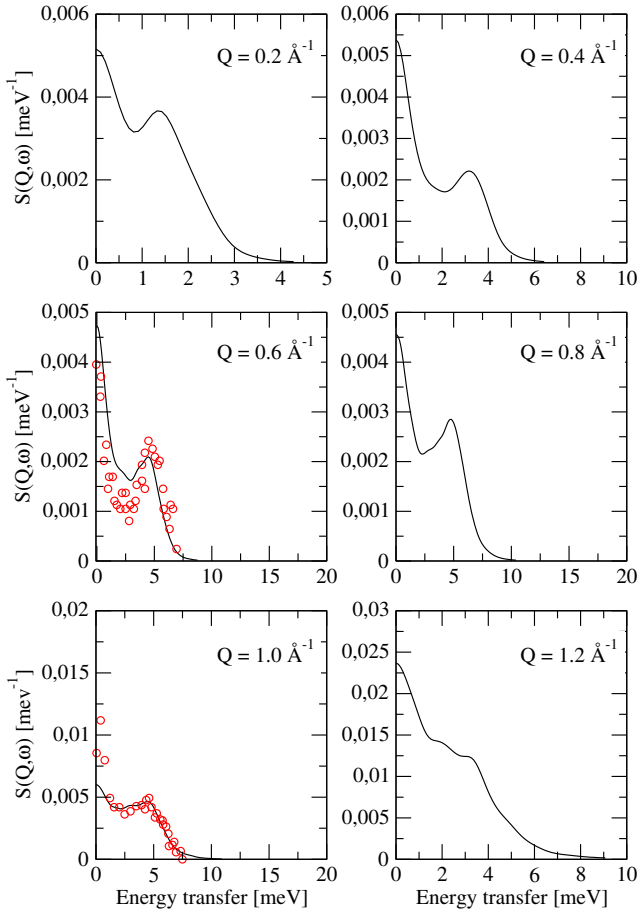

Figure 3.16: Dynamic structure factor for l-Rb: full curve: computed from the MD simulation; circles: experimental data [64].

The phenomenon of *de Gennes narrowing*, discussed in Section 1.2.2.2, is depicted in Fig. 3.17: between $q = 1$ Å^{-1} and $q = 2$ Å^{-1}, the width of the central peak exhibits a decrease near $q_m = 1.5$ Å^{-1}, which is the q-value associated with the first sharp peak of the static structure factor $S(q)$; at the same time, the intensity increases much around q_m. This is related to the slowing down of the dynamics of the system near the first sharp peak, which leads to a more narrow distribution of the frequencies (or energy transfers) around the central peak: near q_m, the system shows long-lived structural features, which involve a slower evolution of the system in this q-range and a stronger intensity of the dynamic structure factor.
This phenomenon also occurs around the following structural oscillations in the static structure factor as shown in Fig. 3.17 on the bottom plots. On the whole range of q comprised between 2.2 Å^{-1} and 4.8 Å^{-1}, the width of the signal tends to increase although it faces several narrowings due to the structural features associated with the oscillations in $S(q)$.
The fluctuations of the width and the intensity are depicted in Fig. 3.18: the phenomenon of *de*

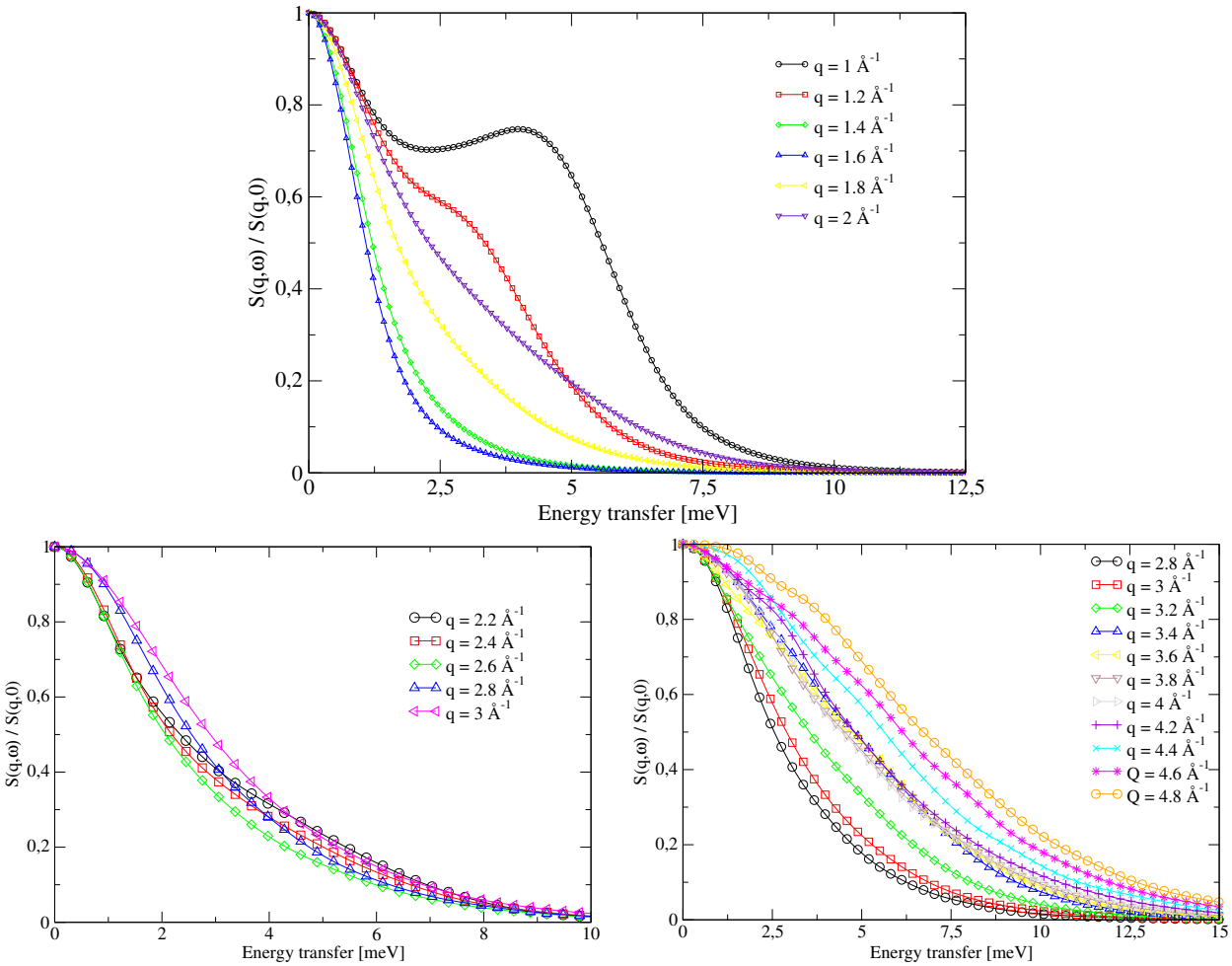

Figure 3.17: Normalized $S(q,\omega)$ (coherent part only) for *l*-Rb: for q values around the first sharp peak in $S(q)$ (top); for q values larger than 2 Å^{-1} (bottom).

Gennes narrowing is clearly identified near the main sharp peak and the next two oscillations of the static structure factor. The half width at half maximum of $S(q,\omega)$ is compared to the theoretical prediction given by Eq. (1.48). The overall shape of the two curves are in agreement concerning the oscillations associated with the de Gennes narrowing. However, we notice discrepancies in the values of the width, with the theoretical width larger than the simulated one. The intensity at zero energy transfer is stronger at the same q values where the de Gennes narrowing is observed and its overall shape is similar to S(q).

Also the self dynamic structure factor was computed from the trajectories. It is shown in Fig. 3.19 together with $\ln(F_s(q,t))/q^2$. We observe an increase in width of the spectra with increasing q values, which is typical of the behaviour of $S_s(q,\omega)$ in liquids as shown in (1.39). We computed $\ln(F_s(q,t))/q^2$ in order to check that (1.38) was satisfied at low wave vectors. In fact, for long times, we observe that the plotted curves can be fitted by a single straight line for low q vectors. However for q higher than 1.4 Å^{-1}, the behaviour of the curves already departs from the diffusive law. From the curves at low q vectors, we can determine the diffusion constant of the system as

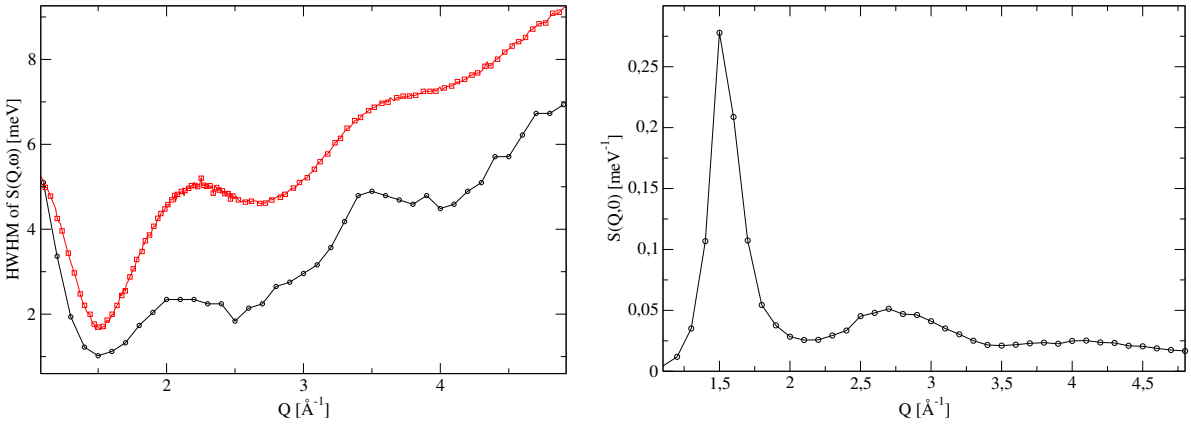

Figure 3.18: l-Rb: left: black circles: HWHM as a function of q extracted from the coherent dynamic structure factor, red squares: HWHM computed using (1.48); right: intensity of $S(q,0)$ as a function of q

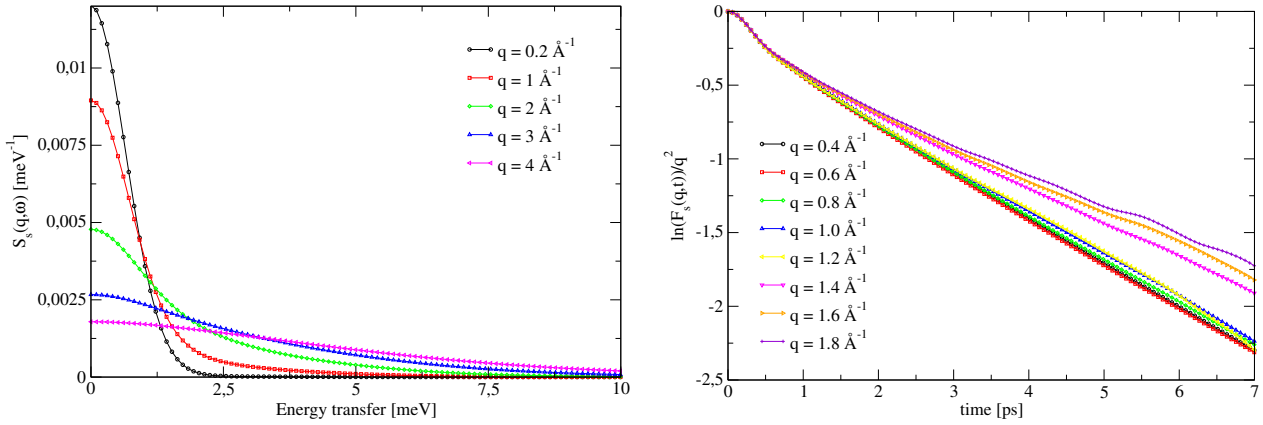

Figure 3.19: l-Rb: left: self dynamic structure factor for several q values; right: $\ln(F_s(q,t))/q^2$ as a function of q (see Eq. (1.38))

being the absolute value of the slope of the fitting line. We obtain $D \approx 3 \cdot 10^{-5}$ cm^2/s in rather good agreement with the experimental values (between $2.5{\cdot}10^{-5}$ and $3.8{\cdot}10^{-5}$ cm^2/s [88]) and the simulated values ($D \in [2.1, 3.4] \cdot 10^{-5}$ cm^2/s [78, 82]).

3.2.2.2 Virtual experiment on a time-of-flight spectrometer

The virtual instrument simulated here is a cold time-of-flight spectrometer. A monochromator is used for defining the wavelength of the beam incident onto the sample. A large detector is placed after the sample, which covers a large solid angle. As stated before, no optical component is used for chopping the beam since the velocity of the neutrons is known at any point in the instrument.
Global simulations of inelastic neutron scattering experiments were performed with the l-Rb sample. For this purpose, the coherent dynamic structure factor computed from the molecular dynamics simulation is used, which gives access to energy transfers ranging from 0 up to 200 meV

and momentum transfers from 0.2 to 5 Å^{-1} by step of 0.1 Å^{-1}.

For information, the self-part of the dynamic structure factor gives very small contributions to the total scattered signal since the incoherent scattering cross-section of Rb is $\sigma_{inc} = 0.5$ barn compared to the coherent scattering cross-section $\sigma_{coh} = 6.32$ barns. That is why the multiple scattering contribution was only computed with the coherent dynamic structure factor. The number density is equal to the density of the MD simulation (0.010288 atom/Å^3).

Size of the sample

The effect of the size of the sample may also be studied by means of such simulations. When varying the radius of the cylinder, the detected intensity and ratio of multiple scattering are affected, due to scattering and absorption cross-sections of the sample. Simulations may help in determining the most appropriate sample size which maximizes the ratio of first to multiple scattering while maintaining a large first scattering probability.

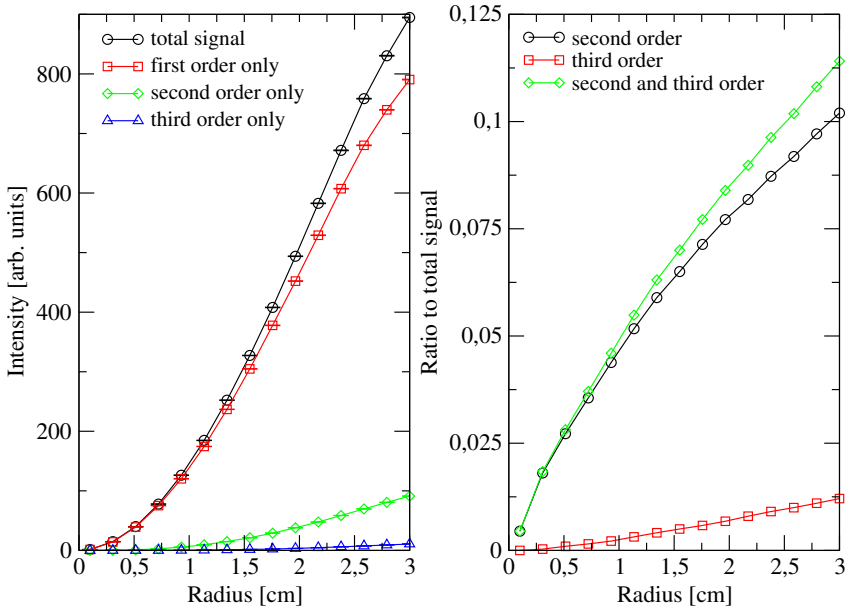

Figure 3.20: *l*-Rb: multiple scattering in a cylinder-shaped sample as a function of its radius; left: different orders of multiple scattering; right: ratio of the multiple scattering orders to the total scattered signal.

Figure 3.20 concerns the simulation of a full cylinder *l*-Rb sample of height 5 cm. On the left graph, the detected intensity is plotted against the sample radius, and the respective contributions of the different orders of multiple scattering are shown. On the right one, the ratios of the different scattering orders to the total scattered signal are shown as functions of the radius.
We realize here that the detected intensity increases with larger radii while the proportion of multiple scattering becomes less and less negligible. The ratio of multiple scattering usually considered as suitable for a neutron scattering experiment is around 10% of the scattered signal. This value is reached for a radius of about 2.5 cm, which seems to be pretty high compared to usual sample thicknesses. Typical cylinder-shaped samples have a diameter of the order of 0.5 to 1 cm. Multiple scattering effects and multi-phonon processes leads to distortions of the

signal from the sample and are quite difficult to take into account in data corrections. From the experimental point of view, thin samples are consequently more appropriate since they minimize the importance of multiple scattering. This may explain why usual samples are much thinner than the predicted radius giving rise to 10% of multiple scattering in the scattered signal.

Figure 3.21 represents the simulation of a hollow cylinder *l*-Rb sample, with height and outer radius of respectively 5 cm and 1 cm. The inner radius varies between 1 mm and 9 mm. As expected, the detected intensity decreases with increasing inner radius, since there is less material in the beam.

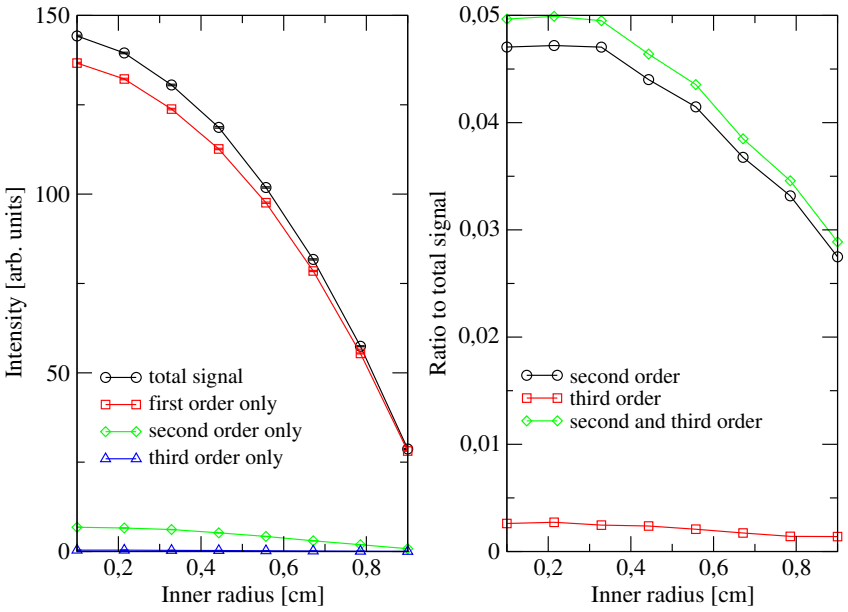

Figure 3.21: *l*-Rb: multiple scattering in a hollow cylinder of outer radius 1 cm as a function of its inner radius; left: different orders of multiple scattering; right: ratio of the multiple scattering orders to the total scattered signal.

For the box-shaped sample (with width = 5 cm and height = 5cm), the evolution of the intensity as a function of thickness (Figure 3.22) is similar to the one of the cylindrical sample. The intensity increases with thickness while the ratio of higher scattering orders to total signal increases.

Let us now compare the shape of the total intensity in the cases of the cylinder- and box-shaped samples. In the range of radii where the multiple scattering is still negligible, as the radius of the cylinder increases, the intensity increases as r^2. Unlike this, in the case of the box-shaped sample, the intensity for rather low thicknesses increases linearly with thickness. Consequently, the scattered intensity is proportional to the volume of the sample and the simulated intensity is consistent with the theory of neutron scattering which states that the scattered intensity is proportional to the number of particles in the sample.
A comparison of the ratio of the total intensity versus the proportion of multiple scattering for the cylinder-shaped and box-shaped samples shows that for small radius or thickness, the ratio intensity/multiple scattering is more favorable for the box-shaped sample.

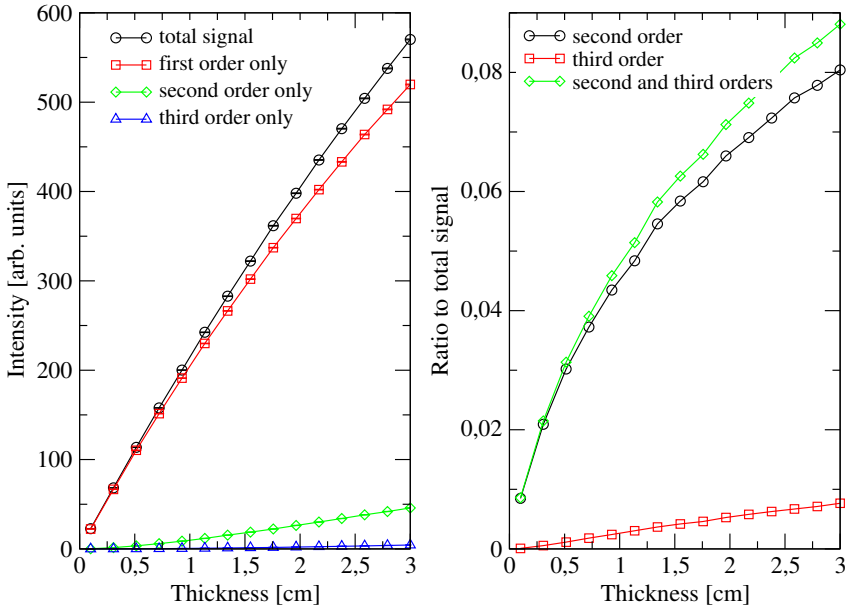

Figure 3.22: *l*-Rb: multiple scattering in a box-shaped sample as a function of its thickness; left: different orders of multiple scattering; right: ratio of the multiple scattering orders to the total scattered signal.

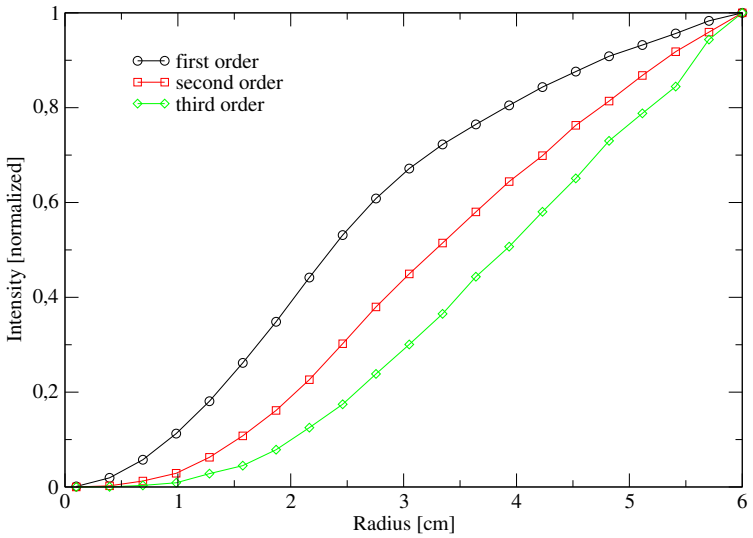

Figure 3.23: *l*-Rb: multiple scattering for a cylinder-shaped sample with large radii

In Figure 3.23, the shape of the intensity of the different scattering orders are compared, in the case of a cylindrical sample. The respective intensities of first, second and third orders are normalized to unity. This allows us to compare the curvatures: we notice that the second derivative of the first order intensity becomes negative very early, around 2.5 cm in radius, compared to higher orders, which have still not started decreasing at 6cm. This shows that the relative importance of first order scattering is decreasing while higher orders are still increasing,

as expected when the radius is higher.

Splitting the whole q-range

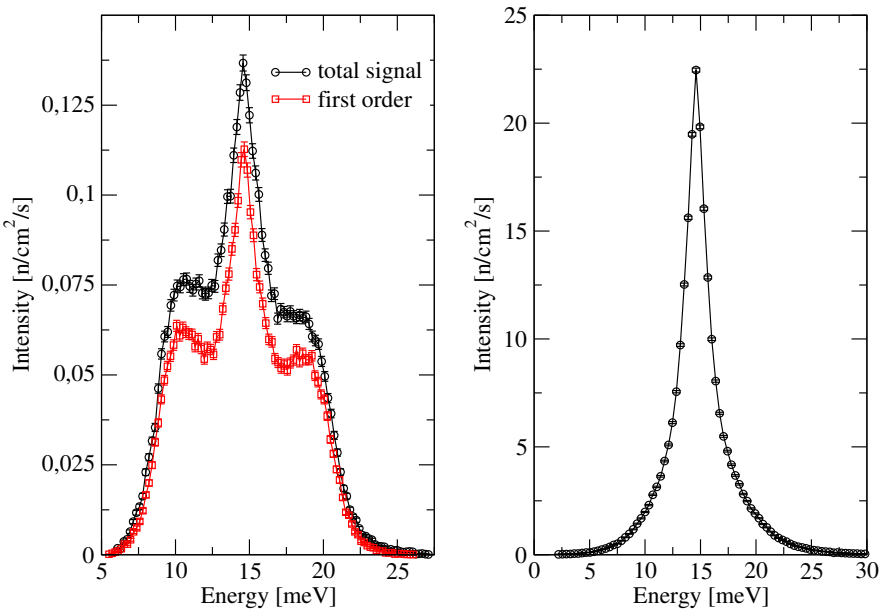

Figure 3.24: Influence of the q range on the observed features: left: only momentum transfers between 0.5 and 1 Å^{-1} are detected; right: the whole q range available from MD is simulated

In simulations, the range of q values scanned by the detectors can be chosen. In Figure 3.24, two similar simulations are shown for a time-of-flight spectrometer: in the first one (left), the detector is only sensitive to momentum transfers between 0.5 and 1 Å^{-1} (left); in the second simulation (right), the detector is sensitive to the whole q-range, which is determined by the extent of the momentum transfers extracted from the molecular dynamics simulation. Note that the intensity of the signal is here plotted against the final energy of neutrons (the incident energy was about 15 meV) and not against the energy transfer between neutrons and sample. Without any restriction on the momentum transfer, the main feature of the energy distribution of the detected neutrons is the very intense quasi-elastic peak due to the main sharp peak of the static structure factor which occurs around 1.5 Å^{-1}. The inelastic features occurring at q values between 0.5 and 1 Å^{-1} are completely smeared out by the huge intensity of the structural features. Now, if we restrict the range of the detected momentum transfers, we can avoid the contribution of the first sharp peak, in order to get insight into the inelastic features of the signal: we can clearly see the contribution of the phonon which energy transfer is around 5 meV for momentum transfers between 0.5 and 1 Å^{-1}. A direct comparison of the respective intensities of the two signals gives insight into the domination of the structural features compared to the inelastic properties.

A map of the (q, ω) events can be computed: this is depicted in figure 3.25 for the q-range where the acoustic phonon of l-Rb is visible, showing clearly the dispersion of the mode.

As with the phonons, the width of the quasi-elastic peak as a function of q may be extracted

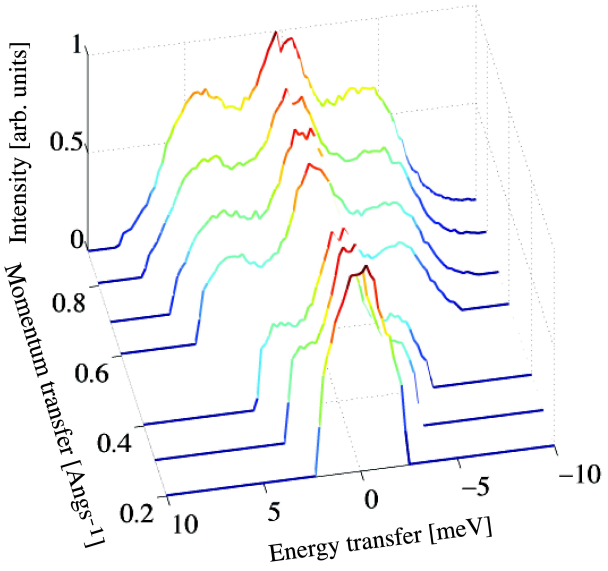

Figure 3.25: Detected intensity as a function of energy and momentum transfers in the region of the acoustic phonon ($q \in [0.2\ ,\ 1]$ Å^{-1}).

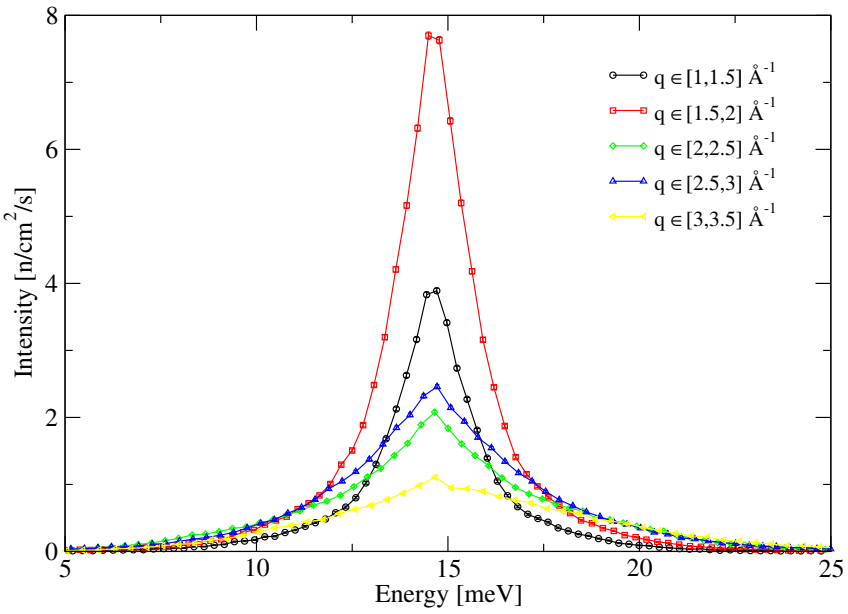

Figure 3.26: Separation of different q ranges in $S(q, \omega)$ simulated on a TOF spectrometer.

from such simulation as in a real experiment. This is shown in Fig. 3.26, where several intervals of q values were simulated separately. From these calculations, we can see that the intensity of the quasi-elastic peak fluctuates as expected from the shape of the computed dynamic structure

factor. Concerning the width of this peak, it is actually much narrower for q values near the position of the first sharp peak.

Separation between coherent and incoherent signals

The separation between coherent and incoherent signals can be done by using only the coherent or incoherent part of the dynamics structure factor. In the previous sections, only $S(q,\omega)$ was accounted for when computing the scattering events. In neutron scattering experiments, this separation can be achieved by means of polarized neutrons, which give separate access to coherent and incoherent neutron scattering, or by contrast effects, which use the relative importance of the coherent and incoherent cross-sections for the isotopes of a given element .
We show here the results of three different simulations with the same instrumental setup. One of them was done with $S(q,\omega)$ only, the second with $S_s(q,\omega)$ only and the third with both of them. The simulated q-range was restricted to [0.5,1] Å^{-1}, in order to observe clearly the difference between coherent and incoherent signals which are quite similar to each other at higher q values. From the coherent signal, the inelastic feature due to collective motions associated with the acoustic phonon may be extracted while the Lorentzian related to diffusion is represented by the incoherent part. Consequently, simulations are helpful for extracting the respective contributions of collective and single-particle motions.

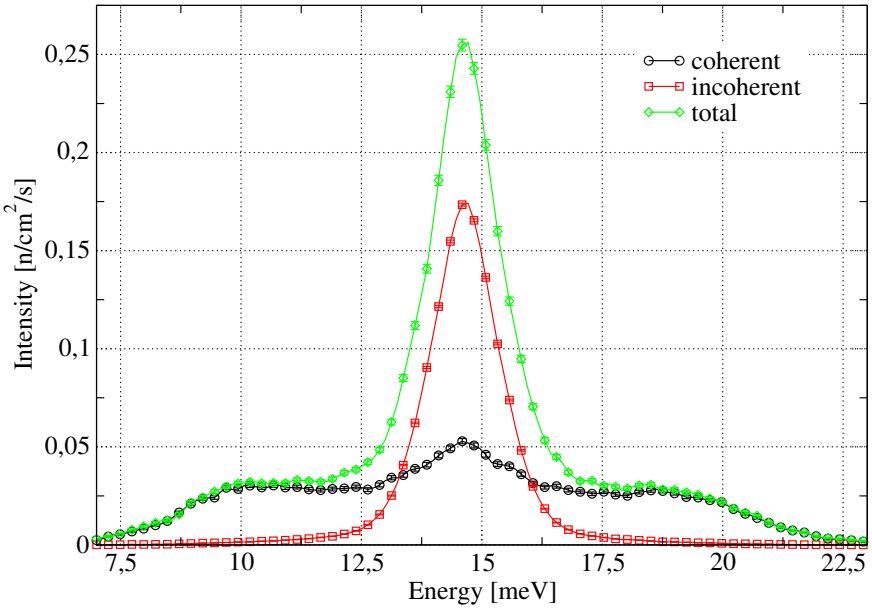

Figure 3.27: Separation of coherent and incoherent signals. The simulated q-range is [0.5,1] Å^{-1}.

3.3 Conclusion

In this chapter, we have presented a method for simulating global neutron scattering experiments, which includes on the one hand the neutron scattering instrument, and on the other hand, the sample of interest.
In these simulations, the instrument is described by its different components from the source of

neutrons to the detector, through different kinds of optical components which define the features of the beam incident on the sample. The sample itself is described by means of its dynamic structure factor: by performing molecular dynamics simulations, either classical or *ab initio*, we are able to compute the dynamic structure factor $S(q,\omega)$ from the trajectories of the atoms. The calculation of this quantity is time consuming: the trajectories have to be quite long and the number of atoms rather high so that the intermediate scattering function is accurately evaluated and its Fourier transform $S(q,\omega)$ does not look too noisy.
The dynamic structure factor is then used as a probability distribution of the (q,ω) events for the sample of interest. It allows us to choose both the energy and momentum transfers, which are the features of any scattering event between neutrons and sample.
Monte-Carlo processes are used in the sample for accounting for absorption and multiple scattering.

Simulations were performed with two kinds of samples. First, the dynamic structure factor of superfluid helium was derived from its measured dispersion curve, thus not accounting for the quantum properties of the material. The purpose was to test the behaviour of the sample module. Then, a classical molecular dynamics simulation of l-Rb was performed, and the corresponding dynamic structure factor was calculated.

These two test cases give an overview of the abilities of such global simulations of neutron scattering experiments. They give insight into some quantities which are actually not readily available from experimental data, such as the different orders of multiple scattering and their respective intensities. This is of interest for determining the most appropriate size of the sample for optimizing real experiments: simulations are able to predict the size for which the best compromise between intensity and multiple scattering is reached. In the case of the helium and triple-axis simulation, the effect of the resolution ellipsoid is clearly seen. Moreover, this simulation enables multiple scattering to be tested on a simple inelastic spectrum.
These simulations also enable a direct access to reduced q ranges which are relevant for some inelastic features. Consequently, both phonons and diffusive properties may be observed as in real experiments. Simulations also give access to the coherent and incoherent contributions of the sample to the total signal.

The global simulation of neutron scattering experiments offer more than the sample simulation in several fields such as the impact of the resolution function on the detected signal, the influence of sample size and multiple scattering and the understanding of parasitic signals, originating from the sample environment for instance.

4

Liquid germanium: experiments and simulations

Contents

When we had to choose a material for performing both experiments and complete simulations of neutron scattering experiments, our attention was first guided towards liquid compounds since our simulation scheme is dedicated to isotropic materials. Consequently, we wanted to find a

liquid for which the experiment was tractable. Thus we chose liquid germanium, which is known to have a structure that differs from most liquid metals. In this chapter, we present both experimental and simulation results about liquid Ge. In the first part, an overview of the former investigations carried out on this material is given; it deals with both experimental and theoretical studies. The next section is devoted to the presentation of both kinds of simulations using either empirical potential or *ab initio* methods for the study of liquid Ge. Then, the experimental results from two kinds of spectrometers are shown. The last part is dedicated to the possible contributions of complete simulations of neutron scattering experiments dealing with liquid Ge.

4.1 Liquid germanium

Structural investigations on condensed phases of germanium are of fundamental interest due to the interplay between the covalent and metallic character of the bonding . Research in this field is also relevant to several applied physics problems and semiconductor technology.
Germanium shows a large degree of polymorphism in its solid phases. In its stable crystalline phase at ambient pressure, the crystal has a diamond structure where each Ge atom is surrounded by four covalently bonded first neighbours in a tetrahedral formation. This phase of Ge is semiconducting and has a very low density with respect to close packing. Upon application of pressure, the tetrahedrally bonded network is broken and the number of neighbours and the density increase. Around 100 kbar, a phase transition to the metallic β-tin (or white-tin) structure occurs and at even higher pressures an hexagonal phase and a close-packed phase are produced [89].
At standard pressure the melting point temperature of crystalline Ge is $T_m = 1210.4$ K. At the melting transition the tetrahedral network is also broken and germanium undergoes a semiconductor to metal transition. The electrical resistivity decreases by a factor of about 11 and the density increases by about 5%, while the average coordination number increases from 4 to about 7, which is rather low compared to other liquid metals with coordination number between 9 and 12.
Amorphous germanium is an amorphous semiconductor made of a continuous random network of slightly distorted tetrahedra with defects.

Experimental investigations

The experimental understanding of the complex interplay between covalent and metallic bonding has been the subject of several investigations with either X-ray [90, 91, 92] or neutron diffraction [93, 94, 95, 96, 97] techniques. The experimental static structure factor is shown in Figure 4.1. In 1972, Isherwood, Orton and Mănăilă [90] noticed that the first diffraction maximum is unusually low and has a shoulder on its high momentum transfer side. In this context, the hard-sphere model does not seem to be appropriate for describing the arrangement of atoms in *l*-Ge and they devised a model based upon the short-range order found in white tin: the "central" Ge atom was surrounded by four nearest atoms in the corners of a flattened tetrahedron with two other atoms slightly further away. This partially anisotropic short-range order model was inspired from the fact that Ge and Sn have similar outer electron shells and both exhibit a high-pressure transition to a white-tin like structure accompanied by a 21% density increase. Since the melting of germanium proceeds with a 5% density increase, it seems to be reminiscent of the high-pressure modification. Consequently, they described *l*-Ge as a white-tin like structure and

the experimental and computed radial distribution functions were in good agreement with this model. In 1975, Waseda and Suzuki [91] obtained results very similar to the former ones and gave an interpretation in terms of the white tin-like arrangement. However, they showed that the oscillations of $S(q)$ in the high q region were less damped in the case of l-Ge and l-Si than for the metal l-Al. This implies that a short-range order related to the crystal structure remains in the liquid, because the persistence of the oscillation in the structure factor in high q region is related to the species having definite bond length and angle. They consequently deduced that the structure of l-Ge may consist of a mixture of molten metal-like atomic arrangement randomly distributed and covalent crystal-like atomic arrangement. In 1979, Gabathuler and Steeb proposed a model consisting of a mixture of fourfold coordinated semiconducting arrangements and highly coordinated metallic arrangements. As stated by [94], the assumption of crystal-like atomic arrangements being responsible for the anomalous structure factor may not be consistent with the shoulder on the high q side of the first diffraction peak: since the liquid is more dense than the solid, if the shoulder were due to crystal-like arrangements, it would be on the low-q side of the main peak in $S(q)$, because $q \sim 1/r$ where r in the interatomic distance. Subsequently, they devised a new model for the structure of l-Ge consisting of a combination of regular and irregular structures [94] in which vacancies are introduced. In the regular structure, an atom is surrounded by approximately 6.5 equivalent atoms which are separated from one another by the mean distance. In the irregular structure, in the vicinity of a vacancy, the first neighbour of the central atom which is close to the vacancy is shifted towards the central atom. Consequently, these two substructures respectively lead to the principal peak in $S(q)$ and to the high q side shoulder. Bellissent-Funel and Bellissent also tried to devise a model of the structure of l-Ge [95]: since the hard-sphere model gave a poor agreement with the experimental results, they used a quasicrystalline model based on the assumption that the local order for the liquid is based on the crystal structure. However, this model gives a good representation of the width of the first peak in $S(q)$ but the shape of the latter is not reproduced, especially the shoulder.

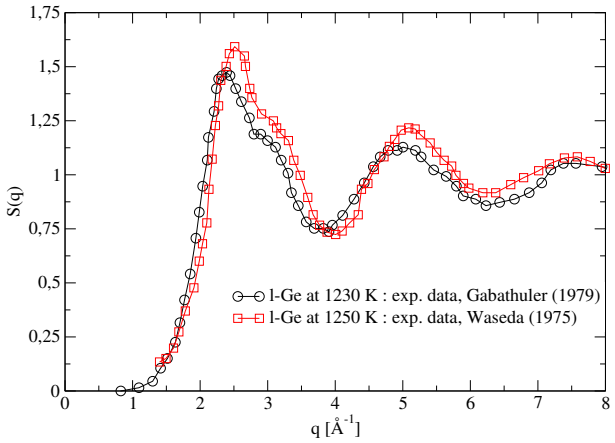

Figure 4.1: Static structure factor for liquid Ge obtained from neutron scattering and X-ray scattering experiments.

Concerning the dynamics of l-Ge, Hosokawa and co-workers used inelastic X-ray scattering [98]. Spectra were measured for momentum transfers from 0.2 to 2.8 Å^{-1}. The phonon dispersion curve extracted from the spectra matches the hydrodynamic sound velocity [99]. The generalized

hydrodynamics theory which predicts a positive dispersion does not apply to the experimental data for *l*-Ge, although it was shown to be satisfied by other liquid alkali metals such as liquid caesium [100] or liquid sodium [101]. In the hydrodynamic limit $(\omega\tau)^2 \ll 1$, where τ stands for the viscoelastic relaxation time, the slope of the dispersion curve is given by the adiabatic sound velocity c_s. At higher frequencies, the viscoelastic damping starts to contribute to the relaxation process in the liquid, causing a shift of $\omega(q)$ to higher frequency, this is the so-called *positive* dispersion. In the case of the high frequency limit $(\omega\tau)^2 \gg 1$, the dispersion relation is determined by $\omega(q) = c_\infty(q)q$, where $c_\infty(q)$ is the high-frequency sound velocity which is ruled by the elastic moduli as in a solid. The authors showed that this theory does not apply to *l*-Ge since no positive dispersion is observed. This may come from two principal reasons: on the one hand, the potential used for determining the high-frequency sound velocity must be harder than the real potential in *l*-Ge, the latter yielding a smaller c_∞; on the other hand, liquid Ge may not belong to the class of liquids which can be approximated as simple monatomic fluids and three-body correlations or the covalent character of bonding may dominate the collective dynamics.
Moreover, the study of the relationship between $S(q)$ and the half width at half maximum of the spectra Γ_q shows that the measured spectral widths do not fit to the relationship given by de Gennes for simple dense fluids [19] (see Section 1.2.2.2) nor to the expression for neutron spectra of dense hard-sphere fluids given by de Schepper and co-workers [102]. This failure supports the view that neither the structure nor dynamics of liquid Ge can be modelled using pair interactions. However, a cluster model with transient covalent structures in the liquid was proposed by Ashcroft [103] which can be interpreted in terms of the experimental results. In this model, the first maximum in $S(q)$ reflects the inter-cluster correlation while the shoulder on the high q side and the remaining oscillations refer to the atom-atom contribution. In the experimental results, a narrowing at the position of the maximum in $S(q)$ followed by a broadening of the quasi-elastic line at higher q values corresponding to the shoulder in $S(q)$ shows that the covalent structures are diffusing slowly while individual atoms are subject to rapid translational motion.

Theoretical investigations

On the theoretical side, much effort was devoted to modelling and reproducing both structural and dynamic features of *l*-Ge. In 1985, Stillinger and Weber devised a model potential function comprising both two- and three-atom contributions to describe the interactions in solid and liquid states of Si [104]. Molecular dynamics simulation of *l*-Si using this potential give structural properties in good agreement with the measurements. This potential was also used for simulating amorphous germanium [105]. However, the set of parameters relevant for both amorphous and solid phase of Ge were not able to give a good description of the liquid phase. This was attributed to the lack of flexibility of the potential for describing the full variety of configurations seen in the three phases. Other studies [106] consisted of molecular dynamics simulations using interatomic forces derived from the pseudopotential theory. Both structure factor and pair correlation function agree well with experimental data. These simulations also showed the evolution of the structure with temperature: as the temperature decreases, the shoulder becomes more pronounced and even forms a second peak and in the supercooled state, the second peak becomes more intense than the first one. More recently, the potential initially devised by Stillinger and Weber for *l*-Si was used with a different set of parameters fitting both crystalline and liquid Ge phases [107]. The corresponding simulations give access to static structure factor and pair correlation function in good agreement with the experimental results. However, the

computed diffusion coefficient is larger than experimental values by a factor of 2.

Let us now move on to the *ab initio* molecular dynamics simulations of *l*-Ge. In 1993, Kresse and Hafner presented the first results dealing with an *ab initio* simulation of liquid germanium [108]. In this study, they used *ab initio* quantum-mechanical molecular dynamics calculations based on the calculation of the electronic ground state and of the Hellmann-Feynman forces in the local density approximation at each molecular dynamics step. The agreement between simulated and experimental pair correlation function was quite good. Also the electronic density of states is in close agreement with the experimental data. In [109], their work was extended to the study of the liquid metal-amorphous semiconductor transition. The results for the pair correlation function and the static structure factor are in good agreement with experimental measurements. According to the authors, the results for the liquid indicate a broad homogeneous distribution of local bonding configurations and shows that both classes of models proposed earlier (mixture of fourfold coordinated and highly coordinated metallic arrangements [93] and both sixfold coordinated and metallic arrangements [90]) are unrealistic. The simulation of undercooled and amorphous Ge shows the increase of the local tetrahedral order with decreasing temperature. The self-diffusion coefficient is extracted from the simulated trajectories $D = 1.0{\cdot}10^{-4}$ cm^2/s and is in good agreement with the measured value. Similar results about the structure and diffusion of liquid Ge were found by Takeuchi and Garzón [110] using the *ab initio* molecular-dynamics scheme developed by Car and Parinello [44]. Another study was performed by Godlevsky and Chelikowsky [111] which yields similar results for both the structure factor and the pair correlation function. However, two kinds of angular distribution functions are computed: the first one deals with the nearest neighbours (*i.e.* the distribution of the angles formed when a vector is drawn from a reference atom to the nearest atom and another vector is drawn from the same reference atom to the next-nearest neighbour) and is strongly localized around the tetrahedral angle which shows a predominantly covalent bonding; the second one deals with more distant neighbours (*i.e.* it is an average of angles between a reference atom and all pairs of atoms within a radius r_m of the reference atom) and shows a peak near angles appropriate to close-packed structures and thus a more metallic configuration is observed. They conclude that this situation is consistent with the coexistence of covalent and metallic bonding in the liquid. Kulkarni and collaborators performed similar simulations and studied the influence of the temperature between 1250 K and 2000 K on the structural properties of the liquid [112]. These simulations show that liquid Ge is a good metal but with some special short-range order arising from residual covalent bonding. At the highest temperatures, *l*-Ge seems to evolve into a more conventional close-packed liquid metal. More recently, the features of the dynamics of liquid Ge were studied: the computed dynamic structure factor was found in good agreement with the experimental data while the self-diffusion properties of *l*-Ge were determined [113], showing three types of diffusion processes: the first one consists of a single atom moving freely when its coordination number becomes smaller; the second one occurs when an atom moves together with its neighbouring atoms in almost the same direction; and the last one happens when an atom is trapped in a group of neighbouring atoms which almost stays at the same position. Calculations of the dynamic structure factor from an *ab initio* MD simulation were also performed by Chai and co-workers [114]. They show good agreement with the experimental data, although the statistical noise due to the small number of atoms (64) is rather important and has to be convoluted with a gaussian of width 2.5 meV representing the experimental resolution function.

As can be seen in these experimental and theoretical studies, experimental investigations of liquid germanium are not able to determine the microscopic arrangements giving rise to the

measured structural properties. They can only show if a given model could be in agreement with the measurements. On the other hand, molecular dynamics simulations have access to atomic positions and hence the local structure can be extracted from this microscopic description of the material. Consequently the actual model of structural arrangement can be understood from simulation.
In this work, we have performed classical and *ab initio* MD simulations of liquid germanium together with the first neutron scattering measurement of the quasi-elastic behaviour of this sample. Although several simulations have been carried out before, the results of some of them are rather uncertain, due to very large simulation time steps, potential parameters in classical MD or statistics and k-point sampling for *ab initio* MD. From the experimental point of view, the measurement of the quasi-elastic behaviour by inelastic X-ray scattering was done with poor statistics and the agreement with the tested models is questionable. For this reason, we can expect to perform neutron scattering measurements with better statistics and more q vectors. Moreover, thanks to modern computers and codes, new simulations improve the quality of the simulated trajectories. Finally, on the viewpoint of global simulations of neutron scattering experiments, the comparison of experiment, simulation and experiment simulation gives information about the importance of the instrument and the interaction between neutrons and sample on the measured quasi-elastic width. Virtual experiments also open new perspectives about what can be inferred from experiment simulations and how they can help to understand the contributions to the measured data.

4.2 Molecular dynamics simulations of l-Ge

In this section, we present the molecular dynamics simulations carried out on l-Ge. Two methods were used for this purpose: the first one uses an empirical potential while the second one is based on *ab initio* techniques. Both kinds of simulations give information about the structure and dynamics of the simulated material.

4.2.1 Classical molecular dynamics simulation

As said before, the first step in this theoretical study of l-Ge was to perform an empirical molecular dynamics simulation.

4.2.1.1 Empirical interatomic potential

This was done by using the well-known potential designed by Stillinger and Weber [104]: it comprises both two- and three-atom contributions and was initially developed for silicon and then adapted for germanium. It is given by:

$$\begin{aligned}\varphi(1,\cdots,N) &= \sum_{i=1}^{N}\sum_{j>i} v_2(r_{ij}) + \sum_{i,j,k;i<j<k} v_3(\boldsymbol{r}_i,\boldsymbol{r}_j,\boldsymbol{r}_k) \\ &= \sum_{i=1}^{N}\sum_{j>i} \epsilon f_2(r_{ij}/\sigma) + \sum_{i,j,k;i<j<k} \epsilon f_3(\boldsymbol{r}_i/\sigma,\boldsymbol{r}_j/\sigma,\boldsymbol{r}_k/\sigma)\end{aligned}$$

where:

$$f_2(r) = \begin{cases} A(Br^{-p} - r^{-q}) \exp[(r-a)^{-1}], \text{ if } r < a \\ 0, \text{ if } r \geq a \end{cases}$$

$$f_3(\boldsymbol{r}_i, \boldsymbol{r}_j, \boldsymbol{r}_k) = h(r_{ij}, r_{ik}, \theta_{jik}) + h(r_{ji}, r_{jk}, \theta_{ijk}) + h(r_{ki}, r_{kj}, \theta_{ikj})$$

and:

$$h(r_{ij}, r_{ik}, \theta_{jik}) = \lambda \exp[\gamma(r_{ij} - a)^{-1} + \gamma(r_{ik} - a)^{-1}](\cos\theta_{jik} + \frac{1}{3})^2, \text{ if } r_{ij}, r_{ik} < a$$

In these equations, the parameters A, B, p, a, λ and γ are positive. θ_{jik} is the angle between $\boldsymbol{r}_j$ and $\boldsymbol{r}_k$ subtended at vertex i. ϵ and σ are the energy and length units.
The generic forms of f_2 and f_3 automatically cut off at $r = a$ and do not show any discontinuities in any r derivatives, which is a noticeable advantage in molecular dynamics simulations. The function f_3 dealing with three-body interactions clearly discriminates in favour of bonding angles such that $\cos\theta = -\frac{1}{3}$, which corresponds to the tetrahedral angle.
For l-Ge, we chose the parameters given by Yu [107].

4.2.1.2 Simulation procedure

We carry out our MD simulations within the so-called (N,V,E) ensemble, i.e. the microcanonical ensemble, in which the number of particles N, the volume of the system V and its energy E are conserved. The simulation cell is cubic and we use periodic boundary conditions. The Newtonian equations of motion are integrated with the velocity Verlet algorithm, with a time step of 0.5 fs. In this approach, $\frac{\Delta E}{\langle E \rangle}$ is about 10^{-6}.
The system consists of 1000 Ge atoms at a density of 2.53 g/cm^3.
The neighbour list has to account for the triplets of nearest neighbours since the potential has a three-body contribution. Thus we worked with a "home made" MD code so we could include this non-standard two- and three-body potential.
The initial configuration is randomly chosen with velocities of the atoms drawn from a Maxwell-Boltzmann distribution at temperature $T = 1700$ K. The simulation starts from a high temperature in order to ensure that the system has melted. The system is then equilibrated during 100000 time steps (50 ps) by scaling the velocities every 50 fs. From this trajectory, we extract 10 configurations equally spaced in time. These configurations are considered as independent ones since the system has evolved during 5 ps between the two closest of them. Each of these atomic configurations is then equilibrated at 1400 K by velocity scaling during 20000 time steps (10 ps). Consequently, we now have ten independent samples at equilibrium at 1400 K.
Ten production runs are finally performed at 1400 K during 50 ps in the microcanonical ensemble in order to accumulate accurate statistical averages.

4.2.1.3 Numerical results

The system has been simulated during quite a long time and the relation given by 1.26 may be applied. From the mean-squared displacements (see Fig. 4.2), we obtain a diffusion constant D = 0.536 10^{-4} cm^2/s. This value is quite low compared to the experimental value of 1.62·10^{-4} cm^2/s [110].
The comparison of the pair distribution function and the static structure factor with experimental results gives an overview of the ability of the potential to reproduce the structural features of the system. However, while $S(q)$ is easily available from the experiments, $g(r)$ is easier to

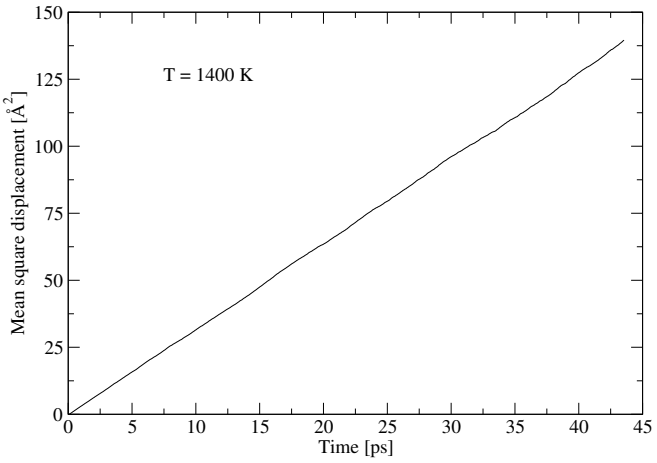

Figure 4.2: Average of the mean-squared displacements of the ten samples during production at $T = 1400$ K.

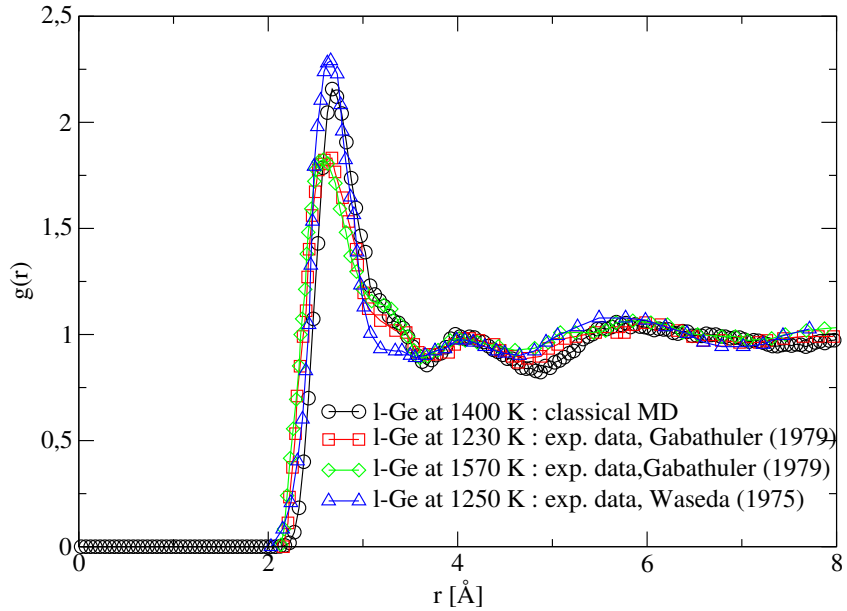

Figure 4.3: Comparison between simulated and experimental $g(r)$.

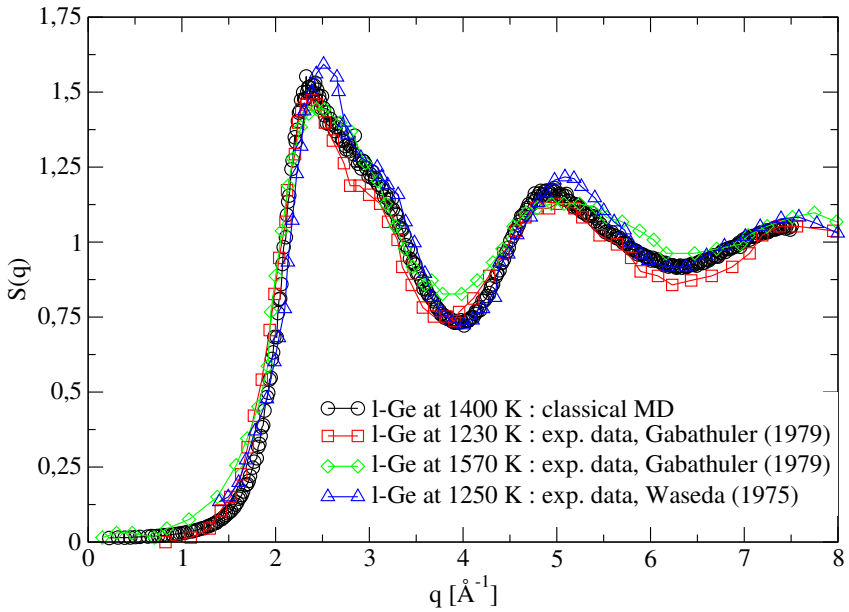

Figure 4.4: Comparison between simulated and experimental $S(q)$.

compute and more accurate from the simulated configurations. Both of these quantities were computed by averaging over 10000 configurations.
The agreement between simulated and experimental data is quite good, although some discrepancies exist: these may come from the inverse Fourier-transform used for computing $g(r)$ from experimental data, since the overall agreement of the $S(q)$ is better than for the $g(r)$. However we also notice some differences between experimental data under similar measurement conditions.
Nevertheless the positions of the main peaks in $g(r)$ are quite well reproduced even if the intensities vary. For $S(q)$, the main peak is observed between 2.4 and 2.5 Å^{-1} which corresponds to the nearest neighbour shell denoted by the first peak in $g(r)$ at $r_m = 2.6$ Å. The shoulder on the high-q side of the first sharp peak ($q = 3$ Å^{-1}) reported by experiments is also reproduced by the simulations.

From the trajectories, the intermediate scattering functions were also computed, which give access to the dynamic structure factor by time Fourier transform. Both $F(q,t)$ and $S(q,\omega)$ are shown for low q values in Fig. 4.5. The longitudinal propagating modes existing in the experiment are also reproduced by the classical MD simulation. The phonon dispersion and the damping of the mode with increasing q values are clearly visible. However a strong discrepancy exists between experimental and simulated data as depicted in Fig. 4.6. The sound velocity is defined as: $c_s = \frac{\omega}{q}$. For l-Ge, it is much higher in the simulation than in reality as shown in Fig. 4.7: both measurements of the adiabatic sound velocity [99] and inelastic X-ray scattering experiments [98] indicate a sound velocity of 2682 m/s, while the simulated value is of the order of 5000 m/s.

Concerning the incoherent behaviour of the sample, we notice that the diffusive regime prevails for q values under 1 Å^{-1} approximately. This is shown on the left plot of Figure ·4.8: we expect a behaviour described by: $F_s(q,t) = \exp(-Dq^2t)$ where D is the self-diffusion constant; above

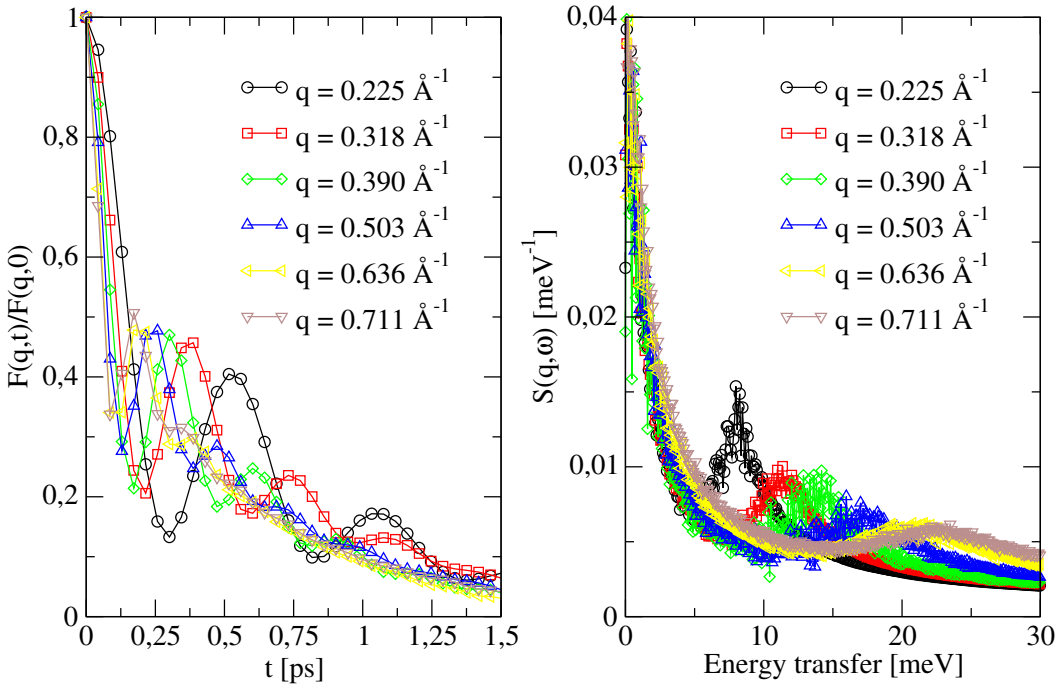

Figure 4.5: Simulated $F(q,t)$ (left) and $S(q,\omega)$ (right) at low q values and $T = 1400$ K.

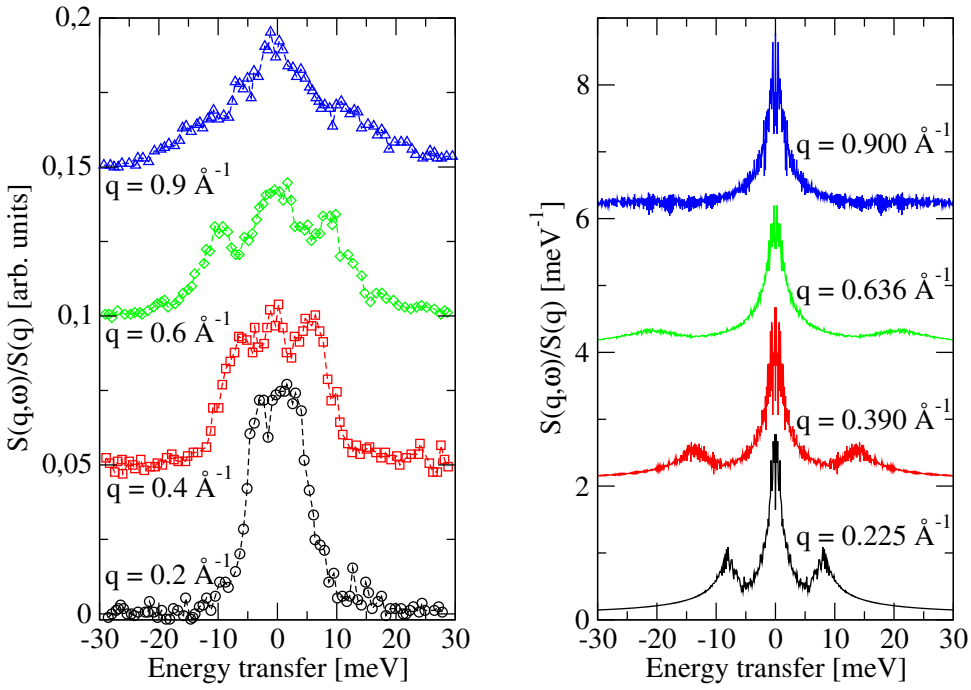

Figure 4.6: Comparison between simulated and experimental $S(q,\omega)$ for different low q values. Left: experimental data, Hosokawa *et al* [98]; right: classical MD simulation at $T = 1400$ K.

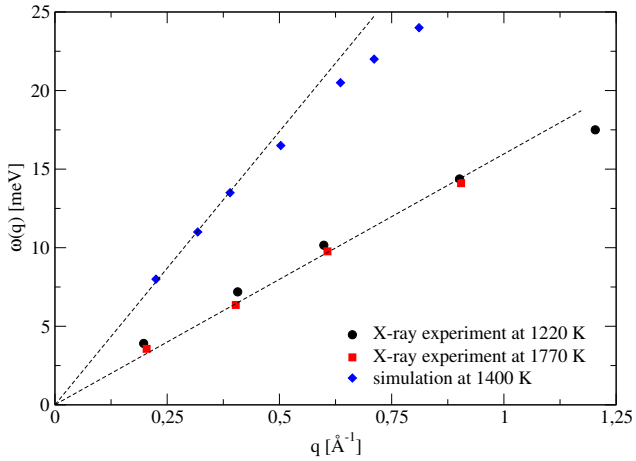

Figure 4.7: Comparison of the experimental [98] and simulated dispersion of the acoustic phonon.

$q = 0.98$ Å^{-1}, the slope of $\ln(F_s(q,t))/q^2$ departs from the constant D value associated with the diffusive regime. The value of D given by fitting these straight lines is $0.59{\cdot}10^{-4}$ cm^2/s, very close to the value determined from the Einstein relation for the mean-squared displacements. On the right plot, the incoherent dynamic structure factor is shown for several q values. We notice both damping of the intensity and increase of the width of the spectra for increasing q values as expected for the incoherent signal: for large q values, that is small spatial correlation distances, we deal with short wavelength inhomogeneities and relaxation over small length scales which is a fast process. Consequently, the width of the spectra for small q values is narrower than for large q values.

4.2.1.4 Discussion

The empirical potential designed by Stillinger and Weber leads to a description of the structural properties of the system which is in agreement with the measurements. However, the dynamic features are not well reproduced.
The discrepancy between the simulated and experimental values of the sound velocity in *l*-Ge may come from the chosen parameters for the potential. Some features of the latter may yield to strong interactions between the atoms and thus increase the typical frequencies involved in the vibrational behaviour of the system. In particular, the three-body interaction seems to emphasize too strongly the tetrahedral arrangements.
Thus the empirical potential seems to be too rigid to give a good picture of the dynamics of *l*-Ge.

In order to cope with these drawbacks, we performed *ab initio* MD simulations of our system. Although this kind of simulations is not usually done for computing dynamic quantities, we are trying to calculate the dynamic structure factor from these trajectories.

4.2.2 *Ab initio* molecular dynamics simulation

As explained in section 2.2.2, in *ab initio* molecular dynamics simulation, there are no parameterized atom-atom interactions, however the nucleus and core electrons are represented by a pseudo-potential and "simple" liquids can be used to probe the accuracy of these pseudo-potentials.

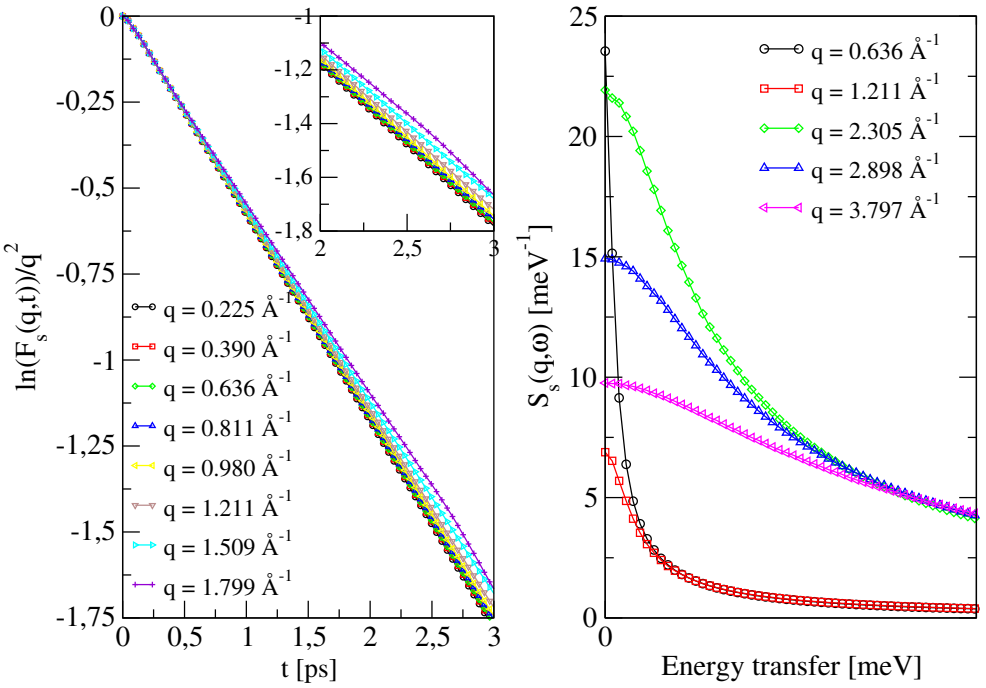

Figure 4.8: Self dynamic properties of l-Ge at $T = 1400$ K: left: $\ln(F_s(q,t))/q^2$ as a function of q (inset: departure from the diffusive law for high q values); right: incoherent dynamic structure factor for several q values (the intensity is multiplied by a factor of ten for $q > 2$ Å^{-1}).

4.2.2.1 Simulation procedure

All calculations presented here were performed with the Vienna Ab initio Simulation Package (VASP) [115, 116], which is based on the density functional theory.
We carried out simulations of l-Ge for an ensemble of 64 atoms in a cubic supercell with periodic boundary conditions. The simulated density was $\rho = 2.53$ g/cm^3, which yields a box of length 11.175 Å.
The atomic dynamics was described in the microcanonical (N,V,E) ensemble. We used ultrasoft Vanderbilt pseudopotentials [117] and the generalized gradient approximation (GGA) with the functional PW91 for the exchange-correlation energy.
The Brillouin zone was sampled by a $3 \times 3 \times 3$ Monkhorst-Pack mesh of k-points [45]. The wave functions were expanded in a basis of more than 32000 plane waves, corresponding to an energy cut-off of 139.2 eV.
Note that we performed a simulation with 300 atoms and only Γ point sampling since physical size and k-point sampling are in some way equivalent. The static structure factor from this simulation did not show any shoulder on the high q side of the main peak.

The starting configurations for the *ab initio* simulations were generated by classical MD simulations using the Stillinger and Weber potential. For this purpose, systems of 64 Ge atoms were equilibrated at the desired temperatures using the same scheme as described earlier for classical MD simulations.
After switching to the *ab initio* (N,V,E) MD, three runs of 30 ps using a time step of 3 fs were performed at three different temperatures corresponding to the liquid (1390 K, 1080 K) and

supercooled (680 K) states. This was done under the assumption that the densities of l-Ge for temperatures between 680 and 1390 K are equal.
Finally, we quenched three independent configurations of the trajectory at 680 K at a cooling rate of 68 K/ps in order to obtain three amorphous configurations of the system.

4.2.2.2 Numerical results

The mean-squared displacements (MSD) is one of the more trivial quantities available from the simulated trajectories. It consists of following a tagged particle as a function of time in order to see for instance if its trajectory is subject to constraints or if the particle diffuses freely. Averaging this quantity over all the particles of the system gives insight into its overall behaviour. The mean-squared displacements are here computed for the three temperatures 1390 K, 1080 K and 680 K. They are plotted in Figure 4.9. We notice quite different behaviours at short and long times. At short times, the mean-squared displacements increase as t^2 as shown by the line of equation $y = t^2$ (denoted quadratic). This is peculiar of the atoms diffusing freely, that is before their motion is affected by the presence of their nearest neighbours. At longer times, the time dependence of the mean-squared displacements becomes linear: we notice that the slope of the MSD is parallel to that of the line of equation $y = t$ (denoted linear). This corresponds to the hydrodynamic regime.

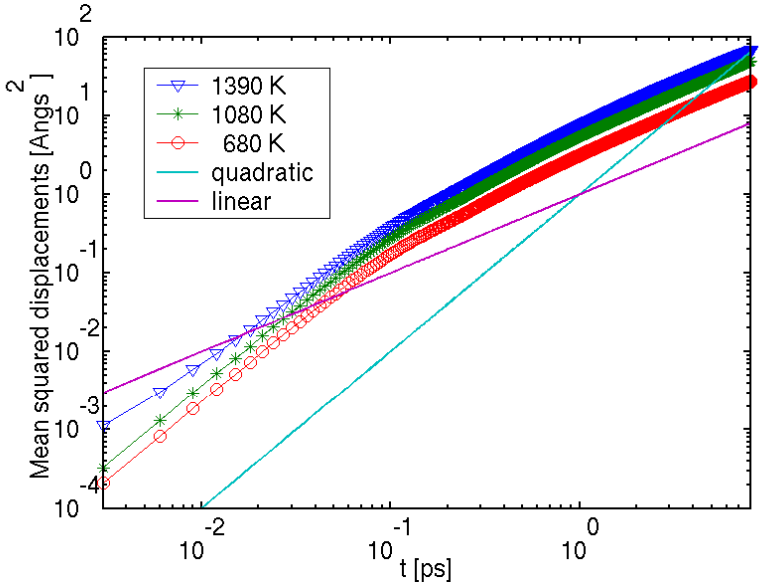

Figure 4.9: Mean-squared displacements (in $\mathring{A}^2$) versus time (in ps) at three different temperatures: T = 680 K, T = 1080 K and T = 1390 K. The lines represent respectively the quadratic and linear behaviour. Note that the scales are logarithmic.

The calculation of the mean-squared displacements gives access to the diffusion constant at three temperatures according to the Einstein relation (1.26):

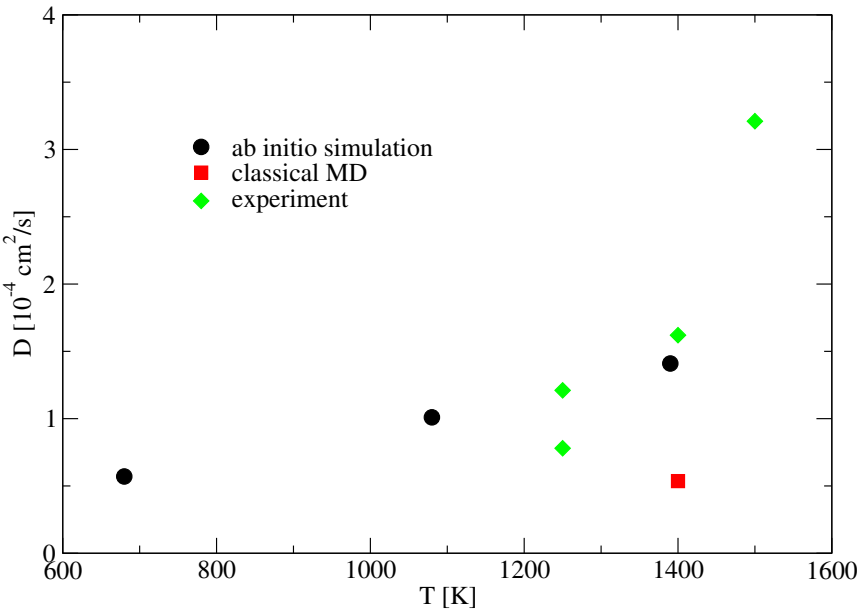

Figure 4.10: Comparison of calculated and experimental diffusion constant at different temperatures (experimental data from [110]).

T [K]	D [10^{-4} cm^2/s]
1390 K	1.41
1080 K	1.01
680 K	0.57

The simulated values are compared to experimental data [118] in Figure 4.10. Around 1400 K, the value of D is available from experiment and from both simulation methods presented here. There is strong discrepancy between the value from the classical MD on the one hand and the values from the experiment and the *ab initio* MD on the other hand. If we consider the temperature dependence of the self-diffusion constant, it seems to be linear according to the results of the *ab initio* simulation while the experimental results are of the same order in the range from 1250 K to 1400 K although they do not show the same linear temperature dependence.

Let us now have a closer look at the pair distribution function $g(r)$. This quantity was computed by averaging over 10000 configurations for each temperature and the results are presented in Fig. 4.11 compared to the experimental $g(r)$ of Salmon [96].
We notice that the first peak corresponding to the nearest neighbour shell is positioned at 2.67 Å, in good agreement with the measured values of 2.67 and 2.66 Å[95, 96]. Moreover this peak does not shift with temperatures, while its intensity increases when temperature goes down. These two features are in good agreement with the X-ray experiments by Filipponi [92]. The rise in intensity is due to the increased ordering of the atoms at low temperatures: at 680 K, the kinetic energy is much lower than at 1390 K and hence the structural features are more pronounced. At $T = 680$ K, we also observe a growing feature at $r \approx 4$ Å, which is slightly indicated at higher temperatures by a non-smooth minimum between the first and second peaks in $g(r)$. This new oscillation in the pair distribution function brings to the fore the appearance of a new typical distance in the system. In the diamond type germanium crystal, the radii of the first and second

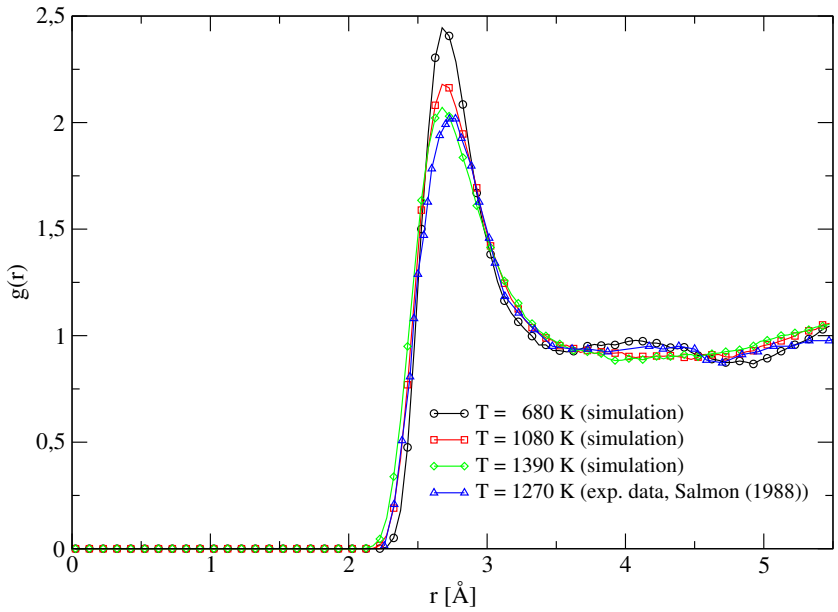

Figure 4.11: Pair correlation function at the three different temperatures and experimental data by Salmon [96].

neighbour shells are: $r_1 = 2.45$ Å and $r_2 = 4.00$ Å. Thus the intermediate peak in $g(r)$ is likely to be related to the atomic arrangement in the solid state.
The comparison with experimental $g(r)$ by Salmon [96] is in overall good agreement. However, the growing intermediate peak observed at 680 K in the range of r $\approx$ 4 Å is already present in the experimental data at $T = 1270$ K. It was already noticed in a simulation study by Kulkarni [112] that this damped peak flattens and eventually disappears at higher temperatures.

The static structure factor was computed from 10000 atomistic configurations for each temperature. The average is also performed over all $\boldsymbol{q}$ vectors of the same magnitude. The results are shown in Fig. 4.12 together with the experimental result by Salmon [96].
The main sharp peak is located at $q = 2.53$ Å^{-1} at $T = 1390$ K. This result is very close to the experimental values [95, 96, 91]. At lower temperatures, the peak is shifted to lower q values, which is consistent with measurements [97]: it was shown that the peak was shifted to higher q values with increasing temperature in the range from 1270 K to 1820 K.
The characteristic feature of l-Ge shown by neutron diffraction studies is well reproduced by the simulation: we observe a distinct shoulder on the high-q side of the first sharp peak of the static structure factor. It occurs at $q = 3.27$ Å^{-1}, in close agreement with the experimental data [97]. As T decreases, the height of the main peak is reduced and the shoulder becomes more distinct. These two features were described at higher temperatures in the simulation work by Kulkarni [112]: at $T = 2000$ K, the shoulder disappears. This is consistent with the previous finding that the shoulder is more pronounced at low temperatures.
The second peak of the static structure factor is found to occur at 5 Å^{-1}. This is shifted from the experimental value found by Salmon [96] (see also Waseda [91]) as shown in Fig. 4.12. However, depending on the measurements, the position of the second peak is found between 5 and 5.12 Å^{-1}, in very good agreement with the value found by Isherwood and Orton [90, 120].

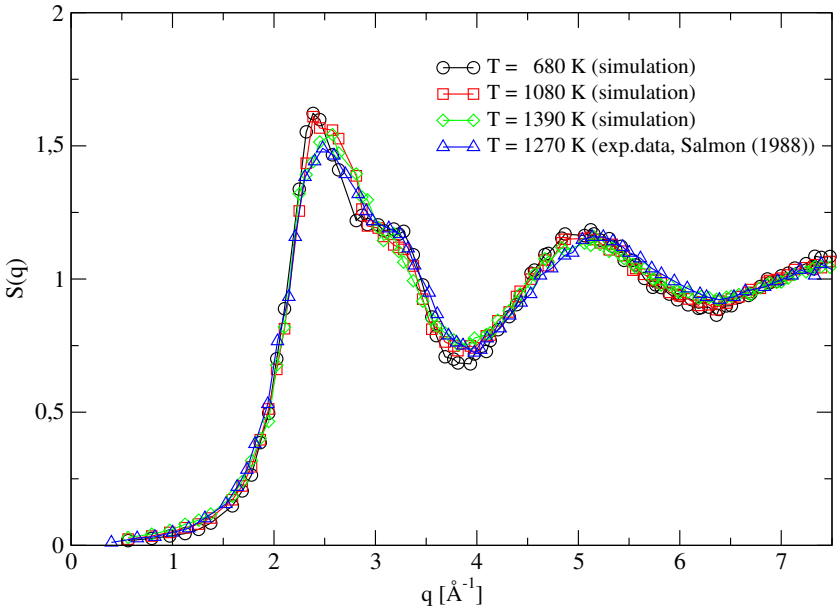

Figure 4.12: Static structure factor at the three simulated temperatures and experimental data by Salmon [96].

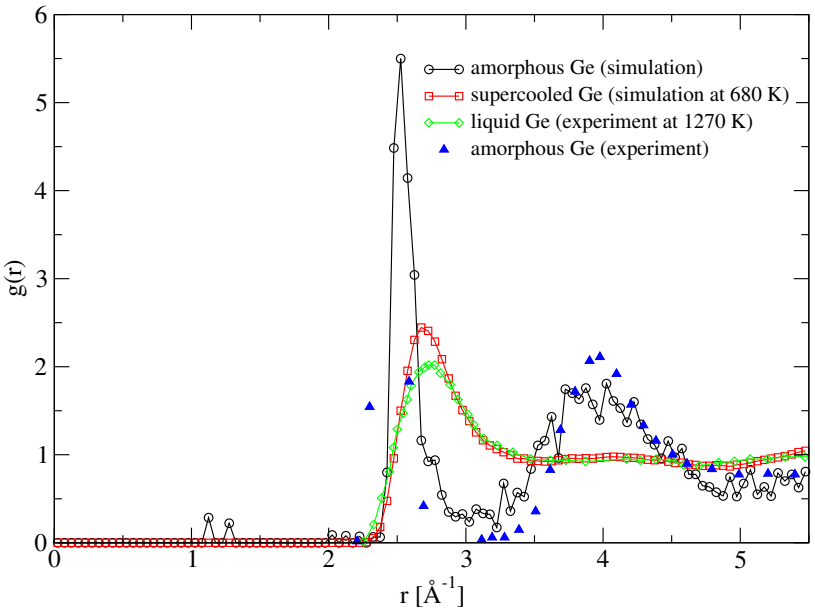

Figure 4.13: Pair correlation function for supercooled and amorphous Ge compared to experimental data (neutron scattering, see [119] for the amorphous phase and [96] for the liquid state).

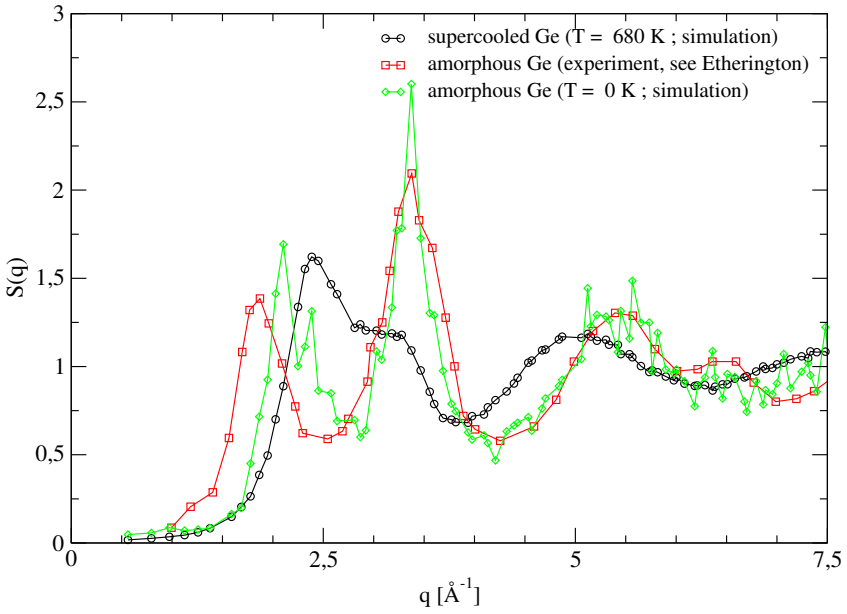

Figure 4.14: Static structure factor for supercooled and amorphous Ge compared to experimental data (neutron scattering, see [119]).

Both the pair correlation functions $g(r)$ and the static structure factors $S(q)$ for the supercooled liquid at 680 K and the amorphous germanium are shown respectively in Figures 4.13 and 4.14. As said before, the amorphous phase was obtained by cooling down three different and independent configurations of the supercooled state at 680 K. Thus the pair correlation function and the static structure factor were averaged over three configurations of the amorphous phase. The agreement between the simulated and experimental $g(r)$ and $S(q)$ is quite good. In $S(q)$ we observe the splitting of the first peak and the shoulder of the liquid phase in two peaks around 2 Å^{-1} and 3.4 Å^{-1}. In the pair correlation function, the main peak is shifted to smaller interatomic distances and sharper than in the liquid or supercooled states. The growing intermediate peak near 4 Å observed at 680 K is much more pronounced in the amorphous state as seen in Figure 4.13. If we have a look at the structure of the amorphous state, we notice the presence of tetrahedra: the main peak in $g(r)$ corresponds to the interatomic distance between the center and a vertex of the tetrahedron while the higher interatomic distance at 4 Å is associated with the distance between two vertices of the tetrahedron (see also Fig. 4.16.

Given the nature of the many-body interactions in germanium, it is interesting to compute the angular distribution of atoms. $g(\theta, r_m)$ is the (not normalized) distribution of angles defined by vectors going from a reference atom i to two neighbours of i which are within a radius r_m of the reference atom. In Fig. 4.15, r_m is shown using various values around the minimum in $g(r)$. This minimum is not clearly defined in the liquid, leading to uncertain definition of the nearest neighbour shell. In contrast, in the supercooled and amorphous states, the first minimum in $g(r)$ is clearly defined. $g(\theta, r_m)$ is computed for the liquid ($T = 1390$ K), supercooled ($T = 680$ K) and amorphous phases.

For both liquid and supercooled systems, we observe a broad peak around $\theta = 98°$ if $r_m = 2.8$ Å. When increasing r_m, this peak tends to be shifted to lower angles, around $\theta = 90°$. For the

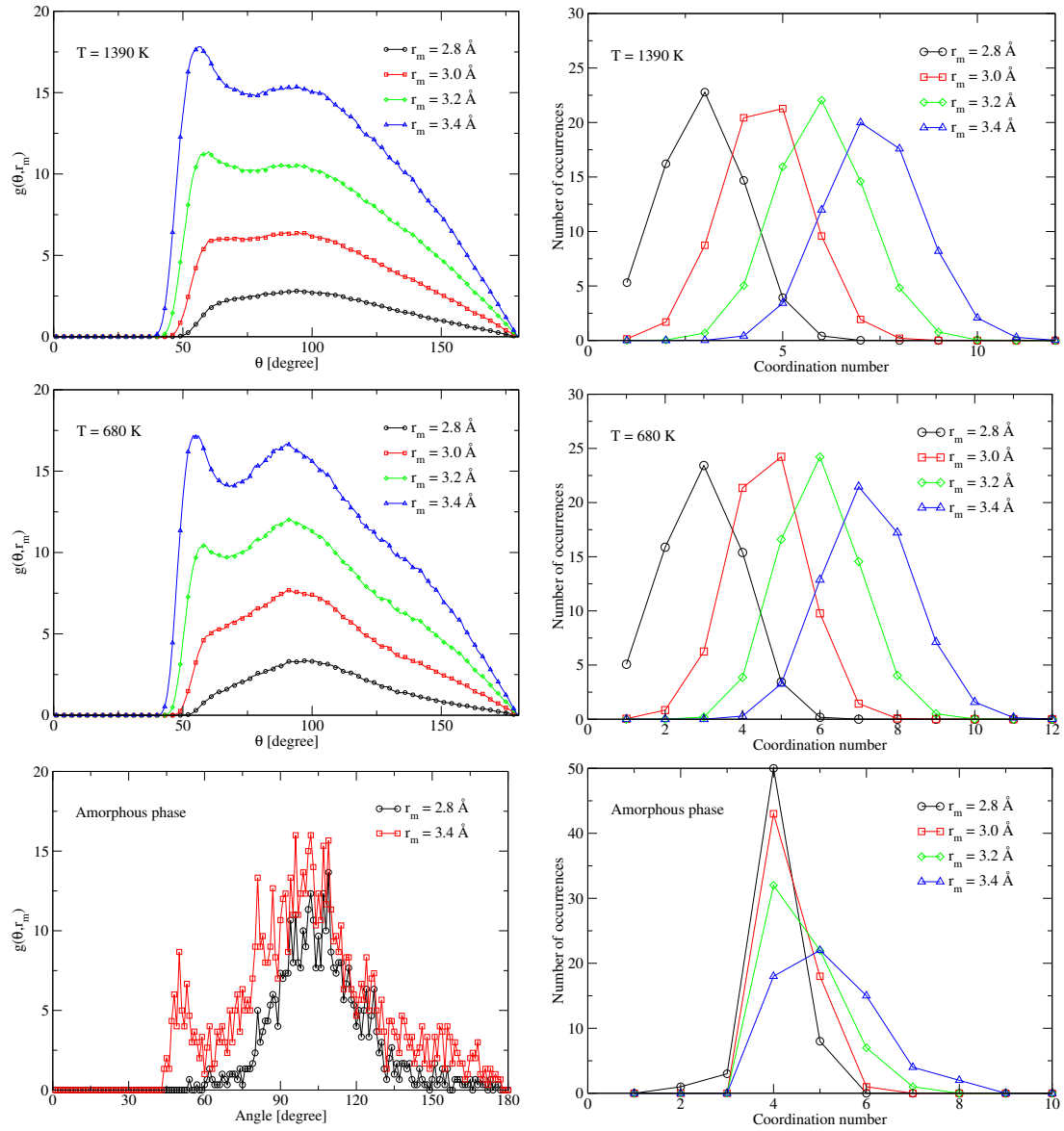

Figure 4.15: Left: angular distribution for liquid, supercooled and amorphous phases for r_m around the first minimum of $g(r)$. Right: coordination number for the same three phases. The quantities for the liquid, supercooled and amorphous phases are respectively averaged over 9000, 6300 and 3 configurations.

amorphous phase, the corresponding peak is observed at slightly higher angles, of the order of 105° for $r_m = 2.8$ Å. With increasing r_m, a new peak appears for angles between 55 and 60° in the liquid and supercooled phases. At $T = 680$ K, this feature is more pronounced than at higher temperatures. In the amorphous phase, this peak appears at smaller angles of the order of 50°.
A bond angle of 60° is characteristic of metallic bonding, that is to say 60° represents the most closely packed structure of the system. The broad peak around 100° may be peculiar to flattened tetrahedra. Note that the characteristic bond angle of a tetrahedron is 109.5°.
For the coordination number of the atoms, we notice that most atoms have either 4 or 5 nearest neighbours in the amorphous phase. On the other hand, in the liquid and supercooled phases, for usual values of the first minimum in $g(r)$ around 3.3 Å, we obtain a coordination number between 6 and 7. Note that the coordination number increases with increasing radius of the coordination sphere for both liquid and supercooled systems. In contrast with these cases, the coordination of the amorphous phase behaves quite differently: the coordination number is around 4 and does not increase much with increasing r_m. This is consistent with the shape of $g(r)$: for the amorphous phase, the first and second shells of neighbours are well separated with a deep minimum around $r = 3.2$ Å. In contrast, the liquid and supercooled systems do not show any obvious minimum in their pair correlation functions after the first sharp peak. That is why the coordination number increases with increasing radius r_m defining the neighbourhood. This continuous increase of the coordination number with increasing coordination sphere may be consistent with the β-tin hypothesis [90]. The latter assumes that in liquid Ge, each atom has four nearest neighbours on a flattened tetrahedron and two other neighbours slightly further away on the perpendicular to the plane of the flattened tetrahedron. As a matter of fact, if we denote by r_0 the main interatomic distance reported from $g(r)$, the β-configuration would lead to interatomic distances of the order of $r_0 \simeq 2.5$ Å (between the center and a vertex of the tetrahedron), $\sqrt{2}r_0 \simeq 3.53$ Å (between two adjacent vertices of the tetrahedron) and $2r_0 \simeq 5$ Å (between two opposite vertices of the tetrahedron) together with distances slightly higher than r_0 associated with the two further neighbours. Consequently this analysis may actually be in agreement with the features observed in $g(r)$ and in the evolution of the coordination number, however a more detailed study is necessary to have a more accurate knowledge of the local arrangements present in the liquid.

Snapshots of the simulated structure of amorphous Ge are shown in Figure 4.16. On the left, the 64 atoms are represented together with the corners of the simulation box. The bonds between atoms correspond to two covalent radii (1.22 Å for Ge) plus a bond tolerance, that is to say a bond is drawn for interatomic distances smaller than 2.84 Å. The two subsequent plots show a zoom in this structure. Three 'tetrahedra' are represented together with some interatomic distances and bond angles. We notice that the covalent bond length of Ge corresponds to the main peak in $g(r)$ around 2.5 Å. On the other hand, the distance between two vertices of a tetrahedron is comprised between 3.5 Å and 4.5 Å. Subsequently the broad peak around 4 Å in $g(r)$ (see Fig. 4.13) is related to this kind of spatial arrangement. If we now have a look at the angles, their values are mainly distributed between 85° and 130°. These bond angles consequently give rise to the observed broad distribution of angles around 105° (see Fig. 4.15). These bond angles come from the angles formed by two 'covalent bonds' of the same tetrahedron. If we consider higher interatomic distances (see distribution for $r_m = 3.4$ Å in Fig. 4.15), another peak appears around 50°. This one is due to the angles formed by the two following vectors: the first one goes from a vertex to the center of the tetrahedron while the second one goes from the same initial vertex to another vertex of the same tetrahedron. This is also shown in Fig. 4.16.

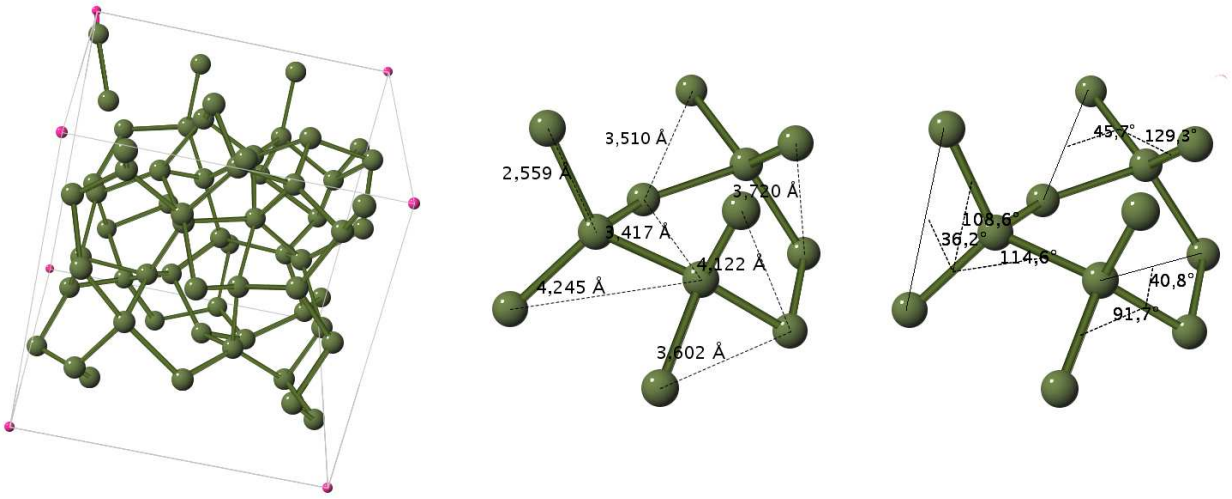

Figure 4.16: Calculated structure of amorphous Ge at $T = 0$ K. Left: snapshot of the whole simulation box (with small balls representing the corners of the box). Middle: interatomic distances. Right: bond angles.

In summary, this study of the structure of liquid, supercooled and amorphous germanium enables insight to be gained into the microscopic arrangements leading to the observed $S(q)$ and $g(r)$. As already stated by Kresse [109], the amorphous state is characterized by the presence of tetrahedra. For the liquid state, the β-tin hypothesis seems to be compatible with the quantities ($g(\theta, r_m)$, coordination number) computed from the simulation. The significant change in the structure between the liquid and amorphous phases, as shown by the static structure factor and the pair correlation function, is rather unusual and is consistent with a transition from tetrahedral formations in the amorphous phase to β-tin like local structure in the liquid.

From the trajectories, we may also extract dynamic features of the system. Note that the low q limit is related to the size of the simulation box. In our case, the lowest accessible q value is 0.562 Å^{-1}. Figure 4.17 shows both the intermediate scattering function and the dynamic structure factor of l-Ge at 1390 K and for low $\boldsymbol{q}$ vectors. On the bottom left, $F(q,t)$ is normalized by its value at time 0. The oscillations are associated with the presence of the acoustic mode at low q. We notice that the period and intensity of these oscillations vary with increasing q: the period decreases and the signal is more damped for high q values. This is directly associated with the shape of the dynamic structure factor shown on the bottom right for the same q values. The raw dynamic structure factor is shown on the top right plot: it is quite noisy due to the small number of atoms in the box. However the overall features can already be distinguished in the raw Fourier transform. As shown on the bottom right plot, the dynamic structure factor was smoothed by convolution with a gaussian ($\sigma = 1.1$ meV) in order to suppress the statistical noise due to the Fourier transform of $F(q,t)$. An overall view of the dispersion of the acoustic phonon is given in Figure 4.18. We notice the excess of intensity beside the elastic line due the presence of the acoustic phonon. In Figure 4.17 we notice that the central peak starts to be split at $q = 0.863$ Å^{-1} and 0.970 Å^{-1}. This feature may be attributed to the transverse mode, which is observable in simulations although it is not available from neutron scattering

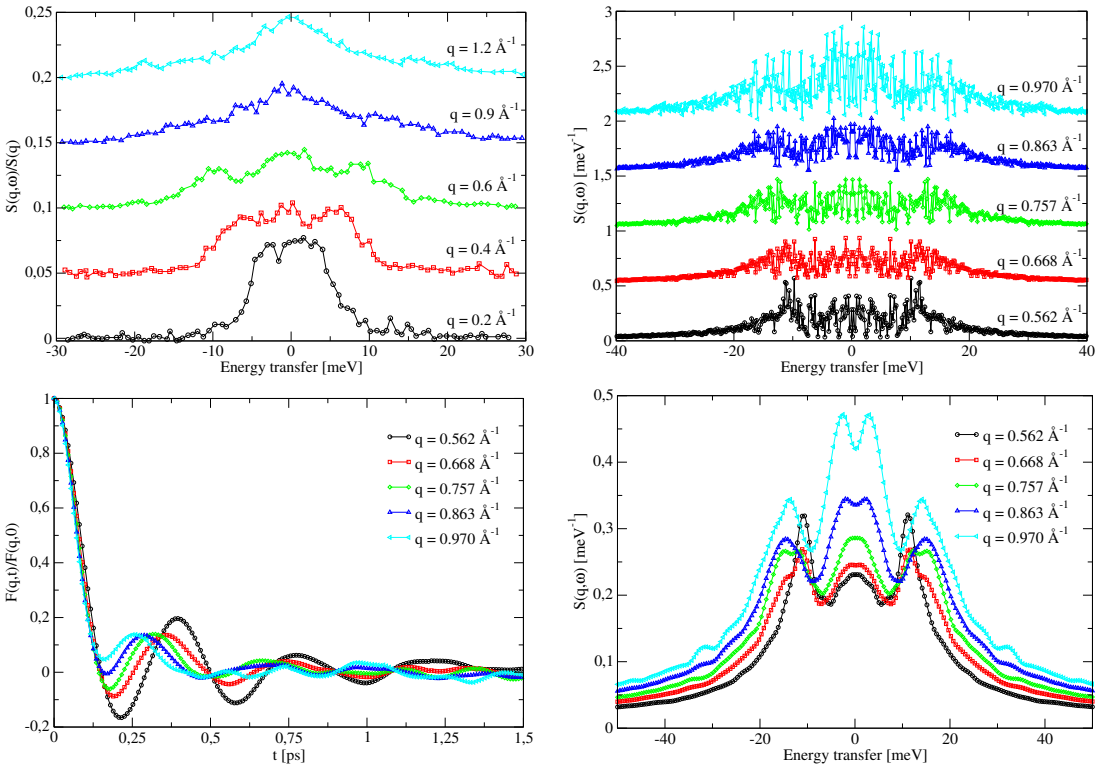

Figure 4.17: Collective dynamic properties of l-Ge at low q values: top left: experimental data at 1250 K; bottom left: intermediate scattering function $F(q,t)$ at 1390 K; top right: raw $S(q,\omega)$ computed by Fourier transform of $F(q,t)$ from the simulation at 1390 K; bottom right: smoothed $S(q,\omega)$.

experiments due to its transverse character. However, such splitting of the central peak is also observed at much higher q values which cannot be associated with the presence of a transverse mode. Moreover if it were a transverse mode it would be more intense at lower temperatures which is not the case. Consequently this feature must be an artefact of the Fourier transform and of the symmetrization of the signal in energy.
From $S(q,\omega)$, we can determine the frequency of the acoustic phonon as a function of q and compare it to X-ray experimental data. This is shown in Figure 4.19. In the case of the simulated $S(q,\omega)$, it is quite difficult to avoid the uncertainty when evaluating the phonon frequency as a function of q. However the available phonon frequencies are quite consistent with the experimental data in what concerns the dispersion of the longitudinal acoustic excitation. A comparison of the dispersion of the acoustic mode at the different temperatures does not show any strong differences between the sound velocities as a function of temperature.

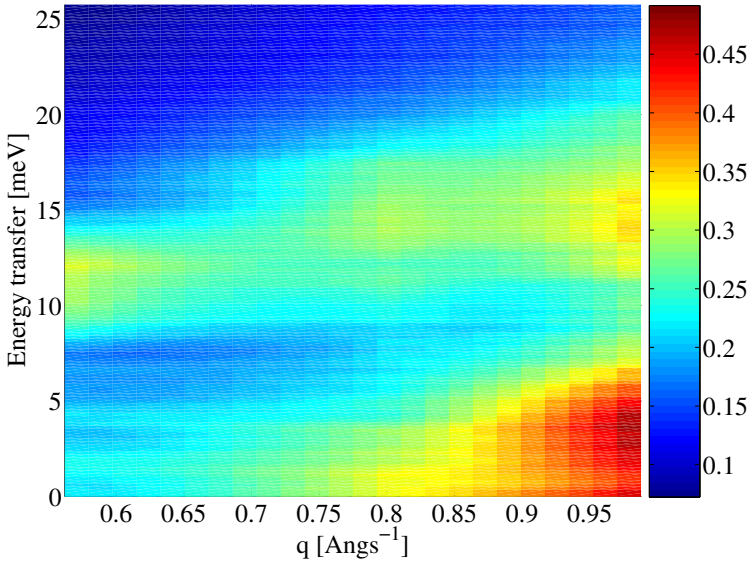

Figure 4.18: Simulated dynamic structure factor $S(q,\omega)$ for low q values at $T = 1390$ K: evidence of the dispersion of the acoustic mode.

Let us now move on to higher q values ($q > 1$ Å^{-1}) where the acoustic excitation is not relevant any more. In this range, we are interested in the quasi-elastic behaviour of the liquid. When fitting the raw $S(q,\omega)$, we obtain the results depicted in Figure 4.20. The widths and intensities extracted from the simulations at 1390 K and 680 K come from the fit of $S(q,\omega)$ with a Lorentzian. In the simulation, we observe the narrowing of the quasi-elastic peak for $q = 2.4$ Å^{-1} and between $q = 2.8$ Å^{-1} and 3.2 Å^{-1}. This corresponds to the phenomenon of de Gennes narrowing occurring close to the positions of the intense features in the static structure factor: the dynamic structure factor is the Fourier transform of correlation functions which describe the rate at which a system forgets its initial state; when the dynamics are on the same length-scale as the local structure, the structure is "preserved", thus there is limited loss of memory and limited broadening of the dynamic structure factor.
The simulated evolution of the quasi-elastic peak can be compared with theoretical predictions based on different models. For the theoretical width ω_h, we use the formula for a measure of

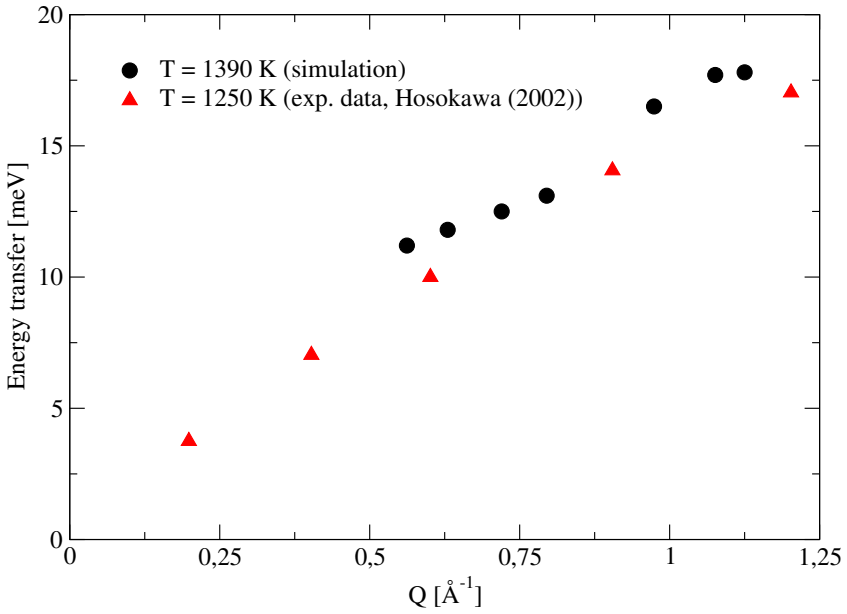

Figure 4.19: Dispersion of the frequency of the acoustic phonon as a function of q: comparison between experiment and simulation (rough estimate of the error bars on the simulated data: 2 to 3 meV).

the half width at half maximum of the spectra as a function of q, denoted $\omega_h(q)$, derived for a dense hard-sphere fluid [102]. This quantity is given by:

$$\omega_h(q) = \frac{D_E q^2}{S(q)} d(q), \tag{4.1}$$

where

$$d(q) = [1 - j_0(q\sigma) + 2j_2(q\sigma)]^{-1}. \tag{4.2}$$

Here D_E is the self-diffusion coefficient of the hard-sphere fluid in the Enskog theory and $j_0(x)$ and $j_2(x)$ are the zeroth- and second-order spherical Bessel functions respectively. Equation (4.1) is only valid for intermediate values of q ($1 < k\sigma < \sigma/l$ where $\sigma/l \gg 1$) and high densities. This quantity $\omega_h(q)$ was computed using the static structure factor from the *ab initio* molecular dynamics simulations at 680 K and 1390 K. For D_E, we use the self-diffusion constant D calculated from the simulation: its overall behaviour with respect to the mass and the density must be similar to that of the self-diffusion constant of the Enskog theory. For the typical size σ of the hard spheres, we use $\sigma = 2.8$ Å at $T = 1390$ K and $\sigma = 2.7$ Å for $T = 680$ K in agreement with the computed pair correlation functions. For the other theoretical prediction denoted ω_q, we use the square root of the normalized second frequency moment defined in 1.48.
We notice that the prediction given by ω_q does not give a good description of the shape of the width $\Gamma(q)$. Thus the description of liquid Ge as a simple dense fluid is not relevant. However, the width ω_h predicted by the hard sphere model seems to give a better description of our system. The overall shape of $\Gamma(q)$ is preserved at both temperatures. We observe the phenomenon of de Gennes narrowing at the same q values than in the simulation. However even if the slowing down of the dynamics around 3 Å^{-1} is well reproduced at 680 K, it is not pronounced at all at 1390 K in the theoretical prediction ω_h. We also realize that the theory underestimates the

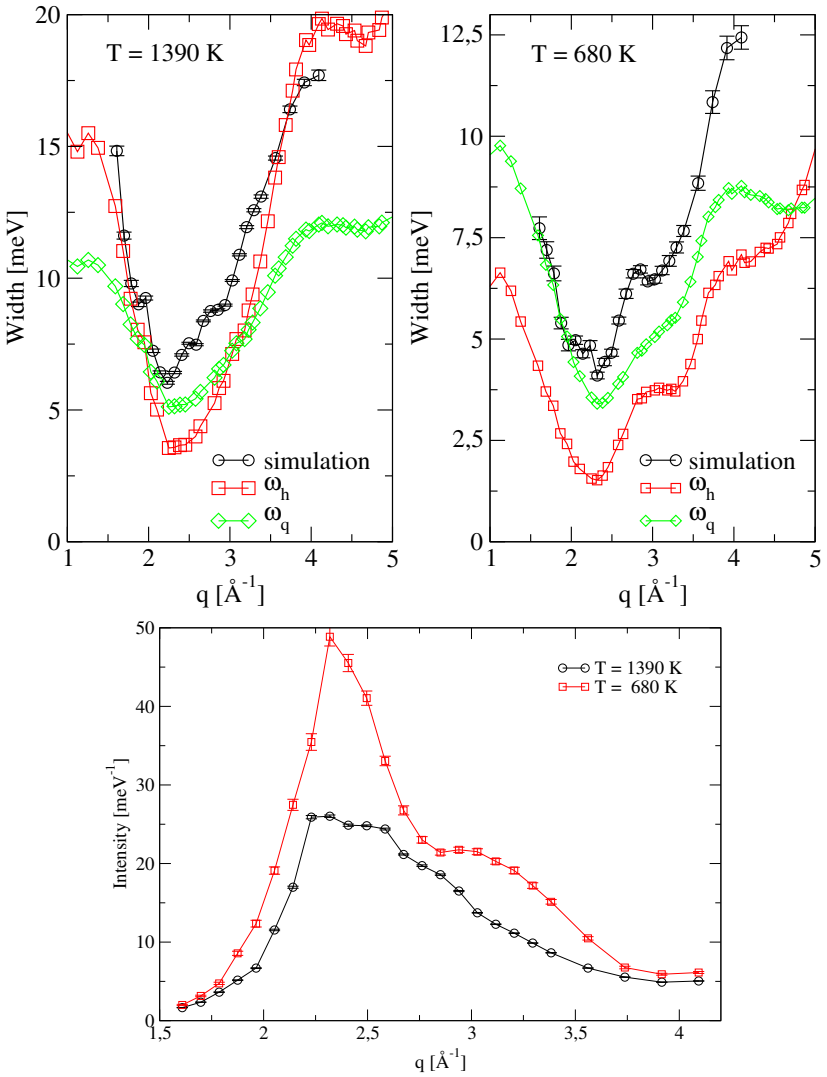

Figure 4.20: Width (top) and intensity (bottom) of the spectra as a function of q for two temperatures: $T = 1390$ K and $T = 680$ K.

value of the width. In the hard sphere model, this may come from the use of D instead of D_E. For the intensity of the spectra at 1390 K and 680 K, its evolution as a function of q is quite similar to the shape of $S(q)$: the main peak is around 2.3-2.4 Å^{-1} and we observe a shoulder between 2.8 Å^{-1} and 3.2 Å^{-1}. The latter is more pronounced at $T = 680$ K as seen in the static structure factor.

As shown in Figure 4.21, we can also extract the width of $F(q,t)$ for $F(q,t)/F(q,0) = \exp(-1)$. We observe a long-lived relaxation near the position of the first maximum in $S(q)$ for the three temperatures $T = 680$ K, 1080 K and 1390 K. We notice that the relaxation time associated with the simulated width increases with decreasing temperatures. This shows that the collective motion leading to the relaxation of the density fluctuations are much slower at low temperatures. The width of $F(q,t)$ is closely related to the width of $S(q,\omega)$. We notice the appearance of a shoulder for q between 2.8 Å^{-1} and 3.4 Å^{-1} at $T = 680$ K. The increasing relaxation times

around 2.5 Å^{-1} and between 2.8 Å^{-1} and 3.4 Å^{-1} are associated with the phenomenon of de Gennes narrowing: the main structural features appear around these q values. Consequently the density fluctuations corresponding to such q values are quite long to relax. This result is in agreement with the width extracted from $S(q,\omega)$ and shown in Fig. 4.20.

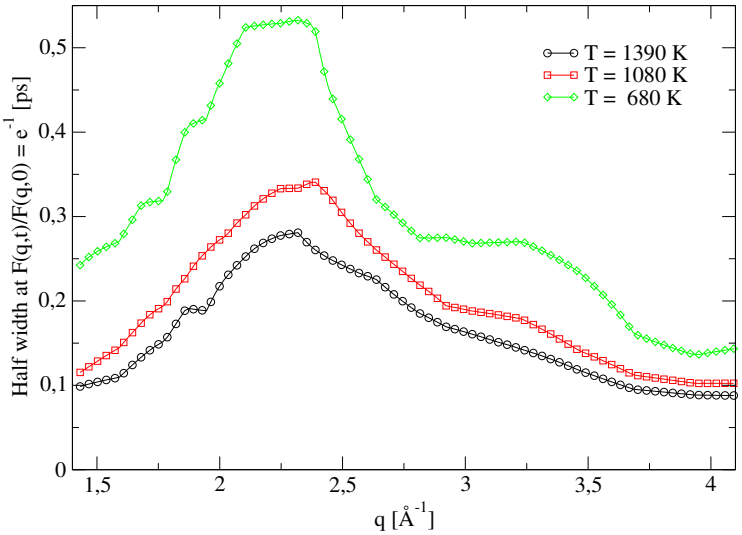

Figure 4.21: Width at $F(q,t)/F(q,0) = \exp(-1)$ as a function of q for different temperatures.

The single-particle correlations were also computed from the trajectories. The self intermediate scattering function $F_s(q,t)$ at $T = 1390$ K is shown in Figure 4.22 together with the corresponding self dynamic structure factor $S_s(q,\omega)$. As in the classical MD, we observe a departure of $F_s(q,t)$ from the diffusive behaviour as shown by the plot of $\ln(F_s(q,t))/q^2$ as a function of t. For q values below 1 Å^{-1}, $F_s(q,t)$ is well represented by : $F_s(q,t) = \exp(-Dq^2t)$. At q values higher than 1 Å^{-1}, the self intermediate scattering function does not probe the diffusive behaviour of the system since we notice a drift of the slope $-D$ of $\ln(F_s(q,t))/q^2$. From $F_s(q,t)$ at small q values, we can extract the self-diffusion constant D. We obtain values between $1.34{\cdot}10^{-4}$ cm^2/s and $1.36{\cdot}10^{-4}$ cm^2/s for q values between 0.56 Å^{-1} and 1 Å^{-1}. At $T = 1080$ K, we obtain from the diffusive behaviour of $F_s(q,t)$ a value of D between $0.98{\cdot}10^{-4}$ cm^2/s and $1{\cdot}10^{-4}$ cm^2/s. At $T = 680$ K, D is of the order of $0.565{\cdot}10^{-4}$ cm^2/s to $0.58{\cdot}10^{-4}$ cm^2/s. These values are in close agreement with those obtained from the mean squared displacements. Note that the diffusive behaviour is respectively valid for q below 1 Å^{-1} at $T = 1390$ K, $q = 1.2$ Å^{-1} at $T = 1080$ K and $q = 1.5$ Å^{-1} at $T = 680$ K.
Concerning the self dynamic structure factor $S_s(q,\omega)$, it shows the classical behaviour observed for liquids: it is very intense and sharp for small q values and becomes broader and weaker as q increases, as shown on the right plot of Figure 4.22. This broadening and damping of the spectra is also observed with increasing temperature: this is directly related to the slowing down of the diffusion processes reflected by the decrease of the self diffusion constant D with decreasing temperatures. As a matter of fact, the width of the Lorentzian spectra of $S_s(q,\omega)$ in the diffusive regime is given by Dq^2 and the energy integral of $S_s(q,\omega)$ is constant and equal to 1. Consequently a decrease of D leads to a damping and broadening of the spectra for a given q value.

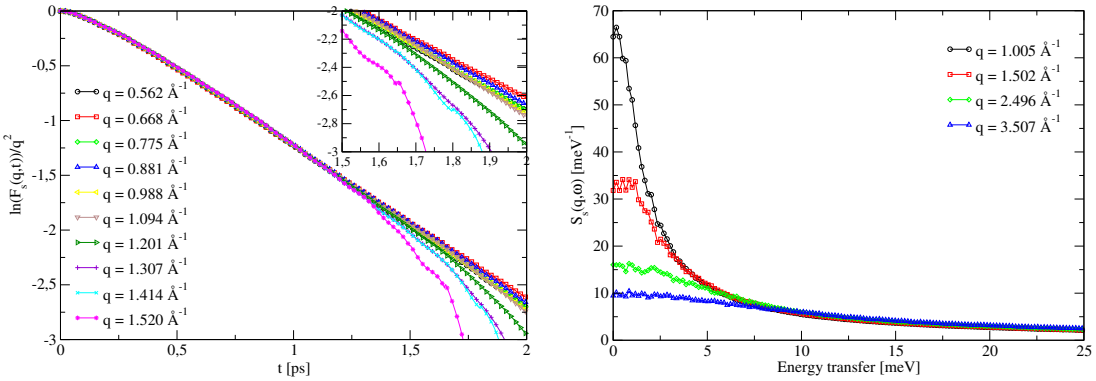

Figure 4.22: Self dynamic properties of l-Ge at $T = 1390$ K: $\ln(F_s(q,t))/q^2$ as a function of t for several q values (left); self dynamic structure factor $S_s(q,\omega)$ for different q values (right).

4.2.2.3 Discussion

This *ab initio* study of liquid germanium allows a better understanding of the structure and dynamics of the system. The accuracy of the simulation scheme can be tested against experimental results and the agreement is generally good. The structural quantities such as the static structure factor or the pair correlation function are very similar to the experimental ones. Hence the structural model provided by the simulation must be quite close to the real typical spatial arrangements of the atoms. Moreover the simulation allows other structural quantities to be computed which give insight into the microscopic features of the structure. For instance the evolution of the coordination number as a function of the size of the coordination sphere and the bond angle distribution are good candidates for the validation of hypotheses on structural arrangements. From these quantities, we determine the local structure in amorphous Ge. Moreover, for the liquid, the coordination number and distribution of bond angles can be consistent with the β-tin hypothesis, although further investigations are necessary to check the validity of this assumption.
On the dynamics side, the *ab initio* simulation gives a sound velocity which is quite close to the measured one. The relaxation times related to the collective diffusion show the expected de Gennes narrowing: this phenomenon is related to the slowing down of the relaxation of the density fluctuations. It occurs for q vectors where $S(q)$ shows intense features. The behaviour of the width of the dynamic structure factor was compared to theoretical models for simple dense fluids and hard-sphere fluids. From this it is obvious that liquid germanium does not behave as a simple dense fluid. However the hard-sphere model tends to give a better representation of the system.

4.3 Neutron scattering experiments on l-Ge

The simulations of liquid germanium give much information about the structure and dynamics of the system. However experimental investigations are necessary in order to check the accuracy of the theoretical study. Consequently we performed two kinds of inelastic neutron scattering experiments on l-Ge. The first one was carried out on the time-of-flight spectrometer FOCUS at the Paul Scherrer Institute in Switzerland, while the second one was planned on a thermal triple-axis spectrometer, but, for reasons of beamtime reduction, was performed on the cold triple-axis

spectrometer 4F1 in Laboratoire Léon Brillouin in CEA Saclay. The first study was dedicated to the investigation of the quasi-elastic behaviour of liquid Ge while the second one, initially planned on a thermal spectrometer, would have given information about the acoustic excitation of the system. Working on two cold neutron spectrometers, both experiments allowed us to get information about the quasi-elastic behaviour of the system since the high sound velocity of the acoustic phonon of l-Ge is not measurable on a cold neutron spectrometer. These investigations were the first quasi-elastic neutron scattering experiments concerning liquid Ge.

4.3.1 Experiment on a time-of-flight spectrometer

This first experiment was performed on the cold time-of-flight spectrometer FOCUS at the Paul Scherrer Institute (PSI, Villigen) in Switzerland.

4.3.1.1 Description of the time-of-flight spectrometer

The general principle of this spectrometer is given in Fig. 4.3.1.1. The basic principle of time

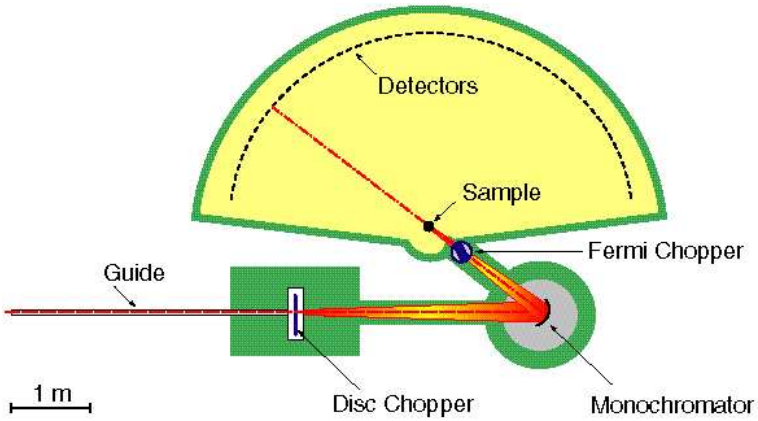

Figure 4.23: General principle of the FOCUS spectrometer

of flight spectrometers is to determine the energy of the scattered neutrons by measuring the time they need to travel from the sample to the detectors. The final energy of neutrons can be deduced from the time of flight since the velocity of neutrons is directly related to their energy. The time scales accessible by this technique vary between 10^{-10} and 10^{-12} s, depending on the energy resolution: if the latter is coarse, only the faster part of these time scales is accessible.

FOCUS [121, 122, 123] is a time and space focusing, time of flight spectrometer for cold neutrons. It is located at the end of a curved guide, which should remove the fast neutrons of the white beam coming from the neutron source: the fastest neutrons have the lowest wavelengths and thus their critical angle is small; using a curved guide, the incidence angle is increased and the rapid neutrons are not reflected. At the end of the curved guide, a vertically converging neutron guide reduces the size of the incoming beam.
In the primary spectrometer, a doubly-curved crystal monochromator consisting of oriented crystals is used to select a specific wave vector $\boldsymbol{k}_i$ depending on the θ angle between the incident beam and the monochromator surface (according to Bragg's law). The monochromatic beam is then pulsed by a Fermi chopper (a set of parallel fast rotating slits).

In order to avoid that the neutrons from pulse n which lose energy in the sample (long flight time between sample and detector) are detected at the same time as the neutrons from the pulse $n+1$ which gain energy in the sample (short flight time), an anti-overlap chopper is placed before the doubly bent monochromator.
Two kinds of curved monochromators, pyrolytic graphite (with a mosaïcity of 0.8°) and mica, are available, which give access to incident wavelengths ranging from 2 Å to 18 Å depending on the order of the reflection used. Both horizontal and vertical curvatures of these monochromators can be tuned in order to focus the beam and optimize the flux at sample position. The θ angle of the monochromator can be varied continuously from 17.5° to 70°.
For incident wavelengths larger than 4 Å, a Be-filter is used together with the first chopper to suppress higher order contamination, that is incident wave vectors corresponding to $m\boldsymbol{k}_i$, m being an integer.
The secondary spectrometer consists of an evacuated sample chamber located at the center of the three spherically arranged banks containing 400 ^{3}He tubes of rectangular shape. The scattering angle ranges from +10° to +130°. The flight path for the neutrons scattered at the sample to the detector bank has a distance of 2.5m. The detector chamber is filled with Argon in order to avoid absorption and scattering from air.
At the exit of the sample, a radial oscillating collimator hides the sample environment (furnace or cryostat) from the detectors: it means that neutrons scattered by the sample environment are not seen by the detectors.
The distances between the neutron guide and the monochromator on the one hand, and between the monochromator and the sample on the other hand are variable in order to operate the spectrometer either in time focusing or in monochromatic focusing mode. Time-focusing in the case of FOCUS is explained in the next paragraph.
At the sample position, space is available for standard sample environments, such as cryostats or furnaces.

Time-focusing

In general, time-focusing increases the data acquisition rates and the energy resolution in a reduced energy range while it degrades the momentum resolution. During the scattering process, neutrons may lose or gain energy, which leads respectively to slower or faster neutrons. This energy transfer to the sample is: $E = E_f - E_i$. All neutrons transferring the same amount of energy may not have the same initial and final energies. The purpose of time-focusing is to detect at the same time all neutrons which transferred the same amount of energy, regardless of their incident or final energies.

In the case of FOCUS, the velocities of the neutrons diffracted by the monochromators depend on the θ angle: when the angle increases, the velocity after diffraction decreases (Bragg's law). Consequently, if we consider the case of elastically scattered neutrons, by scanning the monochromator from high angle to low angle, the Fermi-chopper selects progressively faster neutrons, so that they all reach the detectors at the same time.

Resolution

The resolution function of time-of-flight spectrometers is quite complicated. Unlike triple-axis spectrometers, it is not available from analytical expressions. The resolution function has to be measured ; this is usually done with a vanadium sample, which is an incoherent scatterer.

This measurement is performed in the same experimental conditions as the sample. From this measurement, the energy resolution as a function of $\boldsymbol{q}$ can be deduced for the $\boldsymbol{q}$-range covered by the detectors.
The energy resolution at the sample position depends on the selected incident energy, which means $\frac{\Delta E}{E}$ is a constant. The choice of incident energy therefore determines the energy resolution as well as the accessible range of momentum transfers as depicted in Fig. 2.1.

4.3.1.2 Experimental setup

For the measurement on *l*-Ge, we used a furnace designed to cover temperatures between 500 and 1400 K.
The Ge powder was obtained commercially with a purity of 99.99% in weight. It was inserted in a cylindrical cell made of vitreous silica, under nitrogen atmosphere, in order to reduce oxidation. This cell was sealed under vacuum in order to avoid contamination of dioxygen, which would lead to formation of GeO or GeO_2, at high temperatures. In order to fix the silica cell to the sample stick, it was inserted in a niobium envelope closed at the bottom, the latter envelope being fixed at the bottom of the sample stick.

The measurements were performed at incident wavelengths of 3 Å and 4 Å, with a chopper ratio (between anti-overlap chopper and Fermi-chopper) of 1. We worked at approximately 1260 K and 1400 K, with a sample of approximately 6 mm in diameter, and once melted, the sample cell contained approximately 2 cm of germanium in height.
We made measurements with equal statistics for, on the one hand, the sample and its environment and, on the other hand, the sample environment alone (*i.e.* only the furnace and the empty sample cell with the niobium envelope). We also had to determine the q-dependent resolution function ; this was done with a cylindrical vanadium sample of diameter 10 mm.
The elastic energy resolution at incident wavelength of 3 Å and 4 Å were respectively of the order of 500 μeV and 200 μeV.

4.3.1.3 Results

The raw results of this experiment are shown in Fig. 4.24. Both graphs represent the logarithm of the (time-of-flight,2θ) distribution of events for an incident wavelength $\lambda_i = 3$ Å. The top one depicts the results with the *l*-Ge sample at 1260 K and the bottom one represents the behaviour of the sample holder alone. We notice that the sample environment gives a strong signal compared to the *l*-Ge sample. (Note that the detector at $2\theta = 56°$ was out of order.)
From this raw data, we can already identify some features coming from the sample environment: the sharp peak on the elastic line at $2\theta \approx 80°$ comes from the niobium sheet surrounding the silica cell, it corresponds to a momentum transfer of 2.65 $Å^{-1}$. The two other broad peaks on the elastic line at $2\theta \approx 43°$ and 90° correspond to the diffraction peaks of vitreous silica around 1.5 and 2.9 $Å^{-1}$ [124]. We performed measurement with incident wavelength of 4 Å and increased resolution. However, these data were contaminated by a parasitic peak from the furnace on the right side (Stokes scattering) of the elastic line. This artefact disappeared when decreasing the resolution with incident wavelength of 3 Å. We also observe phonons on the left part (below 1000 μs) of both (t,2θ) maps. We also notice the increased intensity of the quasi-elastic signal on both sides of the elastic line on the data corresponding to the measurement of *l*-Ge (top). This is the sign of quasi-elastic contributions from liquid Ge.

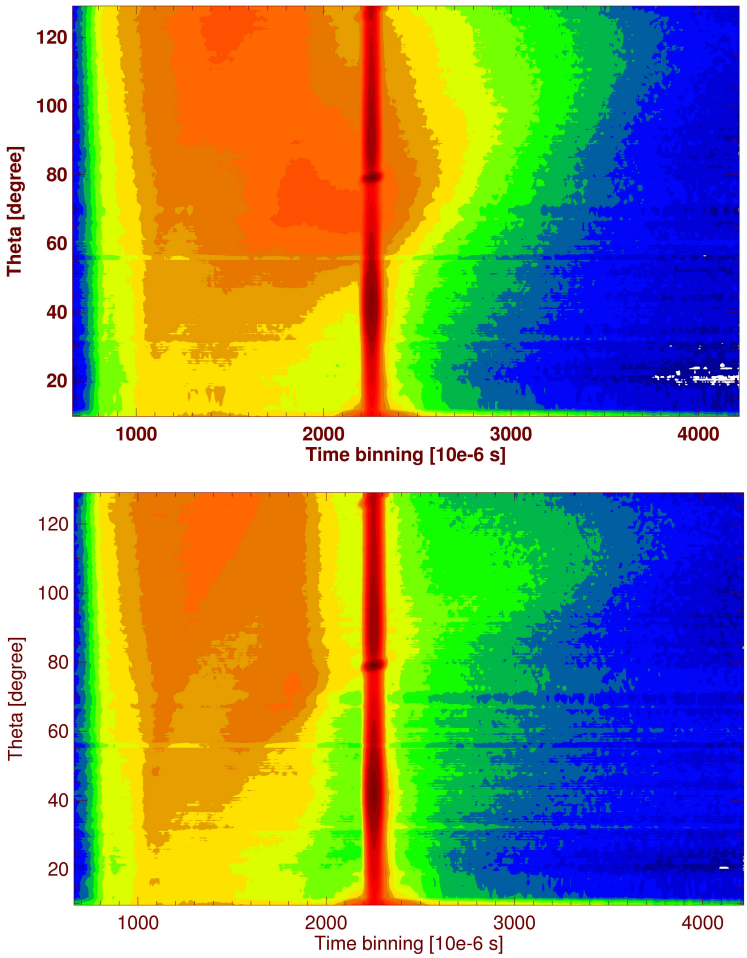

Figure 4.24: *l*-Ge: raw data from the time-of-flight measurement at $\lambda_i = 3$ Å and T = 1260 K: top: liquid germanium in sample holder ; bottom: sample holder only (blue corresponds to low intensity, red to high intensity).

Data treatment was performed with NATHAN, software dedicated to the treatment of time-of-flight data and developed at PSI. It is able to perform corrections for resolution, detector efficiency and sample holder. It can perform time to energy conversions and apply detector grouping as desired by the user. The dynamic structure factor of l-Ge was computed from the measured distributions of scattered angles 2θ and time-of-flight t, which are shown in Fig. 4.24.

According to the dynamic range of FOCUS, the acoustic phonon of l-Ge was not accessible, due to the corresponding sound velocity $c_s = 2682$ m/s [99] which is too high. We consequently measured the quasi-elastic behaviour of l-Ge. The values of momentum transfer accessible at the elastic line are comprised between 0.35 and 3.8 Å^{-1} at $\lambda_i = 3$ Å. Higher momentum transfers were measured, however the spectra did not include the elastic peak and hence could not be fitted properly. This is also a consequence of the dynamic range of the instrument: for high q values ($q/k_i > 1.5$ according to Fig. 2.1), the upper limit of the accessible energy transfers is negative and the instrument is not likely to measure either the elastic line or the Stokes part of the signal.

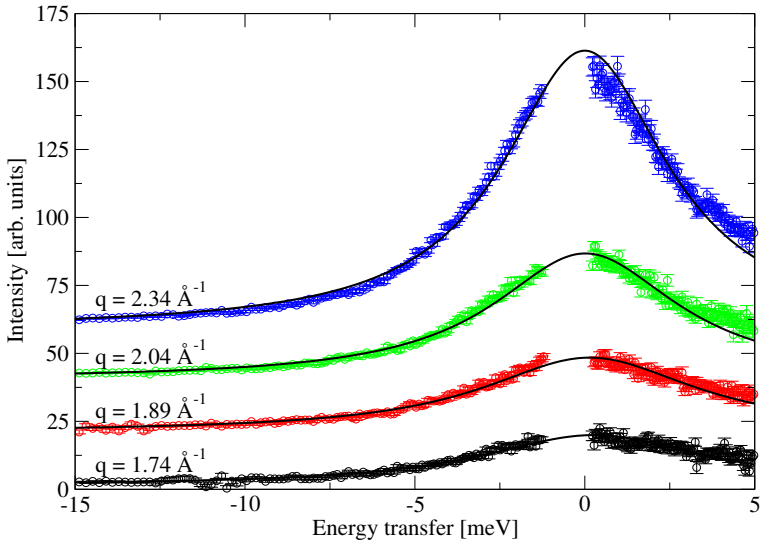

Figure 4.25: l-Ge: energy spectra at several Q values ($\lambda_i = 3$ Å; T = 1260K; time-of-flight measurement); spectra are shifted by 20 counts; solid lines show the lorentzians

Several spectra of the dynamic structure factor are shown in Fig. 4.25, for different q values. These spectra are fitted with lorentzians, with widths describing the evolution of the time scale of the correlated diffusive motions in the liquid. The data around the elastic line were discarded: they showed strong oscillations due to imperfect subtraction of empty cell. This must come from a slight misalignment between the measurements of the sample on the one hand and of the sample cell on the other hand.
Note that the energy spectra is much more noisy on the energy gain side: the transformation from time to energy leads to apparent statistical noise due to energy binning. The accessible energy transfers are also asymmetric in gain and loss of energy: the incident kinetic energy of neutrons determines the maximum amount of energy they can lose when interacting with the sample. It thus sets a threshold to the maximum energy gain of the sample.

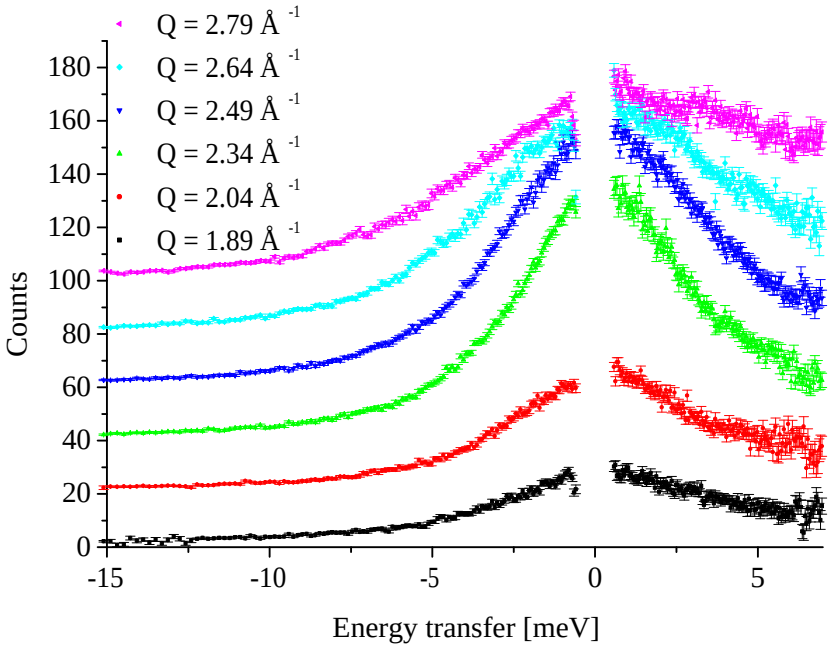

Figure 4.26: *l*-Ge: energy spectra at several Q values (λ_i = 3 Å; T = 1260K; time-of-flight measurement); spectra are shifted by 20 counts

In Fig. 4.26, we represent several energy spectra for momentum transfers around the first sharp peak in the static structure factor, that is $q_m \approx 2.5$ Å^{-1}. We notice that the spectra for $q = 2.49$ Å^{-1} looks sharper and more intense than the others.
This feature is confirmed when fitting each spectra with a Lorentzian, and extracting the width of the latter. The results are presented in Fig. 4.27. As noticed before, the width of the quasi-elastic peak is much thinner around the first sharp peak of $S(q)$. This is associated with the *de Gennes narrowing* process explained in section 1.2.2.2. Narrowing of the quasi-elastic peak is also observed between 3 and 3.25 Å^{-1} which may be associated with the shoulder on the high q side of the static structure factor.

4.3.2 Experiment on a triple-axis spectrometer

This second experiment was performed on the cold triple-axis spectrometer (TAS) 4F1 at the Laboratoire Léon Brillouin (LLB) in CEA-Saclay.

4.3.2.1 Description of the triple-axis spectrometer

Since the first triple-axis neutron spectrometer was designed and installed for the purposes of research by Brockhouse (1958-1962), [Nobel prize 1994], the design of the TAS has changed very little. The general principle of triple-axis spectrometers is depicted in Fig. 4.28.
The primary purpose of triple-axis spectrometers is to study the collective excitations of the atoms or that of their magnetic moments in single crystals. The flexibility of the TAS machine

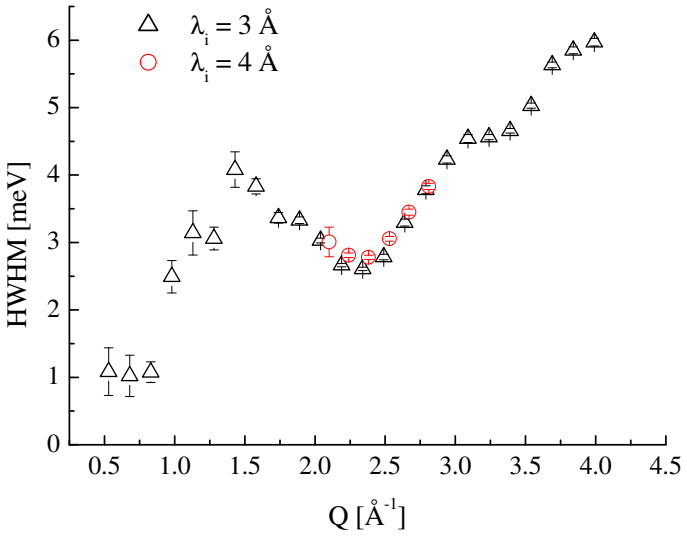

Figure 4.27: *l*-Ge: half-width at half-maximum of the lorentzians as a function of Q (λ_i = 3 Å; T = 1260K; time-of-flight measurement)

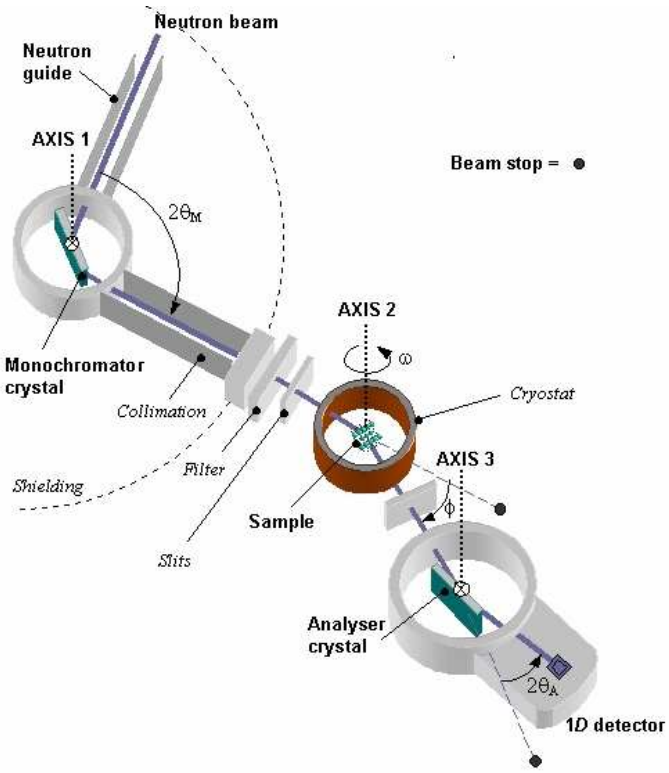

Figure 4.28: General principle of a triple-axis spectrometer [125]

means that it can be used for all kinds of neutron scattering measurements (diffraction, quasi-elastic neutron scattering) . The basic principle of this kind of spectrometers is to select both energy transfer and momentum transfer exchanged between neutrons and sample, thanks to the use of the three axes between monochromator, sample and analyser.

4F1 is a triple-axis spectrometer for cold neutrons [126]. It is placed close to the Orphée reactor at LLB, thus taking benefit of most of the neutron flux delivered. 4F1 and 4F2 are twin triple-axis spectrometers, which receive neutrons from a liquid-hydrogen cold source. They are designed for measuring collective excitations with low energy transfers (*i.e.* $\leq$4 meV).
As they come out from the guide or the beam tube, neutrons have a broad distribution of energies. A specific narrow range of wave vectors around $\boldsymbol{k}_i$ is selected by a monochromator, by means of Bragg diffraction. In the case of 4F1, the incident wave vector is determined by two pyrolytic graphite monochromators in "dog-leg" configuration. This double monochromator can be translated and rotated in order to select the requested incident energy. These may provide neutron wavelengths between 2 and 6 Å (2.7 Å$^{-1} \geq \boldsymbol{k}_i \geq$ 1.05 Å^{-1}). At the exit of the monochromators, the contamination from higher orders of diffraction can be removed by a graphite filter.
The beam then hits the sample. For single crystals, the crystalline direction which is probed depends on the orientation of the crystal on the sample table, while for a liquid (or any amorphous sample), excitations only depend on the length of the scattering vector $\boldsymbol{q}$. Usually, the sample scatters neutrons in any directions, and may exchange energy with neutrons (inelastic scattering with loss or gain of energy at the sample) or not (elastic scattering).
The analyser is positioned to select a particular scattering direction $\boldsymbol{k}_f$ and it is rotated to scan the energy of the incoming neutrons. In the case of 4F1, the analyser is also made of pyrolytic graphite and it is used in horizontal focusing geometry. A detector finally counts the neutrons which emerge from the analyser with the desired energy and scattering angle.
The distances from the sample to the monochromator and from the sample to the analyser can be adjusted in order to accommodate various sample environments such as cryostats and furnaces.

Resolution

When interpreting results of inelastic scattering experiments, one of the main challenges is to take into account instrumental resolution effects. In the case of triple-axis spectrometry, the quantity of interest is the dynamic structure factor $S(\boldsymbol{q},\omega)$ of the system. However, one actually measures the 4-dimensional convolution of $S(\boldsymbol{q},\omega)$ with the instrumental resolution function $R(\boldsymbol{q},\omega)$.
Like the structure factor, $R(\boldsymbol{q},\omega)$ is a 4-dimensional function: 3 dimensions for reciprocal space ($\boldsymbol{q}$) and one dimension for energy transfer ($\hbar\omega$). Accurate analytical expressions of the resolution function exist, however it is often approximated by a 4-dimensional Gaussian function.
As stated before, the resolution may change considerably, depending on the wave vector and energy transfer ($\boldsymbol{q}$,$\hbar\omega$) where the measurement is performed. If a constant $\boldsymbol{q}$ scan is performed, one effectively measures a weighted integral of the structure factor over the corresponding resolution ellipse. From one point to the next in the scan in energy transfer, the resolution ellipsoid twists and stretches, inducing distortions in the measured spectra.

Configurations of the instrument

We may distinguish several kinds of measurements with triple-axis spectrometers. First of all, scans may be performed with either constant momentum transfer $\boldsymbol{q}$ or constant energy transfer $\hbar\omega$, depending on the shape of the expected spectra and the resolution function. The most convenient type of scan is the one in which the spectrum is less affected by the convolution with the resolution function. On the other hand , experiments may be performed either with constant $\boldsymbol{k}_i$ or constant $\boldsymbol{k}_f$ vectors. These different kinds of experimental setups involve several types of corrections to the measured quantities such as the norm of the resolution function (which may vary or not depending if we are in constant $\boldsymbol{q}$ or constant $\hbar\omega$ mode) or the intensity of the beam (depending on the constant $\boldsymbol{k}_i$ or $\boldsymbol{k}_f$ mode).

Consequently, triple-axis spectrometers enable the energy transfer between neutrons and sample as a function of scattering angle to be determined, which is related to momentum transfer. It is a very flexible kind of spectrometer, since it offers several modes of measurement and is particularly efficient for well-localized excitations in ($\boldsymbol{q}$,$\hbar\omega$) space.

4.3.2.2 Experimental setup

As in the time-of-flight experiment, we used a furnace which can reach temperatures of the order of 2000 K.
The sample cell was identical to the one used on FOCUS, although we inserted pieces of solid germanium in the sample cell, instead of powder. This prevents the significant reduction of volume due to the low packing factor of the powder. After melting, the height of the sample was between 4 and 5 cm in height. We performed the same measurements on two cells of respective diameters 6 and 10 mm.
The measurements were also performed on the empty sample cell for further data treatment. This is not usual on triple-axis spectrometers, however it was necessary in our case, since the signal from the sample cell and the sample are almost of the same intensity, as shown by the time-of-flight measurements.
The final fixed wave vector was $k_f = 2.662$ Å^{-1}, corresponding to both a minimum of the transmission of the higher orders and a maximum of the transmission of the first order by the graphite filter. The scans were performed with constant $\boldsymbol{q}$ vectors.

4.3.2.3 Results

Scans were performed between $q = 0.3$ Å^{-1} and $q = 3.9$ Å^{-1}. For q values smaller than 1.8 Å^{-1}, the quasi-elastic peak is still not well separated from the phonon. Consequently, the width of the quasi-elastic peak can be properly extracted only for $q \geq 1.8$ Å^{-1}.
The data were processed with a program developed at LLB and dedicated to the treatment of triple-axis spectrometry data. It gives access to several kinds of fitting curves; in our case, we were especially interested in fitting our data with both lorentzians and gaussians. In this code, the calculation of the resolution function corresponding to the instrumental configuration is included. The signal from the sample itself was obtained by subtraction of the signal of the empty cell from the one of the sample with its sample holder. Subsequently, we fitted the data for each q scan.

Since we expected a quasi-elastic behaviour of the liquid, we tried to perform the fits with a Lorentzian. However, as shown in Figure 4.29, a single Lorentzian was not likely to fit the data

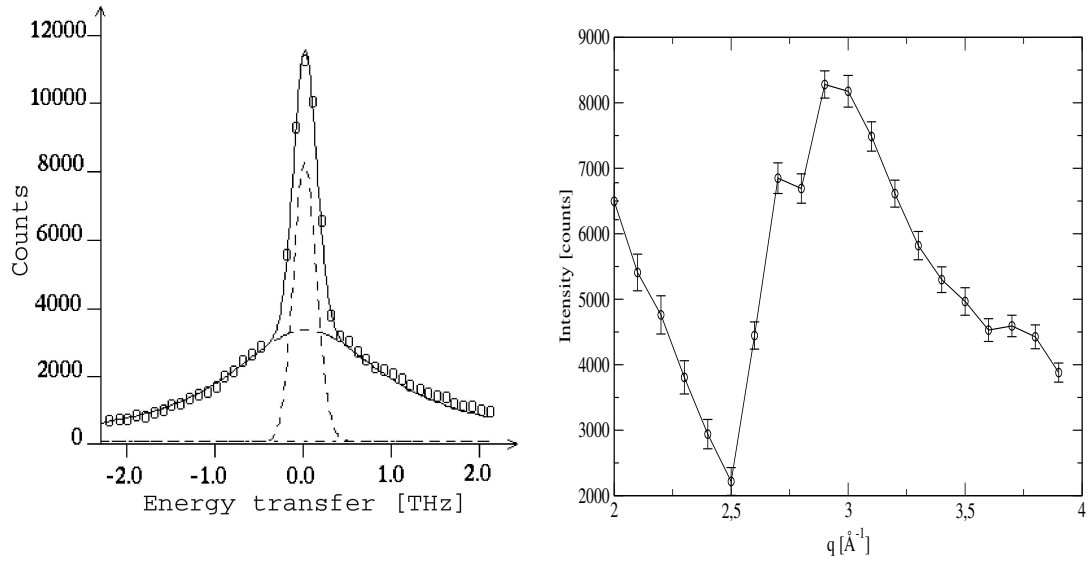

Figure 4.29: Left: scan at $q = 1.9$ Å^{-1}: intensity [counts] against energy transfer [THz]. Experimental data (dots), Lorentzian and gaussian (dashed lines), fitting curve (solid line). Right: intensity of the gaussian component of the fit as a function of q.

properly. In Figure 4.29, the data were fitted by the sum of a gaussian (the peaked dashed line) and a Lorentzian (the broad dashed line). However the fit performed with a gaussian would be the sign of persistent structural features in the sample and one knows that a liquid does not give elastic signal due to structural arrangements. This gaussian, which could be replaced by a Lorentzian without much consequence on the quality of the fit, could consequently be associated with relaxation slower than the time scale available with the resolution of this experiment. Since we do not observe any features in the simulated intermediate scattering function for times bigger than 8 ps, the unexpected intense peak does not come from the existence of relaxation times larger than those available from the experimental resolution. The determination of both intensity and width of the gaussian component of the fit lead us to the conclusion that it comes from the subtraction of the sample holder: the intensity of the gaussian follows the static structure factor of SiO_2 (see Fig. 4.29) and its width is almost constant as a function of q. Moreover subtracting 2.3 times the empty sample holder from the signal of the sample and sample cell enables this peak to be avoided at all q values. We also notice the same kind of artefact as on the time-of-flight experiment: the measurement of the empty sample holder is slightly misaligned leading to a shift in energy of the elastic peak (see Fig. 4.30). This misalignment may also lead to the underestimated intensity coming from the sample holder. Thanks to the mosaicity of the analyser, we detect the elastic signal from the sample cell in spite of the slight misalignment. However the detected signal is shifted from the elastic line and is not as intense as if it were correctly aligned. As a matter of fact the rocking curve of the analyser shows that beside the selected final energy E_f, other energies close to E_f are selected due to the mosaicity of the analyser crystal. However these energies close to E_f are transmitted with less intensity than E_f. The problem due to the subtraction of the empty cell is not relevant for the time-of-flight experiment since scattered neutrons are detected without any analysis of their final energy unlike in a triple-axis experiment.

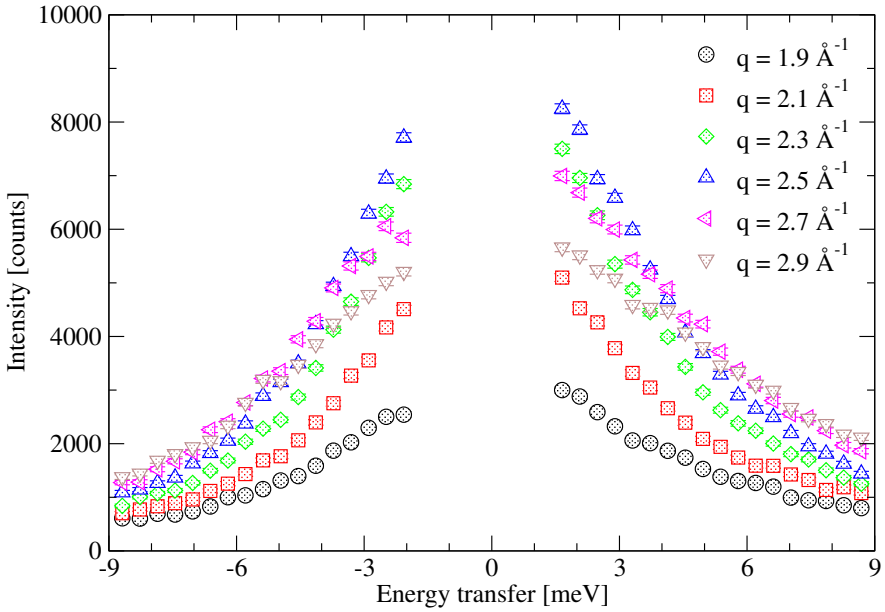

Figure 4.30: Measured spectra for different q values around the position of the first maximum in $S(q)$.

After appropriate subtraction of the signal from the sample holder, we gain insight into the evolution of the intensity and width of the quasi-elastic signal for different q values. This is shown in Figure 4.30 for q values around the first maximum in the static structure factor at $q = 2.5$ Å^{-1}. We notice that the intensity increases as q approaches 2.5 Å $^{-1}$ together with a narrowing of the width of the spectra.

Now let us try and understand the evolution of the width and intensity of the signal as a function of q (see Fig. 4.31). The width of the quasi-elastic contribution strongly depends on q, with a well-defined narrowing around $q_m = 2.5$ Å^{-1} and a second one around 3 Å^{-1}, however less pronounced than the first one. As stated in Section 4.3.1.3, this is related to the phenomenon of *de Gennes narrowing*. Concerning the intensity, its overall shape corresponds to the static structure factor.

We now compare the widths of the signal as a function of the momentum transfer for two samples: the first one is 6 mm in diameter while the second is 10 mm. This is shown in Fig. 4.32. We would expect a difference of width between the two samples due to multiple scattering effects more important in the larger sample. However, the difference between the two lies within the energy resolution and the uncertainty of the fit. Consequently the importance of multiple scattering for the size of our samples is still negligible.

4.3.3 Comparison of the experiments and simulations

We notice some discrepancies when comparing the experimental results from FOCUS and 4F1 (see Fig. 4.33). The evolutions of the widths follow the same kind of shape, however, the intensities are shifted, especially at high q values where the widths measured on the triple-axis spectrometer are much wider. When processing the data from the latter experiment, it was

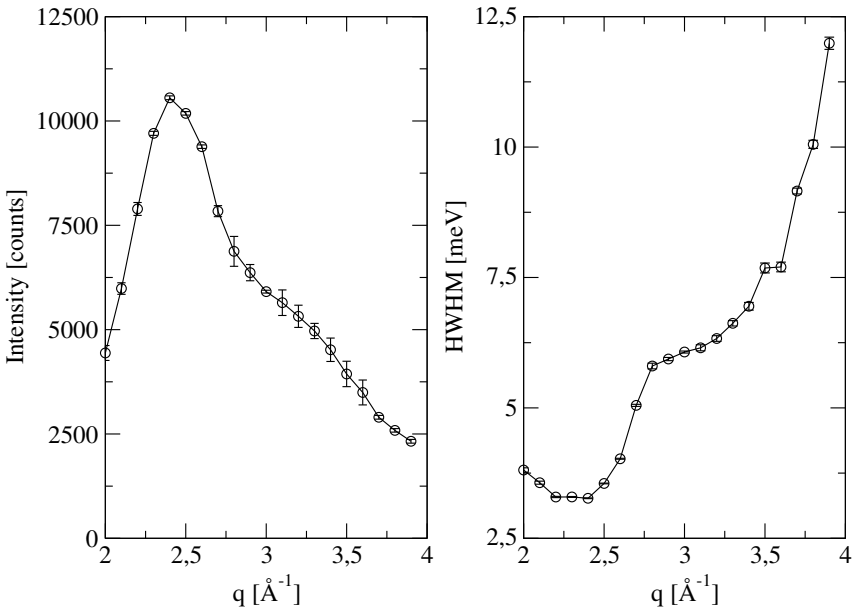

Figure 4.31: *l*-Ge: result of the fit using a Lorentzian as a function of q (diameter of the sample: 10 mm): left: intensity; right: width.

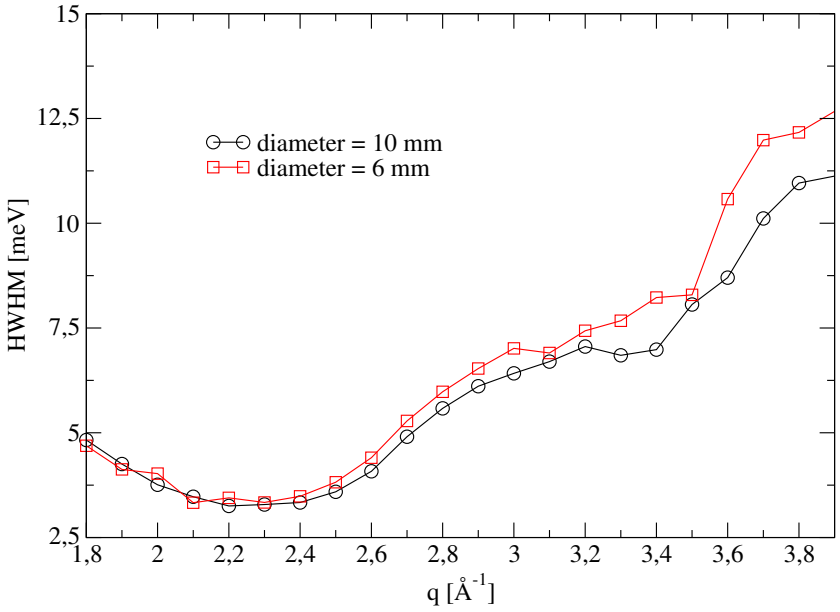

Figure 4.32: *l*-Ge: comparison of the width of the Lorentzian signal for two different diameters of the sample.

actually quite difficult to evaluate the intensity of the background, since the range of accessible energy transfers is not as wide as in TOF experiments. Consequently, it was quite difficult to discriminate the background from the tails of the Lorentzian. On the other hand, at high q values, the range of energy transfer accessible on the time-of-flight spectrometer is very asymmetric in gain and loss of energy. This yields uncertainties in the width of the fitted spectra. The features common to the two experiments are the deep minimum at the position of the first sharp peak in $S(q)$ and the plateau between 2.8 Å^{-1} and 3.2 Å^{-1}.

The theory of liquids gives a relation between the spectral width of the signal and the static structure factor of the system as explained in Chapter 1:

$$\langle \omega_q^2 \rangle = \frac{k_B T}{m S(q)} q^2 \tag{4.3}$$

where k_B is the Boltzmann constant, T is the temperature, m is the mass of an atom of the system. This prediction of the spectral width is valid for dense monatomic liquids. The theoretical prediction and experimental results are compared in Fig. 4.33. The theoretical values for the widths are computed using $S(q)$ from the *ab initio* simulations. Other theoretical values are calculated using the scheme proposed by de Schepper for the model of hard spheres and introduced in equation 4.1. It is referred to as ω_h in Fig. 4.33. This quantity is computed using the self-diffusion constant D from the *ab initio* simulation.
From the comparison of simulations and experiments, we notice that the width of the spectra is clearly overestimated in the simulation. On the other hand, the plateau between 2.8 Å^{-1} and 3.3 Å^{-1} is much more pronounced in the experiment at high temperature than in the simulation. From the theory, we also realize that the experimental data is best described by the hard-sphere model at 680 K although it does not give a very accurate description of the experimental data. Finally we obtain an overall good agreement between experimental and simulated spectra. Even if the magnitude of the width is not very well reproduced (which may come from the rather poor statistics for computing the dynamic structure factor), the evolution of the width as a function of q is well accounted for in the simulation.

4.4 Coupling instrument and sample simulations

As said before, we can compute the dynamic structure factor of *l*-Ge from the trajectories generated by the molecular dynamics simulation. Using the scheme presented in chapter 3, we perform simulations of a neutron scattering experiment using the time-of-flight spectrometer FOCUS and a sample of *l*-Ge.

The simulation of FOCUS was developed by U. Filges from PSI, Switzerland. The virtual instrument consists in a number of components. The first one is a cold source followed by five guide sections one of which is curved in order to remove the faster neutrons. The last guide section is a focusing one, with an entrance section larger than the exit. The beam then goes through a chopper which defines the neutron pulses. After that, the beam crosses three vacuum tubes modelled as slits in the simulation. The next step consists of selecting the desired wavelength thanks to a crystal monochromator with horizontal and vertical focusing. Then time-focusing is achieved with a Fermi chopper and the neutrons arrive at the sample before being detected at a distance of 2.5 m from the sample. The input parameters of the simulation are the desired wavelength and the ratio between disc and Fermi choppers. The distribution

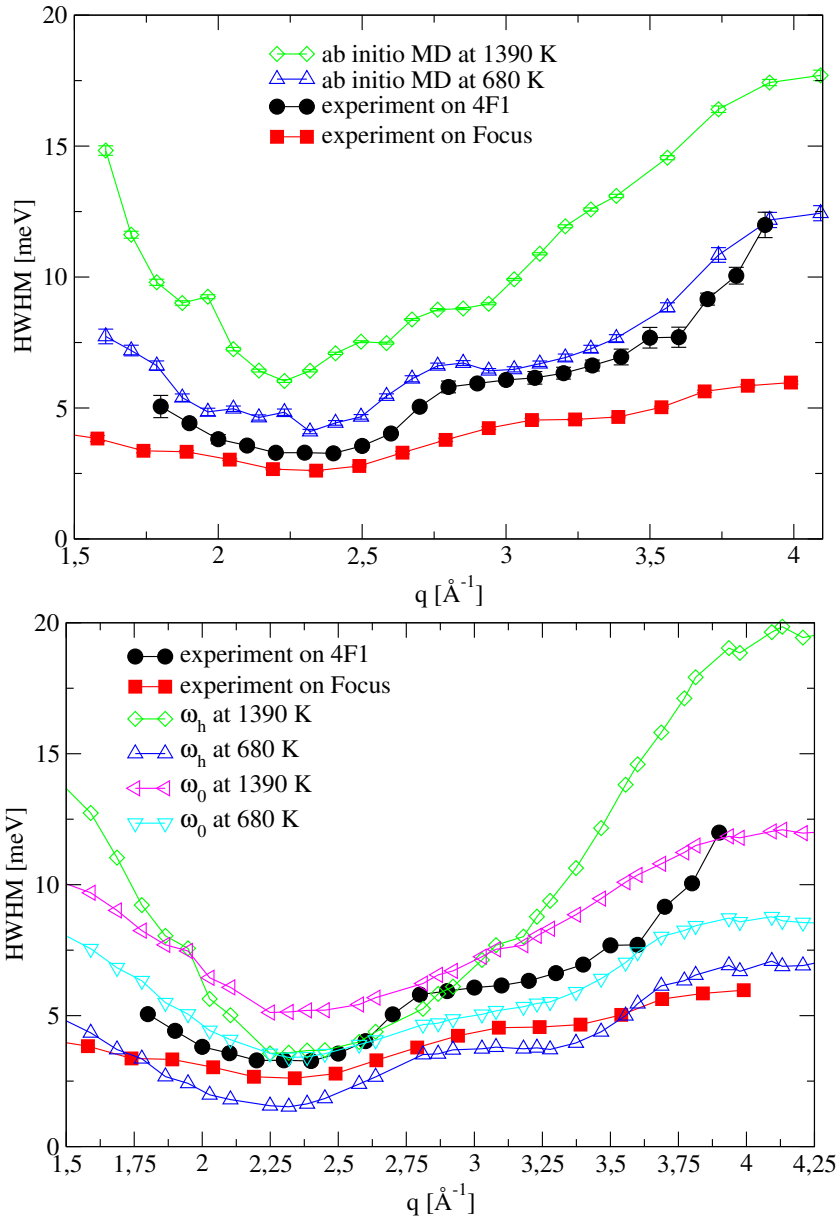

Figure 4.33: Comparison of experiment, simulation and theory: evolution of the HWHM as a function of q. Top: experiment and simulation; bottom: experiment and theory.

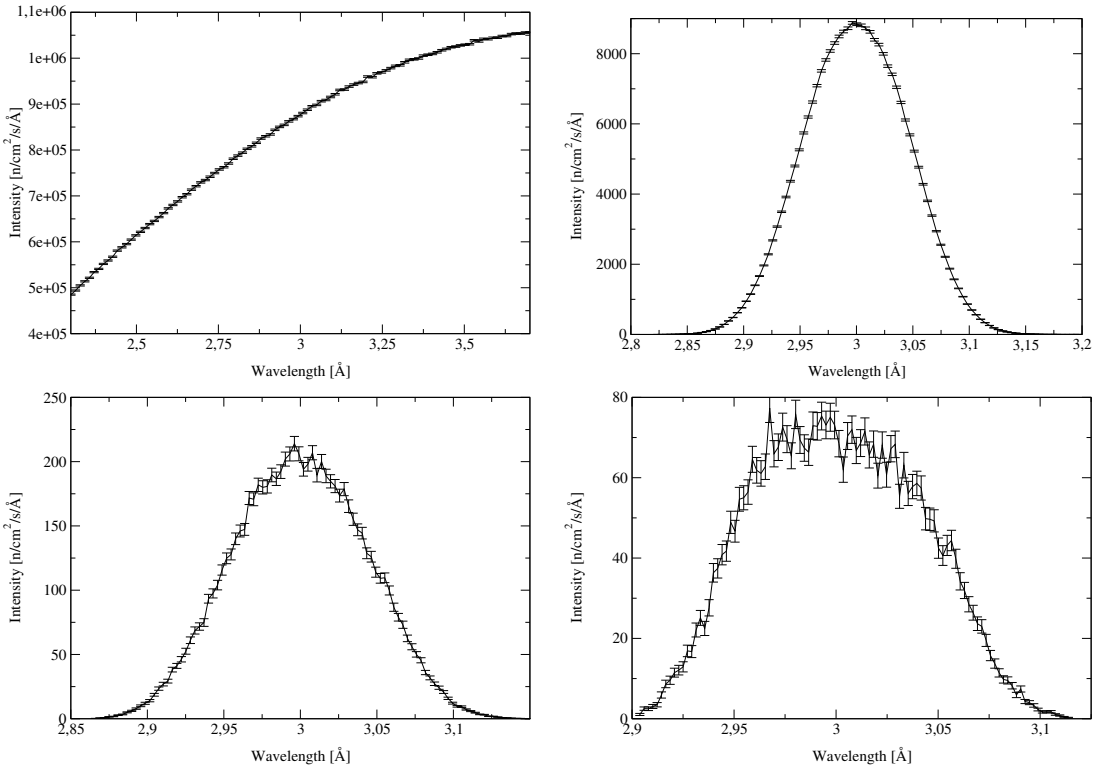

Figure 4.34: Distribution of the wavelengths at different places in the instrument. Top left: after the guide; top right: after the monochromator; bottom left: after the Fermi chopper; bottom right: at sample position.

of the wavelengths is shown in Figure 4.34 at several places in the instrument. The main effect comes from the monochromator which clearly defines the desired wavelength of 3 Å. Note that the distribution of wavelengths at the exit of the guide is already quite narrow thanks to importance sampling: only the range of wavelengths of neutrons that are likely to go further than the monochromator are emitted by the source.
The simulation of the complete neutron scattering experiment dealing with *l*-Ge on the FOCUS instrument is done using the dynamic structure factor coming from the *ab initio* MD simulation at 1390 K. We have previously mentioned (section 4.2.2.2) two kinds of $S(q,\omega)$: the raw one coming directly from the Fourier transform of the intermediate scattering function and the smooth one derived from the raw one by convolution with a gaussian. The comparison of the results of the simulations performed with the raw or the smooth dynamic structure factor are shown in Figure 4.35. We do not notice any strong difference between the two curves in the (q,ω) range accessible with FOCUS. Thus a reasonable smoothing of the input dynamic structure factor may not have any influence when dealing with the simulation of a quasi-elastic signal. We can use the unsmoothed $S(q,\omega)$ because the instrument simulation adds a resolution functions. If the smoothing function has a width comparable to the resolution function then we may get a difference.

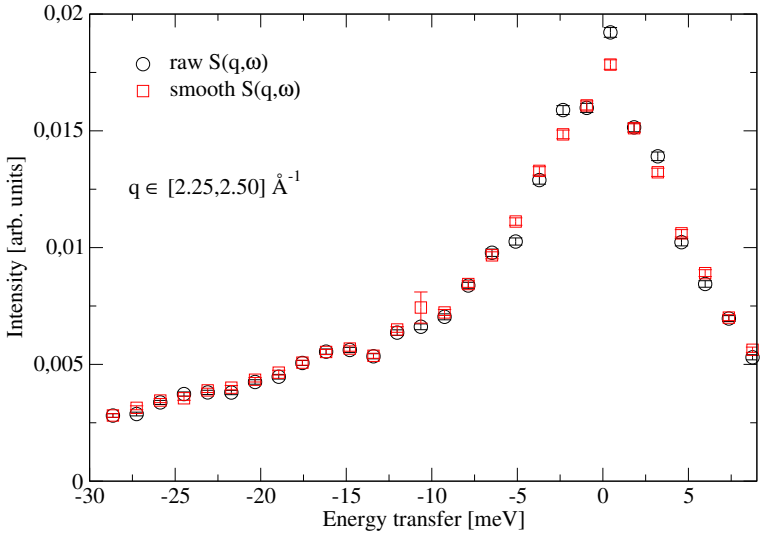

Figure 4.35: Comparison of the energy distributions computed from the raw and smoothed $S(q,\omega)$ integrated between $q = 2.25$ Å^{-1} and 2.5 Å^{-1}.

From such simulations we can get information about the relative amount of multiple scattering in the detected signal. This quantity actually depends on the size of the sample as seen by the neutron beam. We have performed tests on the influence of the size and shape of the sample of *l*-Ge in two main cases. The first one deals with a cylindrical sample and the corresponding results are shown in Figure 4.36. On the left, the intensity of the different orders up to the third one are presented together with the total detected intensity. On the right, the ratio of the different orders with respect to the total signal are shown. The second test deals with a box-shaped sample and the results are shown in Figure 4.37.
The overall behaviour is quite similar to that shown in section 3.2.2.2. However the ratio of 10% of multiple scattering in the scattered signal is reached for a radius (cylindrical sample) or

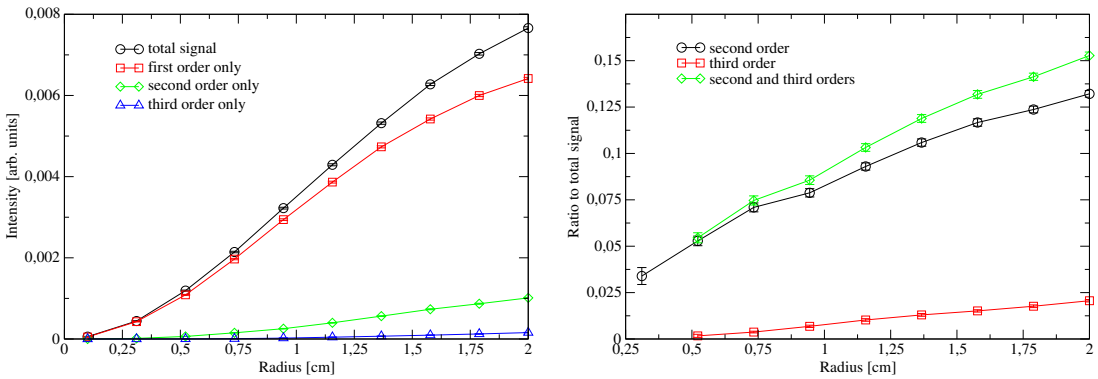

Figure 4.36: Simulation of a TOF experiment on *l*-Ge (cylindrical sample): influence of the radius of the sample on the orders of scattering. The height of the sample is 5 cm. Left: respective intensities of the different orders. Right: ratio of the different orders to the total detected signal.

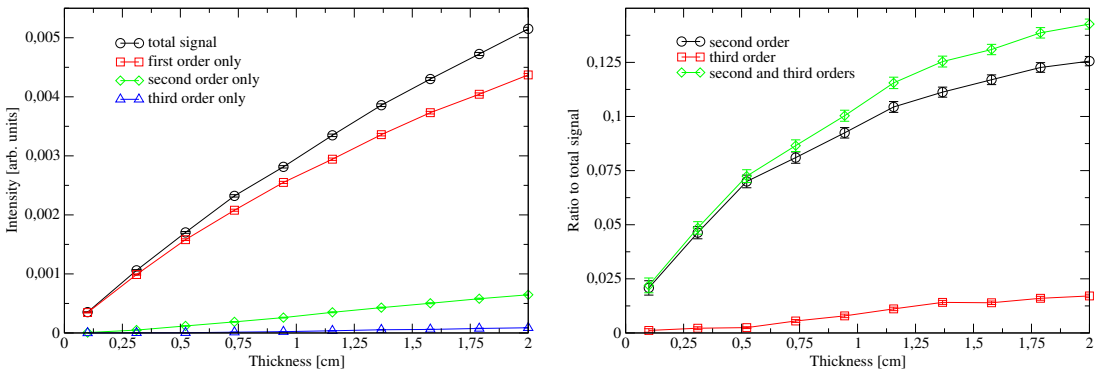

Figure 4.37: Simulation of a TOF experiment on *l*-Ge (box-shaped sample): influence of the thickness of the sample on the orders of scattering. The surface of the sample perpendicular to the beam is 5*5 cm^2. Left: respective intensities of the different orders. Right: ratio of the different orders to the total detected signal.

a thickness (box-shaped sample) much lower than for *l*-Rb. This is consistent with the fact that the ratio $\sigma_{abs}/\sigma_{scatt}$ is much higher for *l*-Ge (0.256) than for *l*-Rb (0.056). From this simulation, we can estimate the global contribution of multiple scattering to be around 6% in our experiment with a cylindrical sample of diameter 10 mm.

Figure 4.38 shows the accessible dynamic range for an incident wavelength of 3 Å. The figure represents the distribution of momentum transfers as a function of energy transfers at the detector. These quantities are directly provided by the simulation. Note that another restriction originates from the calculation of the dynamic structure factor from the molecular dynamics simulation: it gives the low q limit related to the size of the simulation box. In the present case, $S(q,\omega)$ is available for q ranging from 0.56 Å^{-1} to 4.1 Å^{-1}; the energy transfers available are not a limiting factor. The excess of intensity around 2.5 Å^{-1} corresponds to the first sharp peak in $S(q)$.

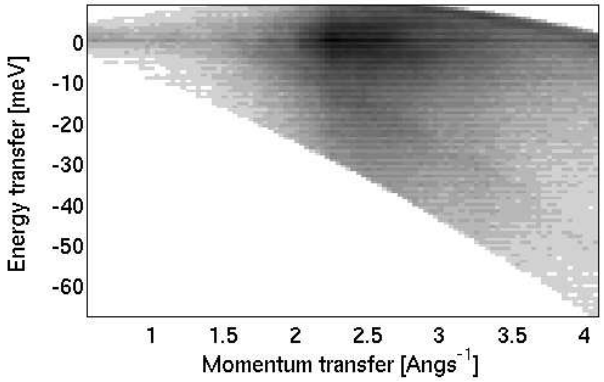

Figure 4.38: Dynamic range accessible in the simulation of FOCUS. (The q range is limited by the range of the computed dynamic structure factor and first order scattering.)

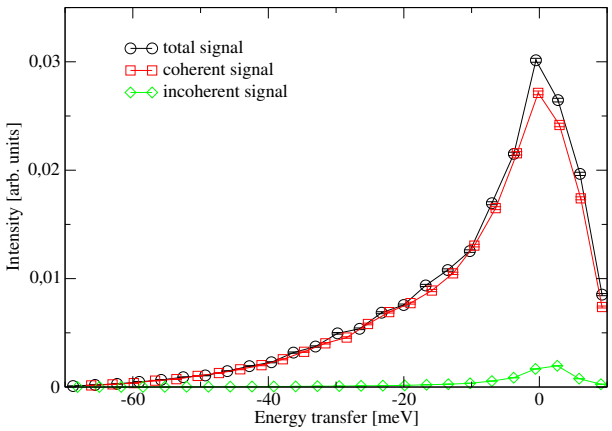

Figure 4.39: Distribution of coherent and incoherent signal integrated over all available q values ($E_i = 9.1$ meV).

The respective contributions of the coherent and incoherent signals are shown in Figure 4.39. In this plot, all momentum transfers are accounted for, only the dependence on energy transfer is shown. We notice that the contribution of the coherent signal is much broader than that of the incoherent one. The asymmetry originates from the energy conservation law: the incident energy is around 9.1 meV. Consequently the neutrons cannot loose more energy than their incident kinetic energy and the energy transfer to the sample cannot exceed the value of 9.1 meV. Note that the last bin (close to 9.1 meV) is erroneous because it corresponds to values of the energy transfer ranging from 9 to 10.25 meV. Hence this bin collects far fewer neutrons than expected from the symmetry of the quasi-elastic peak.

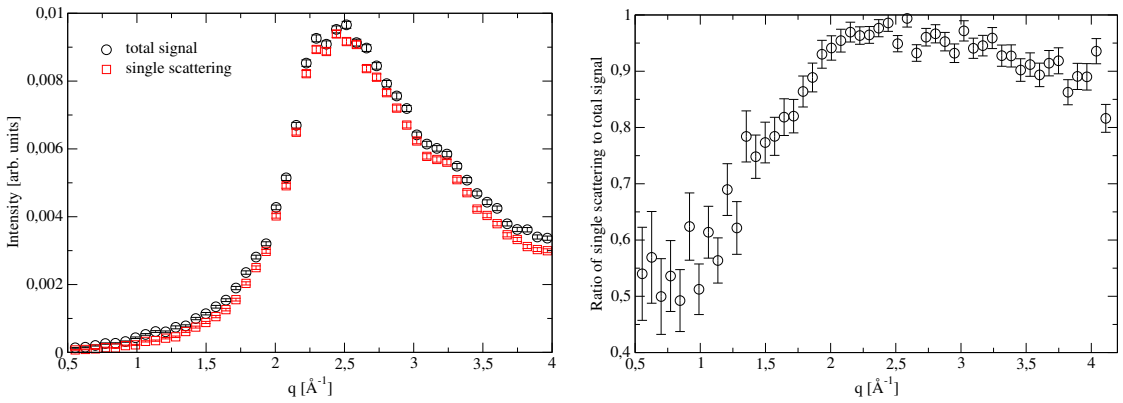

Figure 4.40: Single scattering versus total signal as a function of the momentum transfer q.

Also the q dependence of the amount of multiple scattering can be deduced from the simulation. In the latter, we use a momentum transfer sensitive detector and we distinguish the first order of scattering from the total signal. The intensity of the first order of scattering and of the total signal are plotted in Figure 4.40 as a function of q. The calculation of the ratio of single scattering to total signal is also shown on the right plot. We notice that the ratio of single scattering follows the evolution of $S(q)$ as already stated by Mildner and co-workers [65]: the relative importance of single scattering is the highest around the position of the first sharp peak in $S(q)$. In fact scattering mainly occurs for q values around the position of the first peak in the static structure factor. In the case of l-Ge, when the momentum transfer q_1 associated with the first scattering event occurs around 2.5 Å^{-1}, the next scattering event (if it occurs) adds a second momentum transfer q_2 to q_1 and the total momentum transfer is different from 2.5 Å^{-1}; this multiple scattering event has a total momentum transfer different from 2.5 Å^{-1}. The fraction of multiple scattering is thus lower for q values around the intense features in the static structure factor. Consequently when multiple scattering becomes important in the signal, this property tends to blur the minima in the static structure factor.

From this simulation, we also gain insight into the $\hbar\omega$ dependence of multiple scattering. Figure 4.41 shows for different q ranges the spectra generated either with single scattering only or with total scattering accounted for. For each q range, the single scattering is slightly less intense than the total signal for all $\hbar\omega$ values as expected. The calculation of the ratio of single scattering to total signal as a function of $\hbar\omega$ does not show a clear trend, unlike the q dependence. Consequently, the fraction of multiple scattering does not depend on the energy transfer between

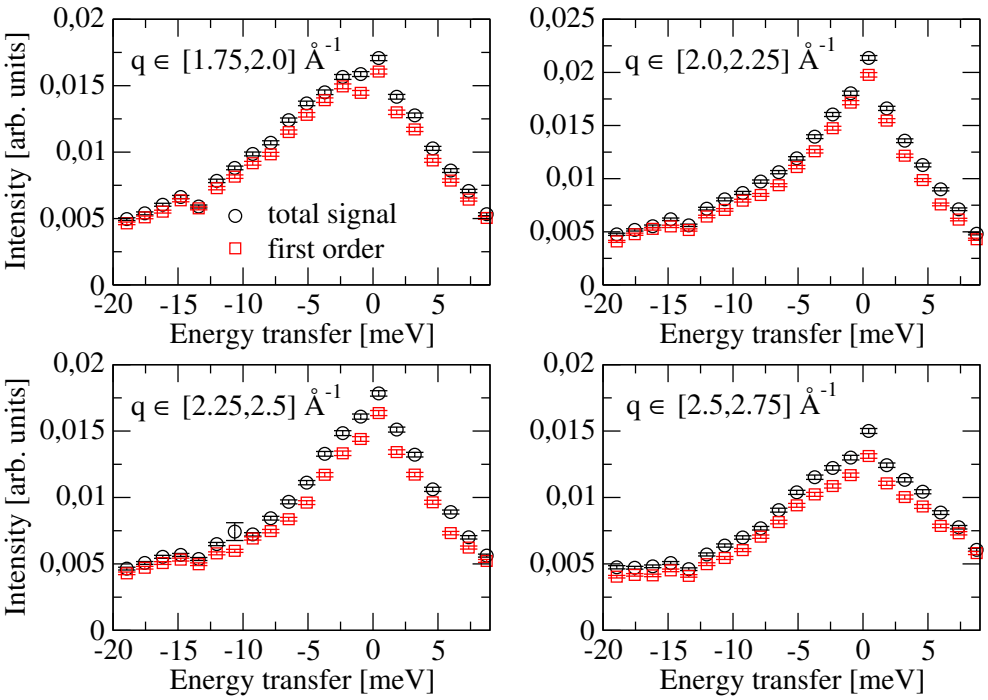

Figure 4.41: Comparison of single scattering to total signal as a function of $\hbar\omega$ for different q ranges.

the neutrons and the sample. However multiple scattering gives rise to a substantial increase of width and intensity of the signal compared to the signal obtained from single scattering only as seen in Fig. 4.41. This comparison is possible irrespective of instrument effects since both simulations (with multiple scattering or single scattering only) are performed in the same configurations.

In Figure 4.42, we compare the simulated spectra with the input dynamic structure factor for different ranges of q values. For this purpose, the q range of the simulation was successively reduced to the different q ranges shown here. Concerning the input $S(q,\omega)$, it was averaged over the different $[q_0, q_0 + 0.25\ \text{Å}^{-1}]$ ranges for the comparison. For the two lower intervals, we notice a decrease in intensity for large negative energy transfers. This comes from the limit of the accessible dynamic range which is between -20 meV and -30 meV for q values between 1.75 Å^{-1} and 2.25 Å^{-1}. This leads to a lowered and even null intensity in this range of energy transfers. Note also that the spectra are not symmetric even if they are centred on the elastic line. This must come from the resolution function since we have shown in Fig. 4.41 that multiple scattering does not depend on the energy transfer and thus cannot lead to this asymmetry of the spectra. The asymmetry may also come from the limitation of the dynamic range on the side of positive energy transfers.
In fact, the discrepancy between the input dynamic structure factor and the data from the global simulation is due to several reasons. We notice an increase in the simulated width compared to the input $S(q,\omega)$ which partly comes from multiple scattering (see Fig. 4.41). However, this discrepancy in the width also exists with single scattering only. Hence it may also be caused by the resolution function of the instrument. The latter is usually determined from a vana-

dium sample, on the elastic line. It does not give any information about energy resolution for quasi-elastic or inelastic processes and the energy resolution is assumed to be constant (equal to its value on the elastic line) for a given momentum transfer. This assumption is actually not true when using time-focusing: when time focusing is done on the elastic line, the energy resolution on the elastic line is much thinner than in the other ranges of energy. This effect is not accounted for in data treatment. This energy dependence of the resolution function may be available from the total simulation: the asymmetry of the signal, especially at small q, may be a consequence of the energy dependence of the resolution function. This asymmetry of the signal may not be visible in our experiments because the represented range of energy transfers (from -15 meV to 5 meV in Fig. 4.26) is reduced compared to the simulation (from -30 meV to 10 meV).

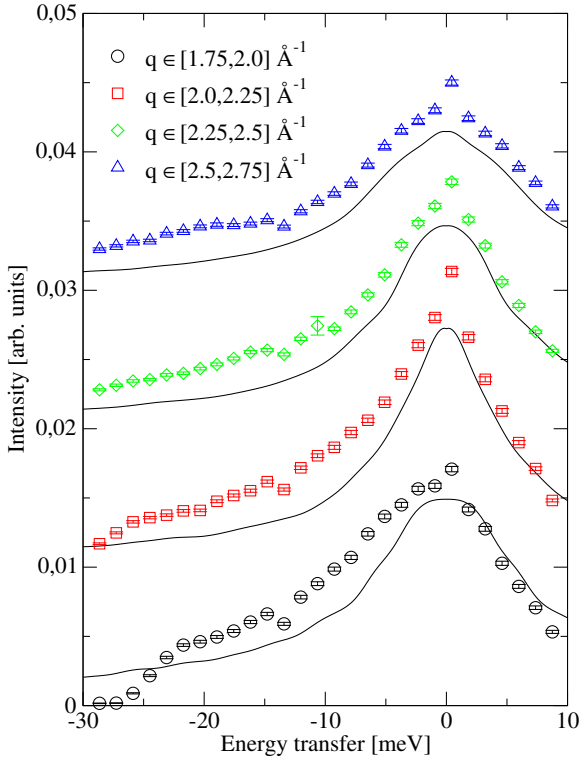

Figure 4.42: Simulated spectra (symbols) compared to input dynamic structure factor (solid line) for different q intervals. The curves are shifted in intensity by 0.01.

As seen in the result of the previous simulation (see Fig. 4.42), we observe some background signal at high energy transfers. We could have performed global simulation of the triple-axis experiment in order to have information about the background which could not be properly estimated in this experiment, thus enabling us to understand the discrepancy in the widths estimated from the time-of-flight and triple-axis experiments.

Thus, global simulations give information about the relevance of the corrections applied to neutron scattering data and the accuracy of what can be understood from experimental results. They help to explain the discrepancies between the results obtained from two different experimental techniques. Further development should include the sample environment consisting of

the silica sample holder and the furnace in our experiments. We actually had problems with the subtraction of the sample holder in the triple-axis measurements and a simulation of the influence of misalignment on the detected intensity could give information about the appropriate subtraction of the signal. Moreover, insight could be gained into the detailed influence (absorption, multiple scattering, inelastic processes) of the sample holder on the measured data. Furthermore, the parasitic signal from the furnace observed in the time-of-flight experiment at incident wavelength of 3 Å could be better understood by including a component describing the behaviour of the walls of the furnace in the simulation.

4.5 Conclusion

In this chapter, we have studied the case of *l*-Ge both experimentally with neutron scattering experiments and theoretically with molecular dynamics simulations.

From the molecular dynamics simulations, either *ab initio* or classical using a three-body potential, we have gained insight into several kinds of properties of the system, some of which are readily available from neutron scattering experiments, some of which are not. The classical MD simulation shows some limitations: it is able to give a global structural description of the system in agreement with the experimental data. However the dynamic properties are not well accounted for: the sound velocity for instance is overestimated by a factor of 2. For a given q the simulated phonon frequency is twice too high compared to the real value. This shows that the chosen potential is too rigid for modelling the dynamics of liquid germanium. Furthermore, structural details obtained from the *ab initio* calculations (see below) could not be obtained from the three-body potential since the local atomic structure is "rigidly" imposed by this.
On the other hand, we have used *ab initio* MD simulations. The structural features such as the static structure factor and the pair correlation function are very well reproduced. The simulations of the supercooled and amorphous phases give more information about the structural arrangements of the system: the amorphous phase is made of tetrahedral formations; the hypothesis of the β-tin local structure of the liquid is consistent with the computed quantities but further investigation could definitely determine the local arrangements in the liquid. Also the dynamic properties are quite well accounted for. The dispersion of the acoustic phonon was also in close agreement with the experimental results although dynamic properties are quite difficult to compute due to rather low statistics. The evolution of the relaxation time characteristic of the system was also computed from this simulation and compared to two theoretical models.
These simulations have shown the relative merits of classical and *ab initio* methods and have increased our understanding of the structure and dynamics of liquid and amorphous germanium. Furthermore, they give reliable trajectories for more detailed investigation of the structural and dynamic aspects.

On the experimental side, two kinds of inelastic neutron scattering experiments were carried out using a time-of-flight and a triple-axis spectrometer. They were the first quasi-elastic neutron scattering measurements of liquid germanium, although inelastic X-ray scattering experiments had already been used albeit with poorer statistics. From the quasi-elastic neutron scattering experiments, the energy width of the spectra was extracted. We also notice a significant difference in the magnitude of the width measured on FOCUS and 4F1. This discrepancy may originate from data treatment: in the triple-axis experiment, the available energy range is almost symmetric although it is not as wide as in time-of-flight experiments. This reduced range of energy

transfers leads to a bad evaluation of the background noise and hence must have consequences on the estimated width of the signal. On the other side, in the time-of-flight experiment, the measured spectra are very asymmetric which must also lead to uncertainties in the extracted width. Also in both experiments, we had problems with the alignment of the sample holder between empty cell and liquid germanium measurements. Moreover, the subtraction of the signal from the sample holder had to be done very carefully. All these facts show the difficulty of extracting accurate and reliable width from two different kinds of experiments. The experimental width can be related to the relaxation time computed from the MD simulation. The comparison of simulated and experimental energy widths gives a rather good agreement: the evolution of the width follows the same shape with a deep minimum around 2.5 Å^{-1} and a plateau between 2.8 Å^{-1} and 3.3 Å^{-1}. However the experimental and simulated widths do not exactly have the same magnitude: the simulated width is almost twice larger than the experimental one. This limited accuracy of the simulation may come from the quite noisy statistics of the dynamic structure factor. Ultimately the accuracy of the simulation will be apparent when the width of the experimental signal has been reliably determined.

Finally we have shown the coupling between instrument and sample simulation. This complete simulation of a neutron scattering experiment was done with the FOCUS time-of-flight spectrometer and a sample of *l*-Ge described by its dynamic structure factor computed from the *ab initio* molecular dynamics simulation. From this simulation, we gain information about the interplay of the different artefacts such as resolution function, multiple scattering and coupling between the contributions from the sample and the instrument. This simulation is likely to show trends in the expected experimental signal rather than to simulate the experimental signal. A simulation of the experiment with the triple-axis spectrometer could have reproduced a reasonable background signal of the experiment and therefore explained why we were not able to extract widths of the same magnitude from both experiments. Thus, helping in the determination of the characteristics of the signal which have a great importance on the extracted properties may be an important application of complete simulations of neutron scattering experiments. Moreover we can imagine including the sample holder and sample environment (cryostat or furnace) in the simulation in order to compute their precise influence on the detected signal. This could have explained the artefact from the furnace we observed in the time-of-flight experiment with incident wavelength of 4 Å. We could also have compared the simulations of an aligned/misaligned sample holder in the detected intensity and gained insight into the appropriate subtraction factor for a misaligned sample holder.

Conclusion

In any neutron scattering experiment, the interaction between neutrons and sample gives insight into the structure and/or dynamics of the material under study. In this work, we have explored a scheme for the simulation of neutron scattering experiments. It consists of performing a simulation accounting for both the instrument and the sample. The propagation and interaction of neutrons in the instrument is accounted for by a Monte Carlo ray-tracing simulation while neutrons interacts with the sample through the dynamic structure factor which gives information about the structure and dynamics of the sample. The nuclear interaction between neutrons and sample consists in exchanges of momentum and energy. In the simulation, the latter occur with a probability given by the relative intensities of the (q, ω) events as represented by the dynamic structure factor. The latter is calculated from molecular dynamics simulations, with classical or *ab initio* methods. The interactions accounted for in $S(q, \omega)$ comprise elastic, inelastic, coherent and incoherent contributions to the signal. Also absorption of neutrons in the sample is accounted for as well as multiple scattering. Concerning the size and shape of the sample, they are variables of the simulation and their effect on the respective intensities of the different contributions to the signal can be studied. In simulations, the correlations and coupling of these effects can be accounted for all together or separately. This is one of the advantages of such simulations upon experiments where the detected signal is due to all effects coming from instrument, sample and their coupling.

The assessment of these simulations of neutron scattering experiments was done on two kinds of isotropic samples. With liquid helium, we modelled the dynamic structure factor from the measured dispersion curve. The simulation of an experiment with this sample shows the effect of multiple scattering on the shape of the detected inelastic features: from the second and higher orders of scattering, we obtain higher energy transfers than those given by the dispersion curve and features that are irrelevant for a liquid, such as the elastic peak observed with the second order of scattering. Moreover with the simulation of a triple-axis spectrometer, scans with constant momentum transfer can be performed as in a real experiment. They show the influence of the resolution function: the position of the maximum of intensity when scanning the energy is shifted with respect to the expected value given as input in the dynamic structure factor. Thus the simulation of a triple-axis experiment on liquid helium shows clearly the influence of the resolution ellipsoid on the measurement. With liquid rubidium, we have calculated the dynamic structure factor from the trajectories of a classical molecular dynamics simulation. The computed $S(q, \omega)$ shows good agreement with the measured one, as well as the structural quantities deduced from the MD simulation. We have also computed several quantities which give insight into the diffusive behaviour of the system. Using the calculated dynamic structure factor, the influence of the size and shape of the sample can be studied and gives information about the compromise between detected intensity and ratio of multiple scattering. In simulations, some detection ranges can be reduced in order to avoid some features of the behaviour of the sample

and emphasize others. For instance the range of momentum transfer can be chosen in order to see the signal due to the acoustic phonon which, otherwise, would be smeared out by the intense quasi-elastic features coming from higher momentum transfers. Moreover the evolution of the shape of the signal, for example the behaviour of the quasi-elastic width, can be computed as a function of q and the contributions from coherent and incoherent scattering can be separated. These two test cases consequently give information about the abilities of such simulations of neutron scattering experiments. We expect the latter to show the trend of the different effects giving rise to the experimental signal.

The next stage consisted of performing both experiment and simulation on a given sample. For this purpose, liquid germanium was chosen for its scientific interest: the structure of this material is not very well understood and its dynamics have not been studied in detail. The properties of this sample have been investigated both theoretically and experimentally.
On the theoretical side, classical molecular dynamics simulations using a three-body potential have given good structural results but poor agreement concerning the dynamic properties of the system as obtained from inelastic X-ray scattering. The sound velocity, for instance, was overestimated by a factor of two compared to the experimental value. This shift of the acoustic excitation to higher frequency can be attributed to the analytical form of the chosen potential with a three-body contribution which strongly emphasizes the importance of tetrahedral arrangements in the liquid. Consequently we decided to investigate *ab initio* molecular dynamics simulations. Although this method is quite time-consuming and gives rather poor statistics as compared to classical molecular dynamics simulations, it does not depend on the choice of an empirical potential since the interaction between nuclei is obtained from the electronic structure and total energy of all the nuclei. The dynamic structure factor computed from this simulation was actually quite noisy due to the small number of atoms included in the simulation. However, we were able to determine the frequency of the acoustic excitation as a function of q as well as the quasi-elastic behaviour of the system at higher q values. Both structural and dynamic features calculated with this method were found in agreement with the experimental results. Moreover a quench to the amorphous state of the system reveals the local structure of this system and allows an hypothesis to be made about the structural features observed in the liquid.
From the experimental point of view, we carried out the first neutron scattering measurement of the quasi-elastic behaviour of l-Ge. This investigation was performed on both time-of-flight and triple-axis spectrometers. Previously an inelastic X-ray experiment had been performed on liquid germanium. In particular it gave insight into the behaviour of the acoustic excitation. Our experiments are the first to study the evolution of the diffusive properties of the sample, the latter being characterized by the quasi-elastic features of the experimental signal. Both experiments gave insight into the de Gennes narrowing phenomenon occurring in the sample at q values where the static structure factor shows intense features. The evolution of the widths of spectra as a function of q values are quite similar in the experiment and in the simulation although we notice some discrepancies in the magnitude of the width.
Finally, the simulation of a neutron scattering experiment on the FOCUS spectrometer with a sample of liquid germanium was performed. Liquid germanium was described by the dynamic structure factor computed from the *ab initio* molecular dynamics simulation. This simulation clearly shows that the simulated (q, ω) events match the predicted dynamic range, which follows from the proper resolution of the conservation equations when dealing with the energy and momentum transfers in the sample. Also the contribution of multiple scattering to the total scattered signal as a function of q was simulated. It indicates that the amount of multiple scattering depends on the static structure factor of the sample. Concerning the simulated spectra,

they show non trivial features which may be attributed to the resolution of the instrument and the interaction between neutrons and liquid Ge leading to absorption, multiple scattering and quasi-elastic processes. These contributions are quite difficult to interpret, but they give insight into the complexity of the features of the measured signal.

In view of these results, rather than giving a very accurate description of the experimental signal, simulation of complete neutron scattering experiments may be regarded as a tool for investigating the impact of the different parasitic contributions to the detected signal. Several problems persist. On the one hand, the description of some optical components (Fermi chopper or monochromators for example) of neutron scattering experiments still lacks accuracy and do not account for the complexity of the interactions between the neutron beam and the instrument. On the other hand, accurate molecular dynamics simulations of both structure and dynamics are quite difficult to do and the shape of structural and dynamic features of liquids is sometimes too smooth for giving rise to clear artefacts, due to multiple scattering for instance. However, due to the smooth behaviour of the structure and dynamics of disordered systems, this approach is much more relevant in this case than for crystals: in liquid and amorphous systems, the smooth structural and dynamic signal from the sample is much affected by the unwanted contributions, while for crystals, the structure and dynamics peculiar to the sample is easily separated from the other less intense features of the measured signal. Furthermore, simulation of neutron scattering experiments may be seen as a training tool for students and new users of neutron scattering facilities, since it allows better understanding of the importance and coupling of the different effects involved in a neutron scattering experiment.

Perspectives

We now have a better view of what can be understood from global simulations. Although it was not originally intended, we performed equivalent quasi-elastic measurements on TAS and TOF machines in France and Switzerland. We should have obtained the same $S(q,\omega)$ for l-Ge but this was not the case. A number of problems relating to the reduction of the data sets have become obvious and demonstrate clearly the need for global simulations which show the different contributions to and perturbations of the measured signals on different instruments, for example general background signals and signals from the sample holders and environment. In the time-scale of this thesis it was not possible to implement an accurate simulation of the 4F1 TAS instrument, coupled to the l-Ge simulation. When this is done, we will be able to converge on a single experimentally determined function for $S(q,\omega)$ for liquid Ge and compare this with the *ab initio* results.

In the simulations presented here, the sample cell is not accounted for. It can sometimes have a great importance in the measured signal as in our experiment with liquid germanium and a vitreous silica sample holder. This kind of container gives even a stronger signal than liquid germanium. The importance of sample holder subtraction was particularly crucial in our triple-axis experiment where misalignment between the two measurements gave rise to a bad sample holder subtraction. Thus simulations accounting for both sample and sample cell can be useful for determining the impact of the sample cell on the measured data. Many sample holders can be represented by a new McStas component for the simulation of powders presently under development. This component is intended to account for elastic and multiple scattering in powder samples and usual sample holders may be considered in this way. However, silica

sample cells, for instance, also give rise to inelastic features and are consequently more difficult to handle, although the sample module described in this work could be useful for this purpose. Moreover, the problem of sample environment also involves heating or cooling devices such as furnaces and cryostats. These may also lead to artefacts in the measured data. This was the case in our high resolution time-of-flight data on *l*-Ge. Note however that these devices are often made of aluminum, tantalum or niobium which could be handled by the powder component.

Moreover the simulation scheme devised for neutron scattering experiments on isotropic samples could be extended to crystalline samples. In such samples, the dynamic structure factor is four-dimensional, with three dimensions associated with the momentum transfer and one with the energy transfer. Thus the computational effort would be much higher than for isotropic samples, concerning both the required memory (handling of four-dimensional well resolved matrices) and the calculation time. Moreover for such samples, the structural and dynamic features are much better defined than for liquids and disordered systems and interpretation of the data, apart from resolution effects, is not so much affected by other contributions than first order scattering. Understanding the resolution function in detail in inelastic measurements on modern spectrometers, with complex neutron optics, will be the main goal of this work.

In the end, in a self-consistent scheme, one could imagine to use experimental raw data as input of the sample module, instead of computing $S(q, \omega)$ from molecular dynamics simulations. The result of the simulated experiment could be properly subtracted from the raw experimental data and the result of the subtraction used as a new input of the experiment simulation. The process could be repeated until convergence is reached between the result of the simulation and the experimental raw data. This would be another way for removing the unwanted contributions from the experimental results.

A

Some details about the sample module

A.1 Choosing the scattering position

Let us now explain how the scattering position in the sample is determined. The probability that the neutron scatters between two positions x and $x + dx$ is given by $\mu e^{-\mu x} dx$, where μ is the linear attenuation.
If the path of the neutron to exit the sample is denoted as d_{out}, the probability that the neutron scatters before exiting the sample is :

$$P(d_{scatt} < d_{out}) = \int_0^{d_{out}} \mu e^{-\mu x} dx = 1 - e^{-\mu d_{out}}. \tag{A.1}$$

If we assume that the neutron scatters within distance d_{out}, then the probability that is scatters within a distance $x < d_{out}$, given that it scatters within d_{out} is :

$$\begin{aligned} P(d_{scatt} < x | d_{scatt} < d_{out}) &= \frac{P([d_{scatt} < x] \cap [d_{scatt} < d_{out}])}{P(d_{scatt} < d_{out})} \\ &= \frac{1 - e^{-\mu x}}{1 - e^{-\mu d_{out}}}. \end{aligned} \tag{A.2}$$

This is the cumulated density or repartition function of the probability distribution denoted as : $G(x) = P(d_{scatt} < x | d_{scatt})$ which has values between 0 and 1.

Let us now generate a random number ξ from the uniform law between 0 and 1 and solve the equation : $x = G^{-1}(\xi)$. The scattering position is thus given by :

$$x = -\frac{1}{\mu} \ln(1 - \xi[1 - e^{-\mu d_{out}}]). \tag{A.3}$$

The last step consists of scaling the weight of the neutron by $1 - e^{-\mu d_{out}}$, in order to account for the initial assumption that the neutron would scatter before exiting the sample.

A.2 Selecting (q, ω) from the dynamic structure factor

The values of q and ω are chosen from the dynamic structure factor $S(q, \omega)$ (or the self part $S_s(q, \omega)$, or the sum of the two (scaled by the respective cross-sections for coherent and incoherent scattering)).

Assume that the computed dynamic structure factor consists of m q values and n ω values.

For drawing ω_i, we first compute the probability of the energy transfer $\hbar\omega_i$ for any momentum transfer :

$$P(\omega_i) = \frac{\sum_{j=1}^{m} S(q_j, \omega_i)}{\sum_{i=1}^{n}\sum_{j=1}^{m} S(q_j, \omega_i)} \tag{A.4}$$

where m is the number of q values for which $S(q, \omega)$ was computed and n is the corresponding number of ω values.
From this set of probabilities, we define the corresponding repartition function :

$$F(\omega) = P(\omega' < \omega) \tag{A.5}$$

which measures the probability that the measured ω' value be inferior than ω. This function has values between 0 and 1. Thus by drawing a random number from the uniform law in [0,1], we get a number ξ such that :

$$F(\omega' < \omega_{i-1}) < \xi \leq F(\omega' < \omega_i) \tag{A.6}$$

which gives the corresponding ω_i value. In this case, we can not use the inversion of the repartition function $F(\omega)$ since we do not know its analytical expression as was the case in (A.1).
For q, the procedure is the approximately the same. We define the following conditional probability :

$$P(q_j|\omega_i) = \frac{S(q_j, \omega_i)}{\sum_{j=1}^{m} S(q_j, \omega_i)}. \tag{A.7}$$

We build the repartition function related to the q values and pick a q value using the property of the uniform law as mentioned above.
If we want to simulate only coherent (resp. incoherent) scattering, we have to account for the relative intensities of these scattering processes. This gives insight into the separate contributions without modifying their relative intensities.
For a coherent signal only, the statistical weights of neutrons have to be scaled by a factor :

$$\frac{\sum_{i=1}^{m}\sum_{j=1}^{n} S(q_i, \omega_j)}{\sum_{i=1}^{m}\sum_{j=1}^{n} S(q_i, \omega_j) + S_s(q_i, \omega_j)}$$

For incoherent scattering only, $S(q_i, \omega_j)$ in the numerator is simply replaced by $S_s(q_i, \omega_j)$.

A.3 Calculation of the scattered wave vector

The calculation of the scattered wave vector is achieved via the use of two conservation laws : the energy and momentum conservation equations.

$$\hbar\omega = E_i - E_f \tag{A.8}$$

$$\boldsymbol{q} = \boldsymbol{k}_i - \boldsymbol{k}_f \tag{A.9}$$

When the final wave vector has to be computed, the variables $\boldsymbol{k}_i$, $\hbar\omega$ and $q = \|\boldsymbol{q}\|$ are known. Equation (A.8) can be rewritten in terms of wave vectors :

$$\hbar\omega = \frac{\hbar^2}{2m}(k_i^2 - k_f^2) \tag{A.10}$$

where k_i and k_f are the euclidian norms of $\boldsymbol{k}_i$ and $\boldsymbol{k}_f$ respectively.
From the latter equation, we can extract the two roots, k_f^+ and k_f^- which may be imaginary, if the energy transfer $\hbar\omega$ is larger than the incident energy $\frac{\hbar^2}{2m}k_i^2$. In such a case, the current neutron is ignored and absorbed, since no real solution can be found.
Let us now assume that a real value of k_f was chosen among the two real solutions.
The scattered wave vector is noted : $\boldsymbol{k}_f = k_f\hat{\boldsymbol{k}}_s$ where $\hat{\boldsymbol{k}}_s$ is a unit vector ($\|\hat{\boldsymbol{k}}_s\| = 1$).
Since we only know the norm of the scattering vector $\boldsymbol{q}$, equation (A.9) is replaced by : $q^2 = \|\boldsymbol{k}_i - \boldsymbol{k}_f\|^2$.
This is equivalent to :

$$q^2 = k_i^2 + k_f^2 - 2k_f\boldsymbol{k}_i \cdot \hat{\boldsymbol{k}}_s \tag{A.11}$$

where $\boldsymbol{k}_i \cdot \hat{\boldsymbol{k}}_s$ stands for the dot product of the vectors.
Now, we have to solve :

$$\boldsymbol{k}_i \cdot \hat{\boldsymbol{k}}_s = \frac{1}{2k_f}(k_i^2 + k_f^2 - q^2) = C \tag{A.12}$$

$$\|\hat{\boldsymbol{k}}_s\| = 1 \tag{A.13}$$

where C is a constant. $\hat{\boldsymbol{k}}_s$ can be decomposed as : $\hat{\boldsymbol{k}}_s = B\boldsymbol{k}_i + \boldsymbol{u}_0$ where B is a constant and $\boldsymbol{u}_0$ is a vector of $Vect(\boldsymbol{k}_i)^\perp$ (that is the orthogonal of the space generated by $\boldsymbol{k}_i$), which is a plane P.
Since we have : $\boldsymbol{k}_i \cdot \hat{\boldsymbol{k}}_s = C$, we can write : $B = \frac{C}{k_i^2}$. The vectors $\boldsymbol{u}_0$ such that $\|\hat{\boldsymbol{k}}_s\| = 1$ define a

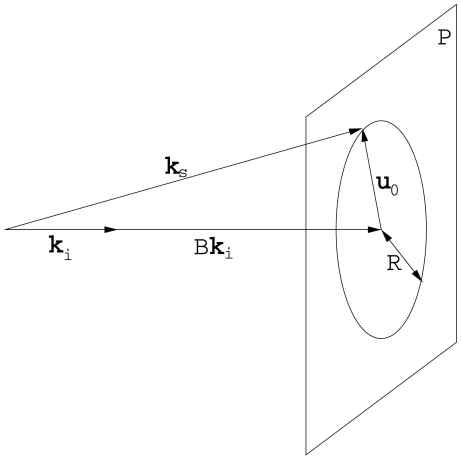

Figure A.1: How to compute $\hat{\boldsymbol{k}}_s$

circle of center of radius R : $\|\boldsymbol{u}_0\| = R$.
Since $\boldsymbol{u}_0$ and $B\boldsymbol{k}_i$ are orthogonal, we have now :

$$\frac{C^2}{k_i^2} + R^2 = \|\hat{\boldsymbol{k}}_s\|^2 = 1 \tag{A.14}$$

from which we deduce the radius of the circle :

$$R = \sqrt{1 - \frac{C^2}{k_i^2}}. \tag{A.15}$$

Let now define an orthonormal basis $(\boldsymbol{u}_1, \boldsymbol{u}_2)$ of the plane containing $\boldsymbol{u}_0$.
$\boldsymbol{u}_0$ can be decomposed as : $\boldsymbol{u}_0 = R(\cos\theta \boldsymbol{u}_1 + \sin\theta \boldsymbol{u}_2)$, where θ can be randomly drawn for a uniform distribution.
Finally, we obtain :

$$\hat{\boldsymbol{k}}_s = \frac{C^2}{k_i^2}\boldsymbol{k}_i + R(\cos\theta \boldsymbol{u}_1 + \sin\theta \boldsymbol{u}_2) \tag{A.16}$$

A.4 Parameters of the sample module

The sample module is defined by several parameters :

- *sqw_file* and *sqws_file* : files containing the coherent and incoherent dynamic structure factors with the corresponding q and ω values ; the q values are in $\mathrm{\AA}^{-1}$, the energy transfers in meV and the dynamic structure factor in meV^{-1} ;
- *coh_incoh* : determines what kind of processes are included in the simulation : 'C' for coherent only, 'I' for incoherent only and 'T' for both coherent and incoherent signals ;
- *nb_events* : determines which orders of multiple scattering are simulated : 0 means all orders are computed ; n > 1 : only n^{th} order is computed ;
- *sigma_abs* and *sigma_scatt* : absorption (for 2200 m/s) and scattering cross-sections of the current material (in barns) ;
- T : temperature for which the dynamic structure factor was computed (in Kelvins) ;
- *V_rho* : number density of the sample (in $\mathrm{\AA}^{-3}$) ;
- *radius_o, radius_i* and h : outer radius, inner radius and height of a cylinder-shaped sample (in m) ; set to 0 for a box-shaped sample ;
- *xwidth, yheight* and *zthick* : width, height and thickness of a box-shaped sample (in m) ; set to 0 for a cylinder-shaped sample ;
- *qmin* and *qmax* : minimum and maximum values of the wave vectors accounted for (in $\mathrm{\AA}^{-1}$) ; may be used for reducing the q range ;
- *epsilon* : threshold for the values in $S(q, \omega)$ (in meV^{-1}).

Bibliography

[1] J.L. Barrat and J.P. Hansen, *Basic Concepts for Simple and Complex Liquids* (Cambridge University Press, Cambridge, 2003)

[2] D.P. Landau and K. Binder, *A guide to Monte Carlo simulations in statistical physics* (Cambridge University Press, Cambridge, 2000)

[3] A. Rahman, *Phys. Rev.*, **136** (1964) A405

[4] K. Sköld and K.E. Larsson, *Phys. Rev.*, **161** (1967) 102

[5] J.R.D. Copley and J.M. Rowe, *Phys. Rev. Lett.*, **32** (1974) 49

[6] J.R.D. Copley and J.M. Rowe, *Phys. Rev. A*, **9** (1974) 1656

[7] A. Rahman, *Phys. Rev. Lett.*, **32** (1974) 52

[8] A. Rahman, *Phys. Rev. A*, **9** (1974) 1667

[9] A. Arbe, J. Colmenero, F. Alvarez, M. Monkenbusch, D. Richter, B. Farago and B. Frick, *Phys. Rev. E*, **67** (2003) 051802

[10] A. Meyer, J. Horbach, W. Kob, F. Kargl and H. Schober , *Phys. Rev. Lett.*, **93** (2004) 27801

[11] A.I. Kolesnikov, J.-M. Zanotti, C.-K. Loong, P. Thiyagarajan, A.P. Moravsky, R.O. Loutfy and C.J. Burnham *Phys. Rev. Lett.*, **93** (2004) 035503

[12] J.C. Smith, F. Merzel, C.S. Vermaa dn S. Fischer, *Journal of Molecular Liquids* **101** (2002) 27

[13] T. Itami, S. Munejiri, T. Masaki, H. Aoki, Y. Ishii, T. Kamiyama , Y. Senda, F. Shimojo, and K. Hoshino, *Phys. Rev. B*, **67** (2003) 064201

[14] R.L. McGreevy, *J. Phys.: Condens. Matter*, **13** (2001) R877

[15] P.A. Egelstaff, *An Introduction to the Liquid State* (Oxford Science Publications, Oxford, 1994)

[16] J.P. Hansen and I.R. McDonald, *Theory of Simple Liquids* (Academic Press, New York, 1976)

[17] U. Balucani and M. Zoppi, *Dynamics of the Liquid State* (Oxford University Press, Oxford, 1994)

[18] P. Damay, *J. Phys. IV*, **111** (2003) 3

[19] P.G. De Gennes, *Physica*, **25** (1959) 825

[20] G.L. Squires, *Introduction to the theory of thermal neutron scattering* (Cambridge University Press, Cambridge, 1978)

[21] S.W. Lovesey, *Theory of neutron scattering from condensed matter. Vol. 1 Nuclear scattering* (Oxford University Press, Oxford, 1986)

[22] J. Schweizer, *J. Phys. IV*, **111** (2003) 19

[23] *Neutron and Synchrotron Radiation for Condensed Matter Studies, Volume 1* (Les Editions de Physique - Springer-Verlag, 1993)

[24] M. Bee, *Quasielastic neutron scattering. Principles and applications in solid state chemistry, biology and materials science* (Adam Hilger, Bristol and Philadelphia, 1988)

[25] R. Kubo, *J. Phys. Soc. Japan*, **12** (1957) 570

[26] J.M. Haile, *Molecular Dynamics Simulation - Elementary Methods* (Wiley Interscience Publication, 1992)

[27] M.P. Allen and D.J. Tildesley, *Computer Simulation of Liquids* (Oxford University Press, Oxford, 1989)

[28] *The CCP5/Marie Curie Actions : Molecular Simulation Summer School 2004*, Cardiff University (July 2004)

[29] M. Born and Th. Von Karman, *Physik. Z.*, **13** (1912) 297

[30] L.R. Pratt and S.W. Haan, *J. Chem. Phys.*, **74** (1981) 1864

[31] L.R. Pratt and S.W. Haan, *J. Chem. Phys.*, **74** (1981) 1873

[32] N. Metropolis, A.W. Rosenbluth, M.N. Rosenbluth, A.H. Teller and E. Teller , *J. Chem. Phys.*, **21** (1953) 1087

[33] L. Verlet, *Phys. Rev.*, **159** (1967) 98

[34] M.C. Payne, M.P. Teter, D.C. Allan, T.A. Arias and J.D. Joannopoulos *Rev. Mod. Phys.*, **64** (1992) 1045

[35] A. Pasquarello, *J. Phys. IV*, **111** (2003) 373

[36] M.E. Tuckerman, *J. Phys.: Condens. Matter*, **14** (2002) R1297

[37] D. Marx and Jürg Hutter, *Ab Initio Molecular Dynamics: Theory and Implementation* (John von Neumann Institute for Computing, Juelich, 2000)

[38] M. Benoit, *Ab initio molecular dynamics*, Formation CNRS-Université de Montpellier II

[39] Y. Pouillon, *Propriétés structurales et électroniques d'agrégats CuO_n (n=1-6) et du composé solide $Cu_2(OH)_3(NO_3)$: une étude par la fonctionnelle de densité*, Thèse (2002), Université Louis Pasteur (Strasbourg I)

[40] K. Ohno, K. Esfarjani and Y. Kawazoe, *Computational Materials Science - From Ab initio to Monte Carlo methods* (Springer Series in Solid-State Sciences, Berlin, 1999)

[41] P. Hohenberg and W. Kohn, *Phys. Rev.*, **136** (1964) B864

[42] W. Kohn and L.J. Sham, *Phys. Rev.*, **140** (1965) A1133

[43] D.M. Ceperley and B.J. Alder, *Phsy. Rev. Lett.*, **45** (1980) 566

[44] R. Car and M. Parrinello, *Phys. Rev. Lett.*, **55** (1985) 2471

[45] H.J. Monkhorst and J.D. Pack, *Phys. Rev. B*, **13** (1976) 5188

[46] H. Hellmann, *Z. Phys.*, **85** (1933) 180

[47] R.P. Feynman, *Phys. Rev.*, **56** (1939) 340

[48] M.J. Cooper and R. Nathans, *Acta Cryst.*, **23** (1967) 357

[49] J. Šaroun and J. Kulda, *Physica B* **234-236** (1997) 1102

[50] D. Wechsler, G. Zsigmond, F. Streffer, J.A. Stride and F. Mezei , *Physica B*, **276-278** (2000) 71

[51] L.L. Daemen, P.A. Seeger, R.P. Hjelm and T.G. Thelliez, *Proc. of the SPIE*, **3771** (1999) 80

[52] W.-T. Lee and X.-L. Wang, *Neutron News*, **13** (2002) 30

[53] K. Lefmann and K. Nielsen, *Neutron News*, **10/3** (1999) 20

[54] K. Nielsen and K. Lefmann, *Physica B*, **283** (2000) 426

[55] E. Farhi, T. Hansen, A. Wildes, R. Ghosh and K. Lefmann, *Appl. Phys. A*, **74** (2002) S1471

[56] P. Andersen, K. Lefmann, L. Theil Kuhn, P.K. Willendrup and E. Farhi, *Physica B*, **350** (2004) E721

[57] P.A. Seeger, L.L. Daemen, E. Farhi, W.T. Lee, L. Passell, J. Šaroun, X.L. Wang and G. Zsigmond, *Neutron News*, **13/4** (2002) 24

[58] W.T. Lee, X.L. Wang, J.L. Robertson, F. Klose and CH. Rehm, *Appl. Phys. A*, **74** (2002) S1502

[59] A.R. Wildes, J. Šaroun, E. Farhi, I. Anderson, P. Hoghoj and A. Brochier, *Physica B*, **276-278** (2000) 177

[60] L. Alianelli, M. Sànchez del Rìo, R. Felici, K.H. Andersen and E. Farhi, *Physica B*, **350** (2004) E725

[61] H. Edwards, K. Lefmann, B. Lake, K. Nielsen and P. Skaarup, *Appl. Phys. A*, **74** (2002) S1492

[62] G. H. Vineyard, *Phys. Rev.*, **96** (1954) 93

[63] V.F. Sears, *Advan. Phys.*, **24** (1975) 1

[64] J.R.D. Copley, *Comput. Phys. Comm.*, **7** (1974) 289

[65] D.F.R. Mildner and J.M. Carpenter, *Acta Cryst. A*, **33** (1977) 954

[66] J. Dawidowski, F.J. Bermejo and J.R. Granada, *Phys. Rev. B*, **58** (1998) 706

[67] J. Wuttke, *Phys. Rev. E*, **62** (2000) 6531

[68] J. Mayers, A.L. Fielding and R. Senesi, *Nucl. Instr. and Meth. A*, **481** (2002) 454

[69] P.A. Seeger, *Nucl. Instr. and Meth. A*, **510** (2003) 290

[70] T. Rog, K. Murzyn, K. Hinsen and G.R. Kneller, *J. Comput. Chem.*, **24** (2003) 657

[71] Z. Jian, Z. Kaiming and X. Xide, *Phys. Rev. B*, **41** (1990) 12915

[72] R.J. Donnelly, J.A. Donnelly and R.N. Hills, *J. Low Temp. Phys.*, **44** (1981) 471

[73] W.C. Pilgrim, R. Winter and F. Hensel, *J. Phys.:Condens. Matter*, **5** (1993) B183

[74] R. Winter, W.C. Pilgrim and F. Hensel, *J. Phys.:Condens. Matter*, **6** (1994) A245

[75] R. Winter, W.C. Pilgrim, F. Hensel, C. Morker and W. Gläser, *J. Non-Cryst. Solids*, **156-158** (1993) 9

[76] G. Kahl, S. Kambayashi and G. Nowotny, *J. Non-Cryst. Solids*, **156-158** (1993) 15

[77] G. Kahl and S. Kambayashi, *J. Phys.: Condens. Matter*, **6** (1994) 10897

[78] G. Kahl, *J. Phys.: Condens. Matter*, **6** (1994), 10923

[79] N.W. Ashcroft, *Phys. Lett.*, **23** (1966) 48

[80] S. Ichimaru and K. Utsumi, *Phys. Rev. B*, **24** (1982) 7385

[81] W.C. Pilgrim, M. Ross, L.H. Yang and F. Hensel, *Phys. Rev. Lett.*, **78** (1997) 3685

[82] S. Munejiri, F. Shimojo and K. Hoshino, *J. Phys.: Condens. Matter*, **12** (2000) 4313

[83] J.F. Wax, R. Albaki and J.L. Bretonnet, *Phys. Rev. B*, **65** (2001) 14301

[84] M. Boulahbak, N. Jakse, J.F. Wax and J.L. Bretonnet, *J. Chem. Phys*, **108** (1998) 2111

[85] R. Albaki, J.F. Wax and J.L. Bretonnet, *Phys. Rev. B*, **66** (2002) 14201

[86] S. Kambayashi and G. Kahl, *Phys. Rev. A*, **46** (1992) 3255

[87] Y. Waseda, *The Structure of Non-Crystalline Materials* (McGraw-Hill, New York, 1981)

[88] W.H. Ohse, *Handbook of Thermodynamic and Transport Properties of Alkali Metals* (Blackwell Scientific, Oxford, 1985)

[89] Y.K. Vorha, K.E. Brister, S. Desgreniers, A.L. Ruoff, K.J. Chang and M.L. Cohen, *Phys. Rev. Lett.*, **56** (1986) 1944

[90] S.P. Isherwood, B.R. Orton and R. Mănăilă, *J. Non-Cryst. Solids*, **8-10** (1972) 691

[91] Y. Waseda and K. Suzuki, *Z. Physik B*, **20** (1975) 339

[92] A. Filipponi and A. Di Cicco, *Phys. Rev. B*, **51** (1995) 12322

[93] J.P. Gabathuler and S. Steeb, *Z. Naturforsch.*, **34a** (1979) 1314

[94] M. Davidović, M. Stojić abd Dj. Jović, *J. Phys. C: Solid State Phys.*, **16** (1983) 2053

[95] M.C. Bellissent-Funel and R. Bellissent, *J. Non-Cryst. Solids*, **65** (1984) 383

[96] P.S. Salmon, *J. Phys. F: Met. Phys.*, **18** (1988) 2345

[97] Y. Kawakita, S. Takeda, T. Enosaki, K. Oshima, H. Aoki, T. Masaki and T. Itami, *J. Phys. Soc. Jpn.*, **71** (2002) 12

[98] S. Hosokawa, Y. Kawakita, W.C. Pilgrim and H. Sinn, *Phys. Rev. B*, **63** (2001) 134205

[99] N. Yoshimoto, H. Shibata, M. Yoshizawa, K. Suzuki, K. Shigematsu and S. Kimura, *Jpn. J. Appl. Phys.*, **35** (1996) 2754

[100] T. Bodensteiner, C. Morkel, P. Müller and W. Gläser, *J. Non-Cryst. Solids*, **117-118** (1990) 116

[101] W.C. Pilgrim, S. Hosokawa, H. Saggau, H. Sinn and E. Burkel, *J. Non-Cryst. Solids*, **250-252** (1999) 96

[102] E.G.D. Cohen, P. Westerhuijs and I.M. de Schepper, *Phys. Rev. Lett.*, **59** (1987) 2872

[103] N.W. Ashcroft, *Nuovo Cimento D*, **12** (1990) 597

[104] F.H. Stillinger and T.A. Weber, *Phys. Rev. B*, **31** (1985) 5262

[105] K. Ding and H.C. Andersen, *Phys. Rev. B*, **34** (1986) 6987

[106] A. Arnold, N. Mauser and J. Hafner, *J. Phys.: Condens. Matter*, **1** (1989) 965

[107] W. Yu, Z.Q. Wang and D. Stroud, *Phys. Rev. B*, **54** (1996) 13946

[108] G. Kresse and J. Hafner, *Phys. Rev. B*, **47** (1993) 558

[109] G. Kresse and J. Hafner, *Phys. Rev. B*, **49** (1994) 14251

[110] N. Takeuchi and I.L. Garzón, *Phys. Rev. B*, **50** (1994) 8342

[111] V. Godlevsky, J.R. Chelikowsky and N. Troullier, *Phys. Rev. B*, **52** (1995) 13281

[112] R.V. Kulkarni, W.G. Aulbur and D. Stroud, *Phys. Rev. B*, **55** (1997) 6896

[113] S. Munejiri, F. Shimojo, K. Hoshino and T. Itami, *J. Non-Cryst. Solids*, **312-314** (2002) 182

[114] J.D. Chai, D. Stroud, J. Hafner and G. Kresse, *Phys. Rev. B*, **67** (2003) 104205

[115] G. Kresse and J. Furthmüller, *Comput. Mater. Sci.*, **6** (1996) 15

[116] G. Kresse and J. Furthmüller, *Phys. Rev. B*, **54** (1996) 11169

[117] D. Vanderbilt, *Phys. Rev. B*, **41** (1990) 7892

[118] P.V. Pavlov and E.V. Dobrokhotov, *Sov. Phys. Solid State*, **12** (1970) 225

[119] G. Etherington, A.C. Wright, J.T. Wenzel, J.C. Dore, J.H. Clarke and R.N. Sinclair, *J. Non-Cryst. Solids*, **48** (1982) 265

[120] B.R. Orton and S.P. Woodisse, *J. Phys. F : Metal Phys.*, **3** (1973) 1141

[121] http://sinq.web.psi.ch/sinq/instr/focus/focus.html

[122] S. Janssen, J. Mesot, L. Holitzner, A. Furrer and R. Hempelmann, *Physica B*, **234-236** (1997) 1174

[123] S. Janssen, D. Rubio-Temprano and A. Furrer, *Physica B*, **283** (2000) 355

[124] S. Susman, K.J. Volin, D.G. Montague and D.L. Price, *Phys. Rev. B*, **43** (1991) 11076

[125] http://www.physics.uc.edu/ jph/emma/tas.htm

[126] http://www-llb.cea.fr/spectros/pdf/4f1-llb.pdf

Titre : Simulation complète d'une expérience de diffusion de neutrons : des systèmes modèles au germanium liquide.

Dans cette thèse, l'étude des liquides est envisagée d'un point de vue théorique et expérimental. La diffusion de neutrons permet l'investigation des propriétés structurales et dynamiques des liquides. Sur le plan théorique, les simulations par dynamique moléculaire sont d'un grand attrait car elles donnent accès aux positions et vitesses des atomes ainsi qu'aux forces qu'ils exercent entre eux. Elles permettent aussi de calculer les corrélations spatiales et temporelles, aussi mesurées par diffusion de neutrons. Par conséquent, les résultats de simulations par dynamique moléculaire et d'expériences de diffusion de neutrons peuvent être comparés afin d'améliorer notre compréhension de la structure et de la dynamique des liquides.

Toutefois, l'extraction de données fiables à partir des expériences de diffusion de neutrons étant délicate, nous proposons de simuler l'expérience dans son ensemble, c'est-à-dire l'instrument et l'échantillon, afin de mieux comprendre et évaluer l'impact des différentes contributions parasites (absorption, diffusion multiple associée à la diffusion élastique et inélastique, résolution instrumentale). Cette approche, dans laquelle l'échantillon est décrit par ses caractéristiques structurales et dynamiques calculées par dynamique moléculaire, est présentée et testée dans un premier temps sur des systèmes modèles isotropes.

Par la suite, le germanium liquide est étudié par diffusion inélastique des neutrons ainsi que par dynamique moléculaire classique et *ab initio*. Ceci permet ensuite de simuler l'expérience réalisée et d'évaluer l'influence sur le signal détecté des contributions de l'instrument et de l'échantillon.

Mots-clés : Diffusion de neutrons, structure et dynamique des liquides, simulation par dynamique moléculaire.

Title : A complete simulation of neutron scattering experiments: From model systems to liquid germanium.

In this thesis, both theoretical and experimental studies of liquids are done. Neutron scattering enables structural and dynamical properties of liquids to be investigated. On the theoretical side, molecular dynamics simulations are of great interest since they give positions and velocities of the atoms and the forces acting on each of them. They also enable spatial and temporal correlations to be computed and these quantities are also available from neutron scattering experiments. Consequently, the comparison can be made between results from molecular dynamics simulations and from neutron scattering experiments, in order to improve our understanding of the structure and dynamics of liquids.

However, since extracting reliable data from a neutron scattering experiment is diffucult, we propose to simulate the experiment as a whole, including both instrument and sample, in order to gain understanding and to evaluate the impact of the different parasitic contributions (absorption, multiple scattering associated with elastic and inelastic scattering, instrument resolution). This approach, in which the sample is described by its structure and dynamics as computed from molecular dynamics simulations, is presented and tested on isotropic model systems.

Then liquid germanium is investigated by inelastic neutron scattering and both classical and *ab initio* molecular dynamics simulations. This enables us to simulate the experiment we performed and to evaluate the influence of the contributions from the instrument and from the sample on the detected signal.

Keywords: Neutron scattering, structure and dynamics of liquids, molecular dynamics simulation.